The Role of the Magnetopause in Outer Radiation Belt Flux Dropouts

Frances Allana Staples

A dissertation submitted in partial fulfilment

of the requirements for the degree of

Doctor of Philosophy

of

University College London.

Mullard Space Science Laboratory

Department of Space and Climate Physics

University College London

9 December 2021

I, Frances Staples, confirm that the work presented in this thesis is my own. Where information has been derived from other sources, I confirm that this has been indicated in the work.

Abstract

The radiation belts are highly dynamic regions of relativistic particles trapped in the Earth's magnetic field. A delicate balance between particle acceleration and loss mechanisms results in the waxing and waning of radiation belt flux. Electrons may be lost by precipitation into the Earth's atmosphere, or through the magnetopause into interplanetary space. Periods of enhanced loss often results in flux dropouts, the near total drainage of electrons from the outer radiation belt. This thesis investigates the role of magnetopause shadowing in flux dropout events, carried out through large multi-satellite analysis of the magnetopause boundary and relativistic electron dynamics.

A database of ~20,000 magnetopause crossings is developed to assess the accuracy of a statistical magnetopause model. The measured magnetopause is found to be systematically closer to the radiation belts under compression than the statistical model suggests. Differences between measurements and model are greater still during interplanetary shock events. The results demonstrate that empirical magnetopause models should be used cautiously to interpret energetic electron losses by magnetopause shadowing.

New, multi-mission electron phase space density calculations are used to decipher electron dynamics during a flux dropout case study. Features of magnetopause shadowing are identified during the net-loss and the net-acceleration storm phases. Observations show that magnetopause shadowing may occur in two distinct ways; through direct intersection of electron drift path, or indirectly by radial transport towards the magnetopause. These observations demonstrate the importance of considering electron dynamics in multi-dimensional adiabatic coordinates. The characteristics of electron loss through atmospheric precipitation are also observed. Consequently, this method of phase space density analysis showed promise for differentiating loss processes. It is demonstrated how the multi-mission dataset improves time resolution of phase space density observations, without which electron dynamics would be misinterpreted. Methods of further work are recommended to verify the multi-dimensional characteristics of different loss processes.

Impact Statement

The Van Allen radiation belts are highly dynamic regions of relativistic particles trapped in Earth's magnetic field. A delicate balance between particle acceleration and loss mechanisms results in the waxing and waning of radiation belt flux. Spacecraft located in the radiation belts, such as telecommunications, navigational, and defence satellites, are vulnerable to the damage which radiation can cause. As well as satellite design, forecasting radiation flux plays a crucial part in protecting this space-based infrastructure. However, forecasting capabilities are limited by our understanding of this extremely complex region.

This thesis investigates events where nearly all radiation is drained from the outer radiation belt, known as flux dropouts. These events are caused by rapid loss through the outer boundary of Earth's magnetic field, the magnetopause, or through precipitation into the atmosphere, which are instigated by sudden changes to the solar wind. Dropouts often precede periods of rapid radiation belt enhancements and can pre-condition the magnetospheric plasma environment to limit particle acceleration, suppressing radiation belt enhancements. Given the importance of these events in forecasting radiation belt dynamics, many details of how they occur are still not understood, specifically the way in which each loss process contributes to the total loss of electrons. By analysing large multi-mission datasets, this thesis advances our understanding of dropouts in two key areas. First, the suitability of a magnetopause model which is used in forecasting models is assessed. From this work we make recommendations on the use of corrections to this model and suggest that new parameterisation of the magnetopause is required. Second, the time scale of a dropout due to magnetopause shadowing is resolved, and methods of deciphering different loss mechanisms is discussed. The latter work demonstrated the time resolution required of future spacecraft missions investigating radiation belt dynamics, which is far greater than is routinely available from current missions, and how new mission objectives must consider invaluable inter-mission spacecraft conjunctions to resolve these dynamics.

Acknowledgements

Foremost I would like to thank my supervisor Jonny Rae. Thank you for the countless skills and knowledge you have shared with me, for the many many hours you dedicated to mentoring me, and for having confidence in me when I had none in myself (and for knowing that carrots are better than sticks). Thank you to my supporting supervisors, Colin Forsyth for our many insightful conversations and for teaching me the meaning of thoroughness, and to Jasmine Kaur Sandhu for setting a shining example of dedication and integrity.

I would also like to give special thanks to two collaborators who have undoubtedly contributed to the successful completion of my thesis. Thank you to Kyle Murphy for taking me under your wing at Goddard, and for your continuing mentorship through my PhD. Thank you to Adam Kellerman for providing the most incredible and complicated dataset of phase space density, it has been both a joy and a nightmare delving into it. I would also like to thank the team of co-authors who contributed to our publications.

Thank you to the wonderful people at MSSL who have supported my PhD journey, especially to the plasma and planetary physics group members (past and present). To the most wonderful office mates, Michaela, Affelia, Richard, Qasim, Seong-Yeop - thank you for tolerating me when I was distracting you. Michaela, we went through this journey together and I couldn't have asked for a better friend and confidante. Thank you Jenny and Divya for *spacing* up my life.

Finally, I would like to thank Rich and my family for their support, without your confidence in me, I would never have finished this PhD. Thank you for being my emotional retreat, and for reading my entire thesis with three days' notice to fix my poor grammar.

I would like to acknowledge STFC for their financial support over the course of my PhD and thank examiners Lidia Van Driel and Robert Fear for dedicating the time to review and assess this thesis.

Table of Contents

List of Figures

List of Tables

Chapter 1 Background

1.1 The Van Allen Radiation Belts

Discovered by James Van Allen in 1958, the Van Allen radiation belts are regions of highly energetic charged particles which are trapped by the geomagnetic field in near-Earth space (Van Allen et al., 1958). Located at altitudes between ~ 0.1 – 7 R_E (where R_E is Earth radii), the Van Allen belts consist of two regions, a relatively stable proton belt where proton energies are ~ 10MeV - 1GeV, and a highly dynamic electron belt where electron energies range from 100s of keV to 10s of MeV.

Many space-based assets are situated in the Van Allen radiation belts, an environment damaging to both spacecraft components and human health. During space weather events called geomagnetic storms, the radiation levels in the Van Allen belts may rise by orders of magnitude (Friedel et al., 2002). The effects of this enhanced radiation exposure to satellites can range from anomalies in spacecraft operations to catastrophic failure of a satellite. For example, during a sequence of intense space weather events in October 2003, radiation levels in the Van Allen belts became so high that at least 20 satellites in Earth's orbit either entered safe mode or experienced temporary failure (initial report by Webb & Allen, 2004). A report by Cannon et al. (2013) later discussed further impacts of this event: The ADEOS-2 satellite, a Japanese Earth observation satellite worth $650 million, experienced severe radiation damage to its solar panels and subsequently failed. Radiation levels close to Earth also posed a risk to human health; such that the astronauts on the International Space Station were forced to take shelter. At lower altitudes airlines rerouted high latitude flights to avoid radiation exposure of cabin crew and passengers, costing airlines $10,000 to $100,000 per flight. It is vital to understand the underlying physical processes acting in the Van Allen radiation belts so that extreme events may be predicted, allowing for mitigation procedures to be carried out, limiting the damage to technology.

A variety of physical mechanisms are needed to understand the intensity of the outer radiation belt. Both large-scale topology and local electromagnetic

environment play a role in the energisation of radiation particles, whereas loss mechanisms act to drain the radiation belts with electrons escaping either into interplanetary space or Earth's atmosphere. The balance between acceleration and loss mechanisms results in the waxing and waning of this highly dynamic radiation region. All physical processes must be fully captured to build an accurate radiation belt forecasting model. Whilst most studies concentrate only on acceleration, this thesis is focused on understanding electron losses.

This chapter introduces the plasma physics concepts governing the dynamics of the radiation belt and the wider magnetospheric environment. Many of the basic plasma physics concepts discussed in this section are adapted from Baumjohann and Treumann (1996), Tsurutani and Lakhina (1997), Walt (1994). The reader is directed to these texts for further detail.

1.2 Single Particle Motion in a Dipolar Magnetic Field

Plasma is the fourth state of matter, perhaps lesser known than solids, liquids, and gases, despite being the most ubiquitous form of matter in the visible universe, making up over 99% of known baryonic matter. The plasma state is reached when a gas becomes highly ionised and the constituent charged particles are in equal numbers, such that the medium appears to behave quasi-neutral when stationary. Because plasmas consist of electrostatically charged particles, the motion of both individual constituent particles and the macroscopic motion of the plasma is governed by fluid mechanics and electromagnetism. To gain insight into the physics which governs the magnetospheric system and wider Solar-Terrestrial interactions, we first need to understand the behaviour of individual charged particles in magnetic fields.

The geomagnetic field extending into the space near Earth can be approximated as a dipole tilted at 11° to Earth's rotational axis. The distance from the centre of the Earth to a position on a dipole field line is given by

$$R = R_{eq} \cos^2 \lambda \qquad 1.1$$

where R_{eq} is the radial distance at which the magnetic field line crosses the equator, and λ is the angle from the magnetic equator, magnetic latitude. The McIlwain parameter, L-shell, is commonly used to describe position in Earth's magnetic field (McIlwain, 1961). L-shell labels a field line in a dipolar regime, where $L = R_{eq}/R_E$. Earth's surface is at $L = 1$.

Energetic particles in a dipolar magnetic field will follow three periodic motions:

1. Gyration about a magnetic field line,
2. Bounce motion between two magnetic mirror points,
3. Azimuthal drift about the Earth (eastward for electrons, westward for protons).

These trajectories may be derived from the Lorentz force equation:

$$\boldsymbol{F_L} = q(\boldsymbol{v} \times \boldsymbol{B} + \boldsymbol{E}) \tag{1.2}$$

where q and $\boldsymbol{v}$ respectively describe the charge and velocity of a particle moving through magnetic and electric fields which are denoted by $\boldsymbol{B}$ and $\boldsymbol{E}$ respectively.

1.2.1 Gyromotion

Let us consider Equation **1.2** in terms of the momentum, $\boldsymbol{p}$, components perpendicular and parallel to the magnetic field.

$$\boldsymbol{F_L} = \left(\frac{d\boldsymbol{p}}{dt}\right)_{\parallel} + \left(\frac{d\boldsymbol{p}}{dt}\right)_{\perp} \tag{1.3}$$

$$\left(\frac{d\boldsymbol{p}}{dt}\right)_{\parallel} = q\boldsymbol{E}_{\parallel} \tag{1.4}$$

$$\left(\frac{d\boldsymbol{p}}{dt}\right)_{\perp} = q(\boldsymbol{v} \times \boldsymbol{B} + \boldsymbol{E}_{\perp}) \tag{1.5}$$

For a particle traversing a uniform magnetic field $\boldsymbol{B}$ where there are no electric fields $\boldsymbol{E} = 0$, then Equation **1.4** and **1.5** become

$$\left(\frac{d\boldsymbol{p}}{dt}\right)_{\parallel} = 0 \qquad 1.6$$

$$\left(\frac{d\boldsymbol{p}}{dt}\right)_{\perp} = q(\boldsymbol{v}_{\perp} \times \boldsymbol{B}) \qquad 1.7$$

There is no change in momentum parallel to the magnetic field, therefore the particle moves at constant velocity along the magnetic field. Equation **1.7** shows there is a change in momentum perpendicular to the magnetic field and to the perpendicular velocity component. Therefore $v_{\perp}$ is constant and $\boldsymbol{F}_L$ acts as a centripetal force, resulting a gyromotion about the magnetic field. Noting that the direction of gyration is dependent on the charge of the particle. The overall trajectory of the particle is helical as the particle gyrates perpendicular to the magnetic field at a constant velocity parallel to the magnetic field, illustrated by Figure 1.1.

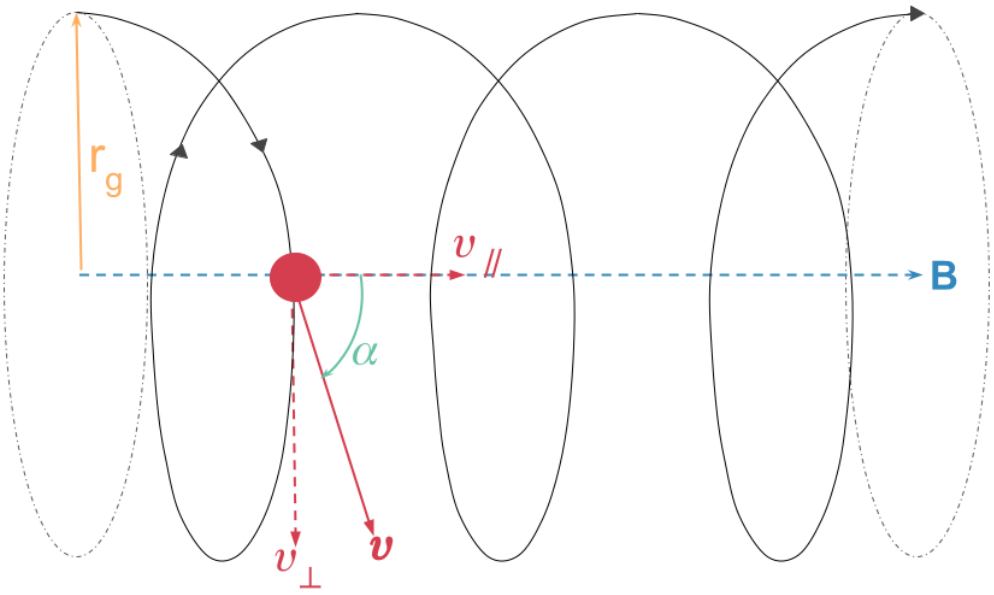

Figure 1.1 Illustration of helical charged particle motion (solid black line), in a constant magnetic field $\boldsymbol{B}$ (dotted blue line). Red lines illustrate the parallel and perpendicular velocity components, α is the pitch angle between velocity and the magnetic field, r_g is the particle gyro-radius.

The radius of gyration, r_g, is determined by considering that the Lorentz force is equal to centrifugal force $\boldsymbol{F}_c = m\theta^2 r_g$, where the angular velocity $\theta = v_{\perp}/r_g$.

$$r_g = \frac{mv_\perp}{qB} \quad 1.8$$

Because the gyrofrequency $\omega_g = \theta/2\pi = v_\perp/2\pi r_g$ (revolutions/second) we can use Equation **1.8** to derive ω_g (radians/second):

$$\omega_g = \frac{qB}{m} \quad 1.9$$

1.2.2 Bounce Motion

Now consider a magnetic field which converges, such as illustrated in Figure 1.2, where there are no electric fields. In this scenario, the magnetic field is no longer perpendicular to the plane of gyromotion, there is a component of the magnetic field, B_x, which is in the same plane as gyromotion. Therefore, there is a component of the Lorentz force which acts perpendicularly to the plane of gyromotion i.e., in the $-v_\parallel$ direction. This force is known as the 'mirror force' because the particle eventually reaches a mirror point where $v_\parallel = 0$ and the direction of particle trajectory reverses.

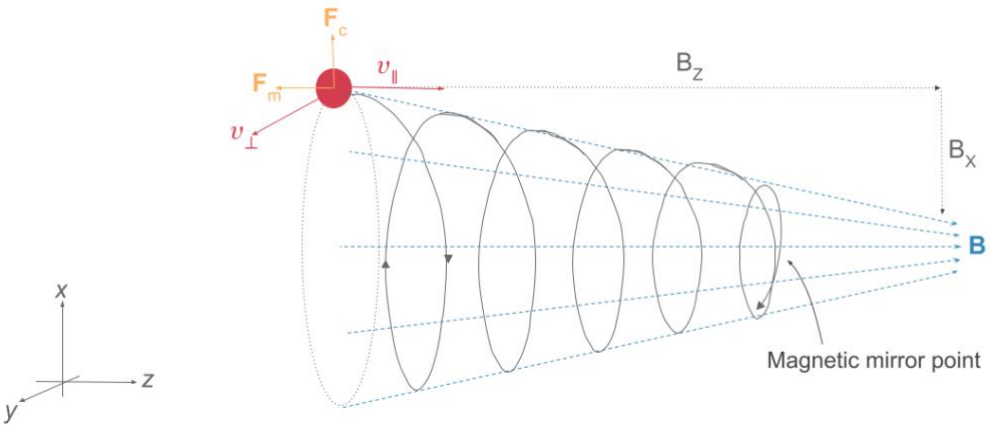

Figure 1.2 Illustration of the mirror effect in a converging magnetic field. $\boldsymbol{B}$ and $\boldsymbol{v}$ denote the directions of the magnetic field and particle velocity components respectively. Components of the Lorentz force are denoted as $\boldsymbol{F_c}$ and $\boldsymbol{F_m}$, which are the centripetal and mirror components respectively.

The consequence of this effect in a dipolar magnetic field, where the magnetic field converges at the northern and southern poles, is that particles become trapped between two magnetic mirror points. This is also known as a magnetic bottle, and particles will undergo a periodic bounce motion between the dipole hemispheres.

The pitch angle, α, is defined as the angle between the magnetic field direction and particle velocity, described by Equation **1**.**10**. Because the Lorentz force acts perpendicularly to particle velocity, the magnetic field does no work on the particle. It follows that, as parallel velocity of the particle decreases, there is a corresponding increase in perpendicular velocity such that the total kinetic energy of the particle remains constant. Through a bounce cycle, the pitch angle varies according to the variations in velocity components.

$$\alpha = \ tan^{-1}\left(\frac{v_{\perp}}{v_{\parallel}}\right) \tag{1.10}$$

The location of the mirror point may be expressed in terms of equatorial pitch angle by considering the conservation of the first adiabatic invariant, Equation **1**.**27**, between two points of magnetic field strength B_1 and B_2.

$$\frac{v_{\perp 1}^2}{B_1} = \ \frac{v_{\perp 2}^2}{B_2} \tag{1.11}$$

The perpendicular velocity may be expressed in terms of the total velocity and pitch angle; $v_{\perp} = v\,sin\,\alpha$.

$$\frac{B_2}{B_1} = \ \frac{(sin\,\alpha_2)^2}{(sin\,\alpha_1)^2} \tag{1.12}$$

At the magnetic mirror point, $v_{\parallel} = 0$, which implies that the pitch angle at the mirror point, α_m, is equal to 90° ($sin\,\alpha_m = 1$). It is therefore useful to define the magnetic field point in terms of equatorial pitch angle, α_{eq}. Substituting B_1 and B_2 as the magnetic field strength at the equator, B_{eq}, and the mirror point, B_m, respectively

$$B_m = \ \frac{B_{eq}}{\left(sin\,\alpha_{eq}\right)^2} \tag{1.13}$$

1.2.3 Electric Drift Motion

So far, it has been assumed there are no electric fields. Let us now consider an electric field, $\boldsymbol{E}$, with components which are parallel and perpendicular to a constant magnetic field.

Equation **1.4** shows that the force due to the parallel component of the electric field produces constant acceleration equal to $q\boldsymbol{E}_{\parallel}$**.** The result is that ions are accelerated constantly in the $\boldsymbol{E}_{\parallel}$ direction, whilst electrons are accelerated in the $-\boldsymbol{E}_{\parallel}$ direction. The electric fields created by the resulting charge separation act to cancel out the force due to the parallel electric field. It is therefore assumed in most geophysical plasmas that there is no parallel component to the electric field.

The perpendicular component of the electric field, $\boldsymbol{E}_{\perp}$, produces a constant force in the perpendicular direction, equal to $q\boldsymbol{E}_{\perp}$ (Equation **1.5**). As the particle gyrates about the magnetic field, the direction of $q\boldsymbol{E}$ acts to decrease the centrifugal force created by the magnetic field in one half of the gyro-orbit, and increase the centrifugal force in the other half, see Figure 1.3. The result of the variable net-force is that the particle drifts perpendicularly to both magnetic and electric fields. The drift velocity, $\boldsymbol{v}_{\boldsymbol{E}}$, is expressed by Equation **1.14**.

$$\boldsymbol{v}_{\boldsymbol{E}} = \frac{\boldsymbol{E} \times \boldsymbol{B}}{\mathrm{B}^2} \qquad 1.14$$

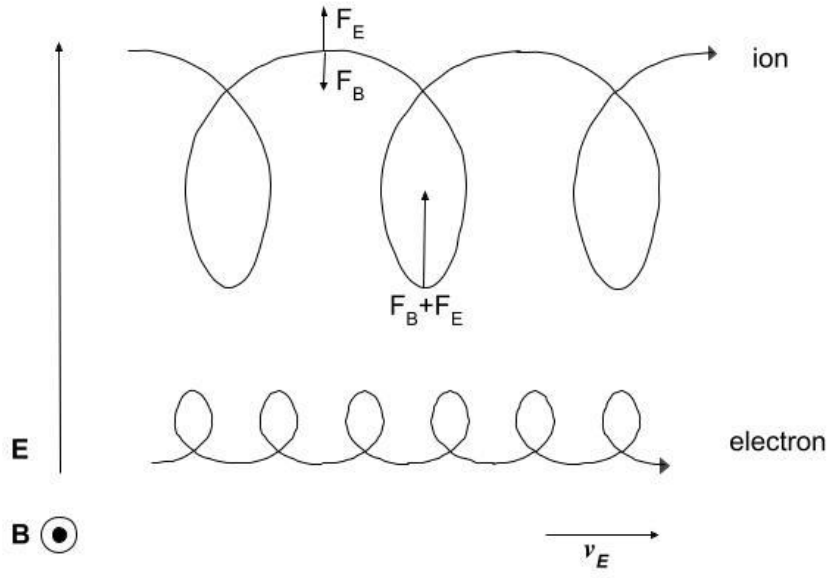

Figure 1.3 Illustration of charged particle motion in constant electric and magnetic fields, denoted by $\boldsymbol{E}$ and $\boldsymbol{B}$ respectively. The resultant forces and 'E x B' drift velocity, $\boldsymbol{v}_{\boldsymbol{E}}$, are illustrated.

1.2.4 Gradient Curvature Drift Motion

The third motion charged particles undergo in a dipolar magnetic field is an azimuthal drift across the field due to the non-uniformity of the magnetic field. These drift motions are called gradient drift and curvature drift as they are caused by the gradient and curvature of dipolar magnetic fields respectively.

Section 1.2.2 discussed magnetic field gradients parallel to magnetic field direction. Consider a magnetic field which is weakly inhomogeneous with a gradient perpendicular to the magnetic field direction i.e., which gets weaker with perpendicular distance from the central dipole. Figure 1.4 illustrates the motion which charged particles follow under this field configuration. The magnetic field is in the -z direction, charged particles gyrate in the x-y plane. There is a gradient in the magnetic field, such that magnetic field strength increases with y. As the particle gyrates, it moves to regions where B is greater, thus the gyro-radius varies through the gyro-orbit according to Equation **1.8**. After many gyrations, the overall effect is the particle drifts perpendicularly to $\boldsymbol{B}$ and $\nabla\boldsymbol{B}$.

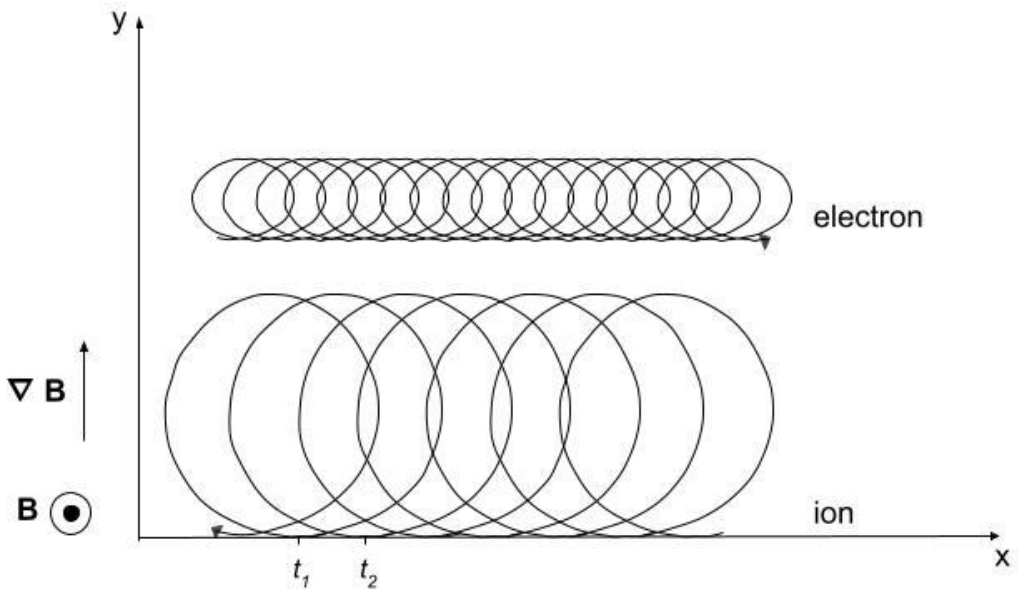

Figure 1.4 Illustration of charged particle drift in a magnetic field, $\boldsymbol{B}$, with a constant gradient, $\nabla\boldsymbol{B}$.

The magnitude of this drift may be estimated by averaging the forces experienced by the particle over a gyro-period. There is no net motion in the y

direction, thus over a whole gyro-period the average force in the y direction, F_y, is zero. Equation **1.2** can therefore be written as an integral between times t_1 and t_2 which denote the minimum y position between two consecutive gyro-orbits.

$$\int_{t_1}^{t_2} F_y = \int_{t_1}^{t_2} q\frac{dx}{dt}B(y)\,dt = 0 \qquad 1.15$$

If we assume that the magnetic field gradient is small compared to a gyro-radius, then $B(y)$ may be approximated using the first two terms of the Taylor expansion.

$$B(y) = B_0 + y\frac{\partial B}{\partial y} \qquad 1.16$$

where B_0 is the magnetic field strength at $y = 0$, and $\frac{\partial B}{\partial y}$ is constant. Substituting Equation **1.16** into **1.15**

$$\int_{x(t_1)}^{x(t_2)} dx = -\frac{1}{B_0}\frac{\partial B}{\partial y}\int_{x(t_1)}^{x(t_2)} y\,dt \qquad 1.17$$

If we assume that $r_g \gg x(t_2) - x(t_1)$ (i.e., the drift over a single gyro-orbit is much smaller than a gyro-radius), then the area under the right integral can be approximated by a circle with a radius equal to the gyro-radius. The time between t_1 and t_2 is equal to the gyro-period, which is expressed by $2\pi\, r_g/v_\perp$. The drift velocity, $\boldsymbol{v}_\nabla$, can therefore be expressed by

$$v_\nabla = \frac{x(t_2) - x(t_1)}{t_2 - t_1} = \frac{1}{2B_0}\frac{\partial B}{\partial y}v_\perp r_g \qquad 1.18$$

We can generalise this equation by setting $B_0 = B$, and substituting Equation **1.8**, and using $\boldsymbol{B} \times \nabla\boldsymbol{B} = B \cdot \frac{\partial B}{\partial y}\,\hat{x}$:

$$\boldsymbol{v}_\nabla = \frac{mv_\perp^2}{2qB^3}(\boldsymbol{B} \times \nabla\boldsymbol{B}) \qquad 1.19$$

In addition to a gradient drift, there is also a curvature drift introduced by the curvature of the magnetic field in each hemisphere of a dipole. This force is a

centrifugal force which arises from the changing direction of the magnetic field and acts to change the gyro-radius of the particle, resulting in a drift motion. This force is expressed in terms of the radius of curvature of the field, R_c, and the unit vector of the radial direction of curvature, $\hat{\boldsymbol{r}}_c$.

$$\boldsymbol{F_c} = \frac{m v_{\parallel}^2}{R_c} \hat{\boldsymbol{r}}_c \tag{1.20}$$

This centrifugal force can be considered analogously to the force exerted by an electric field. Therefore, we can substitute $\boldsymbol{F}_c$ into Equation **1.14** which gives

$$\boldsymbol{v_c} = \frac{m v_{\parallel}^2}{q R_c^2} \frac{\boldsymbol{r_c} \times \boldsymbol{B}}{B^2} \tag{1.21}$$

In a dipolar magnetic field, there are magnetic gradients for increasing distance from the equator of the dipole, and the magnetic field is curved in either hemisphere. In a cylindrically symmetric field, $-\nabla B = (B/R_c^2)\boldsymbol{R_c}$. We can therefore express the summation of drifts due to magnetic forces as

$$\boldsymbol{v_B} = \boldsymbol{v_c} + \boldsymbol{v}_{\nabla} = \left(v_{\parallel}^2 + \frac{1}{2} v_{\perp}^2\right) \frac{\boldsymbol{B} \times \nabla B}{\omega_g B^2} \tag{1.22}$$

The resultant drift of charged particles in a magnetic dipole is a combination of the magnetic drift, and the E x B drift. The net drift is dependent upon the particle pitch angle, energy, and charge, with electrons drifting eastward in Earth's dipolar field, and protons drifting westward.

1.3 The Adiabatic Invariants

Provided that a particle is energetic enough, each of these motions are conserved according to the adiabatic invariants. Adiabatic invariants are described as quantities which are conserved so long as the forces in the system change on much slower timescales than the timescale of particle oscillation. The invariants can be derived using the action integral taken over a periodic orbit (Walt, 1994).

$$J_i = \oint p_i dq_i \approx const. \tag{1.23}$$

where J_i is the constant of motion describing the adiabatic invariant, p_i and q_i are the generalised canonical momentum and coordinate. For a particle undergoing periodic motion due to a restorative force (e.g., in a dipolar magnetic field; gyro-motion, bounce motion, or drift motion), the canonical momentum is analogous to angular momentum. The following sections will describe each of the three periodic motions and their associated adiabatic invariants.

1.3.1 Magnetic Moment, μ

To derive the adiabatic invariant associated with gyromotion, we can use the expression of canonical momentum, $\boldsymbol{P}$, in a uniform magnetic field, $\boldsymbol{P} = \boldsymbol{p} + q\boldsymbol{A}$ (where $\boldsymbol{A}$ is the vector potential of the magnetic field), combined with the action integral (Equation **1.23**), which is integrated over the path of periodic motion, $\boldsymbol{l}$:

$$J_1 = \oint (\boldsymbol{p} + q\boldsymbol{A}) d\boldsymbol{l} \tag{1.24}$$

Integrating over a gyro-orbit, the first term becomes $\boldsymbol{p} \cdot d\boldsymbol{l} = p_\perp dl$. Stokes' theorem, which states that the surface integral ($d\boldsymbol{S}$) of the curl of a vector field is equal to the line integral of the field around the boundary area ($\oint \boldsymbol{A} d\boldsymbol{l} = \iint (\nabla \times \boldsymbol{A}) d\boldsymbol{S}$), is used to rewrite the second term, and then substituting Equation **1.8**

$$\begin{aligned} J_1 &= \int p_\perp d\,l + q \iint \nabla \times \boldsymbol{A}\, d\boldsymbol{S} \\ &= \int p_\perp d\,l + q \int \boldsymbol{B} d\boldsymbol{S} \end{aligned} \tag{1.25}$$

$$\begin{aligned} J_1 &= p_\perp 2\pi\, r_g - qB\pi\, r_g^2 \\ &= \frac{\pi p_\perp^2}{qB} \end{aligned} \tag{1.26}$$

The first adiabatic invariant is often called the magnetic moment, μ. This is because the first invariant is proportional to the magnetic moment of a current loop, Equation **1**.**27**.

$$\mu = \frac{p_\perp^2}{2m_0 B} \tag{1.27}$$

In the case of a gyrating particle, m_0 is the rest mass of the particle. Because particle mass is constant $J_1 \propto \mu$.

1.3.2 Longitudinal Invariant, *K*

To derive the second adiabatic invariant, we integrate the canonical momentum over a single bounce path between two mirror points, using Equation **1**.**25**. Because there is no surface area along a field line, the second term $q\int \boldsymbol{B} d\boldsymbol{S} = 0$. This gives

$$J_2 = \oint \boldsymbol{p}\, d\boldsymbol{l} = 2m_0 \int_S^N v_\parallel d\, l \tag{1.28}$$

where N and S are the northern and southern magnetic mirror points. This can also be written solely in terms of magnetic field geometry if the first adiabatic invariant is also assumed to be conserved. Considering the conservation of kinetic energy, $W(l)$, along the field line.

$$\begin{aligned} W_\parallel(l) + W_\perp(l) &= W_{\perp mirror} \\ v_\parallel^2(l) + v_\perp^2(l) &= v_{\perp mirror}^2 \end{aligned} \tag{1.29}$$

Rearranging Equation **1**.**27** for $v_\perp^2 = 2\mu B/m_0$, and substitute

$$v_\parallel^2(l) = \frac{2\mu}{m_0}\left(B_{mirror} - B(l)\right) \tag{1.30}$$

The second invariant can be rewritten as *K*

$$K = \frac{J_2}{2\sqrt{2m_0\mu}} = \int_S^N \sqrt{B_{mirror} - B(l)}\, dl \tag{1.31}$$

1.3.3 Drift Invariant, *L**

To derive the third adiabatic invariant, we integrate the canonical momentum over a drift orbit due to gradient-curvature drift. This is usually calculated along the magnetic equator. Because the velocity of drift motion is much less than the total particle velocity, the momentum of drift is very small, and so is neglected in the calculation of the action integral for drift motion.

$$J_3 = \oint q\boldsymbol{A}\, d\boldsymbol{l} \tag{1.32}$$

Applying Stokes' theorem to Equation **1.32**, and noting that the charge is constant, the third invariant is equal to magnetic flux enclosed by a drift path, Φ.

$$\Phi = \oint \boldsymbol{B}\, d\boldsymbol{S} \tag{1.33}$$

The third invariant is often expressed as the Roederer L^* parameter, which describes the equatorial distance to the particle drift path in a perfect dipolar magnetic field, in R_E (Roederer, 1967). L^* is defined as inversely proportional to Φ.

$$L^* = \frac{2\pi B_0 R_E^2}{\Phi} \tag{1.34}$$

where B_0 is magnetic field strength at Earth's surface.

1.4 Non-Adiabatic Processes

Each of the adiabatic invariants are associated with a timescale which relates to the periodic motion over which canonical momentum is integrated. In Earth's magnetosphere, a 1 MeV electron at geosynchronous orbit has a gyro-period of ~ milliseconds, a bounce period of ~ seconds, and a drift period of ~ minutes. Any changes in the electromagnetic field on timescales shorter than this may violate the adiabatic invariants, resulting in changes to the total momentum of the particle.

1.4.1 Adiabatic Heating

If the magnetic field is slowly varying compared to a particle's orbital drift period, then the three adiabatic invariants are conserved, and a particle will follow a constant *L** for the whole of its orbit. However, an interesting phenomenon occurs when the magnetic field varies quicker than the timescale of a drift orbit, but slower than bounce and gyro-motions. In this scenario, a particle may radially drift across field lines. Supposing the particle moves from region of field strength B_1 to B_2, where $B_1 < B_2$, the conservation of μ gives

$$\frac{B_1}{B_2} = \frac{W_{\perp 1}}{W_{\perp 2}} \tag{1.35}$$

Therefore $W_1 < W_2$, and the particle is energised in the perpendicular direction to the magnetic field. This is known at Betatron acceleration. This acceleration alone may not change the total energy of the particle, W, which also depends upon parallel kinetic energy. If a particle drifts onto field lines of different mirror geometry, then parallel energisation may also occur. The longitudinal invariant can be rewritten in terms of average parallel velocity and distance between mirror points, l.

$$J_2 = \oint m v_{\parallel} dl \simeq m\langle v_{\parallel}\rangle 2l \tag{1.36}$$

If the particle moves from a field line of length l_1 to l_2 where $l_1 > l_2$ then conservation of the longitudinal invariant gives:

$$\frac{l_1}{l_2} = \frac{\langle v_{\parallel 2}\rangle}{\langle v_{\parallel 1}\rangle} \Rightarrow \frac{l_1^2}{l_2^2} = \frac{W_{\parallel 2}}{W_{\parallel 1}} \tag{1.37}$$

The parallel energy of the particle therefore increases. This is a form of Fermi acceleration, whereby particles bouncing between increasingly close mirror points accelerate. Moving mirror points implies that $dB/dt \neq 0$ and an electric field is induced, changing the total kinetic energy of the particle. When a particle moves radially inwards in Earth's magnetic dipole, the total kinetic energy increases, whereas if the particle moves radially outwards, energy decreases.

1.4.2 Resonant Wave-Particle Interactions

A charged particle may be scattered by the presence of electromagnetic waves if the wave frequency is comparable to the frequency of particle periodic motion. The particle will experience the wave electric field and change energy and momenta as a result. The associated adiabatic invariant is not conserved in this interaction.

One example of this is the interaction of electrons with cyclotron waves. Wave-particle interaction becomes strong when the guiding centre velocity is such that the doppler shifted cyclotron frequency (or a harmonic frequency) of a circularly polarised wave coincides with the frequency of the particle, as illustrated in Figure 1.5. If the angular frequencies of the wave and particle are the same, Landau resonance is achieved (Landau, 1946). The condition for the n^{th} order cyclotron resonance between waves and particles is given by

$$\omega - k_{\parallel} v_{\parallel} = \frac{n\omega_g}{\gamma} \quad , \quad n = 0, \pm 1, \pm 2, \tag{1.38}$$

where ω is wave frequency, $\mathrm{k}_{\parallel}$ is the wave number along the magnetic field, and $\gamma = \left(1 - {v^2}/{c^2}\right)^{-1/2}$ is the relativistic correction factor.

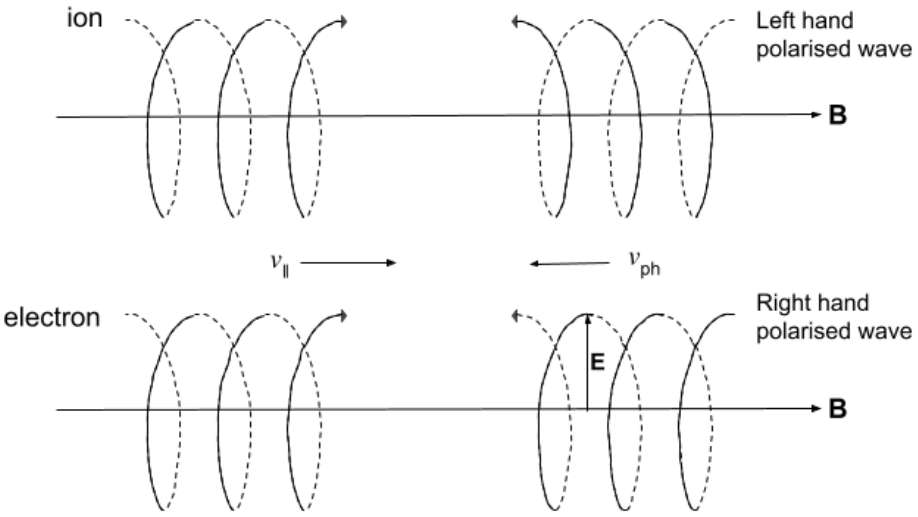

Figure 1.5 Illustration of the relative motion between doppler shifted circularly polarised waves and charged particles for first-order cyclotron resonant interactions.

In the case of resonance, the particle will experience a continual electric field from the wave, which acts to accelerate or decelerate the particle to match phase velocity of the wave. When a particle is accelerated, the wave transfers energy to the particle and its pitch angle moves closer to 90°. When a particle is decelerated, the particle transfers energy to the wave and the particle pitch angle becomes more field aligned. These changes in pitch angle are often referred to as pitch angle scattering.

1.5 Plasma Physics Concepts

1.5.1 Quasi-neutrality

A plasma is defined as a quasi-neutral ionised gas containing electrons and ions (and sometimes some neutral particles) which exhibit collective behaviour. For a plasma to be quasi-neutral, it must contain approximately the same number of positively and negatively charged particles in any region larger than the Debye sphere. The Debye Sphere is a characteristic quantity of a plasma associated with an effect called Debye shielding. This is a phenomenon most easily understood by considering a stationary plasma under an applied electric field. Oppositely charged free plasma particles collectively move towards the applied electric field, acting to shield the electric field. The Debye length, $\lambda_{D,}$ is defined as the distance from the applied electrostatic field at which electrostatic potential energy is equal to the thermal particle energy, defined by

$$\lambda_D = \sqrt{\frac{\varepsilon_0 k_B T_e}{ne^2}} \tag{1.39}$$

where ε_0 is permittivity of free space, k_B is Boltzmann's constant, T_e is electron temperature, n is number density of shielding particles, and e is the charge of an electron. The Debye sphere is a volume with radius λ_D.

1.5.2 Magnetohydrodynamics

Magnetohydrodynamics (MHD) is a formalism used to describe collective plasma behaviour. MHD considers a plasma as an electrically conducting fluid over large spatial and temporal scales, greater than that of an ion gyro-radius, Debye length, and gyro-period. This is a useful tool for characterising the

evolution of macroscopic plasma properties, such as density, velocity, and temperature.

The approach of MHD is to incorporate Maxwell's equations into the hydrodynamics continuity equation, momentum equation, and the equation of state. The MHD equations are as follows:

The mass continuity equation for a particle species, s, is given by

$$\frac{\partial n}{\partial t} + \nabla \cdot (n\boldsymbol{v}) = 0 \tag{1.40}$$

where n is number density of the fluid and $\boldsymbol{v}$ is the bulk flow velocity. This equation describes that, in a classical non-relativistic plasma, the number density (and therefore mass and charge density) is conserved during the motion of the fluid.

The equation of motion is given by

$$\rho\left(\frac{\partial \boldsymbol{v}}{\partial t} + \boldsymbol{v} \cdot \nabla \boldsymbol{v}\right) = -\nabla \cdot \boldsymbol{P} + \rho \boldsymbol{E} + \boldsymbol{j} \times \boldsymbol{B} \tag{1.41}$$

where $\boldsymbol{P}$ is pressure, and ρ is mass density, and $\boldsymbol{j}$ is current density. This equation relates the change in velocity to the density and electromagnetic forces acting on a fluid element (rather than individual particles), and assumes that the plasma is quasi-neutral i.e., $n_e = n_i$.

Generalised Ohm's law closes the system of MHD equations by describing variations in $\boldsymbol{j}$, which can be found by subtracting the equation of motion for electrons from that of ions. For a single-fluid MHD approximation, Ohm's law is given by

$$\boldsymbol{E} + \boldsymbol{v} \times \boldsymbol{B} = \frac{\boldsymbol{j}}{\sigma} + \frac{\boldsymbol{j} \times \boldsymbol{B}}{n_e} - \frac{\nabla \cdot \boldsymbol{P_e}}{n_e} + \frac{m_e}{n_e e^2}\frac{\partial \boldsymbol{j}}{\partial t} \tag{1.42}$$

where σ is conductivity of the plasma, m_e, is electron mass, and n_e is electron number density.

1.5.3 Frozen-in Flow

In many space plasmas, Equation **1.42** can be simplified such that the current flow through the plasma can be expressed in terms of the electromagnetic fields through the fluid.

$$\frac{\boldsymbol{j}}{\sigma} = \boldsymbol{E} + \boldsymbol{v} \times \boldsymbol{B} \tag{1.43}$$

For an ideal MHD plasma, in which displacement currents are neglected, we can substitute Ampère's law, $\nabla \times \boldsymbol{B} = \mu_0 \boldsymbol{j}$, and Faraday's law, $\nabla \times \boldsymbol{E} = -\frac{\partial \boldsymbol{B}}{\partial t}$ into Equation **1.43** to derive the induction equation, which describes changes in the magnetic field:

$$\frac{\partial \boldsymbol{B}}{\partial t} = \nabla \times (\boldsymbol{v} \times \boldsymbol{B}) + \frac{1}{\mu_0 \sigma} \nabla^2 \boldsymbol{B} \tag{1.44}$$

The right-hand terms represent the convection motion of the magnetic field with a plasma, and diffusion of the magnetic field through the plasma respectively. Most space plasmas are collisionless, such that the conductivity tends to infinity. In this scenario, Equation **1.44** shows that the change in magnetic field over time is controlled by the convective term, as the diffusive term is negligible. This is called frozen-in flux, where the magnetic field is embedded in the plasma and flows with the bulk velocity of the plasma (if $\beta > 1$, see Equation 1.47), or that plasma flows with the motions of magnetic field convection (if $\beta < 1$). It is possible to determine whether the plasma is dominated by frozen in flow, or diffusion, by calculating the Reynolds number, R_m. The Reynolds number gives the ratio of the convection and diffusion terms in Equation **1.44**.

$$R_m = \frac{\nabla \times (\boldsymbol{v} \times \boldsymbol{B})}{\nabla^2 \boldsymbol{B} (\mu_0 \sigma)^{-1}} \tag{1.45}$$

If $R_m \gg 1$ then diffusion is dominated by magnetic field convection, and the assumptions of ideal MHD are satisfied. If $R_m \approx 1$ then diffusion cannot be neglected and MHD is not an appropriate representation of plasma dynamics.

The relative importance of particle pressure and magnetic pressure may also be understood from a parameter called plasma beta, β. We can calculate the magnetic force, $\boldsymbol{j} \times \boldsymbol{B}$ by substituting Ampère's law for ideal MHD:

$$\boldsymbol{j} \times \boldsymbol{B} = \frac{1}{\mu_0}(\nabla \times \boldsymbol{B}) \times \boldsymbol{B} = -\nabla \frac{B^2}{2\mu_0} + \frac{1}{\mu_0}(\boldsymbol{B} \cdot \nabla)\boldsymbol{B} \qquad 1.46$$

Where the term $-\nabla\, B^2/2\mu_0$ describes the gradient in magnetic pressure, and $(\boldsymbol{B} \cdot \nabla)\boldsymbol{B}/\mu_0$ describes the magnetic tenson force. The magnetic pressure ($B^2/2\mu_0$) describes the force due to a gradient in magnetic flux density. Plasma beta is the ratio between the plasma thermal pressure and the magnetic pressure.

$$\beta = \frac{2\mu_0 n k_B T}{B^2} \qquad 1.47$$

If $\beta > 1$, then thermal pressure of the plasma is greater than magnetic pressure, so the dynamics of the magnetised fluid is dictated by the dynamics of the plasma. If $\beta < 1$, then the magnetic pressure is greater than thermal plasma pressure, and the magnetised fluid follows the dynamics of the magnetic field.

1.5.4 Magnetic Reconnection

Magnetic reconnection is a process which occurs when two different plasma regimes with different magnetic field orientations meet. If $R_m \gg 1$, then the frozen-in approximation is assumed and there should be no magnetic diffusion between the two systems. Two stationary antiparallel magnetic field topologies can therefore be maintained for long time periods if there is a current sheet between them. However, when two plasma - magnetic field regimes are moving towards one another, $R_m \sim 1$ in the current sheet between the regions. When this occurs, plasma may diffuse across the magnetic fields and there will be a point where the magnetic field vanishes, called the magnetic neutral point. The result is an X-type configuration of the magnetic field, illustrated in Figure 1.6. Plasma and magnetic field are transported towards the neutral point by respective regime flows, then magnetic fields are 'reconnected' between the two systems and the new magnetic field topologies move

perpendicularly away from the direction of flow. As a result, plasma along the reconnected field lines are allowed to mix between regimes.

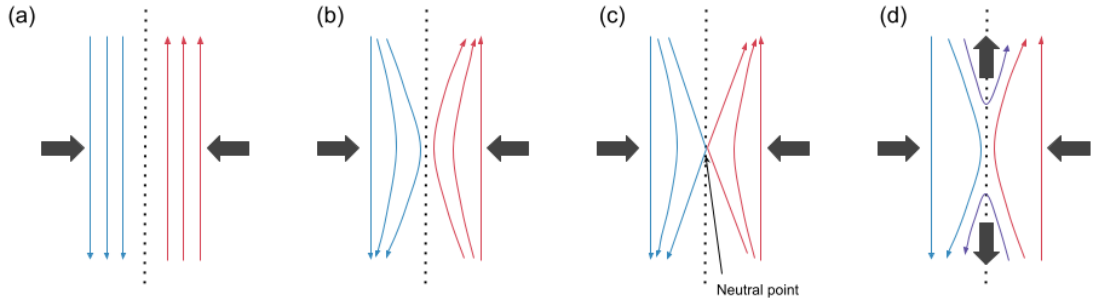

Figure 1.6 Schematic diagram of magnetic reconnection between two antiparallel magnetic fields, shown by blue and red lines, flowing towards a thin current sheet, illustrated by the dotted line.

1.6 Earth's Magnetosphere

A Magnetosphere is a magnetic cavity which lies within the solar wind, where a planetary magnetic field dominates the plasma conditions over the surrounding interplanetary magnetic field (IMF).

1.6.1 The Solar Wind

The solar wind is a continual outflow of plasma from the solar corona which expands into interplanetary space due to its high thermal pressure. The conductivity of the solar wind is high, so has a large magnetic Reynolds number, such that the solar magnetic field is frozen into the plasma flow of the solar wind. The solar magnetic field is dragged by the solar wind into interplanetary space where it forms the IMF. The combination of solar rotation and radial flow of the solar wind forms a magnetic configuration known as the Parker spiral.

The solar wind and IMF conditions are far from constant with two fundamental 'steady' modes, the fast and slow solar wind, and further transient structures which originate from activity in the solar corona. The slow solar wind, which flows at ~ 300 – 500 km s^{-1}, is thought to be frozen into closed magnetic loops with footprints near the solar equator (Walt, 1994). Whereas the fast solar wind, which usually flows at greater velocities > 600 km s^{-1}, is thought to

originate from coronal holes where the magnetic field is open to the interplanetary medium (Zirker, 1977).

Because the solar wind flows at supersonic speeds, MHD discontinuities can form, known as interplanetary shocks (Oliveira, 2017). For example, a stream of fast solar wind propagating into upstream slow solar wind forms an interplanetary shock where solar wind plasma and IMF are compressed. These stream interface regions are called co-rotating interaction regions (CIR) if they co-rotate with the Sun. Another important shock structure formed in the solar wind is produced by the propagation of Coronal Mass Ejections (CMEs) into interplanetary space. CMEs are loops of twisted magnetic field and plasma, called magnetic flux ropes, which are launched into interplanetary space by magnetic instabilities and reconnection in the solar corona. CIRs and CMEs are known to interact with the Earth's magnetosphere to produce dynamic events called geomagnetic storms. CIRs and CMEs are therefore labelled geoeffective solar wind structures (Kilpua et al., 2017).

1.6.2 The Bow Shock and Magnetosheath

If the frozen-in condition is satisfied, the Earth's magnetosphere is impenetrable to the solar wind. The supersonic solar wind forms a shock wave upstream of the magnetosphere, called the bow shock, which typically forms ~ 14 R_E from Earth along the Sun-Earth line (Petrinec, 2002). Between the bow shock and the magnetosphere is a high-density region called the magnetosheath where solar wind plasma is slowed down to subsonic speeds and deflected around the magnetosphere. Plasma in the magnetosheath is heated as kinetic energy is converted to thermal energy via turbulent processes.

The solar wind exerts pressure on the geomagnetic field, distorting it such that the dipole is compressed on the sunwards side and elongated into a 'magnetotail' on the night side, illustrated in Figure 1.7.

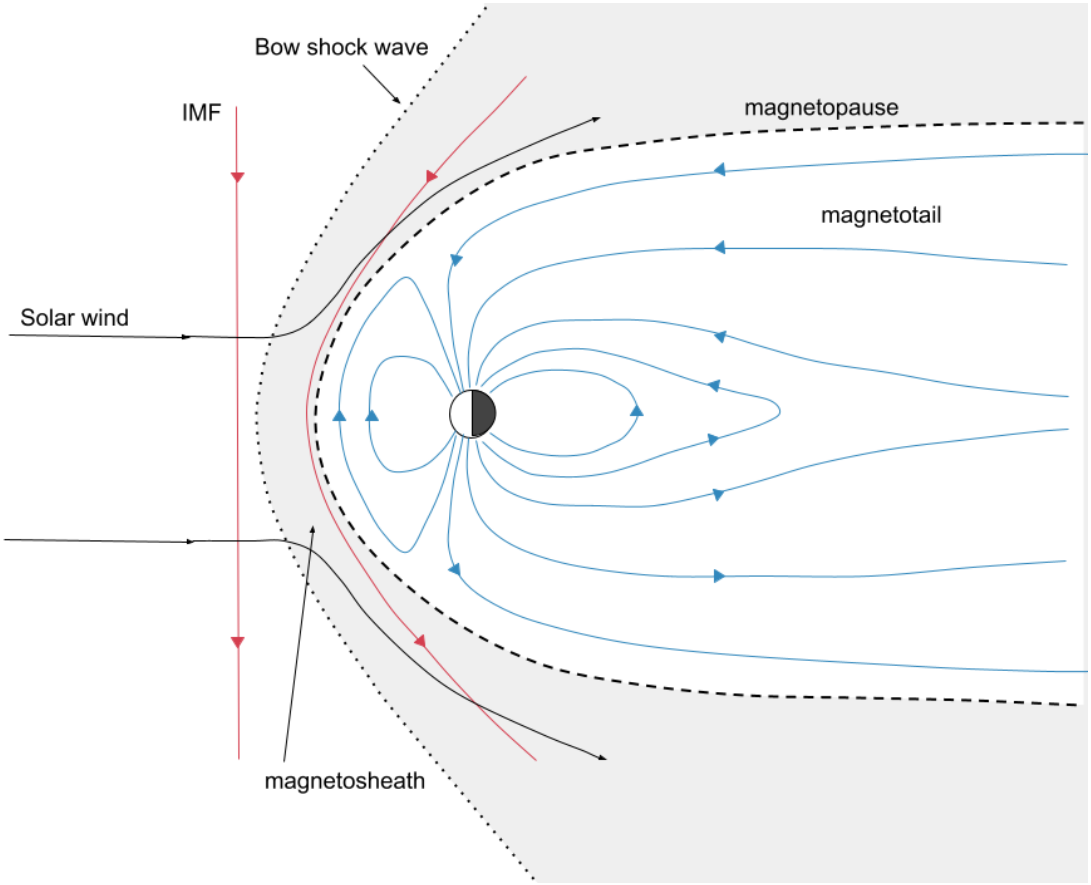

Figure 1.7 Diagram of Earth's magnetosphere, representing a side view of the geomagnetic field (blue lines) during southwards directed IMF (red lines). The bow shock and magnetopause are indicated by dotted and dashed lines respectively. The magnetosheath is indicated by the shaded area.

1.6.3 The Magnetopause

The boundary between solar wind plasma in the magnetosheath and the magnetosphere is given by the magnetopause. As the magnetopause marks a discontinuity between the two magnetic regimes in the solar wind and magnetosphere, there is a thin current sheet on the surface of the magnetopause (Ampère's law). The magnetopause current sheet, also known as Chapman-Ferraro current, arises from the reflection of solar wind particles by Earth's magnetic field. Solar wind particles impinging on the magnetosphere field will complete half a gyro-orbit inside the geomagnetic field, after which their trajectory is reversed, illustrated in Figure 1.8. A surface current is generated by many charged particles performing half gyro-orbits in opposite directions, depending on particle charge. The current itself creates a magnetic field which annihilates the geomagnetic field external to the magnetopause and reinforces the magnetic field inside of the magnetopause.

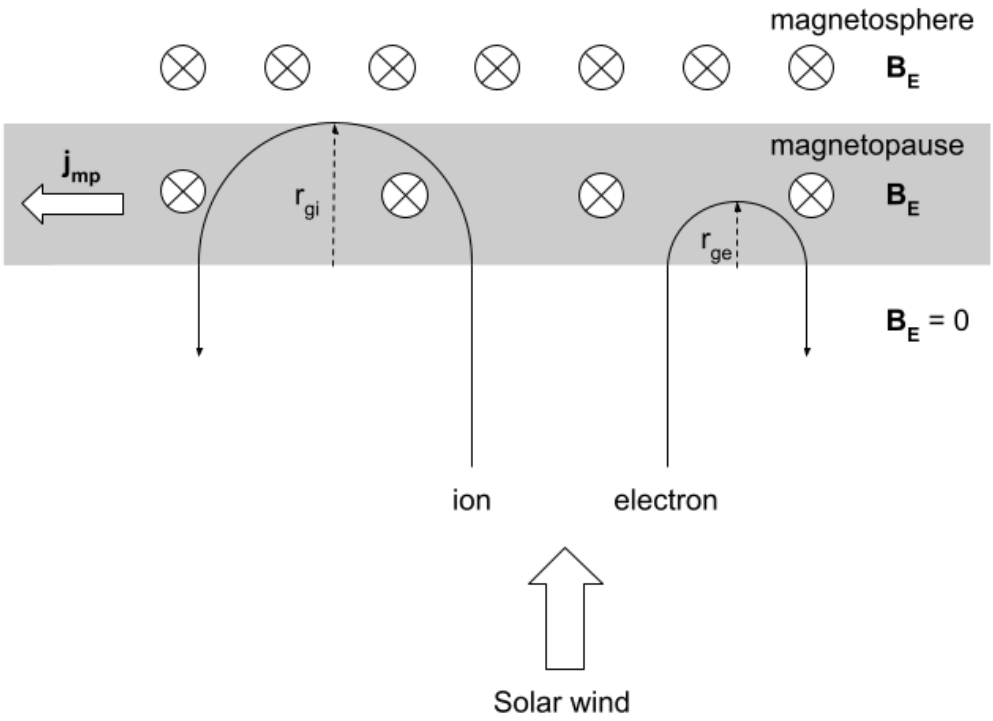

Figure 1.8 A diagram illustrating how solar wind ion and electron drift paths impinging on the magnetosphere are reflected by the Earth's magnetic field, B_E, following half a gyro-orbit with radius r_{gi} for ions and r_{ge} for electrons. The net tangential flow of charge generates electric current, j_{mp}, along the magnetopause.

The thickness of the magnetopause is approximately equal to an ion gyro-radius, $r_{gi} = v_{gi}/w_{gi}$. The location of the magnetopause is where the dynamic and magnetic pressures in the solar wind and magnetosphere balance. To a first approximation it can be assumed that the dynamic pressure of the solar wind, $P_D = \rho v^2/2$, is much greater than the magnetic pressures, and vice-versa for the magnetospheric dynamic and magnetic pressures. Because the dynamic pressure in the solar wind is variable, the standoff distance of the magnetopause responds to this variability by moving location until a new equilibrium is reached.

The magnetopause current system forms rings of current in the northern and southern hemispheres of the dayside magnetopause, and currents along the equator and nightside magnetopause close through the cross-tail current sheet, which flows from dawn to dusk, also known as the neutral sheet. The cross tail current sheet separates the magnetotail lobes which are elongated

by the solar wind creating a magnetic discontinuity where the neutral sheet lies.

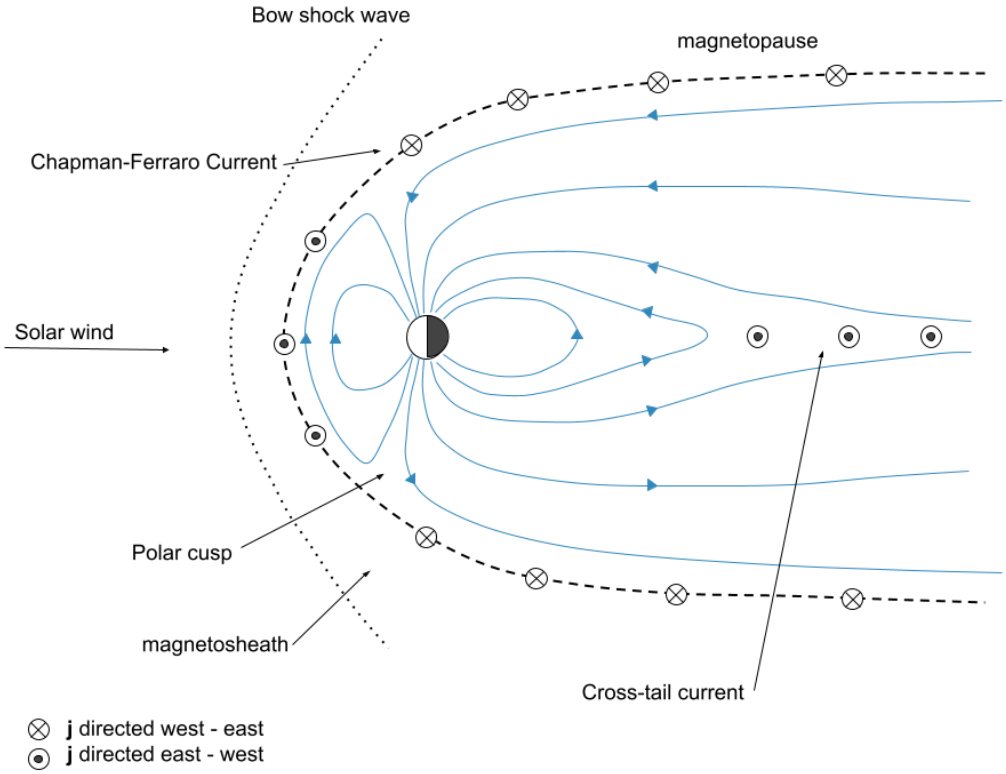

Figure 1.9 Diagram illustrating the direction of Chapman-Ferraro currents on the magnetopause surface, and the direction of the cross tail current sheet. Magnetic field lines of Earth are shown in blue, the bow shock and magnetopause are shown by dotted and dashed lines respectively.

1.6.4 The Dungey Cycle and Substorms

If the IMF is oriented in an opposite direction as the Earth's magnetic field, then the flow of the solar wind can cause magnetic reconnection to occur on the dayside magnetopause, as described in Section 1.5.4. Following dayside reconnection, magnetic field lines are connected to the solar wind and so are termed open. Solar wind plasma may stream along magnetic field lines, entering the polar cap region of the magnetosphere where field lines are open. The flow of the solar wind drags these open magnetic field lines over the polar cap from the dayside to the nightside where this magnetic field forms the magnetotail lobes. As dayside reconnection continues, more magnetic flux is loaded into the magnetotail increasing magnetic pressure until magnetic reconnection occurs in the cross-tail current sheet, on the nightside. Solar wind

plasma can enter closed magnetic field lines via nightside reconnection, forming a plasma population in the magnetotail called the plasma sheet. Following nightside reconnection, newly closed magnetic field lines convect back towards the dayside where they undergo dayside reconnection again. This cyclic process is called the Dungey Cycle, illustrated in Figure 1.10 (Dungey, 1961).

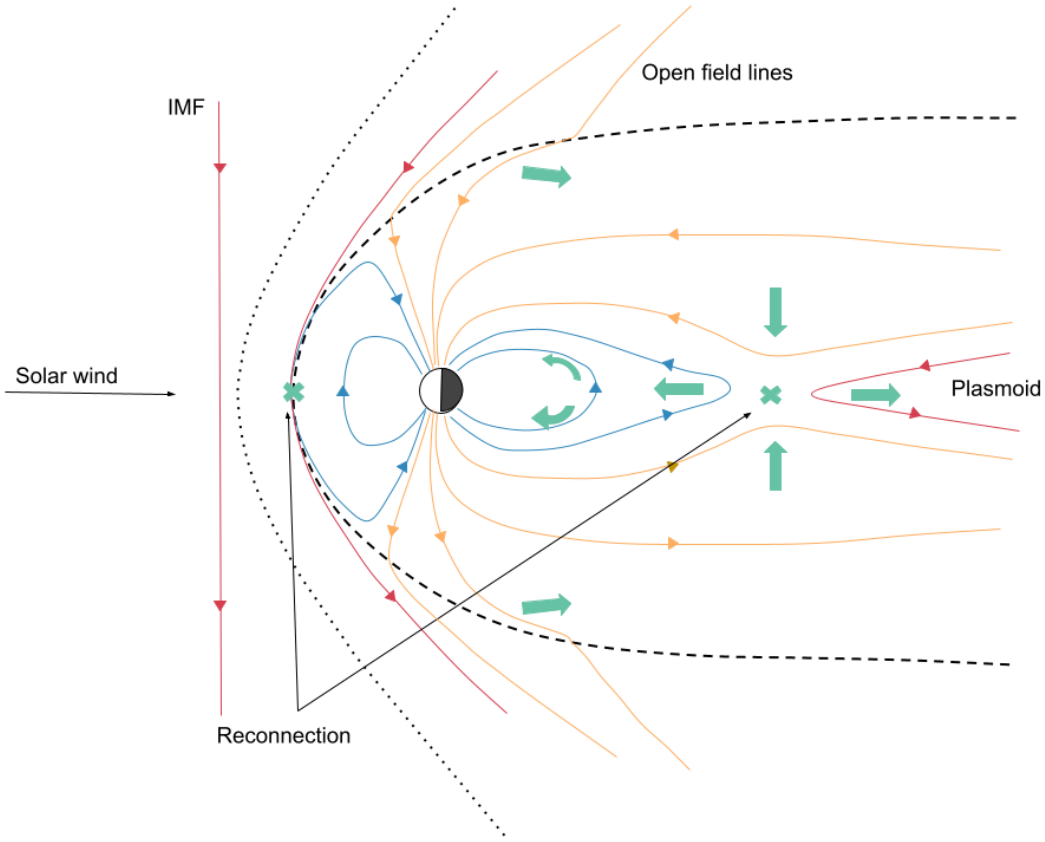

Figure 1.10 Diagram of the Dungey Cycle flow of magnetic convection through the magnetosphere. IMF field lines are red, magnetospheric field lines open to the solar wind are yellow, and closed magnetospheric field lines are blue. Convective flow of Earth's magnetic field is indicated by green arrows, and reconnection sites are labelled by green crosses. The bow shock and magnetopause are dotted and dashed lines respectively.

Because solar wind driving and IMF orientation are rarely constant, the rate of dayside and nightside reconnection varies, in these circumstances geomagnetic substorms occur. Substorms begin with a growth phase where there is enhanced dayside reconnection, and the dayside magnetosphere is eroded by the solar wind. During this phase the size of the polar cap, the area through which open field lines have a footprint, expands as open magnetic flux increases. This open magnetic flux is transported to the magnetotail by the

solar wind flow. The enhanced magnetic pressure in the magnetotail, and rarefaction of the dayside magnetosphere, drives convective flow of closed magnetic flux towards the dayside. Following this there is an expansion phase where a reconnection x-line forms in the magnetotail and reconnection begins on the nightside (Coroniti & Kennel, 1972). The exact sequence of events which leads to reconnection is not fully understood, though most models agree there is a plasma instability in the near-Earth plasma sheet which disrupts the cross-tail current, diverting cross tail current into the ionosphere, forming the substorm current wedge (e.g., Lui, 1991). The substorm current wedge flows from the plasma sheet into the post-midnight ionosphere, flows through the auroral ionosphere in the westwards direction, then back into the current sheet in the pre-midnight sector. In the classical definition, a reconnection site forms along the near-Earth neural line as the plasma sheet thins due to increasing magnetic pressure in the magnetotail lobes (Hones, 1976). During the expansion phase, the rate of nightside reconnection suddenly increases and the magnetotail is rapidly dipolarised. During this phase, ions and electrons from the plasma sheet are injected into the inner magnetosphere (McPherron et al., 1973). In the final recovery phase, the rate of depolarisation decreases until the magnetosphere returns to its average pre-substorm configuration (Hones, 1976).

1.6.5 Plasmasphere

The flow of the solar wind over the polar cap generates a large-scale electric field directed from dawn to dusk called the convection electric field. The magnetospheric electric field is a superposition of the convection electric field and the electric field generated by corotation of Earth's magnetosphere. In the inner magnetosphere the corotation electric field dominates and low energy particles may follow on closed E x B drift paths. In the outer magnetosphere, drift paths are dominated by the convection electric field and particles drift out through the magnetopause on open drift paths. Co-rotational and convective drift paths are illustrated in Figure 1.11.

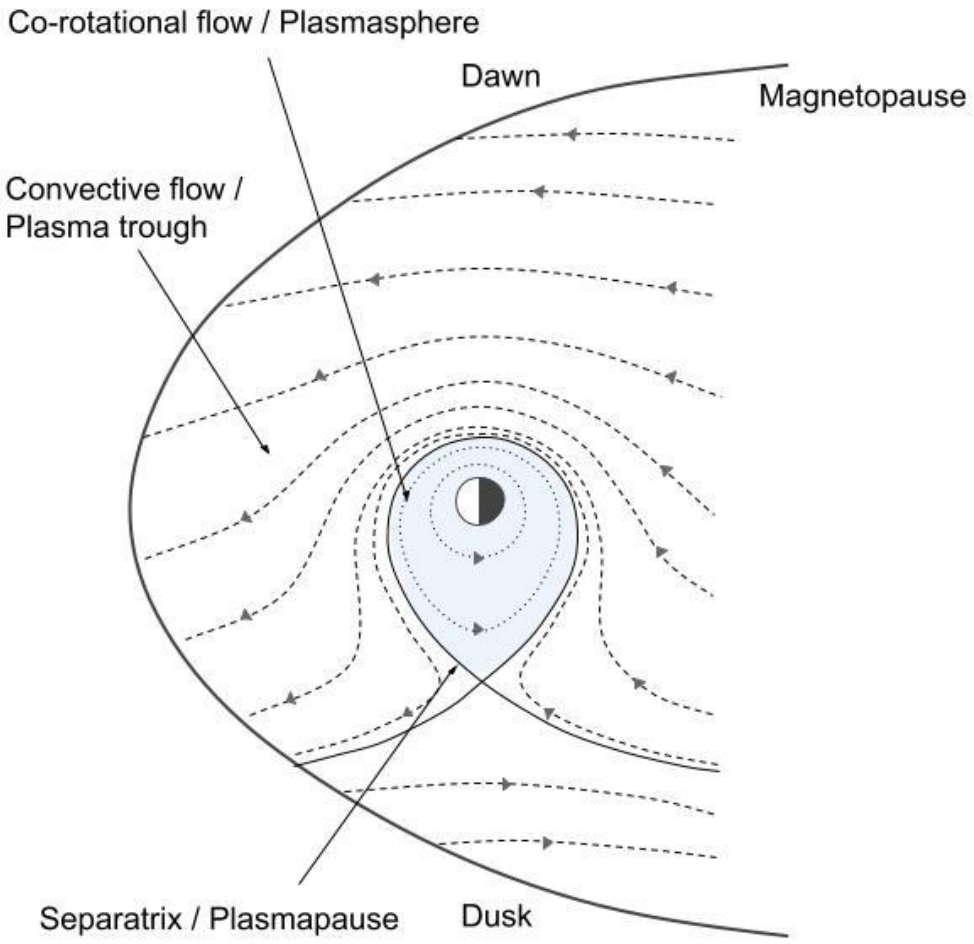

Figure 1.11 Diagram illustrating equatorial flow paths in the magnetosphere due to E x B drift. Convective flow is shown by dashed lines, and corotational flow is shown by dotted lines. The blue shaded area indicates the plasmasphere trapping region. Adapted from Chappell (1972).

The plasmasphere is formed by the up-flow of ionospheric plasma along magnetic field lines. Because this plasma is very cold, with energies of a few eV, plasma near Earth circulates around the magnetosphere following co-rotational E x B drift paths. Within the plasmasphere the density is very high, approximately ten times greater than typical densities in the convective region, called the plasmatrough. There is a sharp drop in plasma density between the plasmasphere and plasmatrough, which is known as the plasmapause, outside of which plasma is lost to the magnetopause (Carpenter, 1966). Because the convection electric field varies under different solar wind conditions, the location of the separatrix between the dominant electric fields varies over time. If the convection electric field is weak then plasmasphere will expand. If the

convection electric field is strong the plasmapause will move Earthwards and plasma is lost to the magnetopause (Chen & Wolf, 1972).

1.6.6 Geomagnetic Storms

A geomagnetic storm is a disturbance in Earth's geomagnetic field caused by intervals of intense solar wind – magnetosphere coupling, resulting in the substantial release of energy into the magnetosphere. These events are usually driven by fast forwards shocks in the solar wind, such as CMEs and CIRs.

A geomagnetic storm is usually characterised by intensifications of the ring current which cause sudden changes in the horizontal component of the magnetic field measured at low latitudes on the ground. The ring current system flows westward around the Earth at distances between ~ 4 – 7 R_E (Daglis et al., 1999), predominantly generated by ions with energies between 10s keV to 100s keV (Williams, 1987). These hot ions drift azimuthally around the Earth, generating a diamagnetic field (following Ampère's law) which diminishes the geomagnetic field within the ring of current i.e., Earthwards.

Ring current intensity is measured using geomagnetic indices such as the disturbance storm-time (Dst) index (Sugiura & Poros, 1971) or the Sym-H index (Iyemori, 1990). These indices quantify perturbations in the horizontal component of the magnetic field measured by ground magnetometer stations at low latitudes. Dst index is calculated from hourly averages of the horizonal magnetic field component measured by four of six low latitude ground magnetometer stations. Sym-H is calculated in a similar manner as Dst, using slightly different magnetic observatories and data processing methods. Sym-H is often used as the de-facto high resolution Dst index (Wanliss & Showalter, 2006).

A geomagnetic storm has three phases: an initial phase, main phase, and recovery phase. A typical evolution of Dst index through these phases is shown in Figure 1.12. The initial phase of a geomagnetic storm is associated with a positive increase in Dst index, which is due to increased solar wind dynamic pressures compressing the dayside magnetosphere and intensifying

magnetopause currents. This phase is also known as ‘sudden storm commencement’ if an interplanetary shock produces an abrupt increase in Dst index (Dessler & Karplus, 1961).

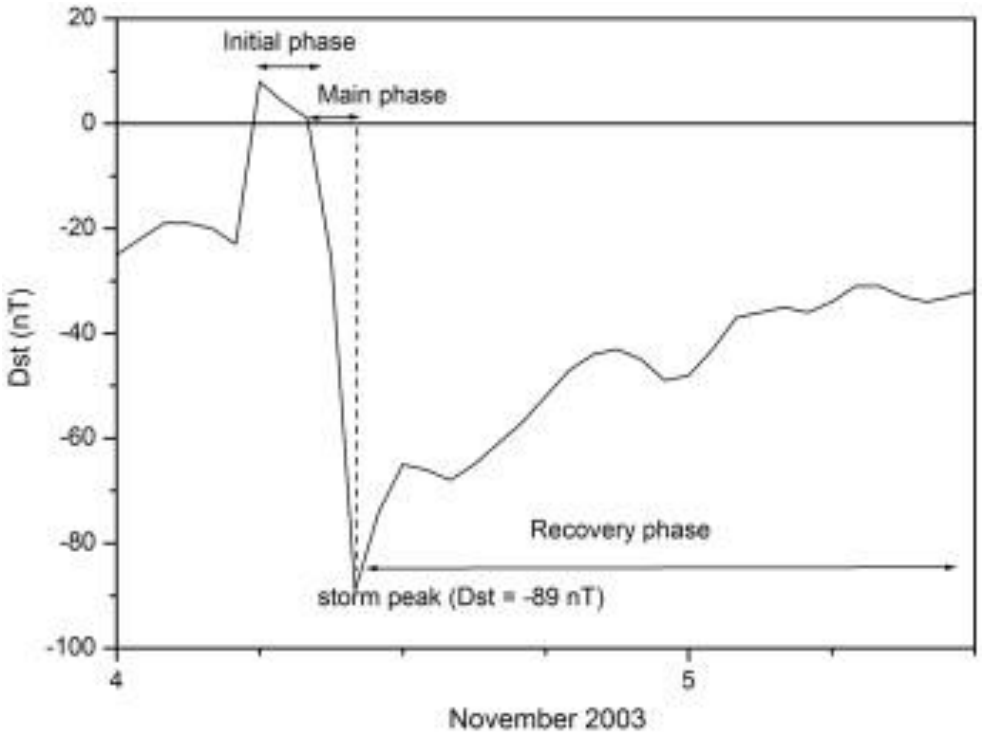

Figure 1.12 Example Dst index during a geomagnetic storm (4 to 5 November 2003) where the initial, main, and recovery phases are labelled (Echer et al., 2011).

The main phase of the storm is associated with a prolonged southwards turning of the IMF. In this configuration, there are high rates of dayside reconnection between the solar wind and magnetosphere which enhance convective flow through the magnetosphere. Just as discussed for geomagnetic substorms, this leads to enhanced rates of nightside reconnection. Energy from this reconnection is transferred to plasma in the plasma sheet, and hot ions are transported to the inner magnetosphere where they enhance the ring current. The rapid enhancement in ring current acts to decrease the Dst index.

The recovery phase of the storm begins when convective flow through magnetosphere decreases as solar wind driving subsides. As nightside reconnection stops, the rate of particle loss from the ring current exceeds the supply. Dst index slowly increases towards a quiet time value as the ring

current is reduced. The primary loss processes are precipitation into the atmosphere (which is discussed in detail in the context of the radiation belts Section 1.7.3) and charge exchange with cold particles in the neutral atmosphere.

Geomagnetic storms may occur in isolation, following the sequence of Dst index described above, or as part of a sequence of several geomagnetic storms known as a compound geomagnetic storm. In a compound geomagnetic storm, the Dst index may repeatedly decrease rapidly, characteristic of main storm phases, throughout the storm recovery phase.

1.7 The Radiation Belts

The radiation belts are regions in the magnetosphere where highly energetic particles are trapped, undergoing gyromotion about the magnetic field, bounce motion between the mirror points in the northern and southern hemispheres, and drift motion about the Earth where the drift path is closed. The radiation belt typically has a two-belt structure, with an inner belt which extends from ~ 1.2 – 2.5 R_E consisting of electrons and protons, and an outer electron belt which extends from ~ 3 – 8 R_E. The belts are separated by a depletion zone called the ‘slot region’.

1.7.1 Energetic Particle Sources: Inner Belt

The primary proton source of the inner radiation belt is cosmic ray albedo neutron decay (CRAND). CRAND is a phenomenon where cosmic rays interact with atmospheric nuclei producing an energetic neutron. A proportion of these neutrons will escape from the atmosphere and decay into a proton, electron, and anti-neutrino. If this decay occurs before the neutron exits the Earth’s magnetosphere, some of the protons and electrons will become trapped in the magnetic field (Singer, 1958; Vernov et al., 1959; Kellogg, 1959). Electrons produced in CRAND are not thought to significantly contribute to the inner electron belt population (Lenchek et al., 1961; Selesnick, 2015).

During periods of increasing sunspot activity, energetic solar protons may also become trapped by the geomagnetic field, diffusing as far as L-shell ~ 1.3

(Lorentzen et al., 2002; Selesnick et al., 2014). The inner proton radiation belt is relatively stable, and protons may become trapped for many years.

Energetic electrons are thought to be transported into the inner belt from the outer radiation belt (Reeves et al., 2016). Particles of 10s-100s keV have the highest rate of enhancements. Though enhancement of 1 – 1.5 MeV electrons are infrequent, electrons have lifetimes on the order of years (Claudepierre et al., 2017; Fennell et al., 2015).

1.7.2 Energetic Particle Sources: Outer Belt

In the outer zone, the rapid variability of relativistic electrons and the lack of an established external source implies an efficient acceleration mechanism acts on magnetospheric electrons, accelerating them to multiple MeV energies on a timescale as short as a few hours. Electron acceleration can be split into two categories; radial diffusion and local acceleration. These processes act by violating one or all the adiabatic invariants, μ, K, and L^* (Section 1.4).

Radial diffusion, first proposed by Fälthammar (1965), is where large-scale variations in the electric and magnetic fields break the third adiabatic invariant, allowing radial transport electrons to lower L-shells. Betatron and Fermi acceleration (described in Section 1.4.1) act to accelerate electrons provided the first and second invariants are conserved. Much of the early work in radiation belt structure and long-term variations could be explained by radial diffusion (Schulz & Lanzerotti, 1974). Radial diffusion may cause more rapid variation in the radiation belts when there are enhanced ultra-low frequency (ULF) pulsations in Earth's magnetosphere or particle injections.

If a particle is drift-resonant with a ULF wave, with frequencies on the order of mHz, the electron will experience electric fields which act to alter the electron drift path (Elkington et al., 1999). These electric fields scatter electron drifts by violating the third invariant. An entire population of electrons can rapidly diffuse radially through interactions with ULF waves to energies > 400 keV (e.g., Mann et al., 2004; O'Brien et al., 2001; Rostoker et al., 1998). ULF waves may be excited by external factors including Kelvin-Helmholtz instabilities at the flanks of the magnetopause (e.g., Claudepierre et al., 2008; Rae et al., 2005; Walker,

1981) or fluctuations in solar wind dynamic pressure (e.g., Allan et al., 1986; Kepko et al., 2002; Wright & Rickard, 1995).

Energetic particles may be injected form the magnetotail into the radiation belts during geomagnetic substorms. In the recovery phase of a substorm, the rapid dipolarisation of the nightside geomagnetic field induces electric fields which move particles into the inner magnetosphere. As particles are transported to regions of stronger magnetic field, they begin to follow gradient-curvature drift paths and are energised up to 300 keV (Gabrielse et al., 2014 and references therein).

Injected particles are wide ranging in energy, from 10s – 100s keV, and are fundamental to local acceleration processes which occur at a fixed radial location. Injected particles with energies of 10s keV are known as the 'source population' as they generate intense plasma waves in the very-low frequency (VLF) range (100s Hz -10 kHz) (Meredith et al., 2001). This occurs through gyro-resonant wave-particle interactions where source electrons transfer energy to VLF waves and are decelerated in the process (see Section 1.4.2). Injected particles with energies of 10s – 100s keV form the 'seed population' (Baker et al., 1997; Baker et al., 1998). The high amplitude VLF waves generated by the source population accelerate seed electrons to very high energies through gyro-resonant interactions (Horne & Thorne, 1998; Li et al., 1997b; Summers et al., 1998).

VLF waves in the magnetosphere act as an important mediator of energy exchange between plasma populations. Figure 1.13 shows a schematic illustration of the zoo of very low frequency waves (VLF) present in the Earth's magnetosphere. Of these waves, whistler-mode waves are capable of local acceleration (Horne & Thorne, 1998). Whistler-mode waves include chorus waves, plasmaspheric hiss, and equatorial magnetosonic waves.

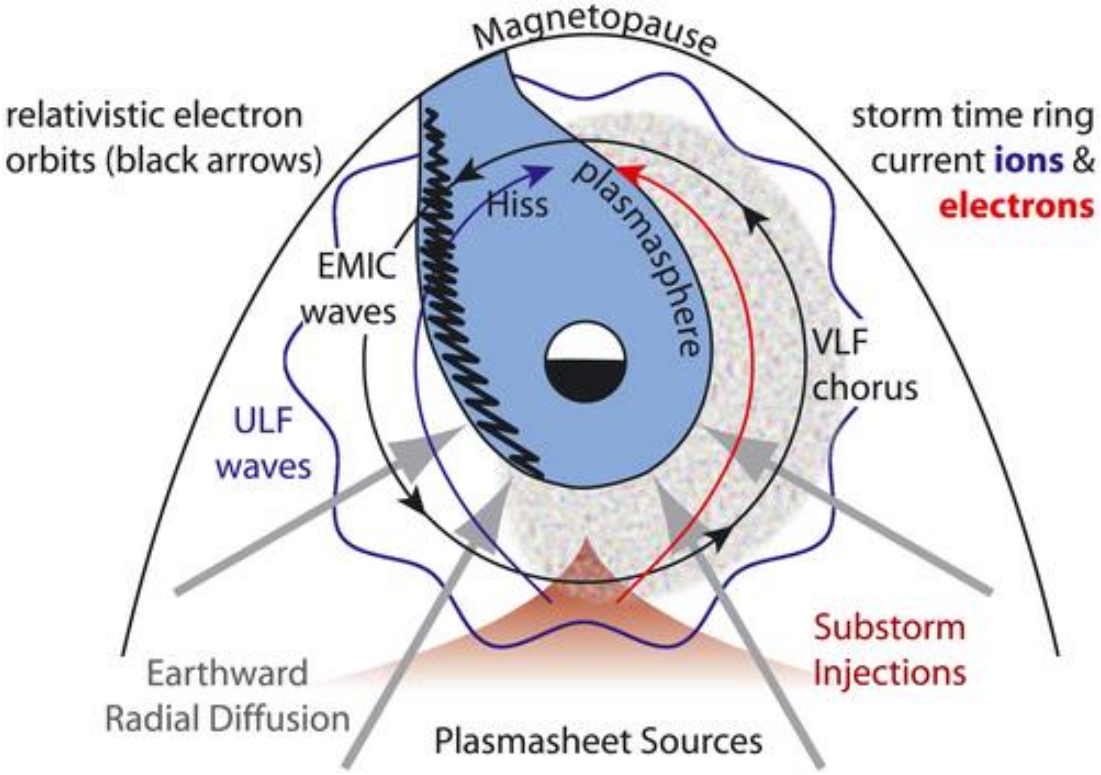

Figure 1.13 Illustration of the important waves in the inner magnetosphere, in relation to the plasmasphere and drift paths of ring current (10-100keV) electrons and ions, and relativistic electrons (≥0.3MeV) (Reeves et al., 2016).

Chorus waves are coherent right-hand polarised whistler-mode waves. These waves have two bands of frequencies above and below half of the local electron cyclotron frequency (Tsurutani & Smith, 1974). These waves are generated through cyclotron resonance in the source population of electrons injected into the inner magnetosphere during geomagnetic substorms (Hwang et al., 2007; Li et al., 2009). Chorus is predominantly observed outside of the plasmasphere, with highest amplitudes in the dawn sector as electrons are injected near midnight and drift towards dawn (Meredith et al., 2001).

Plasmaspheric hiss is a broadband structureless whistler-mode waves, which are primarily observed within the plasmasphere. It is thought that these waves originate from a subset of chorus waves which propagate into the plasmasphere and become trapped and amplified (Bortnik et al., 2008; Chen et al., 2012). These waves are associated with loss of electrons from the radiation belts (see Section 1.7.3) and are thought to be responsible for creating the quiet time slot region (Lyons & Thorne, 1973).

Magnetosonic waves are oblique whistler-mode waves, excited near the magnetic equator with frequencies near the ion gyrofrequency (Santolík et al., 2004). These waves are excited by a cyclotron resonant instability within injected ring current ions (Horne et al., 2000). These waves cause both acceleration and scattering of electrons via Landau resonance (Bortnik & Thorne, 2010; Horne et al., 2007)

Even though whistler-mode waves are highly localised in the magnetosphere (Figure 1.13), electrons may gain large amounts of energy over time through multiple interactions over several drift orbits. This is most likely to occur during geomagnetic substorms, or storms, when waves are excited to high amplitudes for a prolonged period. In addition, the ULF wave activity is often enhanced by solar wind phenomena which cause geomagnetic storms. Therefore, large enhancements to the radiation belts are often observed during period of high geomagnetic activity.

1.7.3 Energetic Particle Sink: Atmospheric Precipitation

Atmospheric precipitation is where radiation belt particles interact with atmospheric particles, such that they dissipate energy into the atmosphere and are lost from the radiation belts. This may occur if a radiation belt particle has a magnetic mirror point at low altitude, such that the collisional cross section with the neutral atmosphere becomes high enough for particles to precipitate. For electrons > 100 keV, this usually occurs in the middle and upper atmospheric levels (~ 30 – 90 km), which is the lowest layer of the ionosphere known as the D-region (Rodger et al., 2007).

We can define the maximum equatorial pitch angle at which particles will precipitate using Equation **1.13**, $\alpha_L = sin^{-1}\sqrt{B_{eq}/B_A}$, where B_A is magnetic field strength in the D-region ionosphere. The range of equatorial pitch angles below this is called the 'loss cone'. There are two loss cones, the bounce loss cone, and the drift loss cone, illustrated in Figure 1.14. The bounce loss cone is where particles precipitate within a single bounce cycle, whereas the drift loss cone is the range of pitch angles where particles are lost within a drift orbit. The difference between the bounce and drift loss cones arises from the

inhomogeneity in the geomagnetic field in longitude. Specifically, the shift of the magnetic dipole from the centre of the Earth results in a localised region where the field is weaker, known as the South Atlantic Anomaly. Thus, B_A varies across magnetic longitudes, resulting in a quasi-trapping region between the bounce loss cone, α_{BL}, and drift loss cone, α_{DL}.

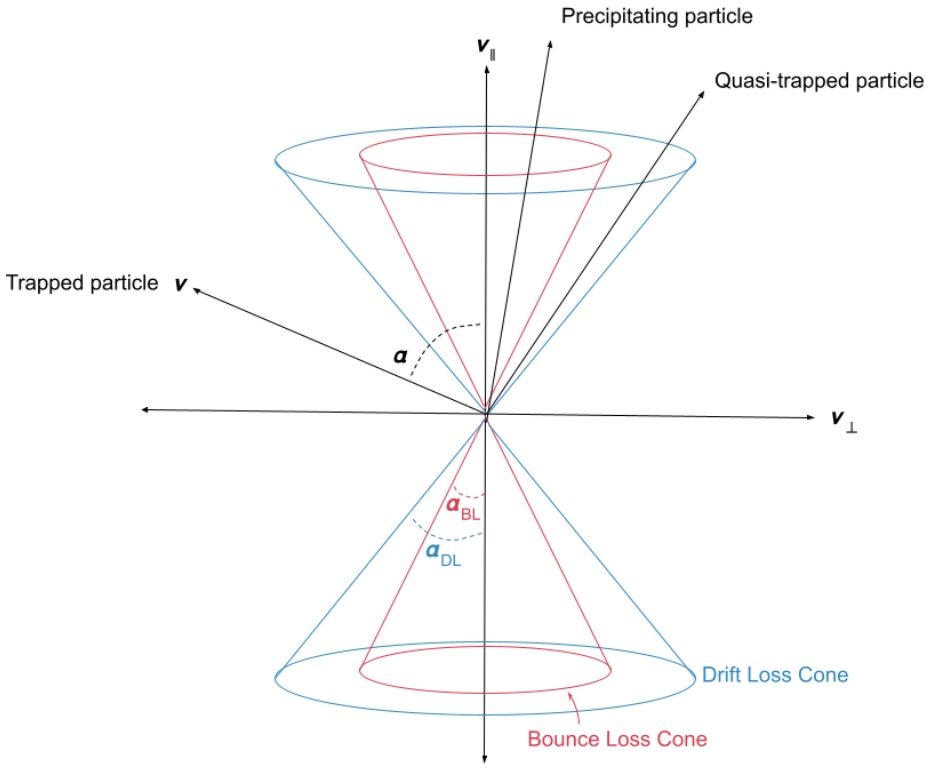

Figure 1.14 Diagram of the bounce and drift loss cones. The angle between particle velocity and the magnetic field, pitch angle α, is shown. Regions of precipitating particles within the bounce loss cone of angular width, α_{BL}, and quasi-trapped particles within the drift loss cone of width, α_{DL}, are shown.

Wave-particle interactions can act to drain the radiation belts by scattering particle pitch angles into the loss cone (Section 1.4.2), where particles subsequently precipitate into the atmosphere (Kennel & Petschek, 1966). Both whistler-mode waves and electromagnetic ion cyclotron waves (EMIC) are candidates of electron scattering (Horne & Thorne, 1998).

EMIC waves are a subset of ULF waves with frequencies in the Pc1 wave band (~ 0.2 - 5 Hz) which are generated by temperature anisotropies ($T_{\parallel} < T_{\perp}$) in ring current ions in three bands, below the H^+, He^+, and O^+ ion gyrofrequencies (e.g. Cornwall et al., 1970; Thorne & Horne, 1992).

Temperature anisotropies may arise when a plasma is adiabatically heated perpendicular to the magnetic field. This occurs during geomagnetic storms when particles are injected into the inner magnetosphere from the plasma sheet (e.g., Cornwall, 1965; Criswell, 1969), or through strong compressions of the dayside magnetosphere by the solar wind (e.g., Anderson & Hamilton, 1993; Engebretson et al., 2002). EMIC waves undergo a cyclotron resonance with radiation belt electrons to scatter electron pitch angles into the loss cone (e.g. Thorne & Kennel, 1971; Usanova et al., 2014).

During quiet geomagnetic times, the presence of the slot regions are understood to be a result of resonant scattering by plasmaspheric hiss (Lyons & Thorne, 1972) and other whistler-mode waves (Abel & Thorne, 1998). Direct observations of precipitation also indicate that losses can be strong enough to empty the radiation belts in a few days, or less in some cases (O'Brien et al., 2004).

1.7.4 Energetic Particle Sink: Magnetopause Shadowing

Magnetopause shadowing is a loss process whereby electrons are lost through the magnetopause into interplanetary space (Li et al., 1997a). It is possible for electrons to cross the magnetopause either by gradient drift across the tangential discontinuity (e.g., Kim & Lee, 2014; Kudela et al., 1992), escape along merged magnetic field lines (e.g., Korth et al., 1982; Mauk et al., 2016), or through magnetic vortices created by Kelvin-Helmholtz instabilities on the magnetopause (Sorathia et al., 2017).

Electrons which complete closed drift shells are trapped, and therefore form part of the radiation belts. Electrons which drift into the magnetopause are described as following open drift paths, where their third adiabatic invariant, or L^*, is no longer conserved. The last closed drift shell (LCDS) before the magnetopause may be considered the outer limit of the radiation belts (Olifer et al., 2018), and electrons on open drift paths beyond the LCDS are in the magnetopause loss cone.

There are several peculiarities to electron drift paths in an azimuthally asymmetric magnetic field, such as the magnetosphere, to consider when

defining the LCDS. The magnetosphere is compressed by the solar wind such that the dayside magnetic field is stronger than the nightside at the same radial distance. Trapped electrons will follow contours of constant magnetic field strength to conserve their third adiabatic invariant, so drift to higher radial distances on the dayside than the nightside. The additional conservation of the second adiabatic invariant (Equation **1**.**31**) means that particles must bounce along a surface of constant J_2. The intersection of this surface of constant J_2 with the surface of constant B is dependent upon the location of the particle's mirror point, or equivalently its equatorial pitch angle. This results in a phenomenon known as drift shell splitting, whereby particles which originate from the same magnetic field line at midnight follow different drift shells, depending upon their equatorial pitch angle at midnight (Roederer, 1967). Particles with very low pitch angles (so mirror at high magnetic latitudes) will drift to lower radial distances on the dayside than particles with high pitch angles (mirroring nearer the magnetic equator), illustrated in Figure 1.15 a.

There are two scenarios in which electron drift paths may intersect the magnetopause, illustrated in Figure 1.15b-c. The first is where there is an incursion of the magnetopause into the radiation belt. In this scenario the magnetopause is compressed by sudden changes in the solar wind, and/or eroded by strong rates of magnetic reconnection between southwards orientated IMF and the magnetosphere. Note that we often use the term 'compressed' to synonymously refer to the inward movement of the magnetopause due to both pressure balance variations and magnetosphere erosion under southward IMF (e.g., Dmitriev et al., 2014; Gosling et al., 1982; Sibeck et al., 1989). If compressions are faster than an electron orbital drift period, electrons are not able to respond by adiabatically moving inwards, so previously closed electron drift paths are intersected by the magnetopause. This shall be referred to as *direct* magnetopause shadowing. In the second scenario, electrons may be transported radially outwards towards the magnetopause, where their drift paths subsequently intersect the magnetopause boundary and are lost. This shall be referred to as *indirect* magnetopause shadowing.

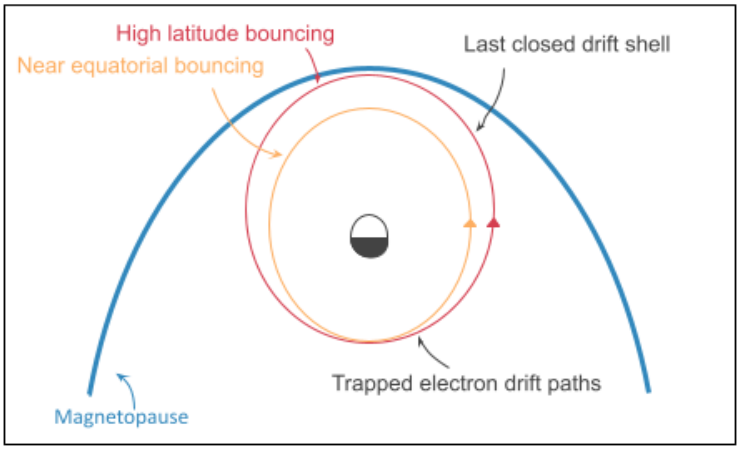

(a) Stable Trapping

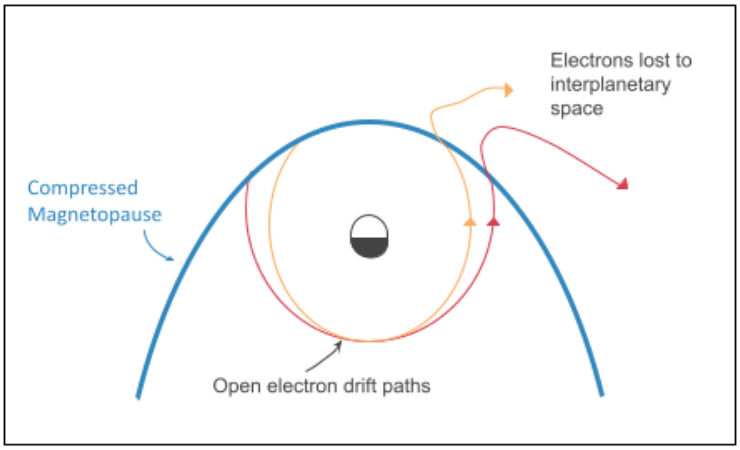

(b) *Direct* Shadowing

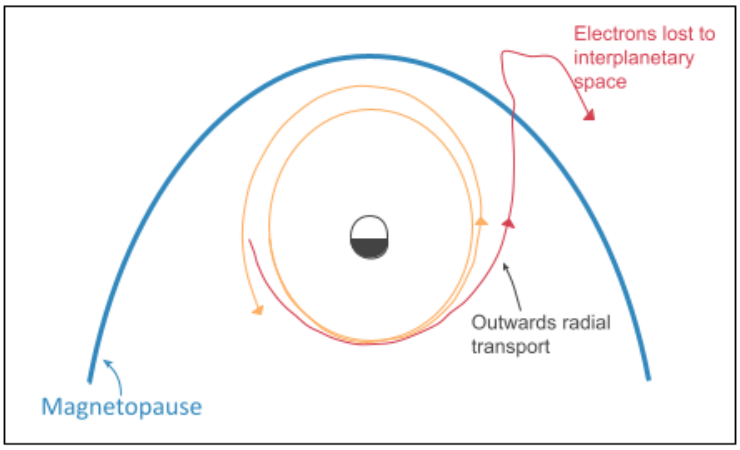

(c) *Indirect* Shadowing

Figure 1.15 Diagram of (a) stably trapped radiation belt electron drift paths at high (yellow) and low (red) equatorial pitch angles; (b) direct magnetopause shadowing due to magnetopause compression; (c) indirect magnetopause shadowing by outwards radial transport of electrons.

Outward radial transport during indirect magnetopause shadowing may occur either adiabatically though the Dst effect, or non-adiabatically through outwards radial diffusion or drift orbit bifurcation. The Dst effect occurs when the ring current becomes enhanced during a geomagnetic storm, which occurs slowly (~hours) compared to electron drift orbits. The enhanced ring current reduces the magnetic flux within an electron drift path, so electrons increase their drift path to conserve the third adiabatic invariant (Equation **1**.**33**). Electrons will also decrease in energy as they are transported outwards to conserve the first and second adiabatic invariants. This is not considered a loss process because energy changes are adiabatic and therefore reversable when the ring current subsides (if they are not lost to the magnetopause).

Electrons are also transported non-adiabatically towards the magnetopause through radial diffusion if the third adiabatic invariant is broken (Kellogg, 1959). Interactions between electrons and ULF waves drive the stochastic diffusion of electrons down negative radial gradients in electron phase space to regions of lower phase space density (Lejosne & Kollmann, 2020). Enhanced ULF wave activity and negative gradients in electron phase space density with increasing L^* can lead to fast transport of electrons towards the magnetopause boundary (Loto'aniu et al., 2010; Shprits et al., 2006; Turner et al., 2012b) – this will be discussed in further detail in Section 2.2.1.

In addition, particles which drift close to the magnetopause may undergo drift orbit bifurcations. This occurs when the compression of the dayside magnetosphere creates a magnetic topology in the outer magnetosphere where equatorial magnetic field strength is stronger than that of particle mirror points. Particles drifting into these regions become trapped in a single hemisphere, bouncing between polar and equatorial mirror points (Shabansky, 1971). This change in bounce configuration through a drift orbit violates the second and third adiabatic invariants, and these particles are described as being quasi-trapped (Öztürk & Wolf, 2007). If, following drift through the bifurcation region, the second adiabatic invariant increases compared to initial value, then the particle is transported to higher radial distances. If this magnetic

topology is maintained over several drift orbits, bifurcating particles are transported outwards and lost to the magnetopause (Desai et al., 2021a).

1.8 Coordinate Systems

There are several coordinate systems used in geophysics. Those which are used in this thesis are described below.

The *geocentric solar magnetic coordinate* (GSM) is defined: The x-axis is directed towards the Sun and z-axis is the projection of Earth's magnetic dipole axis (positive north) on to the plane perpendicular to the x-axis. The y-axis is orthogonal to both the x and z-axis.

Magnetic Local Time (MLT) is a reference system analogous to geographic longitude, only it is static in the geomagnetic reference frame. MLT is measured by the angle formed by two planes: the dipole meridional plane, which contains a subsolar point on the Earth's (or any altitude) surface, and the dipole meridional plane which contains a given point on the surface (that is, the local dipole meridian). 12 h MLT is defined at the dayside along the Sun-Earth line, and 0 h MLT is defined on the nightside along the Sun-Earth line. 6h and 18h MLT correspond to dawn and dusk respectively.

Adiabatic coordinates are a canonical coordinate system represented in phase space. This system describes populations of trapped relativistic particles by defining coordinates relative to specific periodic motions. Canonical momenta are used to specify these coordinates since these quantities are conserved over each periodic motion. The magnetic moment represents gyromotion, which can be determined from a particle's energy, pitch angle, and location in the magnetic field, $\mu(E,\alpha,B)$. Bounce motion is represented by the momentum parallel to the magnetic field integrated between two mirror points, which is determined from a particle pitch angle and location in the magnetic field $K(\alpha,B)$. Drift motion is represented by the magnetic flux enclosed by a drift shell, which is determined from a particle pitch angle and location in the magnetic field $L^*(\alpha,B)$. In this coordinate system we use the CGS units: μ is derived in MeV/G (where G is Gauss), K is in $G^{0.5}R_E$, and L^* is in R_E.

Chapter 2 Literature Review

2.1 Radiation Belt Flux

The population of electrons in the outer radiation belt is commonly discussed in terms of differential particle flux, $j(E,\theta)$, which is described as the number of particles per unit area, $dxdy$, per unit solid angle, $d\Omega$ (in direction $\hat{\theta}$), per unit energy, dE, with units of cm^{-2} s^{-1} sr^{-1} keV^{-1} (sr is steradians). Noting that θ is the azimuthal angle between particle velocity and the magnetic field. If the particle flux is symmetric around the magnetic field, then this is defined using pitch angle, α.

$$dN = j(E,\theta)dx\,dy\,d\Omega\,dE \tag{2.1}$$

Differential electron flux is measured by the rate of particles incident on an in-situ spacecraft particle detector at a given energy (dE). Differential energy flux is also often used, which is the differential particle flux multiplied by energy, $j(E,\theta)E$, with units of cm^{-2} s^{-1} sr^{-1}. By measuring incident electrons in several look directions, the flux can be obtained for different pitch angles. In this way, information on the number of electrons distributed across energy and pitch angle is obtained for the time and location of the spacecraft. As the bounce and drift orbits of relativistic electrons are so fast, a single spacecraft passing through the radiation belt can obtain a snapshot of the entire radiation belt.

Changes in radiation belt flux signify that acceleration, loss, or transport mechanisms are acting to alter a population of electrons. These processes are closely linked with geomagnetic storms, substorms, and strong solar wind-magnetosphere interactions, and so the greatest and most dynamic changes in flux result from these phenomena. The radiation belt response to geomagnetic storms is especially complex due to competing acceleration and loss mechanisms which act in different locations of the magnetosphere, and on different timescales. Radial diffusion towards the magnetopause (Chaston et al., 2017; Mann & Ozeke, 2016; Turner et al., 2014b) and wave-induced precipitation (O'Brien et al., 2004; Thorne et al., 2005; Blum et al., 2013) are thought to deplete outer belt electrons on the timescale of several hours,

whereas whistler-mode wave-particle interactions accelerate electrons over several days during the recovery phase of a storm (e.g. Baker et al., 1994; Horne et al., 2005; Forsyth et al., 2016; Murphy et al., 2018).

2.1.1 Geomagnetic Storms

It is understood that the radiation belts have a two-step response to geomagnetic storms; a net-loss phase during storm onset when the radiation belt flux decreases overall, followed by a net-acceleration phase when radiation flux increases overall (Murphy et al., 2018). Electrons are initially lost from the belts because magnetospheric compressions by solar wind structures lead to fast electron loss via magnetopause shadowing and generation of EMIC waves, which scatter energetic electrons into the atmospheric loss cone (Boynton et al., 2017; Wang et al., 2014). The net-loss period may extend into the main phase of the geomagnetic storm, until acceleration mechanisms increase the radiation belt electron flux at a rate exceeding the rate of loss. The net-acceleration phase is delayed compared to the net-loss phase because the timescales of whistler-mode wave driven acceleration and/or ULF driven diffusion (hours to days) is longer than that of loss (Baker et al., 1994; Boyd et al., 2014; Elkington et al., 2003; Horne et al., 2005; Reeves et al., 2013). Figure 2.1 demonstrates the net radiation belt response by showing changes in the average radiation belt electron content (a proxy for the number of electrons in the radiation belt, Forsyth et al., 2016) for 73 geomagnetic storms (Murphy et al., 2018).

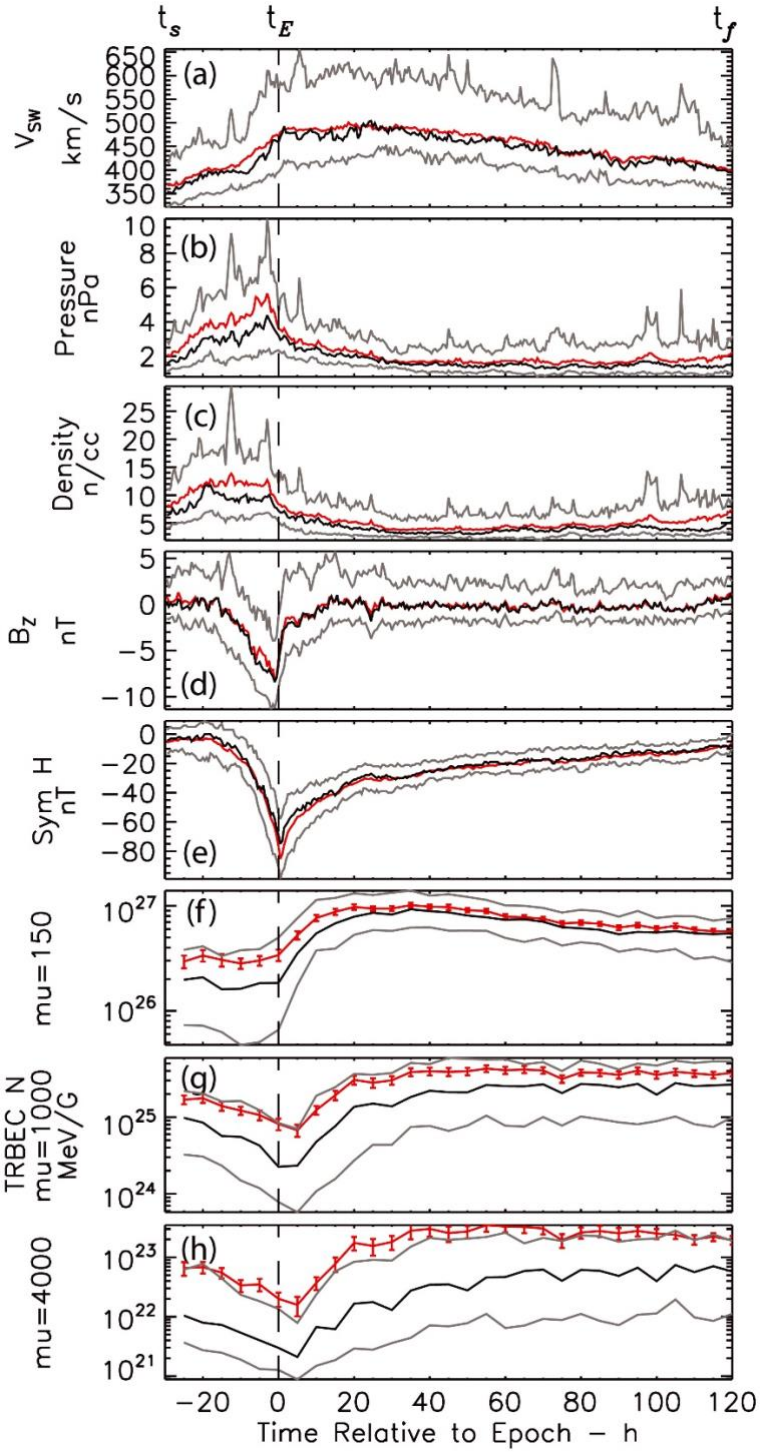

Figure 2.1 Superposed epoch analysis of 73 geomagnetic storms where epoch time zero is defined by minimum Sym-H index, and time is normalised by storm duration. Parameters shown variation in the solar wind; (a) velocity (b) dynamic pressure, (c) density, (d) IMF field strength in the north-south direction; the geomagnetic conditions (e) Sym-H index; and the total radiation belt electron content (TRBEC) at three different values of the first adiabatic invariant, μ, (f) 150 MeV/G (sub-radiation belt energy), (g) 1,000 MeV/G (relativistic to ultra-relativistic energies), (h) 4,000 MeV/G (ultra-relativistic energies). For each parameter the median is shown in black, mean in red, and upper and lower quartiles in grey (Murphy et al., 2018).

Whilst geomagnetic storms often result in large enhancements to the radiation belts, this is not the case for all storms. Reeves et al. (2003) analysed the response of relativistic electron flux to 276 geomagnetic storms, finding that only 53% of the storms resulted in significant flux increase. Flux decreased in 19% of the storms and did not change by more than a factor of two in 28%. This variability in the overall radiation belt response to storms is attributed to differences in acceleration and loss mechanisms driven by large-scale solar wind structures, resulting in variable magnitudes of the net-loss and net-acceleration phases. For example, enhanced solar wind dynamic pressures and strong southward components of IMF are correlated with electron losses during both CMEs and CIRs (Gao et al., 2015; Kilpua et al., 2015; Sandanger et al., 2009), but CMEs are more likely to result in a decrease to > 1 MeV electrons (e.g., Turner et al., 2019). CMEs are also associated with higher convection and substorm activity than CIRs, which leads to a greater likelihood of particle enhancements (Bingham et al., 2018).

2.1.2 Electron Flux Dropouts

Bingham et al. (2018) further discussed that the magnitude of the net-loss phase is an important precursor to the later net-acceleration phase because existing radiation belt electrons and seed electrons are removed. An extremely large loss of radiation belt flux would therefore limit the number of particles that can be accelerated from the seed population. If a solar wind compression of the magnetosphere is large enough, electron losses during storm onset are extreme, and the entire outer radiation belt flux may suddenly decrease by orders of magnitude over a timescale of hours. This is referred to as an electron flux dropout (e.g., Borovsky & Denton, 2009; Onsager et al., 2002), defined by Turner et al., 2012a as '*a decrease of trapped electron flux by a factor of 50 or more at a particular L-shell, equatorial pitch angle, and magnetic local time over a period of 24 hours or less'*.

The extent to which magnetopause shadowing and atmospheric precipitation each contribute to a radiation belt dropout has been a topic of continuing debate. Several studies have shown that magnetopause shadowing is the dominant loss process of a dropout event (e.g. Morley et al., 2010a; Shprits et

al., 2006; Turner et al., 2012b), whilst other studies have found that EMIC wave scattering dominates losses (e.g. Shprits et al., 2016; Xiang et al., 2017), or have found dropouts are caused by a combination of both mechanisms (Bortnik et al., 2006; Turner et al., 2014b). What is more, different regions of the radiation belt have been found to typically be dominated by either mechanism of loss; magnetopause shadowing usually produces losses at $L^* \gtrsim 4$ and EMIC wave scattering is the dominant loss mechanism at $L^* \lesssim 4$ (Bortnik et al., 2006; Turner et al., 2014a), though, this is not always the case. Xiang et al. (2017) showed events where magnetopause shadowing acted to dominate losses at $L^* < 4$, and where EMIC induced precipitation significantly contributed to losses at $L^* > 4$.

The commonality in either loss mechanism during flux dropout events are compressions by the solar wind: magnetopause shadowing is produced by movements in the magnetopause and generation of ULF waves, launched at the magnetopause, and fast precipitation is induced by electron cyclotron resonance with EMIC waves, generated by temperature anisotropies created by magnetospheric compressions (e.g., Anderson & Hamilton, 1993; Engebretson et al., 2002). Perhaps it is therefore unsurprising that observations of loss during flux dropouts cannot reconcile which mechanism is the dominant contributor to loss, since the two mechanisms often act in tandem, with the location and magnitude of each loss dependent on event specific behaviours.

2.1.3 Flux Dropout Observations

Losses through either loss mechanism will have unique signatures which indicate to the observer which process is acting. Precipitating electrons may be observed by; (i) low altitude satellites which can resolve the bounce loss cone to measure precipitating electrons in-situ (Sandanger et al., 2009). (ii) daytime decrease of forward scatter radio signals, resulting from increased ionisation of the D-region ionosphere (Bailey, 1968). (iii) Bremsstrahlung X-rays produced when precipitating electrons collide with neutrals (Rosenberg et al., 1972). It is almost impossible to measure the precipitating flux near the magnetic equator, due to the small size of the loss cone.

Due to the inherently rapid nature of shadowing, it is extremely hard to measure particles in the magnetopause loss cone (i.e., particles following drift paths intersected by the magnetopause). So far, magnetopause shadowing has been inferred by identifications of compressed magnetopause or LCDS simulations to a net-decrease in electron flux (e.g., Morley et al., 2010b; Olifer et al., 2018; Rodger et al., 2019) and/or measurements of butterfly pitch angle distributions in the nightside magnetosphere (e.g., Kang et al., 2018; Ozeke et al., 2020; Tu et al., 2019). Butterfly pitch angle distributions occur where there is a minimum in 90^{o} electron flux, arising through the preferential loss of electrons at high pitch angles via drift shell splitting.

For example, Morley et al. (2010b) studied 67 solar wind stream interface regions, demonstrating electron flux decreased down to L^* ~ 4 in conjunction with magnetopause compressions to an average location of L = 8.5 (as parameterised by the Shue et al. (1997) magnetopause model). Thus, Morley et al. (2010b) attributed the statistical loss of electrons to outward radial diffusion toward a compressed magnetopause. For the same events, Hendry et al. (2012) analysed the precipitating electron flux measured by the Polar Operational Environmental Satellites (POES). The authors observed an average increase in electrons with pitch angles within the bounce loss cone following the arrival of the stream interface, indicating periods of high electron precipitation.

These observations are illustrated in Figure 2.2a, which shows the average trapped 230 – 410 keV electron flux measured by GPS satellites (Figure 2; Morley et al., 2010b) and Figure 2.2b shows the > 100 keV precipitating electron flux measured by POES (Figure 3; Hendry et al., 2012). Interestingly, Hendry et al. (2012) did not observe any increase in precipitating electron flux during the electron flux dropout itself. Therefore, the majority of losses during the dropout occur via magnetopause shadowing.

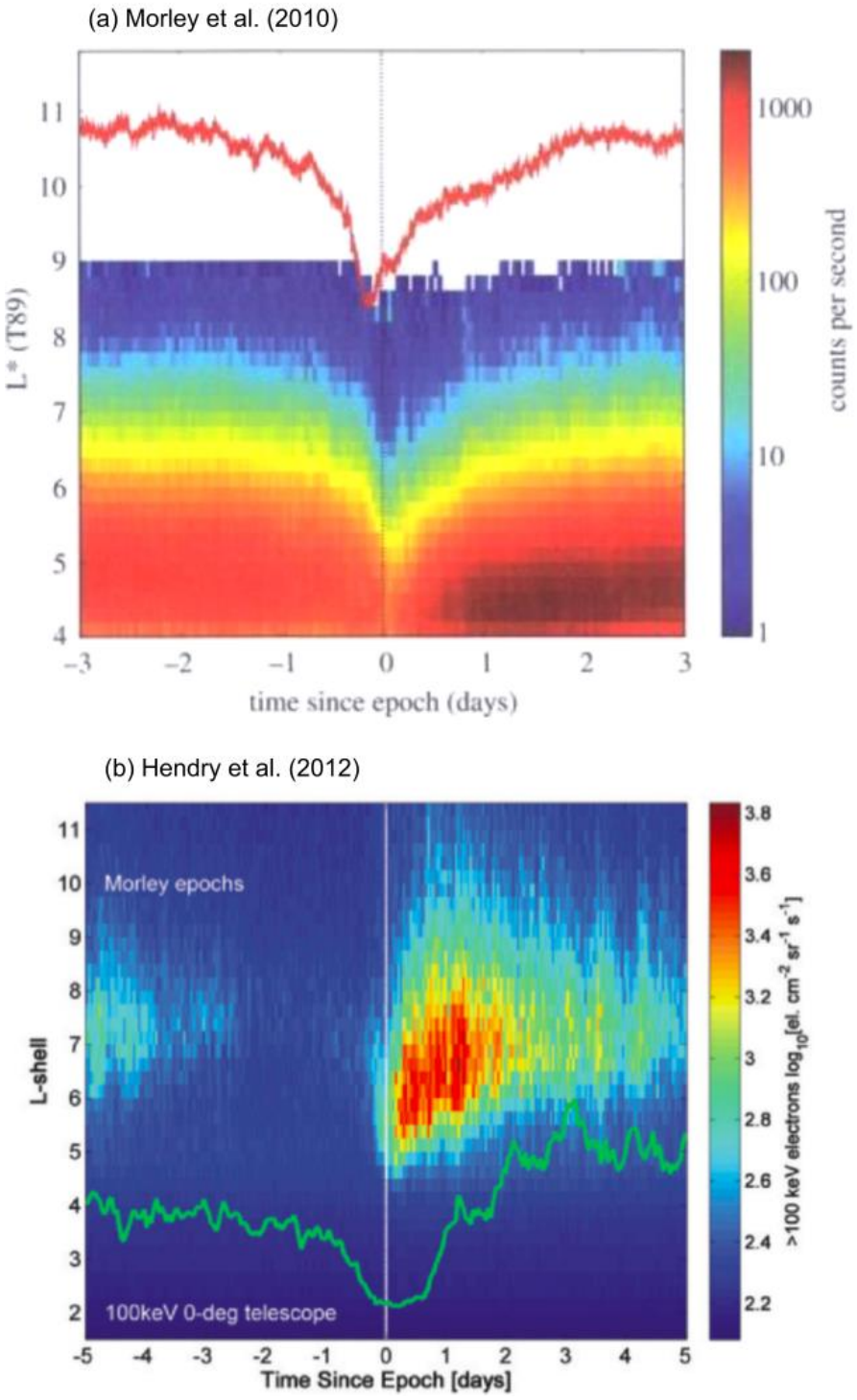

Figure 2.2 Superposed epoch analysis of the radiation belts during 67 solar wind streams classified by Morley et al. (2010b). Epoch time zero is when the stream interface arrives at the bow shock. (a) Figure 2 of Morley et al. (2010b); average 230 – 410 keV electron count by colour as a function of *L, measured by CXD instrument onboard GPS satellites. The overplotted red line shows median standoff distance of the Shue et al. (1997) magnetopause model (in R_E). (b) Figure 3 of Hendry et al. (2012); average integral flux of precipitating >100 keV electron energy flux from the 0^o directed MEPED telescope on board POES.**

2.2 Phase Space Density

Adiabatic changes to radiation belt particles, such as during the Dst effect or slow compressions of the magnetosphere, result in changes to the electron flux observed by a spacecraft at a given location. When interpreting changes to the radiation belts, phase space density (PSD) in adiabatic invariant coordinates (μ, K, and L^*) is commonly used to account for these adiabatic effects.

In real space, the number of particles dN within a volume, d^3r, within a volume of canonical momentum space, d^3p, is given by

$$dN = f(\boldsymbol{r}, \boldsymbol{p}, t) d^3r d^3p \tag{2.2}$$

where $f(\boldsymbol{r}, \boldsymbol{p}, t)$ is phase space density. This is easily related to differential electron flux by dividing by canonical momentum $f(\boldsymbol{r}, \boldsymbol{p}) = j(E, \theta)/p^2$ (Walt, 1994).

Liouville's theorem states that phase space density distribution remains constant along the trajectories of the system. In the radiation belts this has the useful implication that, if PSD is expressed in terms of adiabatic coordinates $f(\mu, K, L^*)$, non-adiabatic changes to the system may be identified through changes in PSD.

2.2.1 Characteristics of Acceleration

Radiation belt studies have notably used PSD to distinguish localized internal sources of high energy electrons (e.g., Boyd et al., 2014; Chen et al., 2006; Green & Kivelson, 2004; Miyoshi et al., 2003; Selesnick & Blake, 2000) from radial diffusion of an external source (e.g., Degeling et al., 2008; Jaynes et al., 2018; Ozeke et al., 2019).

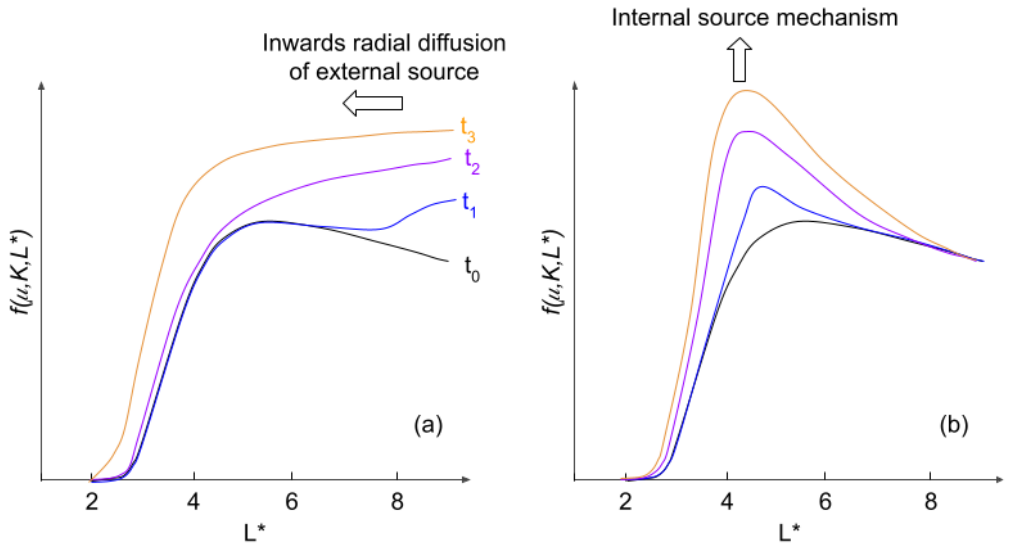

Figure 2.3 Schematic illustrating the evolution of PSD plotted as a function of *L, given a constant μ and *K*, whilst different source mechanisms are acting. An initial distribution is shown in black, t_0, followed by three colour coded PSD profiles where acceleration occurs, t_1 - t_3. Panel (a) shows electron acceleration by inwards radial diffusion; (b) shows electron acceleration by internal source mechanisms, such as wave-particle interactions localised in *L**.**

If the radiation belt becomes enhanced through inwards radial diffusion of electrons, the PSD profile in *L** will evolve such that PSD increases at high *L** first, followed by PSD enhancements at lower *L**. The final PSD profile increases monotonically with increasing *L**. Because radial diffusion results from random walk motion of particles across *L** (much in the same way Brownian motion leads to diffusion of a gas), diffusion will act to decrease any gradients in PSD.

If there is an internal source mechanism, such as VLF wave-particle interactions, the PSD will increase at the *L** location where particles are accelerated. This localised increase in electrons forms a growing peak in PSD as a function of *L**. Local acceleration is often accompanied by high rates of radial diffusion, which transports accelerated electrons away from the local peak, down any radial gradients. In this way, an internal source mechanism can increase PSD at a wide range of *L**.

2.2.2 Characteristics of Magnetopause Shadowing

PSD observations of the radiation belts have been extensively used to study electron acceleration. PSD may be used in a similar manner to study electron losses. Shprits et al. (2006) identified that radial gradients in PSD created by direct magnetopause shadowing can lead to efficient diffusion of electrons towards the magnetopause. Turner et al. (2012b) illustrated how this process could result in a dropout of electrons, Figure 2.4. There is an initial 'high pressure' phase during storm onset where the outer boundary of the radiation belt is compressed such that a significant amount of the PSD distribution is lost to interplanetary space. When the pressure relaxes during the main storm phase, the magnetopause expands and there is a peak in PSD at the minimum radial distance which the magnetopause reached during the compression, and a strong negative gradient in PSD towards the expanded magnetopause. Over time, ULF wave activity during the main phase of the storm will rapidly diffuse the remaining particles down any radial gradients in the PSD profile, resulting in a decrease in the L^* location of peak PSD, and a decrease in PSD at all L^* compared to the pre-storm distribution.

Tu et al. (2019) showed through radiation belt simulations that drift shell splitting leads to a higher rate of loss of particles with low K values (which corresponds to high pitch angle particles). This is because the L^* location of the LCDS is significantly reduced for near-equatorial bouncing particles with lower values of K. This will result in higher rates of particle losses at low K, both through enhanced direct magnetopause shadowing, and higher rates of radial diffusion as radial PSD gradients are stronger.

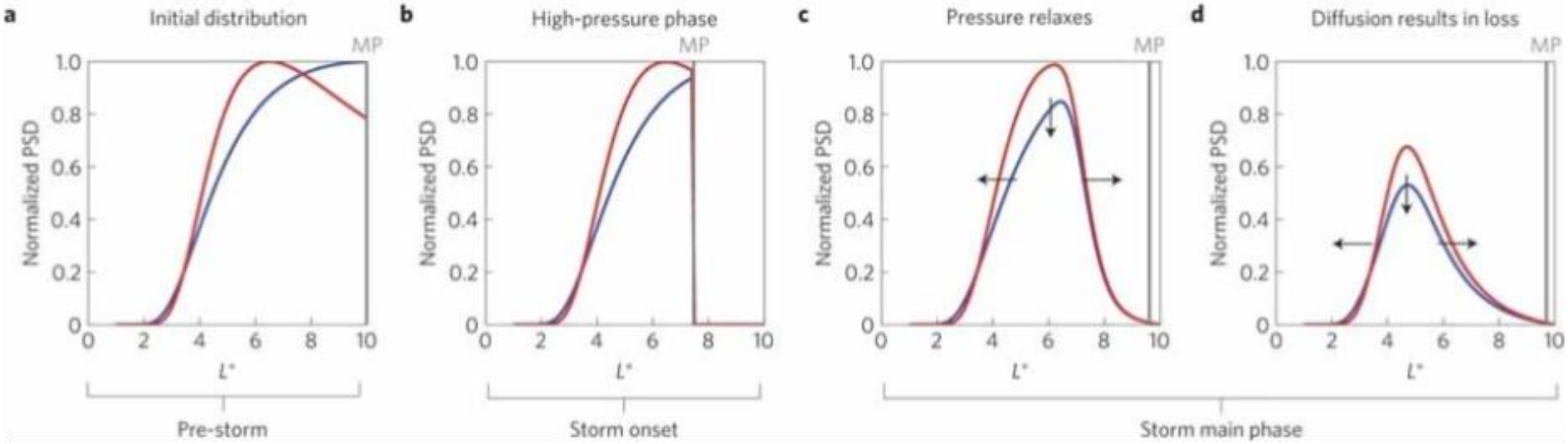

Figure 2.4 Schematic illustration of PSD as a function of *L, given a constant μ and *K*, for the scenario where a magnetopause compression leads to direct magnetopause shadowing at high *L** (b), followed by enhanced ULF wave activity which redistributes electrons (c-d) such that PSD decreases at all *L** (d) (Turner et al., 2012b).**

Xiang et al. (2017) investigated the dependence of magnetopause shadowing loss upon both μ and K. Whilst they were unable to observe a clear dependence upon K owing to lack of data coverage, they found that there were lower rates of loss at high values of μ. The authors discussed that electrons with higher μ have higher resonant frequencies with ULF waves due to their higher drift frequency (Liu et al., 2016; Tu et al., 2012). Because the power spectral density of ULF waves decreases as the wave frequency increases, there is less ULF wave power available to interact with higher energy electrons, resulting in lower radial diffusion rates.

Whilst some studies have successfully made PSD observations which show characteristics of a magnetopause shadowing induced dropout (e.g., Loto'aniu et al., 2010; Turner et al., 2013; Turner et al., 2014b), the rapid timescales of loss via magnetopause shadowing have not yet been fully resolved. Turner et al. (2014b) made significant progress characterizing the timescales of dropouts but found that there was insufficient data to resolve an accurate timescale at all L^*. This is because it is difficult to measure PSD profiles in L^* on the timescales necessary with single or even dual spacecraft in geostationary transfer orbits.

2.2.3 Characteristics of Atmospheric Precipitation

Precipitation loss may either appear through a gradual loss at all L^* (illustrated in Figure 2.5a) or as fast local loss (Figure 2.5c). Slow loss at all L^* may be caused by particle interactions with plasmaspheric hiss or chorus waves. Fast local loss, due to EMIC waves for example, would be observed as minima in PSD when plotted as a function of L^* (Shprits et al., 2017), as illustrated in Figure 2.5c. Mann and Ozeke (2016) highlighted that it is necessary to observe a *deepening* PSD minimum (i.e., a PSD minima which decreases over time) in order to conclude that the minimum is created by electron loss via precipitation. This is because PSD minimum at a local L^* may also be created by magnetopause shadowing followed by inwards radial diffusion which increases PSD at high L^*. Local precipitation loss has been identified by deepening PSD minima observations in Van Allen Probe measurements of PSD (e.g., Aseev

et al., 2017; Blum et al., 2020; Capannolo et al., 2018; Shprits et al., 2017; Shprits et al., 2018).

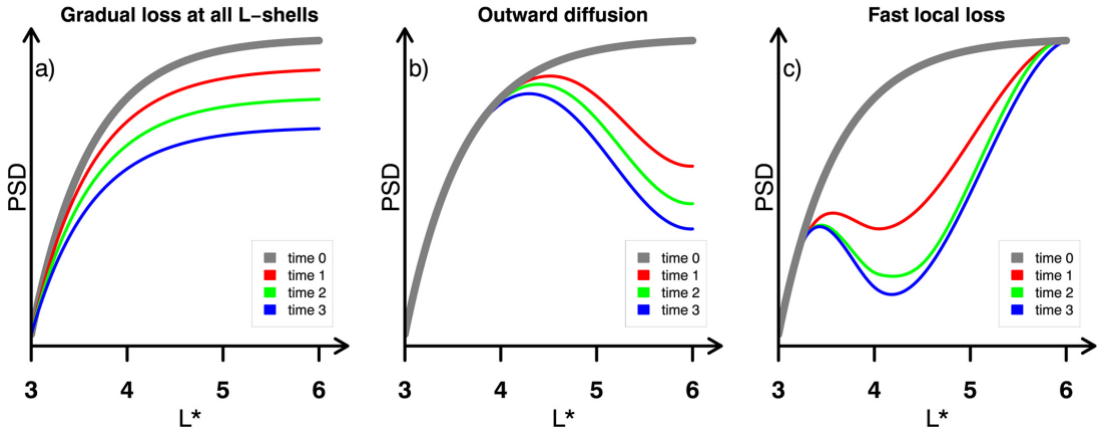

Figure 2.5 Schematic illustrating the evolution of PSD plotted as a function of *L, given a constant μ and *K*, whilst electron loss occurs due to (a) gradual loss at all *L** due to non-localised precipitation (b) outwards radial diffusion towards the magnetopause, (b) precipitation loss at a local *L** (Shprits et al., 2017).**

Xiang et al. (2017) discussed that the dependence of electron PSD loss on the first and second adiabatic invariants, μ and *K*, could also be used to distinguish loss mechanisms. The authors observed that outwards radial diffusion results in less loss in PSD at high μ values whereas there is greater loss at high μ and *K* values during EMIC wave induced loss. Ma et al. (2020) also used Van Allen probe observations of PSD at a range of μ and *K* to identify simultaneous loss via outwards radial diffusion to the magnetopause and EMIC wave induced precipitation. In this instance, depletions in PSD were observed both at low μ, which were attributed to magnetopause shadowing, and PSD depletions at high μ and *K* were attributed to precipitation loss.

2.3 Parameterising the Outer Boundary of the Radiation Belt

It is important to understand where the outer boundary of the radiation belt is located so that the contributions of magnetopause shadowing on electron flux dynamics may be evaluated. The location of the outer boundary is also critical for constraining radiation belt models (e.g., Glauert et al., 2014; Reeves et al., 2012). The outer boundary is defined by the location of the LCDS, which defines the boundary of trapped electrons, and/or by the magnetopause, where electrons are ultimately lost from the system. Both the LCDS and

magnetopause locations have been found to correspond to dynamics in the outer radiation belt (Matsumura et al., 2011; Olifer et al., 2018). However, the model parameterisations of both boundaries rely upon a variety of underlying assumptions which are likely violated during magnetopause compressions.

Considering the LCDS as the outer boundary to the radiation belts could be considered preferable over the magnetopause as it accounts for varied rates of electron loss to the magnetopause for different pitch angles (Xiang et al., 2017). However, there are several reasons why the determination of the LCDS location could be problematic. The LCDS is computed by numerical determination of the maximum L^* for which a particle completes a closed drift path in a modelled global magnetic field (e.g., Tsyganenko et al., 2003). It has been found that the LCDS is heavily reliant upon the global magnetic field model used in computations (Albert et al., 2018). What is more, electrons near the magnetopause may undergo drift orbit bifurcations (DOB) due to the distortions of the magnetic field (Section 1.7.4). In this scenario, the definition of L^* will neglect the presence of DOBs. Computations of the LCDS rely on one of two expedients: (i) DOBs are accounted for by following the guiding centre motion of particles in a distorted field with plausible L^*, such as the AFRL-Shell dynamical code (Brizard & Chan, 1999). (ii) DOBs are discounted and L^* is computed by finding drift paths which conserve all three adiabatic invariants, such as the numerical codes found in the International Radiation Belt Environment Modelling (IRBEM) library (Boscher et al., 2013), and the LanlGeoMag (LGM) code (Henderson et al., 2018).

As the LCDS is expressed as the maximum L^* of a closed drift path, it is dependent upon a particle's pitch angle and so does not relate to a single location in real space. It is therefore not possible to measure a location of the LCDS to verify computations, but instead observed particle behaviour must be examined.

Unlike the LCDS, the location of the magnetopause may be measured through spacecraft crossings of the magnetopause. This is owing to the distinct plasma and magnetic conditions of the magnetosheath compared to the magnetosphere. This means that parameterisations of the magnetopause are

verifiable through measurements, which we will discuss in the following sections. Focusing is given to the Shue et al. (1998) model as it is commonly used in radiation belt physics (e.g., Herrera et al., 2016; Loto'aniu et al., 2010; Morley et al., 2010b; Murphy et al., 2015; Olifer et al., 2018; Turner et al., 2012b).

2.3.1 Shue et al. (1997, 1998) Magnetopause Model

Shue et al. (1997) presented an empirical model of Earth's magnetopause location which fitted a functional form to 553 in-situ measurements of the magnetopause. The magnetopause function is given by

$$r = r_0 \left(\frac{2}{1 + \cos\theta} \right)^{\alpha} \tag{2.3}$$

where r is the radial standoff distance at solar - zenith angle θ. This function contains two parameters, r_0 and α, which respectively represent the magnetopause standoff distance at the subsolar point and the angle of tail flaring. Figure 2.6 demonstrates the shape produced by this function at specified values of r_0 and α. This function can represent a magnetopause which is closed ($\alpha < 0.5$), asymptotes to a finite tail radius ($\alpha = 0.5$), or expands with increasing distance from the Earth ($\alpha > 0.5$).

Parameters r_0 and α are dependent upon the north-south component of the IMF, B_z, and the dynamic pressure of the solar wind, D_p; determined by completing a bivariant fit of magnetopause measurements under different solar wind conditions.

$$r_0 = \begin{cases} (11.4 + 0.14B_z)(D_p)^{-1/6.6}, & B_z < 0 \\ (11.4 + 0.13B_z)(D_p)^{-1/6.6}, & B_z \geq 0 \end{cases} \tag{2.4}$$

$$\alpha = (0.58 - 0.010B_z)\left(1 + 0.010D_p\right), \tag{2.5}$$

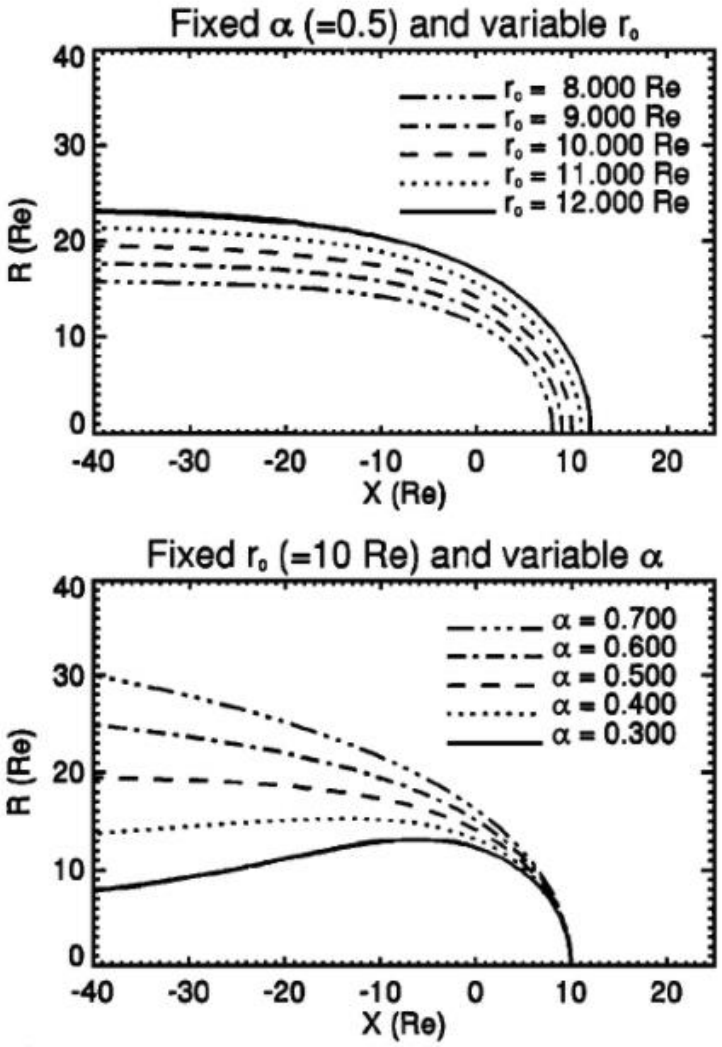

Figure 2.6 Graphical representation of the functional form of the Shue et al. (1997) magnetopause model, Equation 2.3**. The top panel shows radial distance of the magnetopause for fixed α = 0.5 and different values of r_0. Bottom panel shows fixed r_0= 10 R_E and different values of α.**

Thus, by measuring solar wind conditions, the magnetopause location may be calculated by inputting calculations of r_0 and α into Equation **2.3**. This model is valid for the rages -18 $< B_z <$ 15 nT and 0.5 $< D_p <$ 8.5 nPa, limited by the prevailing solar wind conditions during the magnetopause measurements used to fit the model.

Shue et al. (1998) used magnetopause measurements at geosynchronous satellites to test and validate the capabilities of the Shue et al. (1997) model during a sudden solar wind enhancement where D_p reached up to 60 nPa. Whilst the Shue et al. (1997) model correctly predicted spacecraft crossings of the dayside magnetopause, it inconsistently predicted crossings along the

magnetopause flank. Inaccuracies in model predictions were determined to be due to inappropriate linear extrapolation from the solar wind parameter range.

To improve the Shue et al. (1997) model under extreme solar wind conditions, Shue et al. (1998) introduced a non-linear dependence of r_0 and α on B_z and D_p, given by Equations **2.6** and **2.7**. For brevity, the two models shall henceforth be referred to as Sh97 and Sh98 for Shue et al. (1997) and Shue et al. (1998) respectively.

$$r_0 = \left(10.22 + 1.29\tanh\left(0.184(B_z + 1.84)\right)\right)\left(D_p\right)^{-1/6.6} \quad 2.6$$

$$\alpha = (0.58 - 0.007B_z)\left(1 + 0.024\, ln\, D_p\right), \quad 2.7$$

It must be noted that the Sh98 model assumes a rigid parabolic magnetopause that is in equilibrium with cylindrical symmetry around the aberrated Sun-Earth line. This does not account for indentations in the magnetopause location due to cusp regions and dipolar tilt. Furthermore, this implies that the magnetopause responds instantaneously and globally to any changes in upstream solar wind conditions. In reality, the magnetopause is much more dynamic. For example, surface waves are driven at the magnetopause, which oscillates about its equilibrium (Plaschke et al., 2009b). Cahill and Winckler (1992) also observed large solar wind compressions which break equilibrium and drive magnetopause oscillation, and Desai et al. (2021b) further observed interplanetary shock induced magnetopause oscillations in global MHD simulations. Staples et al. (2020) investigated the accuracy of the Sh98 model under interplanetary shocks conditions, finding that the Sh98 model overestimated the location of the magnetopause by over 1 R_E on average. The results of this investigation is presented in Chapter 4 of this thesis.

Shue et al. (1998) discussed the uncertainty arising from magnetopause motion, calculating model uncertainty as a function of IMF B_z, D_p, and θ. The authors argued that any deviation from the modelled average position due to, for example, magnetopause oscillations, are represented by the known Sh98 model uncertainties. Using the method described in Shue et al. (1998), Figure 2.7 presents how the Sh98 uncertainties vary with solar zenith angle and IMF B_z orientation, given (a) moderate (IMF $|B_z|$ and D_p of 4 nT and 2 nPa,

respectively), and (b) strong (IMF $|B_z|$ and D_p of 15 nT and 8 nPa, respectively) solar wind driving.

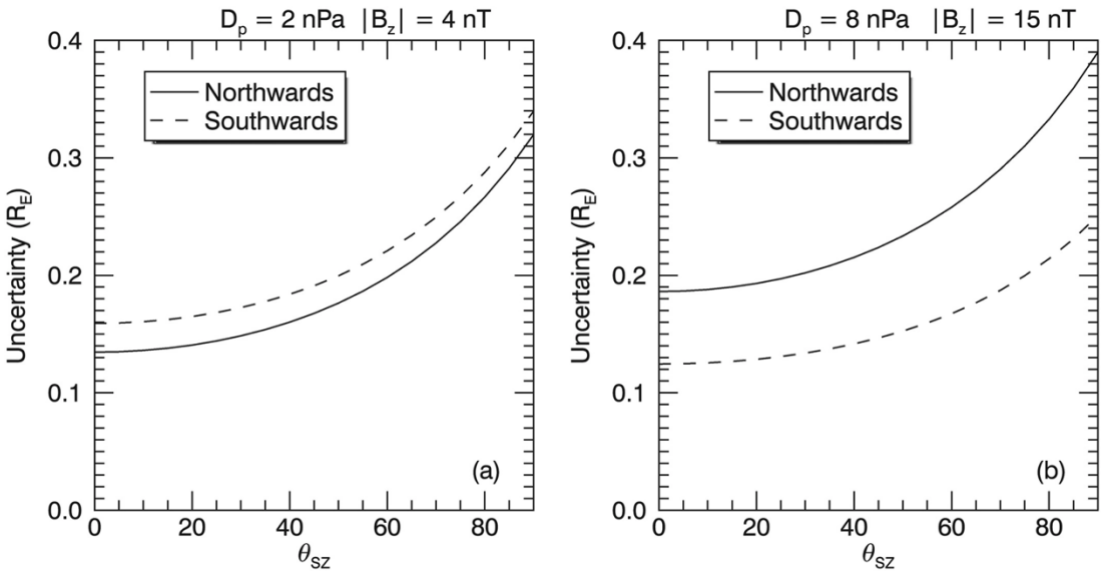

Figure 2.7 Uncertainty of the Shue et al. (1998) magnetopause model as a function of solar zenith angle, θ_{sz}, for southward and northward orientated IMF. (a) shows moderate solar wind driving where $|B_z|$ = 4 nT and D_p=2 nPa; (b) $|B_z|$ = 15 nT and D_p = 8 nPa. (Staples et al., 2020)

Figure 2.7a shows that uncertainty increases from ~0.15 R_E to 0.3 R_E for both northward and southward oriented IMF and is ~0.025 R_E higher for southward IMF as compared to northward. Trends of increasing uncertainty with solar zenith angle were consistent across solar wind driving, but there was a larger difference between southward and northward orientated IMF when solar wind driving is high (Figure 2.7b), and under these conditions southward IMF showed a lower uncertainty than under northward. Comparing the uncertainties for southward IMF across moderate and higher solar wind driving, it is interesting to note that the uncertainty is lower for higher solar wind driving across all solar zenith angles. In contrast, for northward IMF, the uncertainties are increased.

2.3.2 Comparison of Magnetopause Models

The Lin et al. (2010) magnetopause model has also been used in radiation belt studies (e.g., Turner et al., 2014b). This model is an adaptation of the Sh97 model which accounts for north-south asymmetry of the magnetopause, indentations at the magnetic cusps, and includes the magnetic pressures of

the solar wind. It is also a statistical model, fitted to 980 magnetopause crossings from Geotail, IMF and Cluster missions.

Case and Wild (2013) completed a statistical comparison of the Sh98 and Lin10 models to a database of 2709 high-latitude Cluster magnetopause crossings. Figure 2.8 demonstrates statistical differences between the radial distance to Cluster crossing locations and the (a) Sh98, (b) Lin10 modelled magnetopause locations. The Sh98 model tended to overestimate the standoff distance by ~ 1.5 R_E near the cusps, whereas the Lin10 model underestimated standoff distance by ~ 0.2 R_E. The authors therefore demonstrated that the Lin10 model is more successful than Sh98 at predicting the magnetopause cusp location.

Machine learning techniques have also been used to create empirical magnetopause models from spacecraft crossings. The benefit of this method is that an analytic shape of the magnetopause is not assumed, so dipolar tilt, cusp regions, and interhemispheric asymmetries are better captured. For example, Wang et al. (2013) constructed a 3D magnetopause model from ~ 15,000 magnetopause crossings by 23 satellites using a vector regression machine. Whilst this method does not predefine an analytic form, the authors make implicit assumptions about the most probable magnetopause shape to define free parameters used to fit the model.

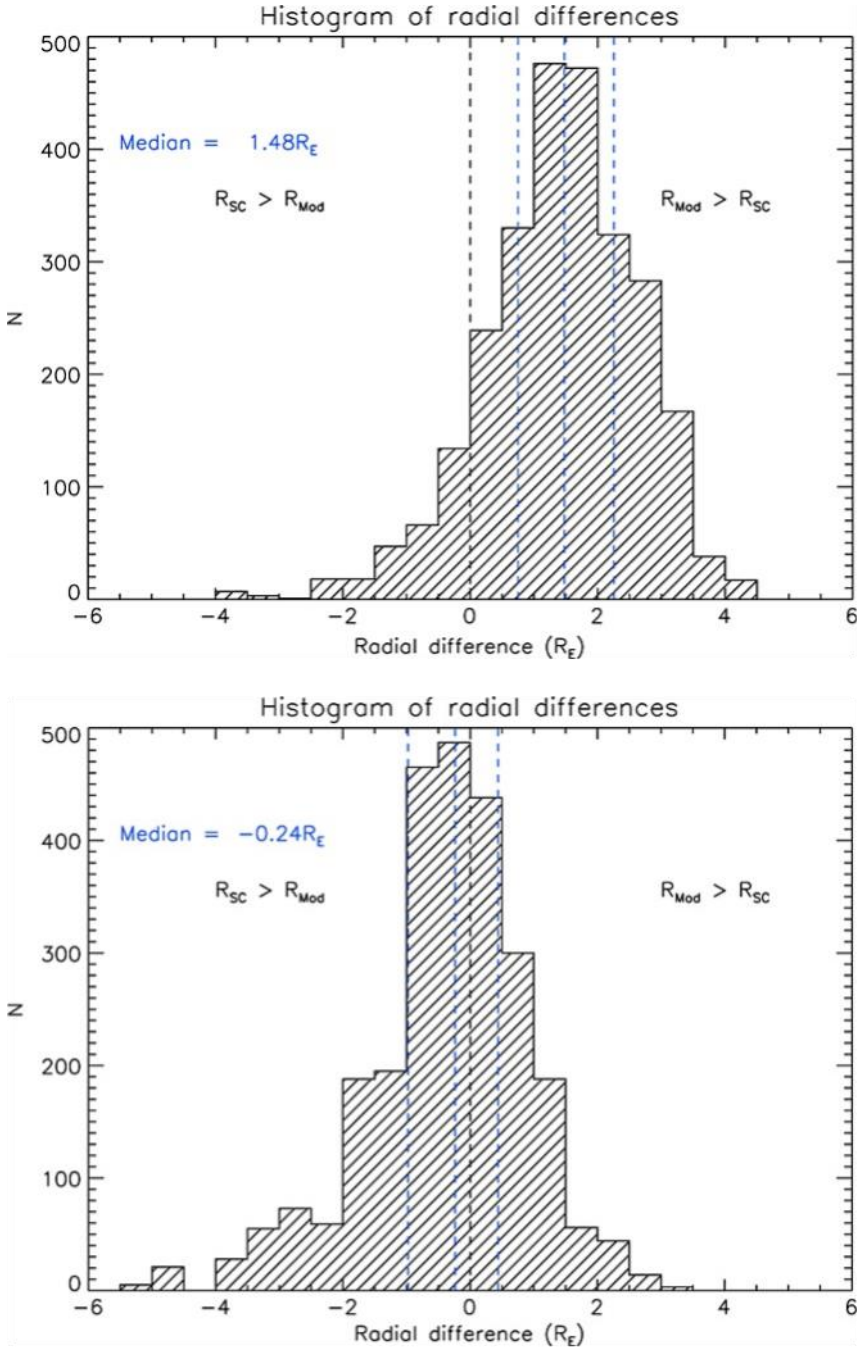

Figure 2.8 A histogram of radial differences between measured locations of magnetopause crossings and (top) Sh98 (bottom) Lin10 model predictions. Dashed vertical blue lines represent the interquartile range and median. R_{SC} and R_{Mod} are the standoff distance to the Cluster magnetopause crossing and Sh98 or Lin10 model, respectively (Case & Wild, 2013).

Samsonov et al. (2016) examined the three empirical magnetopause models described here, (Sh98, Lin10, Wang13) with global MHD simulated magnetopause models. Contrary to empirical models, the pressure balance condition in the MHD approach is satisfied at every point, and the magnetopause shape is always non-axisymmetric. However, global MHD

models do not properly include all magnetospheric current systems, including the ring current. Therefore, the magnetopause position derived from MHD solutions may also be inaccurate. The authors found that axisymmetric empirical magnetopause models do not reproduce the three-dimensional magnetopause and lose information due to the tilt angle averaging. The position of the subsolar point in the axisymmetric Sh98 model is closer to the Earth than in the non-axisymmetric Lin10 and Wang13 models. The authors conclude that that the role of the dipole tilt on the magnetopause position is still not completely understood. Furthermore, they note that magnetopause models should treat magnetopause crossings for nearly radial IMF separately, because these are the times when the magnetosheath pressure becomes significantly lower than the solar wind dynamic pressure (Suvorova & Dmitriev, 2015). If the number of such events in a magnetopause crossings database is relatively large, the models which do not consider the IMF cone angle as an input parameter will overestimate the magnetopause standoff distance.

These studies demonstrate that current parameterisations of the magnetopause location are flawed. The magnetopause shape is ill-defined, with models either using unrealistic assumptions about cylindrical symmetry, or implementing pre-determined ideas about the magnetopause shape. What is more, it is the nature of statistical models to represent an averaged location of the magnetopause. Not only does this lose information on the rapid time-varying nature of the magnetopause, but extreme compressions are uncommon, so may not be well represented by an average. This could have important implications when considering the effects of magnetopause shadowing on the radiation belts, since it is under extraordinarily rapid, strong compressions that the greatest loss the magnetopause will occur. If the location of the magnetopause is not known with confidence, the contribution of magnetopause shadowing to electron flux dropout events may be misinterpreted.

2.5 Motivating Questions

There are several aspects of electron flux dropouts which remain unresolved: principally the relative contributions of magnetopause shadowing and atmospheric precipitation to the overall electron loss. What is more, the relative importance of direct and indirect magnetopause shadowing has not yet been investigated, with most studies treating respective shadowing losses synonymously. This is possibly because magnetopause incursions which are close enough to directly intersect many outer belt drift paths are rare. However, it is under these circumstances which the largest losses the outer radiation belt occurs through flux dropouts.

Because flux dropouts occur on such short timescales, one of the greatest limitations to our understanding is the availability of in-situ measurements of electrons. Indeed, a dropout may occur faster than a spacecraft can orbit through the radiation belts. There is also a reliance upon the modelled magnetopause and/or LCDS to parameterise outer boundary dynamics, though the accuracy of these models has not (or cannot in the case of the LCDS) been tested under magnetospheric compressions.

The goal of this thesis is to develop a greater understanding of the role of the magnetopause in flux dropout events by using large multi-satellite datasets. To do this we shall investigate the location of the magnetopause, and the phase space characteristics of both magnetopause shadowing and electron precipitation.

Chapter 4 of this thesis assesses the accuracy of the Shue et al. (1998) magnetopause model by using the largest dataset of magnetopause crossings to date, compiled for the purpose of this study.

Chapter 5 and Chapter 6 of this thesis analyse the evolution of PSD during a case study in September 2017 where a sequence of interacting CMEs lead to exceptionally strong magnetospheric compressions which depleted the radiation belt. Both magnetopause shadowing and electron precipitation are characterised using PSD measurements which are computed in adiabatic invariant coordinates with unprecedented time and spatial resolution.

Chapter 3 Instrumentation and Methodology

As set out in previous chapters, this thesis investigates the role of magnetopause shadowing in producing electron flux dropouts. Chapter 4 presents an analysis of the modelled magnetopause under sudden solar wind compressions which uses in-situ spacecraft measurements of plasma and magnetic conditions to identify the magnetopause location. Chapter 5 and Chapter 6 investigate the outer radiation belt response to an extreme magnetopause compression by examining electron phase space density from multi-spacecraft measurements of relativistic electrons. These investigations use data from many instruments on board multiple scientific satellite missions.

- Time History of Events and Macroscale Interactions (THEMIS)
- Van Allen Probes
- Magnetospheric Multiscale Mission (MMS)
- Geostationary Operational Environmental Satellite (GOES)
- Global Positioning System (GPS) NavStar
- Cluster II
- Geotail

In this chapter we discuss the details of these missions and describe the principles of key instrumentation. We then describe how data from these instruments were processed to create the multi-satellite databases used in analysis. Finally, the NASA OMNI dataset of solar wind measurements and geomagnetic indices, which are auxiliary to the analysis presented in this thesis, are described.

3.1 Key Instrumentation Principles

The specific design of individual instruments varies from mission to mission. Because the research described in this thesis uses data from many missions, we do not endeavour to describe each individual instrument used. Instead, the key principles of operation for commonly used instruments will be described.

3.1.1 Fluxgate Magnetometer

Fluxgate magnetometers (FGM) are commonly used as magnetic field sensors on spacecraft. FGMs consist of a ring core of magnetically permeable alloy surrounded by two conductive coils: a sensor coil and a drive coil. The basic configuration of an FGM sensor is shown in Figure 1.1, where the drive coil is wound around the ring core, and the sensor coil winding encircles both the ring core and drive coil.

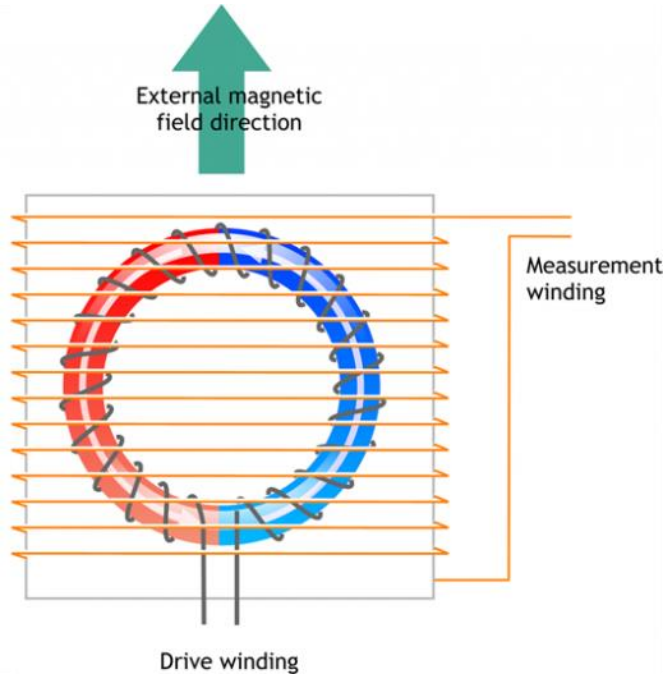

Figure 3.1 A diagram of the basic configuration of a fluxgate magnetometer sensor which measured an external magnetic field parallel to the plane of the ring core, and parallel to the central axis of the sensor winding. Source: CARISMA website, *http://www.carisma.ca/backgrounder/increasing-sensitivity*, via University of Alberta.

The FGM operates using the principle of hysteresis. In ferromagnetic materials, the magnetisation of the material depends upon the alignment of magnetic domains within the material. When an imposed magnetic field is applied, the magnetic domains of the ferromagnet align until magnetisation of the material saturates, and all domains align with the applied field. The magnetisation of the material may be reversed by applying an oppositely directed magnetic field.

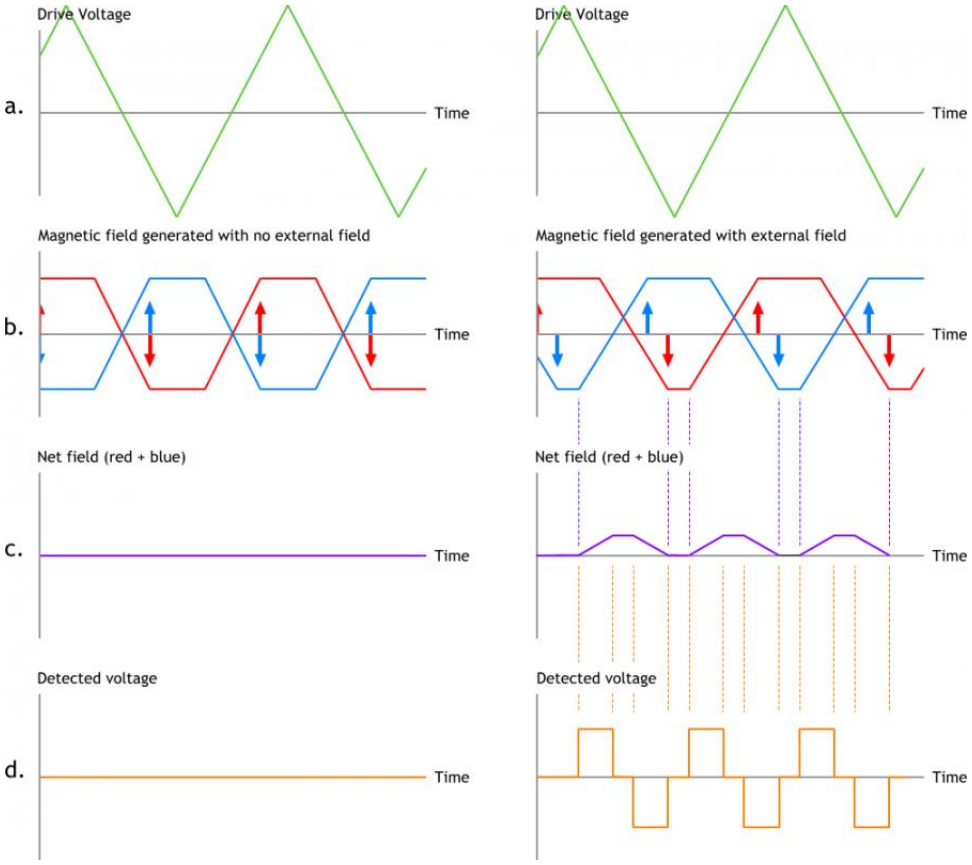

Figure 3.2 Diagram of the operation of an FGM, left column illustrates when there is no external magnetic field, right column shows when there is an external magnetic field present. Each row shows (a) the voltage applied across the drive coil; (b) Magnetic field generated within the ring core, with blue and red illustrating two halves of the core (see Figure 3.1); (c) the net magnetic field across the ring core; (d) the induced voltage across the sensor coil due to changes in the net-magnetic field shown in (c). Source: CARISMA website, *http://www.carisma.ca/backgrounder/increasing-sensitivity*, via University of Alberta.

In an FGM a voltage with a periodic waveform is applied across the drive coil, illustrated in Figure 3.2a. This generates oppositely directed magnetic fields within the two halves of the ring core (illustrated by red and blue colours in Figure 3.1). The magnetic field applied by the drive coil magnetises the ring core in the same direction, up to a saturation value. If there is no external magnetic field through the sensor, then the magnetisation of each half of the ring core cancels each other out, producing no net magnetic field. If there is an external magnetic field present, the half of the ring core where the applied magnetic field is opposite to the external field will come out of saturation sooner than the half where the applied magnetic field is in the same direction. The magnetic field within either half of the ring core does not cancel during this

period, resulting in a changing magnetic flux within the core (Figure 3.2c). The net change in flux induces a voltage in the sensor coil by Faraday's law (Figure 3.2d). The direction and magnitude of the external magnetic field may be deduced from the size and phase of the induced voltage.

FGM experiments flown on spacecraft typically use three ring cores orientated orthogonally so that the three-dimensional magnetic field may be resolved. They are also housed on booms extending several meters from the main spacecraft bus to reduce magnetic contamination.

3.1.2 Electrostatic Analyser

Electrostatic analysers (ESA) are commonly used to measure the energy per charge (E/q) and angular distributions of low energy ($\lesssim$ 30 keV) charged particles in space plasmas. There are several different configurations of ESAs which all operate on the same principle: a voltage is applied across instrument electrodes which produces an electric field to select which particles by E/q are incident on the detector.

A cross section diagram of a top-hat analyser is shown in Figure 3.3. A top hat analyser uses a pair of nested hemispherical electrodes; the outer hemisphere is grounded such that, when a voltage is applied to the inner hemisphere, an electric field is created between the two. Particles which have entered through the aperture experience a force perpendicular to its velocity which acts as a centripetal force; $mv^2/r = qE$. If the radius of particle curvature, *r,* matches the dimensions of the hemispherical deflector plates, it becomes incident on the detector, which in Figure 3.3 is a microchannel plate (MCP). If the radius of particle deflection does not match the hemisphere dimensions, the particle will hit one of the deflection plates before reaching the MCP. This allows the instrument to select an energy range for which to measure incident particles. The MCP amplifies the signal of the incident electron, transmitting an electron current into the anode which can be interpreted to obtain particle flux. The ESA can sequentially vary the voltage applied to the inner hemisphere to measure a full energy spectrum of particles.

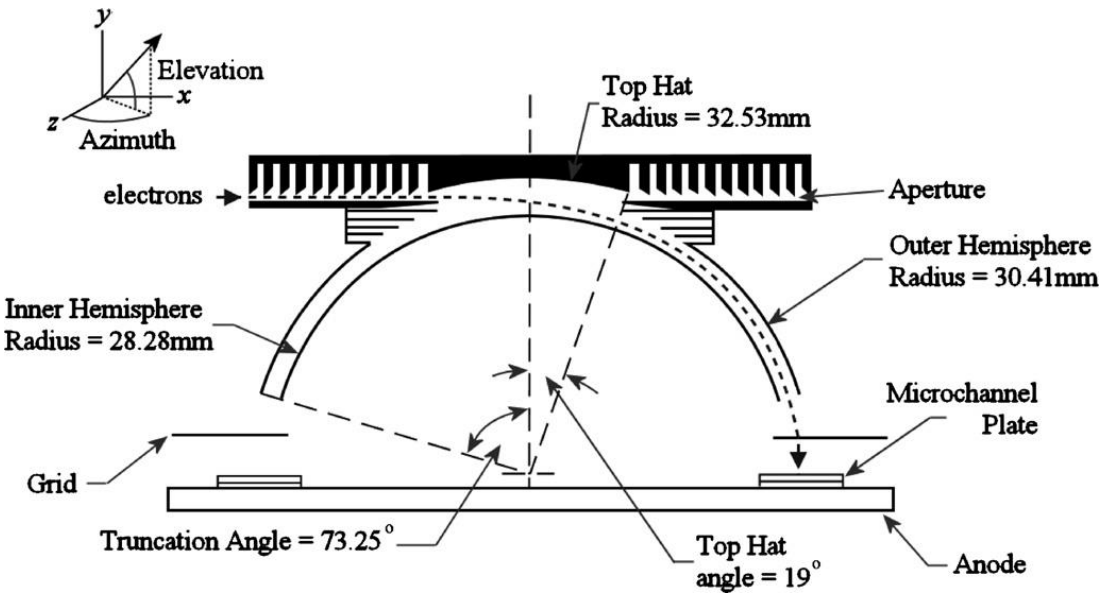

Figure 3.3 Cross sectional diagram of a typical 'top-hat' electrostatic analyser (Collinson & Kataria, 2010).

3.1.3 Solid-State Detector

Solid-state detectors are typically used to measure the high energy particles found in the radiation belts. A simplified cross-sectional diagram of a detector used on the Van Allen Probes is shown in Figure 3.4.

Collimators are used to guide particles to the detector, such that the field of view of the instrument is conical. The solid-state detector itself usually consists of stacked silicon wafers which are each connected electrically in parallel. Incident charged particles deposit energy into the silicone layers, creating electric pulses in the detector. Energy-height analysis of amplified pulses is used to determine the energy deposited by a particle. The maximum energy which a detector can measure is limited by the depth of the stacked silicone. The minimum energy measured by the detector is defined by the encasing of the instrument which shields lower energy particles from the detector.

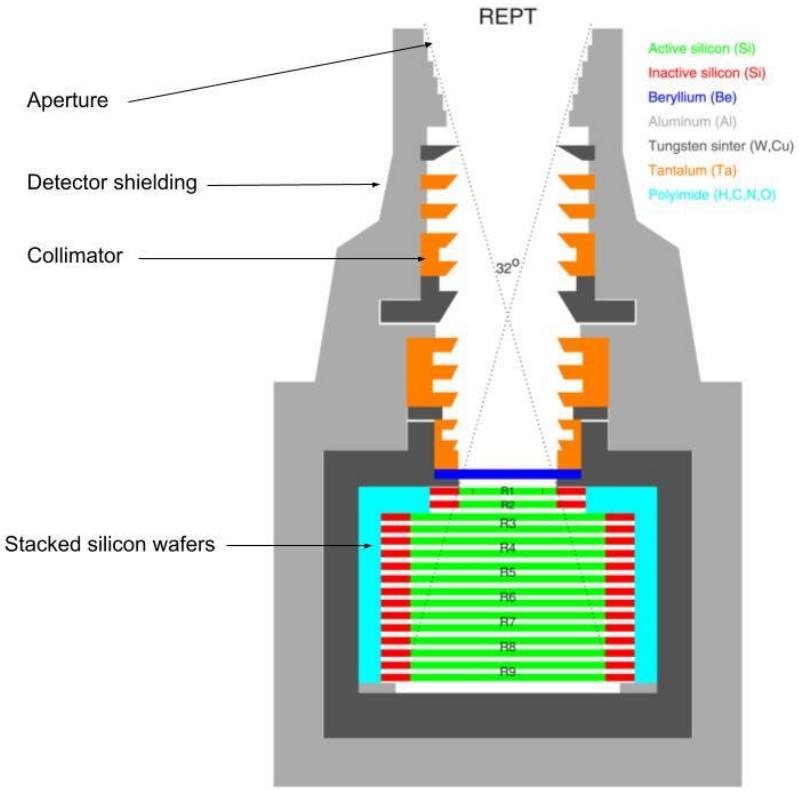

Figure 3.4 A simplified cross-sectional diagram of the relativistic electron proton telescope (see Section 3.2.2) on the Van Allen Probes. Colour coding identifies each material used in the instrument (adapted from Selesnick et al., 2018).

3.2 Mission Overviews

3.2.1 THEMIS

The primary goal of the THEMIS mission was to investigate the nature of substorms. THEMIS comprises of a constellation of five identical micro-satellites (labelled probes A-E), launched in 2007 into ~ 31-hour elliptical orbits in the equatorial plane. Each spacecraft spins with a period of 3 seconds with an axis approximately 8^{o} to the ecliptic plane. Through the mission the satellites have precessed across the dayside to nightside, and through dawn and dusk, to explore different aspects of magnetospheric science. Initially in a 'string of pearls' configuration, whereby they orbited along the same path, the probes later transitioned into orbits with separate apogees at ~ 10, 12, 20, and 30 R_E, synchronising at apogee every four days. In 2010, two of the five probes, B and C, were repurposed as ARTEMIS (The Acceleration, Reconnection, Turbulence, and Electrodynamics of the Moon's Interaction with

the Sun) and moved orbits to study plasma processes closer to the Moon (Angelopoulos, 2014). THEMIS A, D, and E remain in operation to date.

In Chapter 4, magnetic field and plasma data is used from the fluxgate magnetometer (FGM) instrument and the electrostatic analyser (ESA). The FGM measures the background magnetic field and low frequency fluctuations, with amplitude resolution of 0.01 nT (Auster et al., 2008). The ESA measures plasma over the energy range of a few eV up to 20 keV for electrons and 25 keV for ions. The instrument comprises of a pair of top hat electrostatic analysers, which are described in Section 3.1.2. Analysers have a 180^{o} by 6^{o} field of view, which rotates through 360^{o} in a 3 s period, in this way the pitch angle of particles is deduced with resolution depending on the instrument mode (McFadden et al., 2008).

Chapter 5 and Chapter 6 also used the THEMIS solid-state telescope (SST), which measures suprathermal particles with specified energies within the range of 25 keV to 900 keV for electrons and 25 keV to 6 MeV for ions. SST consists of two detector heads, each with two sides which respectively measure electrons and ions over a 37^{o} field of view. The detector is mounted on the skin of the spacecraft with look directions which are 52^{o} and 25^{o} relative to the spin plane. As the probe spins, the fields of view of the detector heads cover nearly a full sphere (Angelopoulos, 2008; Ni et al., 2011).

3.2.2 Van Allen Probes

The primary objective of the Van Allen Probe mission was to investigate the radiation belts. Launched in 2012, the mission was in scientific operation for 6 years. The Van Allen probes consisted of two nearly identical satellites (probes A and B), spin-stabilised with a spin axis directed towards the Sun, orbiting in low inclination (< 18^{o}), highly elliptical geostationary transfer orbits with respective perigee and apogee at ~ 500 km and ~ 5.8 R_E. The probes orbited along the same path with an orbital period of ~ 9 hours, such that the probes traverse the radiation belts twice per orbit, providing near continuous measurement of the radiation belts (Mauk et al., 2014).

Chapter 5 and Chapter 6 use measurements of suprathermal electrons from the MagEIS (Magnetic Electron Ion Spectrometer, Blake et al., 2014) and REPT (Relativistic Electron Proton Telescope, Baker et al., 2014) instruments, which form part of the ECT (Energetic Particle, Composition, and Thermal Plasma) instrument suite (Spence et al., 2014). MagEIS consists of four magnetic spectrometers, a low energy spectrometer covers 20-240 keV, two medium energy spectrometers cover energy range 80 – 1200 keV, and a high energy range unit covers 800 – 4800 keV. The units have apertures of 10^{o} by 20^{o}, with look directions at 75^{o} to the satellite spin axis for the low, high, and one the medium energy units. The other medium energy unit has a look direction at 35^{o} to the spin axis. As the spacecraft spins, the units complete a scan of pitch angles. REPT measures a higher energy range of ~ 1 - 20 MeV electrons, consisting of stacked solid-state detectors, which measure electron energy by penetration depth, a collimator, and thick shielding from penetrating radiation. The collimator has a circular field of view of 32^{o} with a look direction perpendicular to the spin axis of the spacecraft, and so samples a full 360^{o} range.

3.2.3 MMS

MMS was designed to study magnetic reconnection between the solar wind and magnetosphere on the magnetopause and in the magnetotail. Launched in 2015, the mission consists of a constellation of four spacecraft which maintain a tetrahedral or pyramid configuration through regions of interest for reconnection. Up to 2017, during the prime mission phase, MMS orbited in a low inclination (28^{o}) elliptical path with an initial apogee of ~ 12 R_E and perigee of 1.2 R_E. As the mission was extended, the apogee has been altered such that it is now between ~ 25 – 29 R_E (Burch et al., 2016). The probes are spin-stabilised with a period of 20 seconds, and a spin axis in the ecliptic plane.

Chapter 5 and Chapter 6 use suprathermal electron measurements taken by the FEEPS (Fly's Eye Energetic Particle Sensor, Blake et al., 2016) instrument, which is part of the energetic particle detector (EPD) investigation. There are two FEEPS instruments on each spacecraft with opposite look directions. For each instrument there are nine electron 'eyes' with a single

silicone detector telescope which measures electron energies between 25 keV to 650 keV. Each eye has a trapezium field of view plane with dimensions of 23º/40º by 60º, arranged with a 180º angular coverage to maximise the total solid angle coverage between the two detectors' field of view on each satellite.

3.2.4 GOES

GOES are a constellation of Earth observation satellites in geostationary orbit, with the primary purpose of providing meteorology observations, but which also carry instruments for space weather observations. There are a number of GOES satellites dating back to 1966, with GOES-R series satellites currently in operation. This series consists of GOES-13 which operates as GOES-East at 75º longitude and GOES-15 which operates as GOES-West at 13º longitude.

Chapter 5 and Chapter 6 use electron measurements from MAGED (Magnetospheric Electron Detector, Rodriguez, 2014a; Sillanpää et al., 2017) and EPEAD (Energetic Proton, Electron, and Alpha Detector, Onsager et al., 1996; Rodriguez, 2014b) and magnetic field measurements from the magnetometer (MAG; Singer et al., 1996)

MAGED consists of a set of nine collimated solid-state electron detectors which operate in five energy channels ranging between 30 keV to 600 keV, each with a circular aperture of 30º. The detectors are orientated in two crossing fans where the central detector looks directly away from Earth. The nine telescopes provide partial coverage of the hemisphere in the anti-Earthward direction. There are two EPEAD instruments on each satellite, one looking east and one looking west. The current design of this instrument was first flown on GOES-8 (Onsager et al., 1996; Sellers & Hanser, 1996). The detectors comprise of telescope and dome detectors, and a high energy proton and alpha detector head. Electrons are measured by the dome detectors (D3 and D4) in three energy bands between >0.6 MeV (D3), > 2 MeV (D3), and > 4.0 MeV (D4) (Rodriguez et al., 2010). The dome detectors have field of view of 70º by 110º (D3) or 130º (D5). The magnetometer comprises a pair of three-axis fluxgate magnetometers mounted on an 8.5 m boom. This gives a range of $\pm$ 1000 nT and an accurate resolution to 1 nT.

3.2.5 GPS

Navstar is a network of over twenty-four satellites providing global positioning system (GPS) services. Satellites follow medium Earth orbits with 12-hour periods which are at ~ 3 R_E altitude. There are six orbital planes, each at inclination of ~ 55^o, each separated by a 60^o angle along the equatorial plane from a reference point to the orbit's intersection (Hofmann-Wellenhof et al., 2012, and references therein). Chapter 5 and Chapter 6 use measurements of radiation belt electrons from the CXD (Combined X-ray Dosimeter) instrument package (Tuszewski et al., 2004), which is on board 21 GPS satellites. The CXD instrument measures electrons in the energy range 100 keV to 70 MeV and protons in the energy range 6 MeV to 50 MeV using a solid-state detector. There are four collimating channels which sample a solid angle of ~ 110^o in the Earthward direction, providing an omnidirectional measurement of flux, so pitch angle is not resolved.

3.2.6 Cluster II

The Cluster II mission consists of four spacecraft flying in tetrahedral formation. With the scientific objective to study small scale plasma structures during solar wind – magnetosphere interactions, it may be considered a predecessor to MMS. It launched in 2000 and remains in operation today (Escoubet et al., 2001). The satellites are highly elliptical polar orbits with a perigee of ~ 3 R_E and apogee of ~ 19 R_E. The satellites are spin-stabilised, with a period of 4 seconds, the spin axis 09^o to the ecliptic plane, apart from Cluster 3 which has a spin axis at 45^o to the ecliptic. The locations of the orbits have varied through its lifetime to study different regions of the magnetosphere. Chapter 4 uses magnetopause crossing identifications by Case and Wild (2013), classified from magnetic field measurements by the FGM instrument. FGM consists of two three-axis fluxgate magnetometers mounted on a five-meter boom (Balogh et al., 2001; Gloag et al., 2010).

3.2.7 Geotail

The mission objective of Geotail was to study the dynamics of the magnetotail (Nishida, 1994). With a planned mission duration of 20 years, the Geotail spacecraft was launched in 1992 into an equatorial orbit (7^o inclination) with an

apogee of 210 R_E. The spacecraft is spin-stabilised with a period of 3 seconds, and a spin axis between 85-89^o to the ecliptic plane. The mission remains operational to date, and for the majority of its duration (since 1996) the orbital apogee and perigee are ~ 30 R_E and ~ 8 R_E. Chapter 4 uses magnetopause crossings identified by Raymer (2018), who classified crossings from the magnetic field experiment and the low energy particle experiment. The magnetic field experiment comprises of a fluxgate magnetometer, a search coil magnetometer (Kokubun et al., 1994). The low energy particle experiment (LEP, Mukai et al., 1994) consists of two electrostatic potential analysers, LEP-EA and LEP-SW, measuring velocity distributions of hot plasmas or solar wind ions respectively, and a mass spectrometer which measures ion species.

3.3 Magnetopause crossing identification

The only way in which the magnetopause is currently observable is through in-situ measurements by a spacecraft traversing the boundary. Although the magnetopause can vary in thickness from around 400 to 700 km (Berchem & Russell, 1982), a spacecraft will pass through in less than a minute, measuring sudden changes to magnetic and plasma conditions. The measured magnetic field will transition between a strong, steady, and northward orientated field within the magnetosphere, to a rapidly varying magnetic field characteristic of the magnetosheath that may be orientated in any direction. Plasma density transitions from low values in the outer magnetosphere, to higher densities in the magnetosheath where the shocked solar wind piles up and stagnates (Crooker & Siscoe, 1975).

To conduct our analysis of the Sh98 magnetopause model, a database of in-situ magnetopause observations was compiled to compare to the modelled location. This includes a new dataset of THEMIS magnetopause crossings created for this study, supplemented by three datasets classified for previous works Case and Wild (2013), Raymer (2018), and Plaschke et al. (2009b). The details of the final dataset of magnetopause crossings are summarised in Table 3.1. The orientation of satellite orbits is illustrated for a 72-hour period starting 29 December 2015 is shown in Figure 3.5.

Table 3.1 Details of the dataset of satellite magnetopause crossings used in Chapter 4.

Satellite Mission	Instrumentation	Data Timespan	Number of Crossings	Dataset Authors
Cluster	FGM	2002- 2010	2,688	Case and Wild (2013)
Geotail	FGM, LEP	1996 – 2015	8,548	Raymer (2018)
THEMIS	FGM, ESA	2007	6,697	Plaschke et al. (2009b)
THEMIS	FGM, ESA	2007 - 2016	34,428	Staples et al. (2020)
Final Dataset of Dayside Crossings		**1996 - 2016**	**19,973**	

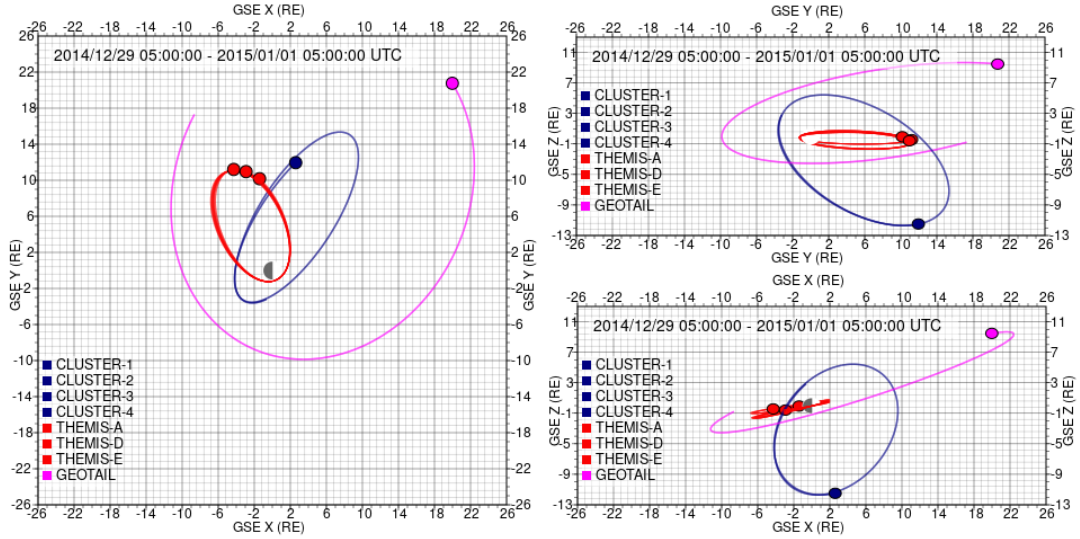

Figure 3.5 Diagram of Cluster, Geotail, and THEMIS satellite orbits in the X_{GSE}-Y_{GSE} plane (left) Y_{GSE}-Z_{GSE} plane (top right) and X_{GSE}-Z_{GSE} plane (bottom right). Individual probes are labelled by colour. Diagram was obtained through Van Allen Probes Science Gateway *https://rbspgway.jhuapl.edu/home*.

In the following section the classification criteria used for each dataset is briefly described, with focus given to the classification of a new database of THEMIS crossings.

3.3.1 Cluster Crossing Classification

Case and Wild (2013) created an automated routine which classified a dataset of Cluster crossings of the magnetopause to test the accuracy of different magnetopause models near the polar cusp. The authors identified 2709 crossings between 2002 and 2010 which satisfied criteria based upon changes in the magnetic field orientation and variability. The criteria were applied to 3-minute sliding window intervals of Cluster FGM magnetic field measurements.

1. Transit across the magnetopause must occur within 32 s.
2. Only the first magnetopause crossing is included if multiple crossings occur within 10 minutes.
3. The magnetosheath magnetic field must have a standard deviation greater than 4.5 nT over interval, which is at least 2.5 greater than the standard deviation during the magnetosphere interval.

4. The average magnetospheric field over the interval must be 1.3 times greater than the magnetic field during the magnetosheath interval.

Because the Cluster orbits were at high inclinations between 2000-2010, the Case and Wild (2013) dataset primarily measured the high latitude magnetopause.

3.3.2 Geotail Crossing Classification

Raymer (2018) also created an automated routine to classify Geotail crossings between 1996 and 2016. On the dayside (when Geotail is $X_{GSM} > 5\ R_E$), the author applied criteria modified from Case and Wild (2013) to a 3-minute sliding window over Geotail magnetic field data:

1. Transit of the magnetopause must occur within 36 s.
2. The magnetosheath magnetic field must have an average standard deviation greater than 4.5 nT over the interval, which is at least 2.5 greater than the average standard deviation during the magnetosphere interval.
3. The average magnetospheric field strength must be greater than that of the magnetosheath.
4. The average magnetospheric field must have a component in the B_z direction, in GSM coordinates, which is greater than 10 nT and 1.3 times larger than the magnetosheath interval.

Raymer (2018) developed new criteria for Geotail crossings of the magnetopause flanks and magnetotail ($X_{GSM} < 5\ R_E$) which primarily rely upon changes to plasma conditions. In these locations it is more reliable to use plasma measurements because changes between the magnetospheric and magnetosheath fields are less distinct due to distortions of the geomagnetic field and IMF as it passes by the magnetosphere. These new criteria are applied to a 3-minute sliding window of Geotail FGM and LEP data:

1. The average bulk flow velocity in the X_{GSM} direction is greater than -100 km s^{-1} for magnetospheric plasma and less than -100 km s^{-1} for magnetosheath plasma.

2. The flow velocity in the X_{GSM} direction must change by 100 km s^{-1} or more in 36 s.
3. The average plasma density must be less than 3 cm^{-3} in the magnetosphere and greater than 1 cm^{-3} in the magnetosheath.
4. The standard deviation of the magnetic field must me greater in the magnetosheath than in the magnetosphere.

8548 Geotail magnetopause crossings were classified over the 20-year period. This dataset had good azimuthal coverage, especially over the magnetotail. However, the orbital configuration of Geotail meant that crossings confined to the equatorial plane, but more crucially for this thesis, magnetopause crossings within a radius of ~ $8R_E$ could not be measured due to Geotail perigee.

3.3.3 THEMIS Crossing Classification

Since the goal of Chapter 4 is to assess the accuracy of the Sh98 model during strong compressions of the magnetopause, it is necessary to include an additional dataset of magnetopause crossings. The THEMIS probes are chosen as they follow near-equatorial orbits with a perigee at low enough altitudes to cross the magnetopause under compression.

Plaschke et al. (2009b) manually classified a dataset of 6697 magnetopause crossings from plasma and magnetic field measurements taken by THEMIS FGM and ESA instruments between February to September 2007. During this period, THEMIS was in a string of pearls configuration, which was advantageous as sequential magnetopause crossings may be used to study magnetopause inhomogeneity. With this purposes, Plaschke et al. (2009b) specifically selected crossing events where there were multiple crossings by the THEMIS probes. To take full advantage of the THEMIS data set since its launch in 2007, a semi-automated method was developed to classify an additional 12,621 THEMIS magnetopause crossings from 2007 to 2016. Data from THEMIS probes A, D, and E were used from 2007–2016, and THEMIS B and C from 2007–2010, after which these spacecraft were moved to lunar orbit.

In this approach, an algorithm used a set of criteria to classify candidate magnetopause crossings from THEMIS FGM and ESA data. These candidate crossings were then manually verified on a daily basis. Misclassifications that were clearly within the magnetosheath or magnetosphere were discarded. A small number of misclassifications may still exist due to human error.

To create the crossing criteria, 18 magnetopause crossings by the THEMIS E probe were manually classified between 17:00 and 23:00 UT on 16 June 2007. The crossing criteria were empirically determined by optimizing the number of correct crossing classifications, while minimizing the number of false positives. The final criteria were empirically determined as follows: When THEMIS is crossing from the magnetosphere to the magnetosheath,

1. The transit of the magnetopause must occur within a 60 s interval.
2. The B_z component of the magnetic field, in GSM coordinates, must decrease by at least 36 nT (i.e., $dB_z/dt > -0.6$ nT s^{-1}) and the ion density must increase by at least 48 cm^{-3} (i.e., $dn/dt > 0.08$ cm^{-3} s^{-1}).
3. Within the magnetosphere, the average B_z component of the magnetic field must be greater than 5 nT and the average ion density must be less than 7 cm^{-3} for a 48 s interval.

If THEMIS is crossing from the magnetosheath to the magnetosphere, the second criterion is reversed. To prevent spurious measurements from high-frequency noise when calculating the second criteria, the magnetic field measurements were down-sampled from a 3 s resolution to 24 s, and measurements of ion density were reduced from 3 to 36 s resolution.

Once these crossings were visually verified, the database contained 34,428 confirmed magnetopause crossings. Multiple crossings of the magnetopause that occurred within 10 minutes were removed, reducing the database to 12,621 crossings. The innermost crossing was retained so that the database is comparable to the Sh98 model, which used only the innermost crossing in a series of crossings to fit the model. To incorporate the Plaschke et al. (2009b) dataset of THEMIS crossings into the dataset, multiple crossings within 10 minutes were removed, retaining only the innermost crossing for each probe.

The Plaschke et al. (2009b) database was then cross referenced with the new THEMIS database to ensure THEMIS crossings are not double counted. As before, the innermost crossing of the magnetopause from either database within a 10 min interval was retained. This reduces the Plaschke et al. (2009b) database to 1,910 crossings and the newly classified THEMIS database to 11,821 crossings.

This renders a final combined database of 24,967 THEMIS, Cluster, and Geotail magnetopause crossings spanning almost two solar cycles from 1996–2016. Figure 3.6 shows the spatial distribution of magnetopause crossings over all solar zenith angles for 2 × 2 R_E bins. The maximum number of crossings in any bin is 1,892 crossings between X_{GSM} = 8 to 10 R_E and Z_{GSM} = 0 to −2 R_E (Figure 3.6c). The lowest number of magnetopause crossings occur on the magnetopause tail (X_{GSM} < 0 R_E in Figure 3.6a c) where many spatial bins only contain a single crossing. The coverage of the down-tail magnetopause is significantly less than the dayside since these crossings are sampled by Geotail.

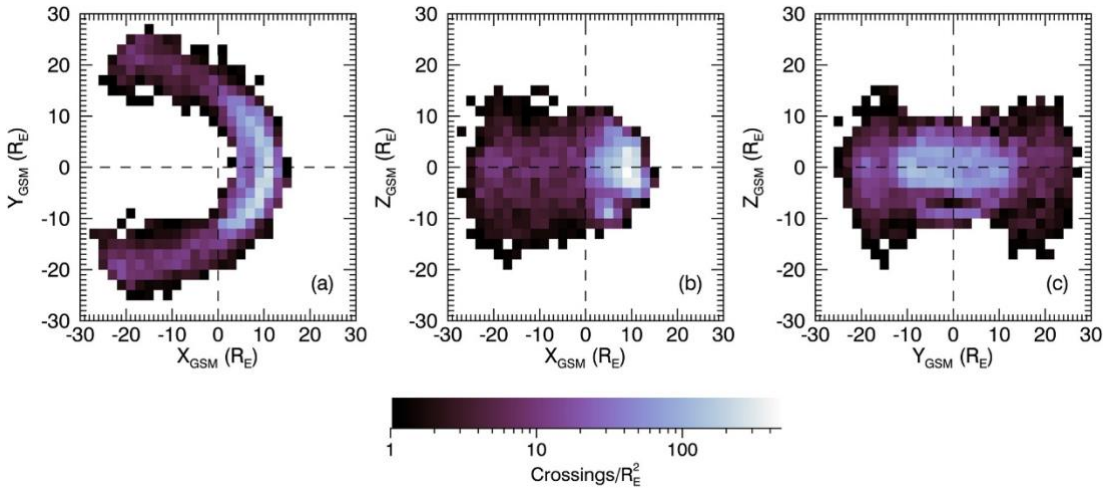

Figure 3.6 2D histogram of magnetopause crossings in the (a) X_{GSM}-Y_{GSM} plane; (b) Y_{GSM}-Z_{GSM} plane; (c) X_{GSM}-Z_{GSM} plane.

Note, in the analysis, only magnetopause measurements from the dayside magnetopause are used (with coordinate X_{GSM} > 0) since our focus is to investigate the role of magnetopause shadowing on the radiation belts, which is most likely to occur on dayside. This reduces the database to a total of

19,973 measurements of the dayside magnetopause, which is used to perform a statistical analysis for the remainder of this thesis.

3.4 Phase Space Density Computation

Chapter 5 and Chapter 6 primarily use multi-mission PSD observations computed in adiabatic coordinates to characterize the radiation belt response to a geomagnetic storm from 6-10 September 2017. This new dataset of intercalibrated PSD, developed by Adam Kellerman at UCLA, is used to demonstrate radiation belt characteristics for the first time in Chapter 5 and Chapter 6. This section describes the method of PSD computation.

Through the September 2017 storm PSD measurements are computed from; Van Allen Probes MagEIS and REPT instruments, THEMIS ESA and SST, MMS FEEPS, GOES MAGED and EPEAD, and GPS CXD (See Section 3.2 for instrumentation specifics). The satellite orbits for the missions used besides GPS are illustrated in Figure 3.7 to demonstrate spatial data coverage. THEMIS data is only included above L = 6 due to instrumental contamination within the radiation belts. The final PSD dataset comprises of measurements from 32 satellites, providing PSD observations of unprecedented resolution.

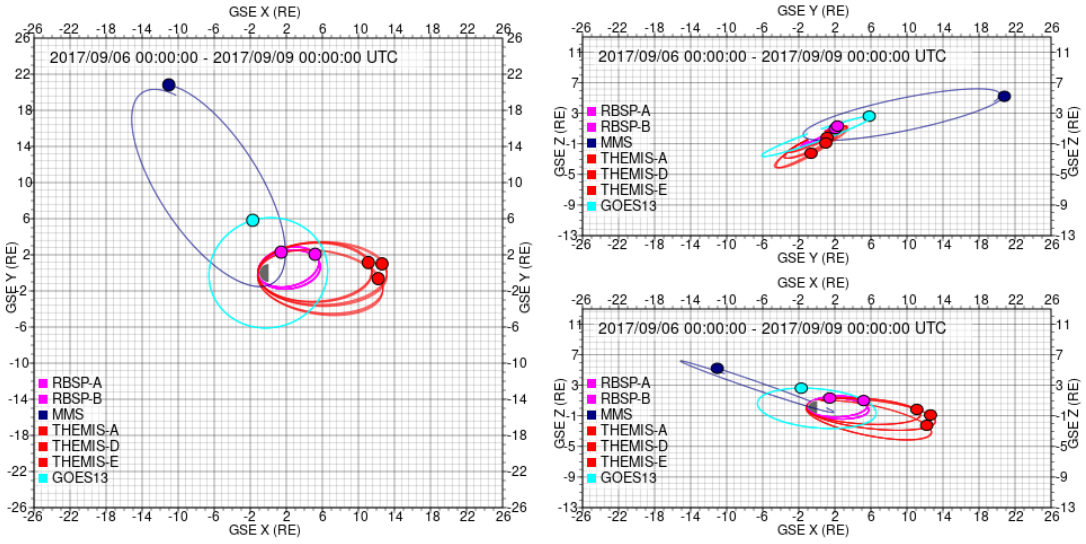

Figure 3.7 Diagram of Van Allen Probes (RBSP), MMS, THEMIS, and GOES satellite orbits in the X_{GSE}-Y_{GSE} plane (left) Y_{GSE}-Z_{GSE} plane (top right) and X_{GSE}-Z_{GSE} plane (bottom right). Individual missions are labelled by colour. Diagram was obtained through Van Allen Probes Gateway, *https://rbspgway.jhuapl.edu/home.*

The electron PSD is calculated by dividing measured differential electron flux, resolved by energy and pitch angle, by the conjugate momentum. For this analysis a sinusoidal pitch angle distribution is assumed for the GPS data, since CDX instrument is not pitch angle resolved, and the pitch-angle distribution obtained from the upper energy channel on GOES MAGED is employed for the EPEAD observations. PSD is defined in units of $(c/cm/MeV)^3$.

For each spacecraft and instrument, the adiabatic invariants μ, K, and L^* are computed using the International Radiation Belt Models library (IRBEM; Boscher et al., 2013), which provides a set of routines to complete magnetic coordinate transforms for given magnetic field models. The magnetic field models used in this thesis are the International Geomagnetic Reference Field model, representing the internally generated geomagnetic field (Thébault et al., 2015), and the semi-empirical Tsyganenko 2001 storm external magnetic field model (T01s; Tsyganenko et al., 2003) which models external magnetic fields generated by magnetospheric current systems induced by solar wind-magnetosphere interactions.

A novel method is employed to remove identified statistical systematic bias, and to define the error in each observation. Using pairs of spacecraft, one spacecraft and instrument is chosen as a “gold standard”, and a correction is applied to each fixed energy channel on the other spacecraft. Corrections are performed for conjunctions in phase space found within 10 minutes, within 0.1 L^*, and for fixed values of the three adiabatic invariants during all conditions and times. For this study, Van Allen Probe B and bias corrected GOES 15 data (see following paragraph) are used as gold standards to calibrate all the other data.

The bias and error corrections are specific to each energy channel, and to bins of the magnitude of the PSD, but not to any specific period. For each bin, the distributions of the change in PSD after calibration are analysed to determine the 5^{th} to 95^{th} percentiles. The 50^{th} percentile (median) represents the bias at a given PSD magnitude, while the interquartile range describes the error in the distribution. A numerical search for the best function to describe the bias offsets is conducted, including exponential, power law, and polynomial

functions; with and without y-intercept offsets. The function that provides a fit with the lowest sum of absolute deviation over all the binned median values is chosen as the preferred solution for a given pair of spacecraft, instruments, and specific energy channel. The correction process is repeated for every energy channel, instrument, and spacecraft.

Rather than interpolating PSD observations to find PSD for specific μ and K, as is traditionally practiced, in this thesis PSD measurements which lie within specified ranges of μ and K are used to represent a specific population of electrons. Chapter 5 and Chapter 6 take slightly different approaches when specifying ranges of μ and K, based upon the goals of each investigation. Chosen ranges of μ and K are chosen by visually inspecting profiles of PSD across L^* for a variety of data ranges to find the range which (i) provides PSD profiles with sufficient data across L^* and (ii) does not present PSD with multiple distinct characteristics which are dependent upon K. A relatively large range of K was chosen to maximise PSD data availability across all L^*, whilst a small μ range was chosen to limit any overlap between measurements taken by different energy channel ranges for different satellites. Figure 3.8 shows a comparison of different ranges of K to demonstrate how data ranges are chosen, where Figure 3.8b is the optimal data range of K.

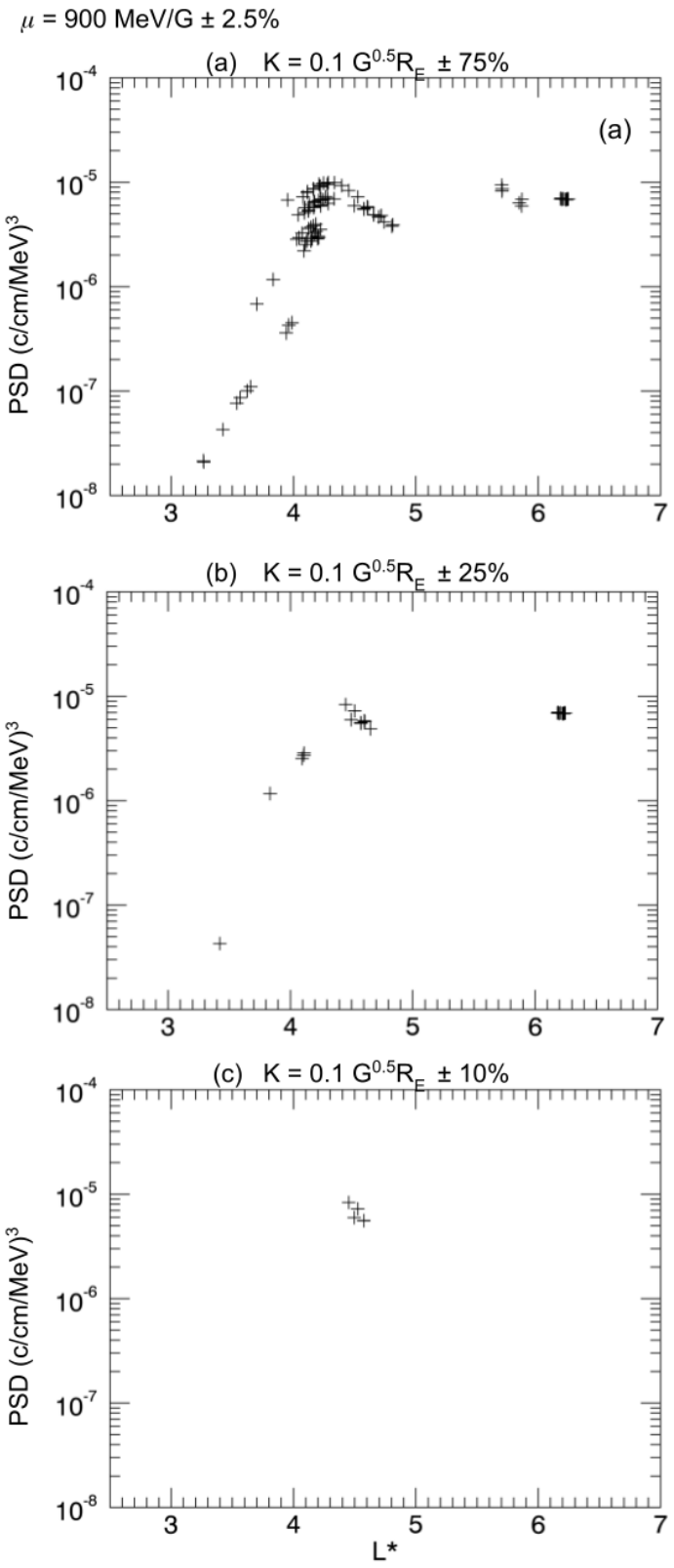

Figure 3.8 Intercalibrated PSD data over a 1-hour time interval, plotted as a function of *L for μ = 900 MeV/G ± 2.5% and $K = 0.1\ G^{0.5}R_E$ within a range (a) *K* ± 75% (b) *K* ± 25% (c) *K* ± 10%.**

3.5 OMNI Dataset

The OMNI dataset, provided by the Goddard Space Flight Centre, NASA (*https://omniweb.gsfc.nasa.gov/index.html*), is used for high resolution (5 minute) measurements of the solar wind and Sym-H index. Measurements of the solar wind are obtained from satellites upstream of the magnetosphere, including the Advances Composition Explorer (ACE), Geotail, and Interplanetary Monitoring Platform-8 (IMP-8), Wind, and Deep Space Climate Observatory (DSCOVR) satellites. ACE, Wind, and DSCOVR orbit the L1 point, which is located between the Sun and the Earth. IMP-8 is in orbit around the Earth with an orbital apogee of 45 R_E. Measurements of the solar wind are time shifted to when the solar wind reaches the bow shock nose. This routine calculates a phase front normal from measurements of IMF and bulk flow velocity of the solar wind, and assumes that the phase front of the solar wind propagates over the spacecraft towards the magnetosphere on a planar surface. The location of the bow shock for the time at which the solar wind arrives is modelled by the Farris and Russell (1994) model.

The Sym-H index is determined using low latitude ground magnetometer stations with locations across multiple longitudes. There is a three-step procedure used in the calculation: (i) the disturbance magnetic field is found by subtracting the geomagnetic main field and the average daily variation on solar quiet days, (ii) The disturbance magnetic field is transformed into a dipolar coordinate system, (iii) the longitudinally symmetric component of the disturbance field is calculated by the average from six magnetometer stations, with a latitudinal correction applied to obtain the horizontal magnetic field disturbance. Full details of Sym-H index derivation can be found in Iyemori et al. (2010).

Chapter 4 Do statistical models capture the dynamics of the magnetopause during sudden magnetospheric compressions?

The results of this chapter have been published in the *Journal of Geophysical Research*: *Space Physics* as:

Staples, F. A., Rae, I. J., Forsyth, C., Smith, A. R. A., Murphy, K. R., Raymer, K. M., et al. (2020). Do statistical models capture the dynamics of the magnetopause during sudden magnetospheric compressions? Journal of Geophysical Research: Space Physics, 125, e2019JA027289. https://doi.org/10.1029/2019JA027289

4.1 Introduction

Current understanding of the magnetopause is entirely based upon in-situ observations of plasma and magnetic conditions as the magnetopause passes over a spacecraft. Depending on the configuration of a spacecraft's orbit, the magnetopause may pass over a spacecraft several times through an orbit, or not at all. Unfortunately, this means that there are no continuous measurements of the magnetopause since spacecraft crossings are incidental. Therefore, we are heavily reliant upon model parameterisation of the magnetopause location when analysing its effects on magnetospheric plasma.

As discussed in Chapter 2, it is of special importance to know the location of the magnetopause during incursions into the inner magnetosphere so that the effects of magnetopause shadowing of the radiation belt may be quantified. To do this, many radiation belt studies have used the Shue et al. (1998) magnetopause model (Sh98) (e.g., Herrera et al., 2016; Loto'aniu et al., 2010; Morley et al., 2010b; Murphy et al., 2015; Olifer et al., 2018; Turner et al., 2012b). The Sh98 model is a statistical model of the magnetopause size, shape, and location, which is based upon a statistical fit of 553 spacecraft magnetopause crossings (described in full in Section 2.3.1). Section 2.3.2 discussed how the Sh98 model may not give an accurate depiction of the magnetopause shape, as demonstrated by Case and Wild (2013).

Furthermore, because the Sh98 model is a statistical parameterisation, we postulated whether it well represents magnetopause location under highly dynamic solar wind driving, such as those which lead to radiation belt flux dropouts.

This chapter presents the results of an investigation of the Sh98 model accuracy under solar wind conditions which lead to incursions of the magnetopause into the inner magnetosphere. To do this we construct a multi-spacecraft database of magnetopause crossings and statistically compare these measurements to the modelled magnetopause for prevailing solar wind conditions. Statistical differences between the measured magnetopause location are identified for interplanetary shock conditions and sudden storm commencements. These statistical results are further examined for a case study of the 2013 St. Patrick's day storm, which is known to have a clear and well-studied radiation belt response (e.g., Albert et al., 2018; Ma et al., 2018; Olifer et al., 2018). Finally, we discuss whether a statistical correction of the Sh98 magnetopause model is useful in determining the relative contributions of direct and indirect magnetopause shadowing during electron dropout events.

4.2 Comparing Magnetopause Observations to Modelled Location

To compare the location of the modelled magnetopause to our dataset of spacecraft observations, we defined ΔR as the radial distance between the measured location of a spacecraft magnetopause crossing, R_{SC}, and the distance to the aberrated Sh98 model magnetopause, R_{Mod}, for the same solar zenith angle of the spacecraft, such that $\Delta R = R_{Mod} - R_{SC}$. If $\Delta R > 0$ then the model overestimated the magnetopause location; that is, the Sh98 magnetopause was located at a larger radial distance than the measured magnetopause. Conversely, if $\Delta R < 0$ then the Sh98 model underestimated the magnetopause location; that is, the Sh98 model was closer to the Earth than the measurement.

Finally, if $\Delta R = 0$ to within an uncertainty of ± 0.4 R_E, then we concluded that the model and the measurement agree. The uncertainty of ± 0.4 R_E for the

Sh98 model was chosen for this study because it was the maximum uncertainty calculated for the model across the dayside magnetosphere (see detailed discussed in Section 2.3.1 and Figure 2.7).

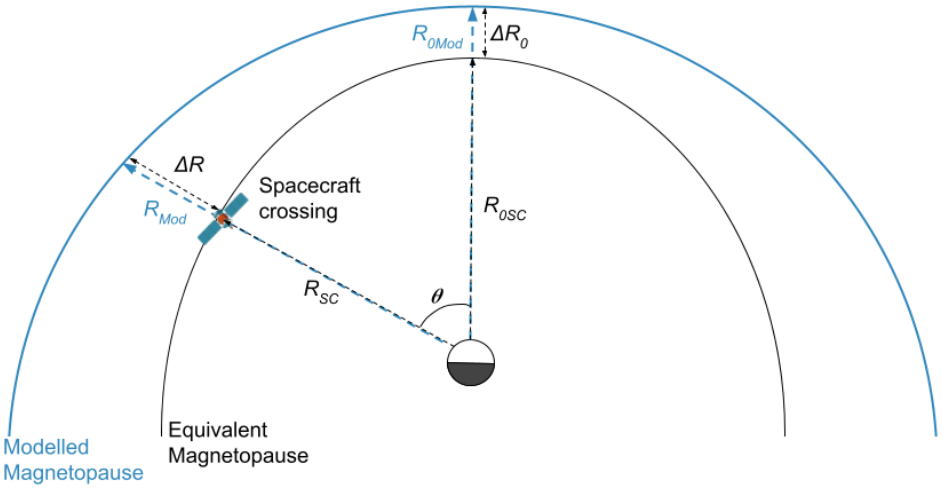

Figure 4.1 Diagram illustrating the radial distances of the magnetopause observed by a spacecraft, R_{SC}, and modelled magnetopause standoff, R_{Mod}, for the same solar-zenith angle, θ, and the difference between the two ΔR. The equivalent distances to the subsolar magnetopause are also shown by $R_{0_{SC}}$, (calculated from the spacecraft crossing assuming the shape of the Sh98 model, Equation 4.1), the modelled subsolar standoff $R_{0_{Mod}}$, and the difference between the two ΔR_0.

It is also important to estimate the position of the subsolar magnetopause, which is where an electron drift path is most likely to intersect the magnetopause. By assuming that the functional shape of the Sh98 magnetopause is correct (i.e., that the shape and flaring angle, α, is correct) the Sh98 model was adjusted to spacecraft measurements from any dayside magnetopause crossing to the aberrated subsolar point, $R_{0_{SC}}$, by rearranging the Sh98 functional form (Plaschke et al., 2009a; Plaschke et al., 2009b)

$$R_{0_{SC}} = R_{SC}\left(\frac{2}{1 + \cos\theta}\right)^{-\alpha} \quad 4.1$$

where θ is the solar zenith angle of the spacecraft crossing position, calculated by taking the inverse cosine of the dot product between the aberrated Sun-Earth line and the position vector of the spacecraft in GSE coordinates. The difference between the modelled subsolar standoff distance and the measured

equivalent subsolar standoff distance was defined as $\Delta R_0 = R_{0_{Mod}} - R_{0_{SC}}$, where $R_{0_{Mod}}$ is the modelled subsolar standoff distance.

If $\Delta R_0 = 0$ to within an uncertainty of ± 0.2 R_E, then we concluded that the model and the measurement agree. The uncertainty of ± 0.2 R_E for the subsolar standoff distance of Sh98 model was chosen based upon the maximum uncertainty calculated for the subsolar magnetopause, see detailed discussed in Section 2.3.1 and Figure 2.7.

Finally, the percentage change in distance was defined as $\Delta R/R_{SC}$, to normalise for the level of magnetopause compressions, and to compare crossings across all dayside solar zenith angles to each other.

4.3 Statistical Evaluation of Magnetopause Location

The distributions of ΔR and ΔR_0 for our magnetopause crossing dataset are shown in Figure 4.2. Figure 4.2a shows that ΔR was not normally distributed since the mean and median values were not equal; the mean ΔR = 0.13 R_E and the median ΔR = 0.05 R_E. This asymmetry implies that there were a higher number of instances where the measured magnetopause was closer to Earth than the modelled distance, and that for these instances ΔR was a greater magnitude. Furthermore, 74% of measurements occurred within 1 standard deviation of the mean, which in this case was 0.97 R_E. The upper and lower quartiles of ΔR were −0.43 R_E and 0.64 R_E, respectively. The difference between the median and the mean was less than the Sh98 model uncertainty of ± 0.4 R_E, but there was a large spread in ΔR, with only 40% of measurements being within ≤ 0.4 R_E.

Figure 4.2b showed that ΔR_0 was also not normally distributed as the mean and median values were not equal; with a mean ΔR_0 = 0.09 R_E and median ΔR_0 = 0.05 R_E. Furthermore, 70% of measurements occurred within a standard deviation of the mean, which is ± 0.84 R_E. The upper and lower quartiles of ΔR_0 were = −0.40 R_E to 0.56 R_E, respectively. The difference between the median and the mean is less than the Sh98 model uncertainty of ± 0.2 R_E,

though there was a large spread in ΔR_0, with only 24% of measurements ≤ 0.2 R_E.

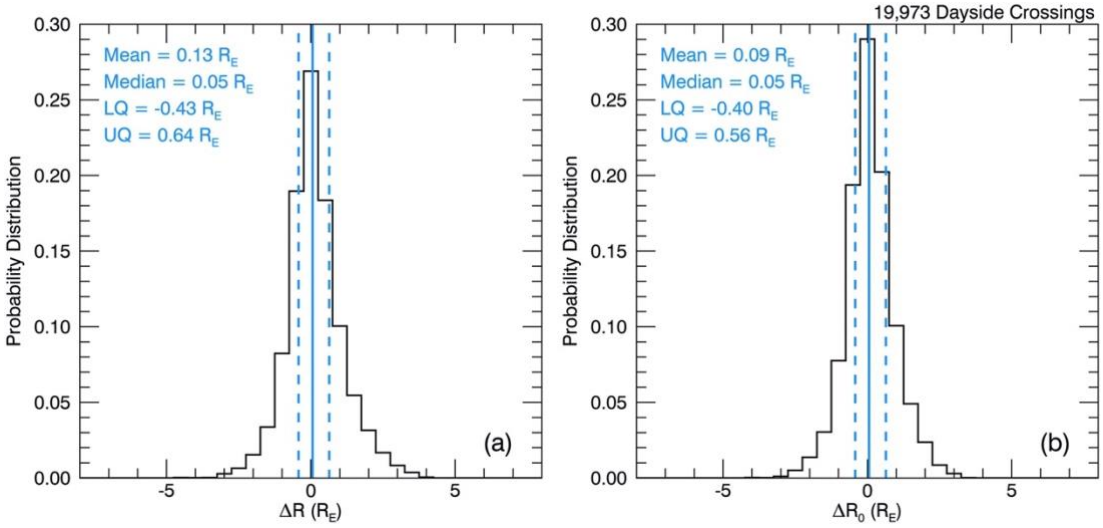

Figure 4.2 (a) The distribution of ΔR for measurements of the dayside magnetopause. (b) The distribution of ΔR_0 for measurements of the dayside magnetopause. The solid blue line shows the median value for each panel and the dotted blue lines show the interquartile range (Staples et al., 2020).

To see how ΔR varies for different measured standoff distances, Figure 4.3 shows the median magnetopause distance calculated by the Sh98 model, R_{Mod}, as a function of observed magnetopause distance, R_{SC}. Note that this figure describes spacecraft crossings at all measured solar zenith angles. The shaded area indicates the interquartile range of the measured magnetopause location, R_{SC}. Within the shaded region, the distribution was closest to the line of unity, i.e., $R_{SC} \simeq R_{Mod}$. This indicated that for half of the measurements, the Sh98 model accurately calculated magnetopause standoff distance at locations between 10.6 and 12 R_E. However, the whole distribution did not follow this relationship, showing a gradient other than unity. A multiple linear regression to the distribution of median R_{Mod} is given by the purple line in Figure 4.3. This showed that the experimentally measured magnetopause distance as a function of the median modelled magnetopause distance was best described by the relationship $R_{SC} = (R_{Mod} - 3.68)/0.68$.

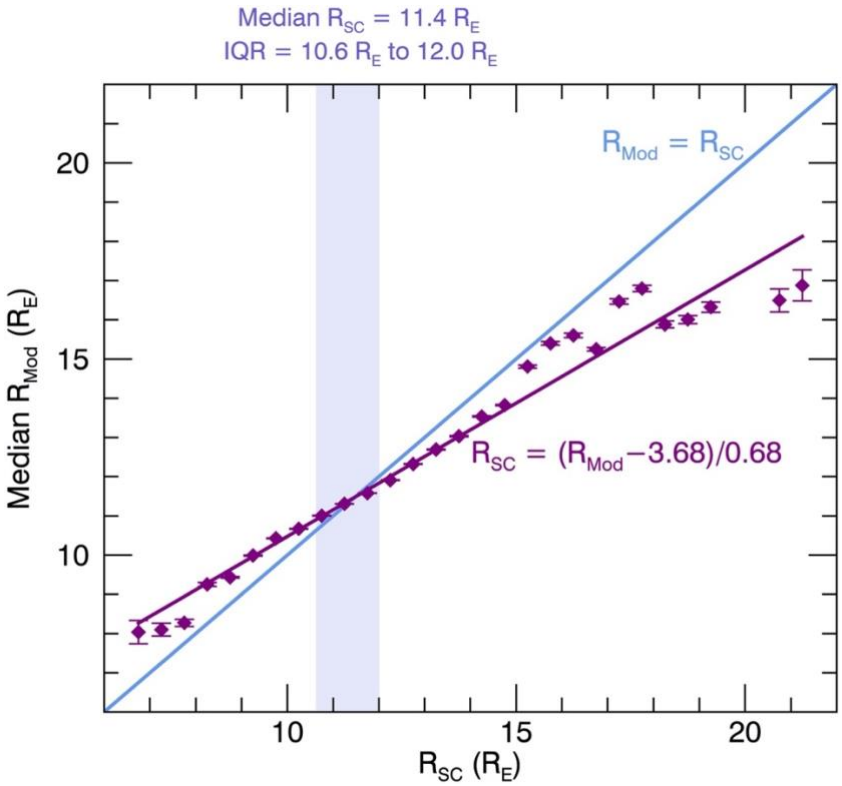

Figure 4.3 Purple diamonds show the median standoff distance calculated by the Shue et al. (1998) model, R_{Mod}, corresponding to spacecraft magnetopause crossing measured at a given standoff distance, R_{SC}. The error bars show the propagated error of the Shue et al. (1998) model. The blue line gives where $\bar{R}_{Mod} = R_{SC}$. The shaded area indicates the interquartile range (10.6 to 12.0 R_E) of observed magnetopause distance, R_{Mod} (Staples et al., 2020).

To assess whether the different solar wind conditions used were systematically influencing the calculation of the Sh98, we examine distributions of $\Delta R/R_{SC}$ for varying solar wind dynamic pressure and north-south IMF, shown in Figure 4.4.

Figure 4.4a shows a 2D histogram of $\Delta R/R_{SC}$ as a function of D_p, which is column normalised since there were many more measurements when D_p is low. There was a weak dependence of $\Delta R/R_{SC}$ on D_p, in that the average magnetopause location may be up to 4% closer to Earth than the Sh98 model location for increasingly low dynamic pressures (D_p < 4 nPa), but with a very large spread in values. For dynamic pressures above 4 nPa, median $\Delta R/R_{SC}$ decreased until the measurements agreed with the model location. There were less than 10 measurements per column for dynamic pressures exceeding 8 nPa, so a reliable relationship between median $\Delta R/R_{SC}$ and D_p could not be

ascertained. Whilst there was a weak relationship between $\Delta R/R_{SC}$ and D_p, there was no evidence that strong dynamic pressures (D_p > 4 nPa) were associated with large positive $\Delta R/R_{SC}$.

Figure 4.4b shows a column normalised 2D histogram of $\Delta R/R_{SC}$ as a function of B_z. The median measured magnetopause location was closer to Earth for higher magnitudes of both northwards and southwards IMF, by up to 4% at B_z of -8 nT and 10 nT, but with a very large spread in values. Below B_z of -12 nT and above 10 nT, there were less than 8 measurements per column, so we could not ascertain a reliable relation between $\Delta R/R_{SC}$ and IMF B_z.

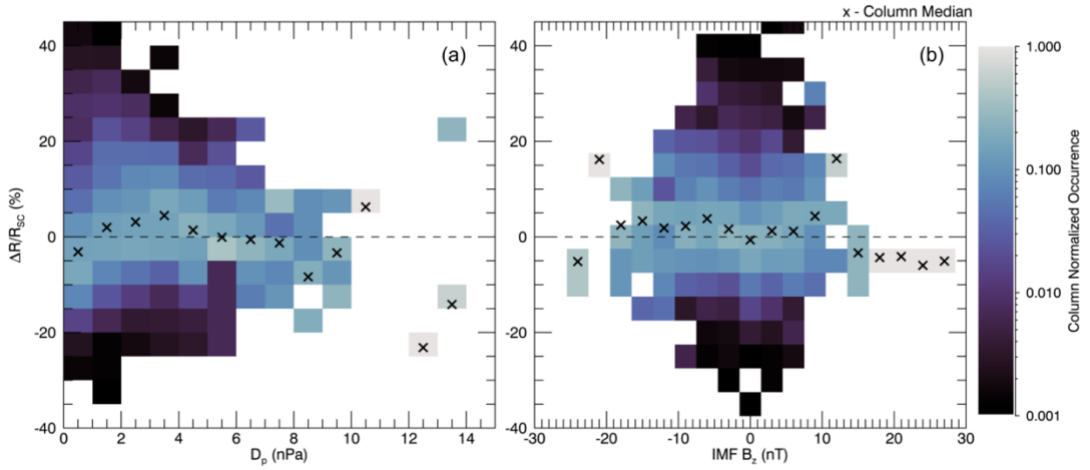

Figure 4.4 Column normalised distribution of fractional change in magnetopause standoff distance ($\Delta R/R_{SC}$) as a function of (a) solar wind dynamic pressure; (b) north-south component of the IMF, B_z. Medians for each column are indicated by black crosses (Staples et al., 2020).

The distribution of $\Delta R/R_{SC}$ was further examined for varying geomagnetic conditions in Figure 4.5a, which shows a column normalised 2D histogram of $\Delta R/R_{SC}$ as a function of the Sym-H index. Figure 4.5a demonstrated that the relationship between $\Delta R/R_{SC}$ and the geomagnetic conditions, as defined by Sym-H index, varied depending on phase of the geomagnetic storm. For geomagnetically quiet times (−50 < Sym-H < 15 nT), the maximum occurrence probabilities were peaked and centred on zero. However, for geomagnetic storm time conditions (Sym-H ≤ −50 nT), the median offset between measurement and model varied greatly between −5% to 15% for decreasing Sym-H. Moreover, for positive Sym-H, $\Delta R/R_{SC}$ had a near-constant positive

offset which increased with increasingly positive Sym-H. This positive offset indicated that the magnetopause was closer to Earth than the model prediction. Large positive and sudden increases in Sym-H typically correspond to the storm sudden commencement phase (SSC) of a geomagnetic storm. During an SSC, Sym-H index can increase by 10s of nT on minute timescales (Dessler et al., 1960) in response to the arrival of an interplanetary shock front which rapidly compresses the dayside magnetosphere. Figure 4.5a would therefore suggest that the magnetopause was closer to Earth than the Sh98 model by up to 15% during SSCs.

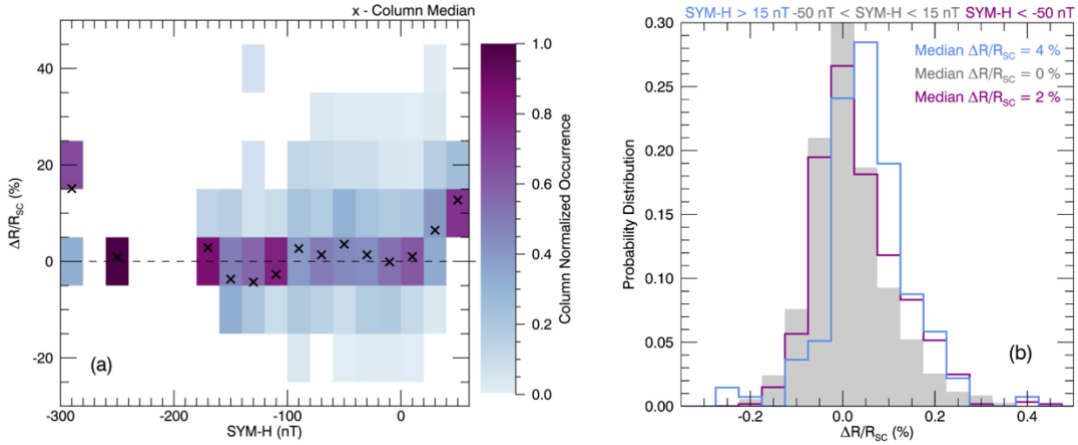

Figure 4.5 (a) Column normalised distribution of percentage change in magnetopause standoff distance ($\Delta R/R_{SC}$) as a function of Sym-H. Column medians are indicated by black crosses. (b) Probability distributions of $\Delta R/R_{SC}$ under different geomagnetic conditions; quiet times are shown by the grey histogram (−50 nT < Sym-H < 15 nT), storm sudden commencement phase is shown by the blue histogram (Sym-H ≥ 15 nT), main storm phase is shown by the purple histogram (Sym-H ≤−50 nT) (Staples et al., 2020).

The observed offsets between modelled and measured magnetopause under different geomagnetic conditions is further demonstrated in Figure 4.5b: the probability distributions of $\Delta R/R_{SC}$ are shown for geomagnetically quiet times (Sym-H between −50 and 15 nT), during the main phase of geomagnetic storm (Sym-H ≤ −50 nT) and for storm sudden commencement (Sym-H ≥ 15 nT). The majority of magnetopause observations occurred during quiet times (19,140 crossings). This quiet time distribution was peaked at $\Delta R/R_{SC}$ = 0%, with upper and lower quartiles of −4% and 6%, respectively. Thus, during relatively quiet times the observed location of the magnetopause is located inside the Sh98 model location as often as it is located outside the model

location. In contrast, during geomagnetically active times, when Sym-H ≤ −50 nT or Sym-H ≥ 15 nT, the peak of the distribution was positive; 2% and 4%, respectively, with upper and lower quartiles of −3% and 9% for Sym-H ≤ −50 nT and 0% and 10% for Sym-H ≥ 15 nT. There were 601 magnetopause measurements during geomagnetic storms (Sym-H ≤ −50 nT) and 137 measurements during SSCs (Sym-H ≥ 15 nT). We used the Mann-Whitney U test (Nachar, 2008) to confirm whether the SSC and main storm phase distributions were statistically different to the quiet time distribution, to a 95% confidence level. As such, during storm times (Sym-H ≤ −50 nT) it was more likely that the magnetopause was measured inside of the model location. During periods when SYMH ≥ 15 nT, which typically correspond to SSCs, the magnetopause location was almost exclusively measured inside of the model location. Thus, the magnetopause was statistically closer to the Earth than the Sh98 model during both the main phase of a geomagnetic storm and during storm sudden commencement.

To test the more extreme deviations from the Sh98 model, we perform a superposed epoch analysis (SEA) of solar wind drivers during strongly positive Sym-H conditions. We select events for this analysis where there is a peak in Sym-H which exceeds 15 nT, and where there is a spacecraft measurement of the magnetopause within a day of the peak Sym-H. Epoch time zero, t_0, is chosen as the peak value of Sym-H. We then perform the superposed epoch analysis for ± 1 day of t_0. Figure 4.6 shows the results of this SEA. In total there were 392 individual events used in the analysis, and 3,629 spacecraft crossings of the magnetopause across the epochs used. Figure 4.6f shows median $\Delta R/R_{SC}$ at a 2-hour resolution for the superposed epochs, whereas Figure 4.6a-e show a 5 min resolution. The 2-hour resolution of Figure 4.6f was chosen such that the variability of $\Delta R/R_{SC}$ through the epoch analysis was retained, while maximizing the number of crossings used to calculate each median value of the epochs.

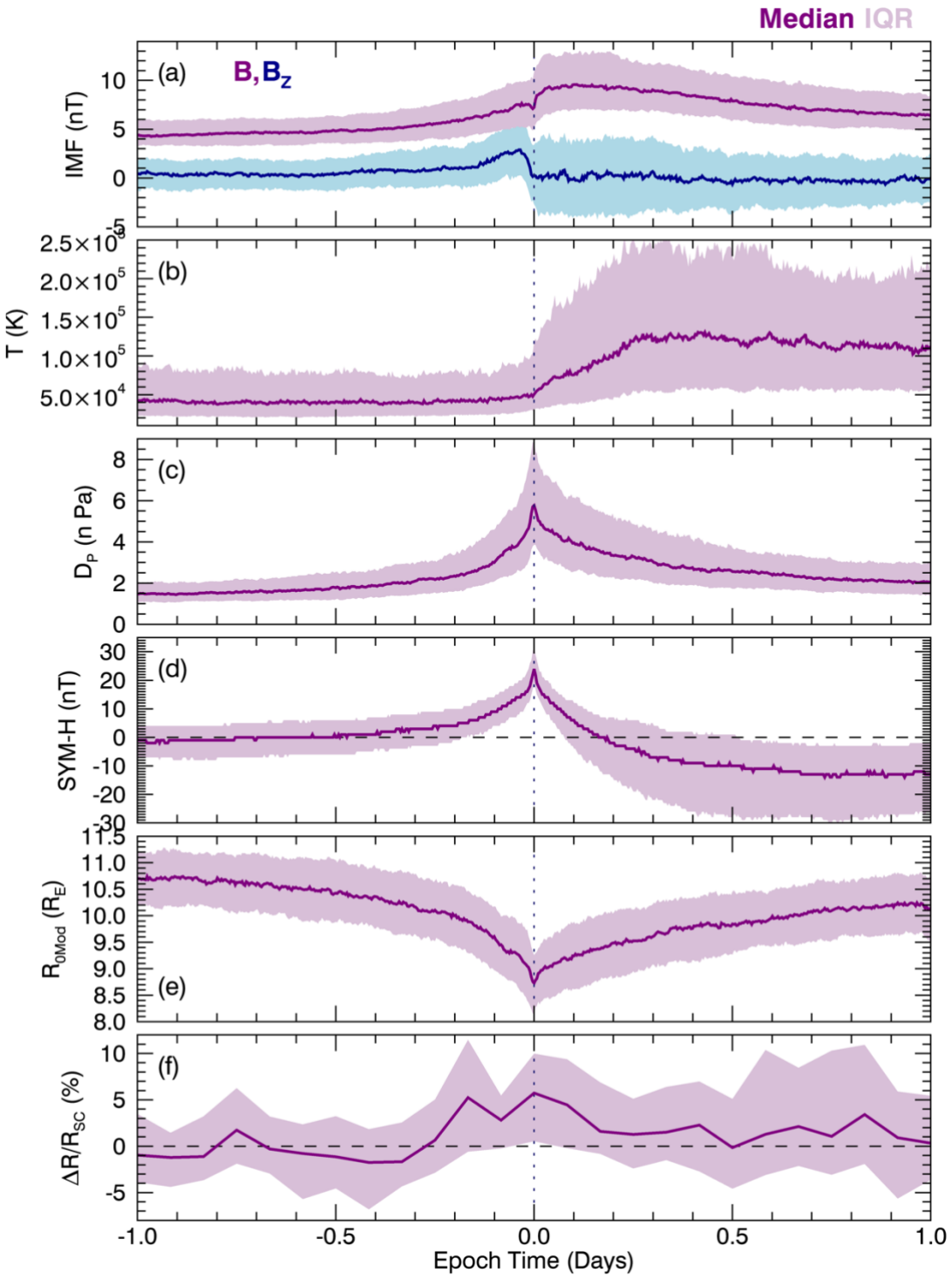

Figure 4.6 A superposed epoch analysis of (a) interplanetary magnetic field strength $|B|$ (purple) and B_z (blue); (b) solar wind temperature, T; (c) solar wind dynamic pressure D_p; (d) Sym-H index; (e) $R_{0_{Mod}}$; (f) $\Delta R/R_{SC}$. Epoch time zero is defined as the time that Sym-H reaches a peak value ≥ 15 nT. The purple lines show the median values across the epochs on a 5-minute bases for (a-e) and 2-hour basis for (f), and the interquartile range is denoted by the shaded regions. The vertical dotted line shows t_0 (Staples et al., 2020).

Figure 4.6 shows strong evidence of solar wind discontinuities at t_0, characteristic of forward interplanetary shocks; a sudden increase in temperature and an increase in magnetic field strength following t_0 (Figure 4.6a-b), and a sharp peak in D_p at t_0 (Figure 4.6c). It is well understood that fast forward interplanetary shocks play a large role in the storm sudden commencement phase due to enhancement of magnetopause currents (e.g., Taylor, 1969). Empirical relationships have been derived between SSC amplitude and the change in the square root of D_p at the shock/discontinuity (Russell et al., 1992).

In response to the sudden dynamic pressure increase, the Sh98 model demonstrated a compression of the median subsolar magnetopause from 10.7 R_E to 8.7 R_E (Figure 4.6e). We observed that the Sym-H index showed a tendency to become negative following t_0 in Figure 4.6d. Further investigation showed that 33% of the epochs contained moderate to intense geomagnetic storms with minimum Sym-H ≤ −50 nT. A further 30% of epochs contained a minimum of Sym-H between −30 and −50 nT, indicating weak geomagnetic storms (Loewe & Prölss, 1997). This supports our suggestion that a peak in Sym-H ≥ 15 nT indicates a storm sudden commencement phase of shock-driven geomagnetic storms.

The median percentage difference between the spacecraft measurements of the magnetopause and the Sh98 model, $\Delta R/R_{SC}$, was noted to be relatively small and slowly varying between −2% and 2% until 4 hours (0.2 days) before t_0, when $\Delta R/R_{SC}$ rapidly increased to 6% (Figure 4.6f). At the same time, the lower quartile of Sym-H exceeded 0 nT (Figure 4.6d). Following this rapid increase, $\Delta R/R_{SC}$ reached a maximum of 6% at t_0. Median values of $\Delta R/R_{SC}$ remained high until 2 hours (0.1 days) after t_0 and, as shown in Figure 4.6f, the entire interquartile range is greater than 0%, which means that in the majority of cases the Sh98 model overestimated magnetopause distance. At times greater than 2 hours after t_0, median $\Delta R/R_{SC}$ decreased but remained positive, fluctuating between 0% and 3%, though the interquartile range was notably larger than times preceding t_0+2 hours.

It is important to comment that in Figure 4.5b, the median $\Delta R/R_{SC}$ was calculated as 4% when we used a threshold of Sym-H ≥ 15 nT to define magnetopause measurements taken during an SSC. Whereas in the SEA presented in Figure 4.6f, median $\Delta R/R_{SC}$ = 6% at t_0, which was defined as the time Sym-H peaks at a value greater than 15 nT. This difference was due to the SEA resolution: Magnetopause measurements which occurred within one hour of the Sym-H peak ≥ 15 nT were included in the median calculation, even though Sym-H may be less than 15 nT at the time of the crossing.

4.4 Case Study: 2013 St Patrick's Day Storm

Finally, a case study of a large geomagnetic storm associated with a significant radiation belt response is evaluated. The chosen event is the 2013 St. Patrick's day storm, which has been studied extensively by the Geospace Environment Modelling (GEM) program radiation belt modelling focus group, who identified the event for quantitative assessment (e.g., Albert et al., 2018; Olifer et al., 2018; Ma et al., 2018). The 2013 St. Patrick's day storm was a large CME-driven geomagnetic storm where magnetopause shadowing is thought to have played an important role in producing a dropout in radiation belt electron flux (Olifer et al., 2018). There were 93 individual magnetopause crossings observed by the THEMIS probes in our dataset between 14 and 20 March, all of which were visually verified. These crossings are used to assess the accuracy of the Sh98 model magnetopause location through the storm. Three separate solar wind enhancements which lead to magnetopause variations on 14, 15 and 17 March 2013 (indicated by dashed lines in Figure 4.7) shall be discussed in turn.

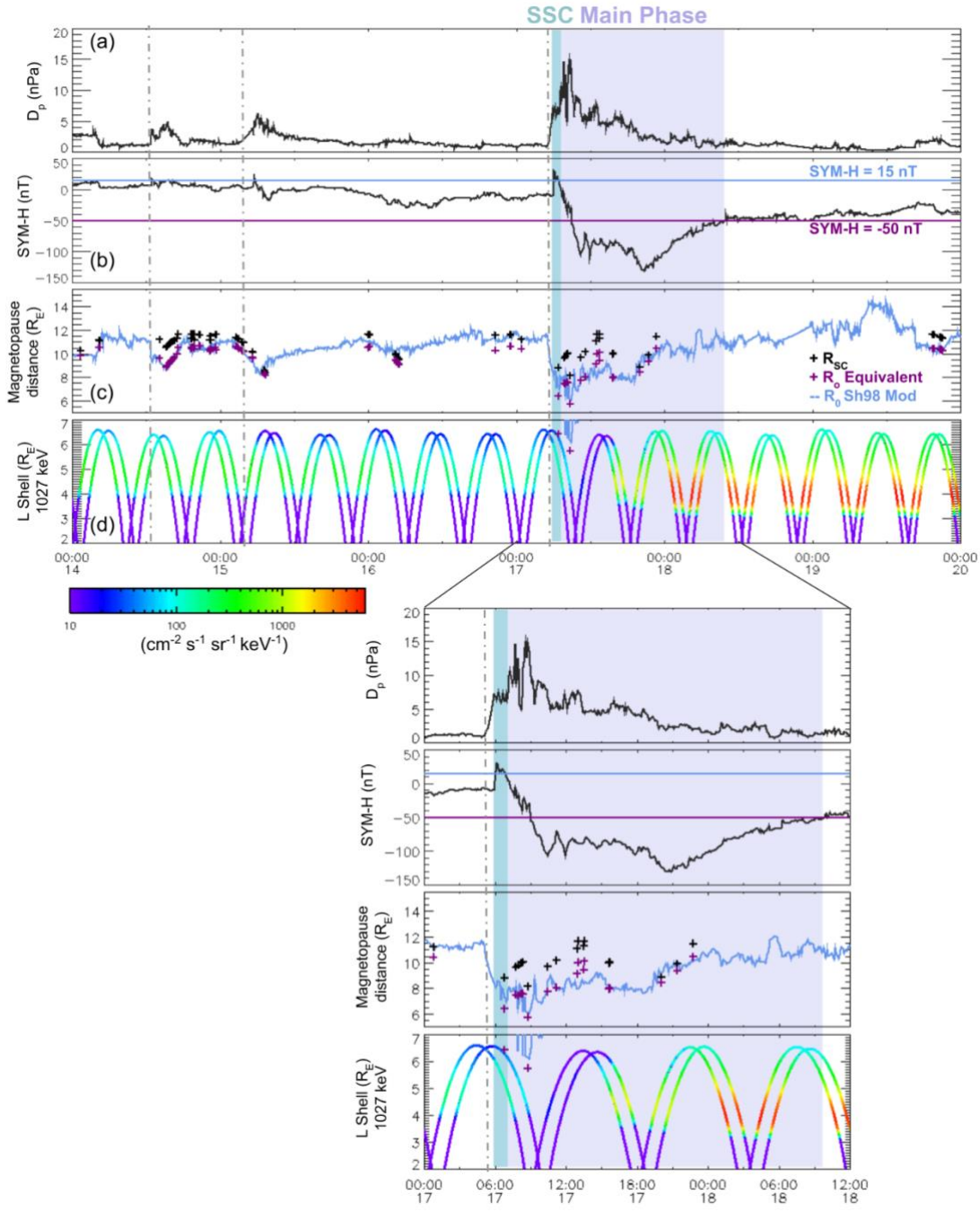

Figure 4.7 St. Patrick's day storm, 14–20 March 2013; (a) solar wind dynamic pressure, D_p; (b) Sym-H index, blue and purple horizontal lines denoting Sym-H = −15 and −50 nT, respectively; (c) subsolar standoff distance of the Sh98 model in blue, $R_{0_{Mod}}$, black crosses denoting magnetopause crossing distance at any solar zenith angle, R_{SC}, and purple crosses denoting equivalent standoff distance of those magnetopause crossings, $R_{0_{SC}}$; (d) ~1 MeV electron flux from the Van Allen Probes A and B MagEIS instruments. Vertical dashed lines indicate pressure enhancements. Blue and purple shaded areas denote the SSC and main phase of the geomagnetic storm respectively. Bottom panel shows a zoomed-in plot of panels (a)–(d) during the geomagnetic storm on 17 March (Staples et al., 2020).

At ~ 13 UT on 14 March 2013, there was a comparatively small increase in D_p of up to 5 nPa (Figure 4.7a), which had a small corresponding Sym-H increase to 16 nT but no obvious radiation belt response (Figure 4.7b and d). The Sh98 model standoff location was compressed to 8.8 R_E. The equivalent standoff distance of magnetopause crossings during this compression, agree remarkably well with the Sh98 location (Figure 4.7c).

At ~ 06 UT on 15 March 2013, there was a second small increase in D_p of up to 6 nPa (Figure 4.7a). In this case there was a clear and rapid increase in Sym-H by 20 nT, to a peak of 25 nT. There was a reduction in the ~ 1 MeV electron fluxes by a factor of ~ 10 at the outer boundary of the radiation belt, for L > 6 R_E (Figure 4.7d), which persisted until the major geomagnetic disturbance which began on 17 March 2013. During this second pressure pulse, the Sh98 model standoff location was compressed to 8.3 R_E. The observed magnetopause crossings continued to agree with model values until the magnetopause was maximally compressed at 07 UT. Immediately following this maximum compression on 15 March, there were two magnetopause crossings where the observed magnetopause was 0.9 R_E and 1.2 R_E (10% and 15%) closer to the radiation belts than the Sh98 model distance.

On 17 March 2013, the CME arrival was accompanied by a sudden increase in D_p from 1 to 15 nPa. The Sym-H index responded accordingly, with a sharp increase to 31 nT, before the main phase of the storm where Sym-H decreased down to −131 nT. During the main phase of the storm, the ~ 1 MeV electron fluxes decreased by approximately 2 orders of magnitude, a reduction that persisted for 7 hours. During the recovery phase of the storm on 18 March, enhancements dominated over the losses, and the ~ 1 MeV electron fluxes increased by 3 orders of magnitude with a radial peak in flux at L ~ 4 R_E. The Sh98 model standoff location ($R_{0_{Mod}}$) was compressed down to 6.1 R_E during the storm main phase in response to the pressure enhancement. At 08:45 UT, where the Sh98 model output was at its minimum standoff distance, the subsolar projection of an observed THEMIS E magnetopause crossing was 5.7 R_E, which is 0.4 R_E (7%) closer to Earth than the Sh98 model calculation

of 6.1 R_E. During the storm sudden commencement, there was one crossing of the magnetopause made by THEMIS D at 06:48 UT, with an equivalent subsolar standoff distance of 6.4 R_E. At this time, the Sh98 model was calculated as 7.3 R_E, which was 0.9 R_E (or 14%) further from Earth than the measured magnetopause. Equivalent subsolar standoff measurements during the main phase of the storm were even more variable, ranging between 5.7 and 10 R_E, indicating that the Sh98 model does not reflect the true magnetopause location during this highly disturbed time. Taking the model uncertainty as ~0.2 R_E at the subsolar point, only 15% of measurements on 17 March 2013 were within this error. The Sh98 model underestimated standoff distance by > 0.2 R_E for 40% of measurements and overestimated standoff distance by > 0.2 R_E for 45% of measurements.

4.5 Discussion

This chapter presents an analysis of the Sh98 magnetopause model location under solar wind compression and periods of dynamic solar wind driving, specifically during storm sudden commencements. An empirical database of ~20,000 spacecraft crossings of the dayside magnetopause was constructed, the largest dataset of this kind to date. Spacecraft crossings of the magnetopause were compared to the location of the Sh98 magnetopause model, given the prevailing solar wind conditions.

4.5.1 Accuracy of the Sh98 Model

Distributions of the radial difference between the measured and modelled magnetopause location showed that, for all dayside crossings, the Sh98 model accurately predicted the location of the magnetopause. The distributions were centred around zero with upper and lower quartiles of ~ −0.5 R_E and 0.6 R_E, respectively, for all dayside locations (Figure 4.2a) and when mapped to the subsolar point (Figure 4.2b). However, there was high variability in these distributions, showing that there was a low confidence level of 40% within calculated errors of the Sh98 model. The standard deviations of the distributions were ~ 1 R_E, implying that the Sh98 model accurately represented the magnetopause location to within ~ 1 R_E, on average.

It was further identified that the Sh98 model location was accurate to within ~ 1 R_E when the magnetopause was measured between 10.5 R_E and 12 R_E, which was where half of measurements were observed. However, when the measured magnetopause location was outside of this range, systematic differences between measured and modelled locations were identified (Figure 4.3). On average, the Sh98 model underestimated standoff distance for crossings measured at distances > 12 R_E, and overestimated standoff distance for crossings measured at distances < 10.6 R_E. A multiple linear regression was conducted on the observed and average modelled values showing that, across all prevailing conditions between 1996–2016, the relations can be described by a linear function $R_{SC} = (R_{Mod} - 3.68)/0.68$. Fitting the model to the crossing database in this way might suggest that a simple correction to the Sh98 model would better reflect the average magnetopause location. However, we emphasise that the linear regression shown in Figure 4.3 should not be used to correct the Sh98 model on an event-by-event basis without careful consideration. This is particularly important for values of R_{Mod} smaller than those used in the linear regression (R_{Mod} < 7.4 R_E), where the prediction of R_{SC} becomes unrealistically small. For example, applying this correction to a modelled prediction of 6.6 R_E would imply that the magnetopause position is 3.9 R_E.

We propose that the systematic discrepancy between measurements and the model outside of 10.5 - 12 R_E result from two contributing factors: inaccuracies in the paraboloid Sh98 model shape and dynamics of magnetopause motion. Whether the influence of dynamic pressure or IMF on the magnetopause location contributed to differences between measurements and the model was also considered. While dynamic pressure and IMF did not appear to be responsible for systematic discrepancies between measured magnetopause location and the Sh98 model, we would recommend that the Sh98 model should only be used in the range of 0.5 nPa < D_p < 8 nPa and −15 nT < B_z < 10 nT. This recommendation is based on the distribution of median $\Delta R/R_{SC}$ in Figure 4.4, and the range of dynamic pressures and IMF magnitudes used to fit the Sh98 model (Section 2.3.1).

Inaccuracies in the paraboloid Sh98 model shape could explain why the magnetopause was consistently observed at larger radial distances than the model for R_{SC} > 12.0 R_E. That is, the magnetopause may be closer than the model near the nose, and further away near the flanks, which would be suggestive of a more flared magnetotail. Further inaccuracies in the paraboloid Sh98 model shape may arise from the non-axisymmetric shape of the magnetopause, that is, dawn-dusk asymmetries (Haaland et al., 2017) and indentations due to the magnetospheric cusp regions (Case & Wild, 2013). It must be noted that the calculation of $R_{0_{SC}}$ and ΔR_0 assumed that the shape of the Sh98 model, specifically the level of tail flaring, α, was correct. If a spacecraft crossing is at a large solar zenith angle (i.e., not near the magnetopause nose) this method of mapping to the subsolar point may introduce error in $R_{0_{SC}}$ and ΔR_0 if calculations of α are inaccurate.

The observed discrepancy between model and measurements whilst the magnetopause was compressed below 10.5 R_E may also be, in part, due to rapid solar wind fluctuations. Processes such as solar wind fluctuations would mean that the magnetopause location is not in equilibrium, as assumed by the Sh98 model. For example, an interplanetary shock will set the magnetopause in motion until it reaches an equilibrium position, analogously to a damped harmonic oscillator, and so an average magnetopause correction is not necessarily representative of event specific behaviour (Desai et al., 2021b; Freeman et al., 1995). Hence, any empirical parameterisation of the magnetopause should be used with extreme caution for these events.

The distance between the measured magnetopause and the modelled location was shown to vary under different geomagnetic conditions (Figure 4.5). We highlight that, for increasingly positive Sym-H, the magnetopause location was increasingly overestimated by the Sh98 model. This overestimation was up to a maximum median of 13% between 40 nT ≤ Sym-H ≤ 60 nT and maximum single event value of 42% at a Sym-H of 18 nT (Figure 4.5a). Periods of positive Sym-H correspond to the SSC phase of a geomagnetic storm (Figure 4.6). Hence, for increasingly large SSCs, the magnetopause location can be

expected to be significantly closer to the Earth than previously thought. Figure 4.6 showed a SEA of solar wind drivers during strongly positive Sym-H conditions associated with SSCs. The solar wind driver of strong positive increases of magnetopause compressions was found to show characteristics of fast forward shocks which were associated with magnetospheric compressions (Figure 4.6e). At maximum Sym-H, the magnetosphere was maximally compressed, and observations of the magnetopause were overestimated by 6% on average by the Sh98 magnetopause model (Figure 4.6f).

Statistical observations of the magnetopause location compared to the Sh98 model were corroborated by analysis of the St Patrick's day storm case study. This enabled the investigation of the time-dependent accuracy of model magnetopause motion during a radiation belt dropout event. We found that during more quiescent times, between 14 and 16 March 2013 before the geomagnetic storm, the observed and model magnetopause locations agreed. During storm times between 16 and 17 March 2013, the Sh98 model magnetopause standoff distance was rarely accurate compared to observed magnetopause crossings. Of the observed magnetopause standoff distances 85% were either greater than (40%) or less than (45%) the Sh98 magnetopause standoff by distances greater than the model uncertainty. From our measurements of the magnetopause, we calculated the equivalent dayside magnetopause to reach a minimum of 5.7 R_E, 0.4 R_E closer to the outer radiation belt than the Sh98 calculation. Figure 4.7d showed that the magnetopause compression was capable of directly shadowing the outer radiation belt. Indirect shadowing will also have played a role in this dropout event as ULF wave power was high during this period (Ma et al., 2018), transporting electrons at lower L-shells toward the compressed magnetopause, resulting in the entire outer radiation belt decreasing in flux by 2 orders of magnitude.

4.5.2 Implications for Radiation Belts

Solar wind pressure pulses and fast forward shocks are understood to be associated with radiation belt responses (e.g., Hietala et al., 2014; Kilpua et

al., 2019; Sibeck et al., 1989), which are usually attributed to shock-driven ULF waves which radially diffuse electrons toward the magnetopause (e.g., Claudepierre et al., 2010). For example, Morley et al. (2010b) showed results of a SEA where electron flux drops out at *L** as low as 4.5 in response to high-speed solar wind stream interface regions. By using the Sh98 model, the authors observed that the average magnetopause compression was to 8.5 R_E, concluding that rapid outward radial transport of electrons was required to explain the electron flux losses. The results presented in this chapter suggest that the magnetopause is compressed significantly closer to the radiation belts than the Sh98 model predicts during fast forward shocks, such as high-speed solar wind stream interfaces.

Figure 4.8 explores the use of a correction to the Sh98 model location for the 67 stream interface events which produce flux dropouts (Figure 2.2a), identified by Morley et al. (2010b). A SEA is performed for the stream interfaces in the same manner as Morley et al. (2010b), where t_0 is the time at which the interface reached the bow shock. Figure 4.8a shows a SEA of Sym-H during the stream interface events, and Figure 4.8b shows a SEA of the Sh98 subsolar magnetopause standoff (pink-purple colours) and corrected magnetopause standoff distances, R_{Cor} (blue colours). The correction to the Sh98 model is applied within ±12 hours of the maximum Sym-H value for each epoch. The subsolar standoff distance is either increased or decreased by a time-dependent factor, $\Delta R/R_{SC}$, according to the results presented in Figure 4.6f. For example, 5 hours after a Sym-H peak, $R_{0_{Mod}}$ is decreased by 5%.

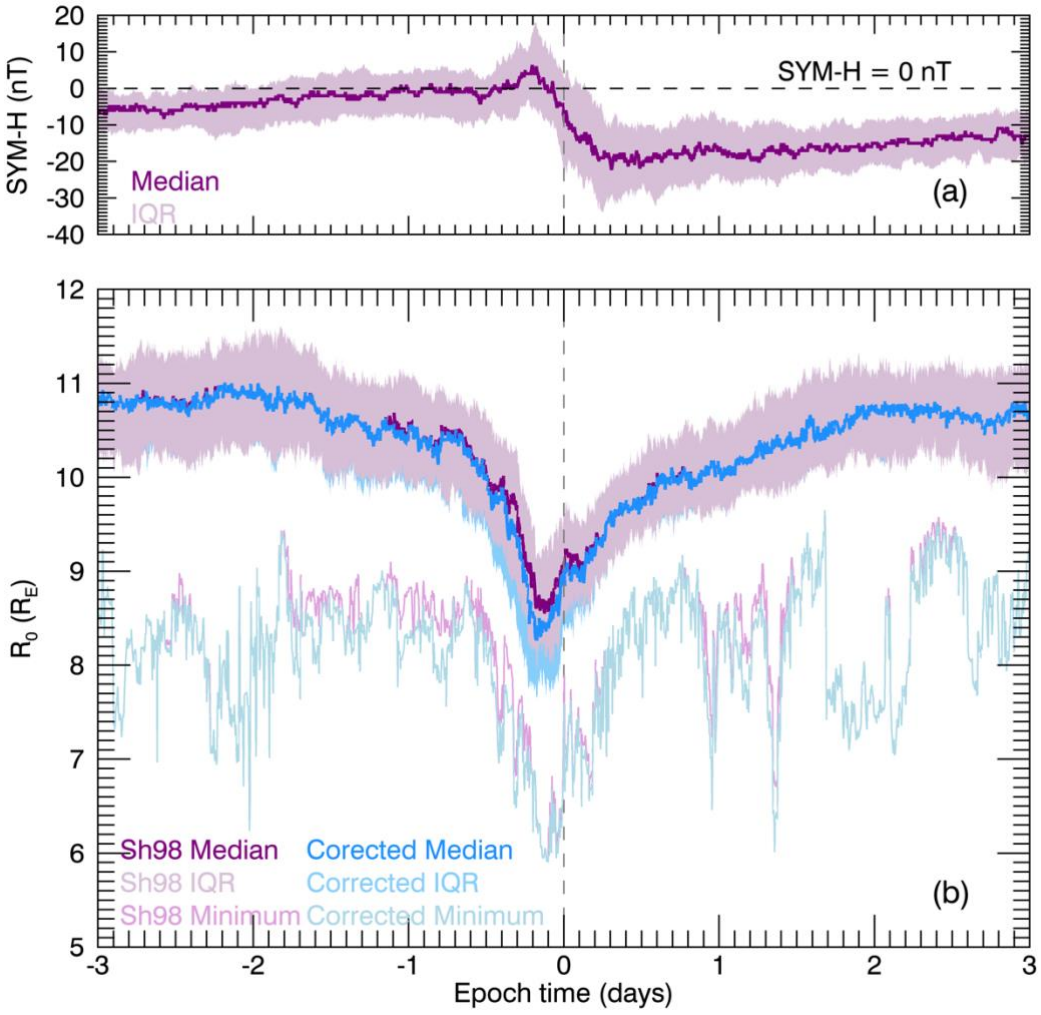

Figure 4.8 Superposed epoch analysis of 67 high-speed solar wind stream interface events identified by Morley et al. (2010b). (a) The dark purple line shows median Sym-H index and the light purple-shaded region shows the interquartile range; (b) The dark purple line shows the median Shue et al. (1998) subsolar standoff distance of the magnetopause, $R_{0_{Mod}}$, the light purple-shaded area shows the interquartile range and the light pink line shows the minimum standoff distance of $R_{0_{Mod}}$ at a given epoch time. The dark blue line shows the median corrected magnetopause standoff distance, the shaded blue area shows the interquartile range, and the light blue line shows the minimum standoff distance, R_{Cor}. The correction factor is based on variations in $\Delta R/R_{SC}$ associated with a peak in Sym-H index (Figure 4.6f) (Staples et al., 2020).

In addition to the magnetopause location averaged across the epochs, the interquartile range and the minimum standoff distance are show in Figure 4.8b. By including these statistics, we demonstrate the variability of modelled magnetopause location across the events: the Sh98 magnetopause became compressed to 8.5 R_E on average, with lower quartile of 8 R_E, but more

extreme events were compressed as low as 6 R_E. This shows that, at least in some circumstances, direct magnetopause shadowing of the outer belt is predicted to occur by the Sh98 model following several stream interfaces Moreover, when a correction is applied to the modelled standoff distance, the estimated average magnetopause location is compressed to 8.2 R_E, with a lower quartile value of 7.6 R_E, and the minimum magnetopause compression during all the epochs was 5.9 R_E. Using a correction to account for systematic errors in the Sh98 model under compressed conditions would predict magnetopause compressions capable of depleting the outer radiation belt more often, and to a greater extent. However, Figure 4.8 showed that the change in magnetopause location when a correction is applied was no greater than 1 R_E, the error which was recommended earlier in this discussion. Therefore, it is more likely that the variability in magnetopause location due to event specific behaviour will affect the observed accuracy to a greater extent than systematic errors in the Sh98 model location.

We now discuss several additional aspects concerning how our analysis might be affected by both small-scale transitory structures in the magnetopause and by large-scale motion of the magnetopause. First, models such as the Sh98 model aim to characterise the global shape and location of the magnetopause, but in reality, the magnetopause contains smaller scale structures. For example, Kelvin-Helmholtz waves occur at the magnetopause flanks due to an instability created by a velocity shear at the magnetopause boundary layer (e.g., Hasegawa et al., 2004; Pu & Kivelson, 1983). Hot flow anomalies in the solar wind are known to decrease pressure in regions of the magnetosheath for short periods of time (~7 min) allowing the magnetopause to bulge outward by up to 5 R_E near the hot flow anomaly core (Archer et al., 2014; Jacobsen et al., 2009; Sibeck et al., 1999). Conversely, fast magnetosheath jets can produce local magnetopause indentations of up to ~1–2 R_E depth if a jet penetrates to the magnetopause (Amata et al., 2011; Hietala et al., 2014; Plaschke et al., 2016; Shue et al., 2009). Surface waves on the magnetopause have also been observed as a result of impinging magnetosheath jets (Amata et al., 2011; Plaschke et al., 2009b). If a magnetopause crossing takes place in a location where the magnetopause is locally perturbed, then the crossing

may not represent the global magnetopause location, if such a function exists. Not only do these structures add uncertainty to the estimation of magnetopause location, they also potentially affect the dynamics of magnetospheric plasma. Both Kelvin-Helmholtz waves and magnetospheric jets are known drivers of ULF waves (Archer et al., 2013; Chen & Hasegawa, 1974; Claudepierre et al., 2008; Hughes, 1994; Southwood, 1974), which act to diffuse magnetospheric plasma. Earthward perturbations of the magnetopause due to fast magnetosheath jets could intersect radiation belt electron drift paths. What is more, local magnetopause compressions due to fast magnetosheath jets only occur for tens of seconds up to 3 min (Archer et al., 2012). If a magnetosheath jet is sustained for several minutes near the subsolar magnetopause, it could certainly contribute toward a substantial loss of the ultra-relativistic electron population, which have drift periods of ~ 5 minutes. However, electron losses in the outer radiation belt have not yet been observed directly in connection with magnetosheath jets (Plaschke et al., 2018). We expect global changes in magnetopause location to largely govern radiation belt dropout events as most of the relativistic electron population have drift orbits longer than the timescale of a magnetosheath jet.

Secondly, in this analysis only the innermost of a sequence of magnetopause crossings is used to represent the position of the magnetopause. Measured magnetopause crossings will primarily be due to the magnetopause passing over a quasi-stationary spacecraft, and hence the minimum magnetopause location will lie somewhere inside the spacecraft location. In part, this is addressed by the Sh98 model since the innermost magnetopause crossing was taken to be the minimum standoff distance in their model. However, during a large compression by an interplanetary shock, or local compression due to a fast magnetosheath jet, the minimum magnetopause crossing may not reflect the minimum magnetopause location. Moreover, any interplanetary shock that leads to an SSC will set the magnetopause in motion until it reaches an equilibrium position, and so an average magnetopause correction is not necessarily representative of specific event behaviour (Desai et al., 2021b ; Freeman et al., 1995). Freeman et al. (1995) analysed the oscillation of the magnetopause due to changes in dynamic pressure. In their idealised system,

the magnetopause oscillation was highly damped with a natural eigen-period of ~7 min. Hence, it is certainly possible that electrons with drift periods of ~5 min could intersect the oscillating magnetopause location when the magnetopause is undergoing this damped harmonic motion before reaching equilibrium. This would involve the total loss of ultra-relativistic electrons but only a small disturbance to the medium energy radiation belt electron population - much like the reports of ultra-relativistic electron losses due to EMIC wave-driven precipitation.

Ideally, continuous observations of the magnetopause location would elucidate the time-dependent response of the magnetopause to variable solar wind driving and geomagnetic storms. These observations could be conducted by the Solar Wind-Magnetosphere-Ionosphere Link Explorer, or “SMILE,” a small class science mission which is under development between the European Space Agency and Chinese Academy of Sciences (Raab et al., 2016). This novel experiment will use observations of soft X-ray emissions from charge exchange interactions in the Earth's magnetosheath, from which a three-dimensional magnetopause location can be inferred. The SMILE mission provides a unique opportunity to investigate the role of the global magnetopause on radiation belt dynamics.

Chapter 5 Resolving Magnetopause Shadowing Using Multi-Mission Measurements of Phase Space Density

The results of this chapter have been submitted to the *Journal of Geophysical Research*: *Space Physics.* The submitted manuscript is archived, publicly available via:

Staples, F.A., Kellerman, A.C., Murphy, K.R., Rae, I.J., Sandhu, J.K. and Forsyth, C., 2021. Resolving Magnetopause Shadowing Using Multi-Mission Measurements of Phase Space Density. Washington: American Geophysical Union. DOI:10.1002/essoar.10506455.1.

5.1 Introduction

Chapter 4 discussed the location of the magnetopause with respect to the outer radiation belt. The statistical parameterisation of the magnetopause was analysed to determine its accuracy whilst the magnetopause is compressed. It was concluded that, though the compressed magnetopause was observed systematically closer the outer radiation belt than the model predicted, the variability of event specific behaviour when the magnetopause is suddenly compressed may lead to misinterpretations of radiation belt dynamics. It is therefore important to measure the magnetopause in addition to using model parameterisations for such events.

In this chapter we analyse event specific interactions between the magnetopause and the outer radiation belt during a case study in early September 2017. During this event, a series of CMEs and interplanetary shocks interacted with the Earth's magnetosphere, resulting in strong magnetopause compression and a compound geomagnetic storm, with a radiation belt response. Both measurements of the magnetopause and phase space density observations are used to interpret a dropout in electron flux during the main phase of the geomagnetic storm.

Due to the level of magnetospheric compression observed during this event, it was important to use PSD observations of the radiation belts to discount adiabatic effects. Moreover, PSD observations allow the specific loss

mechanisms to be identified by observing the characteristics of electron dynamics. The necessity of using multi-satellite observations of PSD to resolve electron dynamics during both the flux dropout and the latter acceleration phase is discussed.

5.2 Case Study Overview: September 2017

Between the 6 - 10 of September 2017 a complex sequence of interacting interplanetary shocks and coronal mass ejecta (CME) (Scolini et al., 2020; Shen et al., 2018; Werner et al., 2019) drove an equally complex magnetospheric and radiation belt response. Figure 5.1 summarises the solar wind, IMF, magnetospheric parameters, and radiation belt electron flux over this case study. The times of the interplanetary shocks and CMEs, classified by Shen et al. (2018), are displayed by the red lines and blue shaded areas respectively. Measurements of electron flux at 0.8 MeV and 2 MeV energies are taken by the combined X-ray dosimeter on board LANL GPS Navstar satellites (Tuszewski et al., 2004). As the orbits of GPS satellites are highly inclined, measurements of flux at L shells $\gtrsim 5.5$ are taken at high magnetic latitudes where fewer electrons complete their bounce orbit, and therefore flux decreases rapidly with L shell.

The arrival of the first interplanetary shock is indicated by an increase in solar wind speed (Figure 5.1b) and dynamic pressure (Figure 5.1c), by 200 km s^{-1} and 9 nPa respectively, and an increase in IMF strength by 15 nT (Figure 5.1a). At 01:00 UT on 7 September 2017, the increased dynamic pressure resulted in a compression of the modelled magnetopause from 11.5 R_E to 8 R_E (Figure 5.1d), and an increase in Sym-H index from ~ 10 nT to 50 nT (Figure 5.1e). Increased Sym-H will be due to a combination of enhanced as magnetopause currents by the increased solar wind number density (not shown) and compression of the magnetopause towards Earth. Both 0.8 MeV and 2 MeV flux increased by a factor of ~ 2 at all L shells < 5 (Figure 5.1f-g). When Sym-H index returned to the pre-storm value of ~ 10 nT, so did electron flux at both energies.

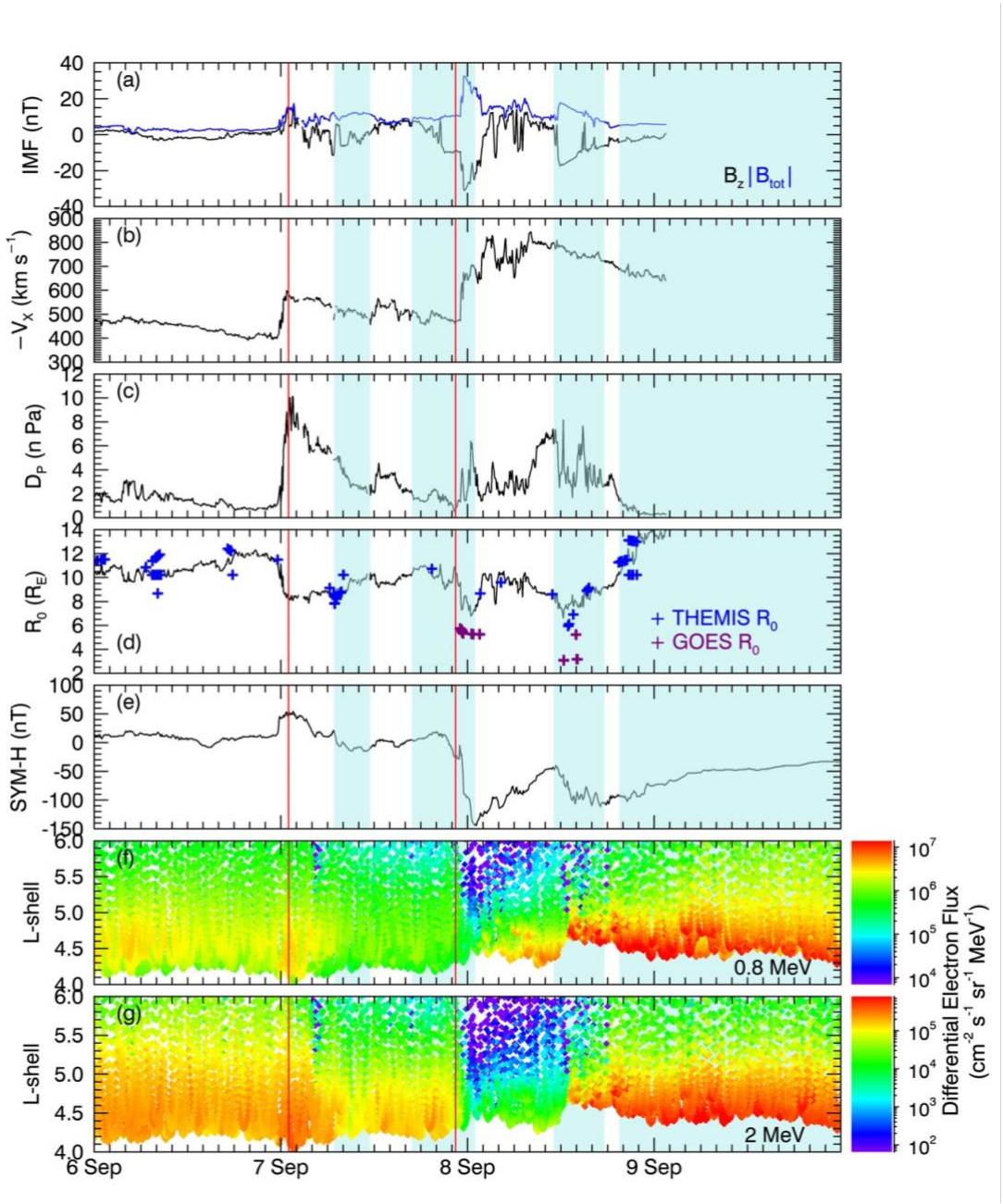

Figure 5.1 The solar wind and magnetospheric conditions for the 6 - 10 September 2017; (a) total IMF (blue) and the north-south component of IMF B_z (black); (b) solar wind speed; (c) solar wind dynamic pressure; (d) subsolar standoff distance of the magnetopause, calculated by the Shue et al. (1998) model (black line), and equivalent subsolar standoff distance measured by THEMIS (blue) and GOES (purple) spacecraft; (e) Sym-H index; differential electron flux as a function of L shell, measured by GPS satellites at (f) 0.8 MeV and (g) 2 MeV. Interplanetary shocks are indicated by red lines and blue shaded areas show when there are CME ejecta as stated by Shen et al. (2018) (Staples et al., in review).

The second CME arrived at 16:50 UT 7 September and lasted until 01:00 UT 8 September. A second interplanetary shock arrived at 22:28 UT 7 September, propagating through the second CME. This shock region was associated with

the third CME which propagated at much faster speeds than the second CME, thus creating an interaction region within the second CME (Scolini et al., 2020; Shen et al., 2018). When the second CME arrived at 16:50 UT 7 September, solar wind speed and pressure continued to decrease gradually (Figure 5.1b & c respectively), and IMF B_z decreased from 8 nT to –10 nT (Figure 5.1a). Interestingly, the modelled magnetopause did not change location significantly (Figure 1d), there was no geomagnetic activity (Figure 5.1e), and no change to electron fluxes (Figure 5.1f-g). However, when the interplanetary shock arrived, IMF field strength suddenly increased from 10 nT to ~35 nT and B_z decreased further from –10 nT to –32 nT. Solar wind speed increased from 500 km s^{-1} to 700 km s^{-1}, and dynamic pressure increased from 1 nPa to 4 nPa. The modelled magnetopause was compressed within geostationary orbit (~ 6.6 R_E) where there were multiple magnetopause crossings by GOES 13. The Sh98 magnetopause model calculated a minimum standoff distance of 7 R_E, whereas the equivalent standoff distance calculated for the GOES magnetopause crossings is 5.5 R_E. The Sym-H index decreased from 0 nT to a minimum of –142 nT following the shock. The 0.8 MeV electron flux decreased by a factor of ~ 100 across L shells > 5 and ~ 10 for L shells < 5. Similarly, 2 MeV electron flux also decreased following the interplanetary shock, but by a factor of ~ 1000 for L shells > 5 and a factor of ~ 100 at L shells < 5. At both energies, this dropout in flux started at the highest L shells first, followed by the lower L shells over a 3-hour period.

Following the second CME, the solar wind speed remained high at 800 km s^{-1} (Figure 5.1b), whilst dynamic pressure fluctuated, increasing from 1 nPa to 6 nPa (Figure 5.1c). IMF B_z also fluctuated rapidly between –10 nT and 10 nT (Figure 5.1a). Sym-H began to increase (Figure 5.1e), indicating the start of the storm recovery phase. The magnetopause expanded outwards to ~ 10 R_E, as measured by THEMIS (Figure 5.1d). Electron flux increased across both energies; 0.8 MeV flux increased by a factor of $\gtrsim$ 10, first limited to L shells < 4.5 but slowly expanding to all L shells prior to the third CME arrival (Figure 5.1f). The 2 MeV electrons showed a similar increase in flux, though the rate of increase was slower (Figure 5.1g).

The third CME arrived on 8 September at 11:05 UT and lasted until 17:38 UT. Solar wind speed remained high at 800 km s^{-1}, decreasing to 700 km s^{-1} through the ejecta (Figure 5.1b), and solar wind pressure fluctuated rapidly between 2 and 8 nPa (Figure 5.1c). The IMF strength suddenly increased by 8 nT, and B_z rapidly decreased to –10 nT, and both field strength and B_z slowly returned to ~ 0 nT by the end of the CME (Figure 5.1a). Sym-H index decreased from –50 nT to a minimum of –120 nT (Figure 5.1e). The magnetopause was compressed within geostationary orbit, as measured by GOES 13 and 15 magnetopause crossings (Figure 5.1f). The Sh98 model is compressed to 7 R_E at the subsolar point, and the equivalent subsolar magnetopause calculated from GOES 13 crossing was 5.5 R_E, and 3 R_E for GOES 15. In actuality, the magnetopause is not compressed to this level at the subsolar point; Van Allen Probe A is at apogee near noon at this time and does not cross the magnetopause. Simultaneous to the compression of the magnetopause, there is a sudden increase in flux for L shells < 5; the 0.8 MeV increased by a factor of ~ 10 and 2 MeV flux increased by a factor of ~ 100 (Figure 1f-g). At L shells > 5 there is some reduction in flux, at both energies, compared to the flux at the beginning of the third CME.

The inconsistency between the equivalent magnetopause calculations is due to inaccuracy in the shape of the Sh98 model. The equivalent subsolar magnetopause is calculated from spacecraft crossings at any azimuth using Equation **4**.**1**, which assumes that the tail flaring angle of the Sh98 model is correct. Figure 5.2 demonstrates how inaccuracies arise from this assumption by illustrating two magnetopause locations from geostationary crossings, shown in orange, assuming the same shape of the magnetopause. The two estimations of the magnetopause do not agree at the subsolar point, indicating that the tail flaring angle is incorrect. The black magnetopause curve indicates the “actual” magnetopause location in this scenario which crosses both spacecraft. Noting that spacecraft at higher azimuth produce greater inaccuracies in the equivalent subsolar magnetopause estimation. Additionally, the shock normal to the magnetopause may affect the minimum location of the magnetopause, which is assumed to be at the aberrated subsolar point by the Sh98 model, by producing asymmetric compressions of

the magnetopause (see Samsonov et al., 2015). Because the magnetopause is measured by both GOES 13 and 15, we can at least state with certainty that the magnetopause was located somewhere within geostationary orbit (~ 6.6 R_E).

The fourth CME ejecta arrived at 19:30 UT 8 September and continued until 00:00 UT 11 September. Solar wind conditions are no longer recorded in the 5-minute resolution OMNI-database during this period (Figure 5.1a-c), the source of this data gap is under investigation (Redmon et al., 2018). The magnetopause expanded to 13.5 R_E, as measured by THEMIS on 8 September (Figure 5.1d). For the remainder of the period, electron flux at both energies, and all L shells, continued to increase to values ~ 10 times greater than the pre-storm flux (Figure 5.1f-g). The SYM-H index slowly increased during the recovery phase of the storm (Figure 5.1e).

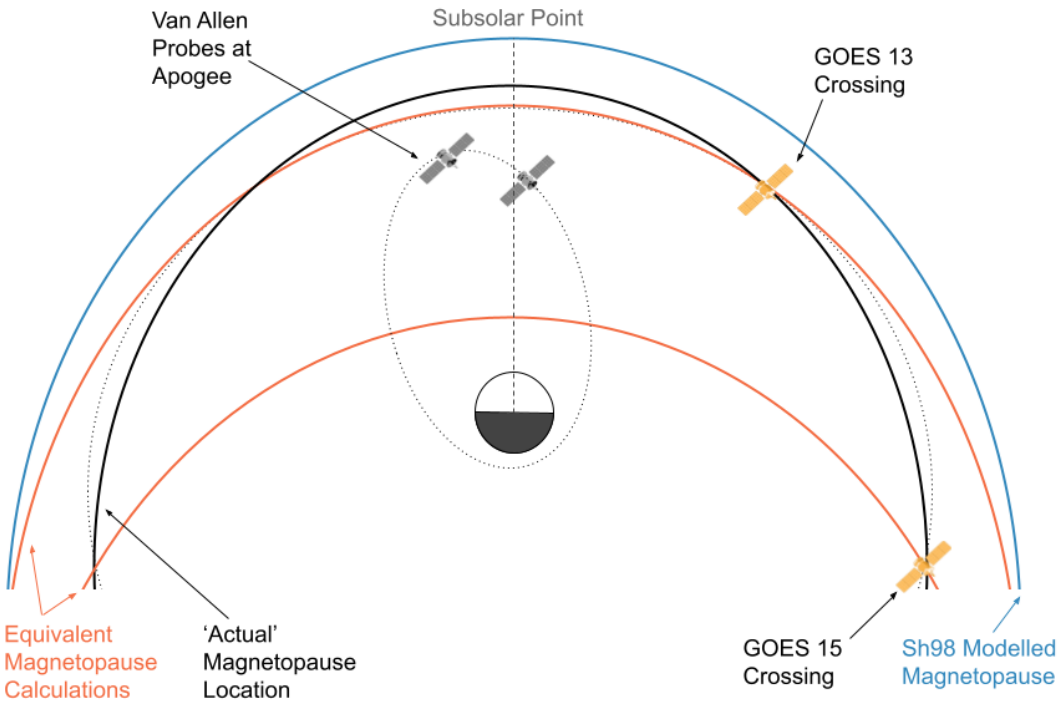

Figure 5.2 Diagram visualising the equivalent magnetopause calculated from GOES crossings on 14 September by assuming the Sh98 model tail flaring angle is correct. Sh98 modelled magnetopause is shown in blue, the equivalent magnetopause from GOES magnetopause crossings is shown in orange, the 'actual' magnetopause with a different tail flaring angle is shown in black.

5.3 Phase Space Density Observations

Figure 5.3 shows PSD of electrons measured by Van Allen Probes, THEMIS, MMS, GOES, and GPS. Full computation of PSD in adiabatic coordinates, and method used to intercalibrate multi-satellite data, are described in Section 3.4. The adiabatic coordinates differentiate populations of electrons based upon their periodic motions (gyro-motion, bounce motion, and drift motion) by specifying invariant quantities for each motion i.e., the canonical momenta. For a given location in the magnetic field, μ is dependent upon particle energy and pitch angle, K and L^* are dependent upon pitch angle. Note that in this chapter, specific populations of electrons across L^* are represented by PSD measurements within specified ranges of μ (± 2.5%) and K (± 25%). While ± 25% is a seemingly large range of pitch angle, this approximately corresponds to equatorial pitch angles between ~ 40^o – 70^o during the pre-storm period, or between ~ 30^o – 50^o at minimum Sym-H.

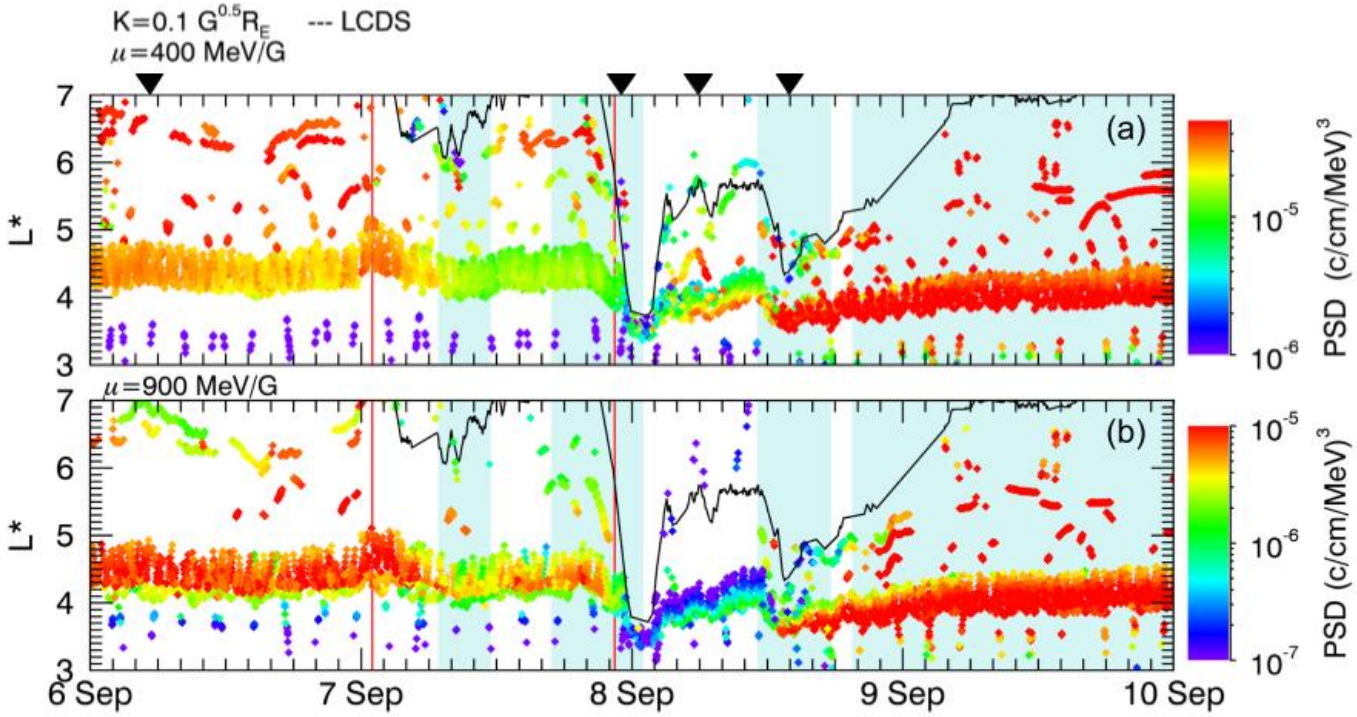

Figure 5.3 Phase Space Density shown as a function of *L over time as measured by multiple spacecraft for 6 - 10 September 2017; panels show PSD values where *K* ~ 0.1 $G^{0.5}$ R_E and μ is (a) ~ 400 MeV/G; (b) ~ 900 MeV/G. Interplanetary shocks are indicated by red lines, and blue shaded areas show when there are CMEs, as stated by Shen et al. (2018). The LCDS for K = 0.1 $G^{0.5}$ R_E is overplotted in the black solid line on all three panels. The black triangles indicate the time periods depicted in Figure 5.4 (Staples et al., in review).**

Figure 5.3 shows the evolution of PSD as a function of L^* where $K \sim 0.1\ G^{0.5}R_E$ and $\mu \sim 400$ MeV/G and 900 MeV/G (panels a and b respectively). As with Figure 5.1, solar wind features are indicated by the red lines (interplanetary shocks) and blue shaded regions (CMEs). The LCDS, plotted by the black line, was computed by numerically computing the maximum L^* at which particles of a given pitch angle follow a closed drift orbit in the T01s magnetic external field model. The L^* location of the LCDS was then interpolated for a constant value of $K = 0.1\ G^{0.5}R_E$.

At the beginning of 6 September, PSD at $\mu = 400$ MeV/G increased rapidly with increasing L^* from < 1 $x10^{-6}$ at $L^* = 3$ to ~2 $x10^{-5}$ $(c/cm/MeV)^3$ at $L^* = 4$, then increased at a slower rate with increasing $L^* > 4$, up to 7 $x10^{-5}$ $(c/cm/MeV)^3$ at $L^* = 6.5$. PSD at $\mu = 900$ MeV/G similarly increased rapidly with increasing L^*, from ~ 1 $x10^{-7}$ to 1 $x10^{-5}$ $(c/cm/MeV)^3$ at $L^* = 4.2$ but decreased with increasing $L^* > 4.2$ down to 2 x 10^{-6} $(c/cm/MeV)^3$ at $L^* = 6.7$. The LCDS was beyond L^* of 7, so was not plotted for this period. Changes in PSD across L^* approximately correspond to radial distance since observations are for a specified K value (or pitch angle), accounting for the effects of drift shell splitting. Therefore, on 6 September, PSD shows that the outer radiation belt particles were largely located at $L^* > 4$, with $\mu = 400$ MeV/G electrons monotonically increasing with L^* (~radial distance) and PSD of $\mu = 900$ MeV/G electrons peaking at $L^* = 4.2$.

When the first interplanetary shock reached the magnetosphere, spacecraft measurements showed the location of L^* increased briefly. This indicated that drift paths of electrons moved Earthwards with respect to spacecraft orbits (Figure 5.3 - red line). There were no large changes to the PSD distribution in L^* for $\mu = 900$ MeV/G, however the PSD of the 400 MeV/G population doubled. As L^* returned to the pre-shock location, the increased PSD returned to the level prior to the interplanetary shock arrival. Simultaneously the LCDS moved inwards to 6.3 L^*.

When the first CME reached the magnetosphere at 06:50 UT on 07 September, the LCDS moved inwards to $L^* \sim 6$. PSD decreased across all μ,

though these decreases in PSD were not uniform across L^* and energies. PSD of the μ = 400 MeV/G population decreased by half between 4 < L^* < 5, and by a factor of ~ 3 at L^* > 5. PSD of electrons with μ = 900 MeV/G decreased by a factor of ~ 5 between 4 < L^* < 5 and decreased by a factor of ~ 3 at L^* > 5.

The second interplanetary shock arrived during the second CME. In response, the LCDS was compressed to L^* = 3.8 for 2 hours. The PSD at L^* > 3.8 could therefore not be expressed in adiabatic coordinates during this time, so we assume these particles no longer followed closed drift paths. At locations within the LCDS, spacecraft measurements showed the computation of L^* decreased. PSD at a given L^* did not change significantly for μ = 900 MeV/G during this period. PSD where μ = 400 MeV/G increased by a factor of ~ 2 at L^* > 3.2 compared to corresponding measurements prior to the compression.

During the interval between the second and third CME, the LCDS expanded to higher L^* of ~ 5.5. In tandem, the L^* location of spacecraft measurements moved outwards (so electron drift paths move inwards with respect to spacecraft orbits). Initially there was little to no change in PSD for μ = 400 MeV/G at a given L^*, then PSD increased by a factor of 10 over the interval for L^* ~ 4. At μ = 900 MeV/G, PSD decreased by a factor of 10 compared to PSD prior to the interplanetary shock. Through the remainder of the interval PSD increased by a factor of ~10 at L^* ~ 4. Note that the latter increase in PSD for μ = 900 MeV/G is limited to L^* ~ 4, and PSD at L^* > 4 did not change.

Upon the arrival of the third CME, the LCDS was compressed a second time to L^* = 4.4. Simultaneously, PSD at both μ increased by a factor of 10 at L^* = 3.6, and PSD decreased with increasing L^*. As the LCDS began to expand outwards in L^*, PSD began to increase at all L^*. When the fourth CME arrived, the LCDS continued to expand to higher L^*, and PSD universally increased at all L^* and μ shown in Figure 5.3.

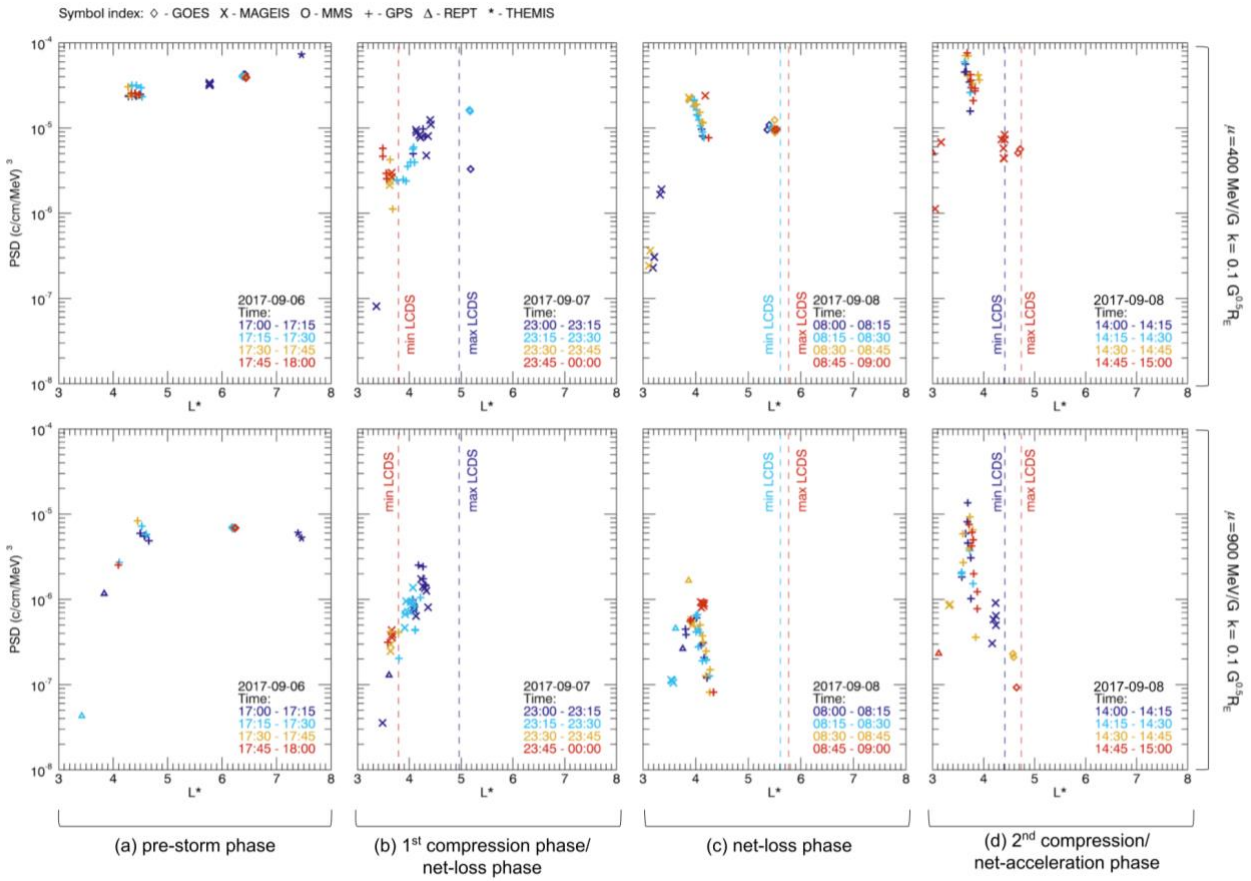

Figure 5.4 PSD profiles in *L for μ of 400 MeV/G (top row) and 900 MeV/G (bottom row) with $K = 0.1\ G^{0.5}R_E$. Each column (a-d) shows a single hour period through different phases of the storm. Symbol colours indicate when measurements were taken within the hour period. Symbol shapes (see legend) identify the spacecraft of each measurement. Dotted lines show the minimum and maximum *L** of the LCDS (Staples et al., in review).**

To evaluate the radial evolution of PSD profiles in further detail, four different 1-hour time periods were selected to represent the stages of a direct magnetopause shadowing induced dropout described by Turner et al. (2012b) (depicted in Figure 2.4). Data availability, storm phase, and coincident magnetopause crossings are considered when choosing the intervals. Figure 5.4 shows the PSD profiles as a function of L* for the chosen periods which correspond to (a) pre-storm, (b) first compressive/net-loss phase, (c) net-loss phase, and (d) second compressive/net-acceleration phase. Periods (b) and (c) coincide with geostationary magnetopause crossings. Within the hour time periods 15-minute intervals are identified by symbol colour so that changes to PSD and the LCDS within the hour can be identified. To give the four 1-hour time periods in the context of the storm, the four intervals are indicated by black triangles in Figure 5.3.

Prior to the arrival of the first interplanetary shock, Figure 5.4a shows PSD for electrons with μ = 400 MeV/G increased with increasing L^*, reaching maximum measurement of 8 x10^{-5} (c/cm/MeV)^3 at L^*= 7.4. For electrons with μ = 900 MeV/G, PSD increased rapidly between 3 < L^* < 4.2 and reached maximum PSD of 1 x10^{-5} (c/cm/MeV)^3 at L^* = 4.2, and PSD decreased slightly with increasing L^*. During this period, the LCDS was located at L^* > 8.

During the first compression/net-loss phase (Figure 5.4b) the LCDS was located at L^* = 5 at the beginning of the hour, then is further compressed to L^* = 3.8 by the end of the interval. PSD profiles at all μ show a clear difference between the first half hour of the interval and the latter half. In the first half hour, PSD at all μ values had a positive gradient with increasing L^*, and PSD was measured at a maximum near the maximum LCDS for the interval. In the latter half hour PSD measurements are limited to L^* < 3.8. For μ = 900 MeV/G, PSD measured within the minimum LCDS did not substantially change through the hour. PSD for μ = 400 MeV/G electrons was also measured within the minimum LCDS but increased by a factor > 2 through the second half hour.

Later during the net-loss phase (Figure 5.4c), the LCDS was located at L^*~ 5.7 and remained there throughout the interval. Measurements taken through the hour were co-located indicating no substantial changes in PSD profiles through

the interval. For both μ, the PSD peaked at $L^* = 3.8$, which was the location of minimum LCDS during the compressive phase. PSD had also increased by a factor of 10 or more for $L^* < 3.8$. At $L^* > 3.8$, PSD for $\mu = 400$ MeV/G electrons decreased with increasing L^* until $L^* = 4.2$, and PSD measurements taken by GOES at $L^* = 5.5$ were similar values to those at $L^* = 4.2$. PSD for $\mu = 900$ MeV/G electrons had a strong negative gradient with increasing $L^* > 3.8$. PSD distributions presented during this phase are characteristic of direct electron losses to the magnetopause at $L^* > 3.8$, which occurred during the LCDS compression (Figure 5.4b), and subsequent radial diffusion after the magnetopause expanded (Figure 5.4c).

During the secondary compression phase (Figure 5.4d) the LCDS was compressed at $L^* = 4.4$ towards the beginning of the phase and expanded slightly to $L^* = 4.8$ by the end of the hour. PSD measurements taken throughout the hour were constant for a given L^*, showing that there were no substantial changes to PSD within the hour. For both μ, there were peaks in PSD at $L^* = 3.7$ with an increased PSD compared to all previous intervals (Figure 5.4a-c). PSD at $L^* < 3.7$ also increased by a factor ≥ 10 compared to the previous net-loss interval (Figure 5.4c) at both μ. This growing peak in PSD, and increased PSD at lower L^*, indicates localised electron acceleration processes occurring at $L^* = 3.7$, with radial diffusion of electrons away from this location. PSD at $L^* > 3.7$ shows that there was a strong negative gradient as PSD decreased rapidly with increasing L^* for both μ. PSD at these higher L^* remained relatively stable compared to the previous net-loss interval, though there were few measurements for comparison at common L^* between the two intervals. At $L^* > 4$, PSD universally decreased during the second compression compared to the pre-storm phase; for $\mu = 400$ MeV/G, PSD was up to 10 times less than the pre-storm interval, for $\mu = 900$ MeV/G PSD was up to 1000 times less than the pre-storm interval. In other words, despite the secondary compression phase occurring during the acceleration phase of this geomagnetic storm, losses at $L^* > 4$ mean that the PSD was not yet replenished to its pre-storm values.

Finally, we evaluated whether using the multi-satellite dataset is a beneficial addition to the Van Allen Probe data. Figure 5.5 shows PSD profiles over *L** using only Van Allen probe data. The time at which each profile was measured is indicated by the colour, with 1-hour resolution. Figure 5.5 intervals a – d correspond to the intervals shown in Figure 5.4. To maximize data coverage across *L**; (i) a larger range of μ is used in Figure 5.5 than was used for multi-satellite data in Figure 5.3 and Figure 5.4, (ii) to account for the orbital configuration of the Van Allen Probes, the pre-storm interval (Figure 5.5a) at 20 UT on 6 September is three hours later than Figure 5.4a, (iii) and the net-loss interval (Figure 5.5c) was extended to two hours at 8 - 10 UT on 8 September. The range of *K* is the same ($0.075 < K < 0.125$ $G^{0.5}R_E$), and data is interpolated across *L*.*

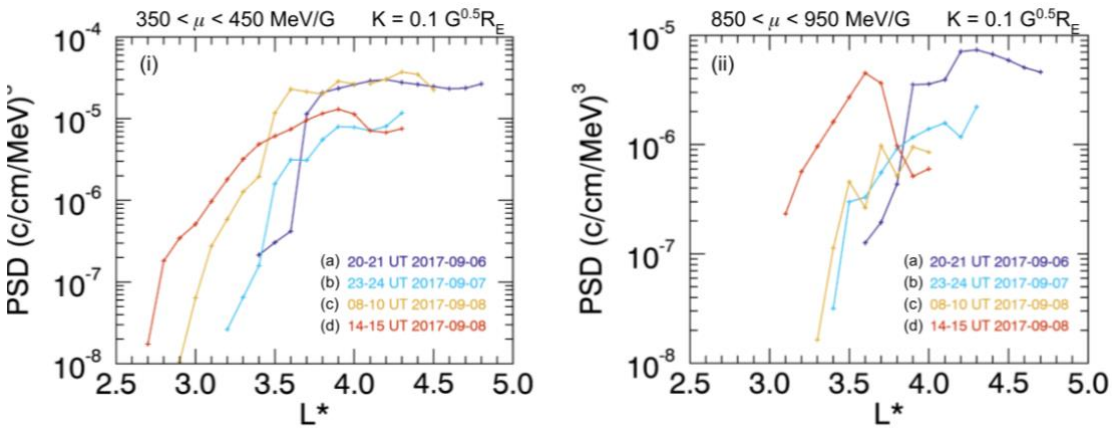

Figure 5.5 PSD profiles in *L for (i) $350 < \mu < 450$ MeV/G and (ii) $850 < \mu < 950$ MeV/G with $K = 0.1$ $G^{0.5}R_E$, as measured by the Van Allen Probes. Profiles a, b, and d show hour long time periods, c shows a 2-hour long period, through different phases of the storm. PSD measurements within the specified μ range is linearly interpolated across *L** for each hour interval with a resolution of L* = 0.1 (Staples et al., in review).**

The development of PSD at $350 < \mu < 450$ MeV/G measured by the Van Allen Probes (Figure 5.5) show similar features between intervals Figure 5.5a - c to observations of PSD at μ = 400 MeV/G using the multi-satellite database (Figure 5.4). During the final interval (Figure 5.5d) the PSD peak, at $L^* = 3.7$ observed by multi-satellite data (Figure 3d), was not observed since there were no Van Allen observations between $3.2 < L^* < 4.1$ at the specified range of μ (350 - 450 MeV/G).

The development of PSD at 850 < μ < 950 MeV/G measured by the Van Allen Probes (Figure 5.5) also showed similar features between intervals Figure 5.5a, b, and d, to observations of PSD at μ = 900 MeV/G using the multi-satellite database (Figure 5.4a,b,d). During the net-loss phase (Figure 5.5c), the Van Allen Probes did not measure the negative PSD gradient at L* > 3.8 observed by multi-satellite data (Figure 5.4c) since there were no Van Allen observations at L^* > 4 at the specified range of μ (850 - 950 MeV/G).

Comparing Van Allen Probe observations shown in Figure 5.5 to the multi-mission observations shown in Figure 5.4, the dynamics of radiation belt electrons could be misinterpreted if only Van Allen Probe data were available. Specifically, at μ ~ 400 MeV/G Van Allen probes did not have sufficient resolution across L^* to measure a growing peak in PSD, so radiation belt enhancement could wrongly be attributed to radial diffusion. Whereas at μ ~ 900 MeV/G, the negative gradient in PSD created by magnetopause shadowing is not observable during the dropout as measurements were limited to L^* < 3.8, so the stages of magnetopause shadowing were not observable.

5.4 Discussion

This chapter presented an overview of the outer electron radiation belt response to a sequence of interacting CMEs and interplanetary shocks propagating through the solar wind in early September 2017. Spacecraft crossing of the magnetopause and multi-mission observations of relativistic electrons were used to evaluate the role of magnetopause shadowing in producing changes to electron flux.

Between 7 - 10 September there were two interplanetary shocks and four separate CMEs propagating through the solar wind. The solar wind characteristics of this event have already been studied in detail (e.g., Scolini et al., 2020; Shen et al., 2018; Werner et al., 2019), and so here focus is given to the relativistic electron response to these drivers. There was a complex response in electron flux at 0.8 MeV and 2.0 MeV energies corresponding to each interplanetary shock and CME. Most flux changes corresponded to

changes in measured PSD, indicating that the electron flux response to solar wind driving were largely due to non-adiabatic processes.

Not all changes in electron flux were due to non-adiabatic processes. Specifically, in response to the second interplanetary shock, flux measured by GPS satellites decreased by orders of magnitude at all L shells. Corresponding PSD measurements showed that, whilst electrons were irreversibly lost at high L^* where drift paths were intersected by the LCDS, there were initially no changes to PSD measured below $L^* = 3.8$. Instead, computations of PSD in adiabatic coordinates showed that GPS satellites measured electrons at different L^*, i.e., electron drift paths moved radially outwards with respect to GPS orbits. Therefore, GPS satellites measured a different population of electrons at higher L^*, which appeared as a decrease in the measured electron flux on all L-shells. This shows why it is important to consider electron measurements in adiabatic coordinates, rather than flux alone.

Profiles of PSD as a function of L^* at four 1-hour time intervals in Figure 5.4, were chosen to closely correspond to the four intervals depicted in Figure 2 of Turner et al. (2012b) (shown in Figure 2.4). The first interval (Figure 5.4a) at 17:00 –18:00 UT on 6 September showed the pre-storm distribution of PSD which either increased monotonically with increasing L^* (μ = 400 MeV/G) or reached a peak PSD at $L^* = 4.2$ (μ = 900 MeV/G). The second interval (Figure 5.4b) showed PSD profiles during a high-pressure phase at 23:00 UT 7 September to 00:00 UT 8 September, during which the magnetopause was measured by geostationary satellites. The LCDS moved towards Earth from $L^* = 5$ to $L^* = 3.8$ during the hour. When the evolution of PSD within the hour was considered, large scale changes to PSD were observed as the LCDS is compressed. Electrons outside of the LCDS were no longer stably trapped, and PSD within the LCDS in the latter half of the hour was distinctly different from the previous half hour for μ = 400 MeV/G. If we were to assume that the PSD did not change within an hour timescale, then these observations would be interpreted as false peaks or troughs in the PSD. These false peaks and troughs are produced by the dynamics of the system rather than non-adiabatic acceleration or loss processes. The third period (Figure 5.4c) at 08:00 – 09:00

UT 8 September corresponded to the net-loss phase during the storm main phase. The magnetopause and LCDS expanded outwards and there were dropouts in electron flux at all L-shells, and PSD at $L^* > 3.8$. PSD profiles at the μ investigated were peaked at $L^* = 3.8$, increased at $L^* < 3.8$, and decreased by orders of magnitude at $L^* > 3.8$. This was consistent with electron loss due to direct magnetopause shadowing, followed by a redistribution of electrons via radial diffusion. The first three intervals (Figure 5.4a-c) correspond remarkably well to the PSD dynamics discussed by Turner et al. (2012b), despite the complexity of the external solar drivers during our chosen case study.

The fourth interval (Figure 5.4d) does not correspond directly to the phases of direct magnetopause shadowing described by Turner et al. (2012b). Instead, the interval corresponds to a secondary compression of the magnetosphere during the net acceleration phase between 14:00 – 15:00 UT 8 September, where the magnetopause was measured within geostationary orbit. At all μ PSD increased across L^*, and there was a growing peak in PSD at $L^* = 3.7$ compared to the previous period, with steep PSD gradients across L^*. This is characteristic of a localised non-adiabatic acceleration process, likely due to resonant VLF wave-particle interactions, combined with radial diffusion redistributing electrons down PSD gradients (inwards for $L^* < 3.7$ and outwards for $L^* > 3.7$), thus increasing PSD at any given L^*. The LCDS was compressed to $L^* = 4.4$, thus electrons would be lost to the magnetopause via direct magnetopause shadowing at $L^* > 4.4$. Furthermore, characteristics are suggestive of indirect magnetopause shadowing; strong negative gradients in PSD towards the compressed LCDS means that radial diffusion will transport particles towards the LCDS, where they will be subsequently lost. This final interval (Figure 5.4d) corresponds well to the PSD dynamics during indirect magnetopause shadowing such as discussed by Loto'aniu et al. (2010) and Shprits et al. (2006).

To understand how radial diffusion acted upon the electron populations, Van Allen Probe electric and magnetic field measurements are used to analyse power of field fluctuations. In-situ magnetic field observations from the Van

Allen probe EMFISIS instrument (Kletzing et al., 2013), and electric field observations from the EFW instruments (Wygant et al., 2014), are used. The magnetic and electric field measurements had a time resolution of 4 seconds. The background magnetic and electric fields were identified by taking a running average over a 20-minute sliding window, and the background fields were then subtracted from the instantaneous measurement. To identify fluctuations, the residual field observations were transformed into a magnetic field-aligned coordinate system, defined by the background magnetic field unit vector (parallel component), the geocentric position vector (azimuthal component), and the poloidal direction. In this transformed coordinate system, the parallel magnetic field perturbation and azimuthal electric field perturbation were selected to estimate the associated power spectral densities using a Morlet wavelet transformation. The power spectral density was limited to a frequency range of 1-15 mHz (corresponding to the ULF wave band (Jacobs et al., 1964) and an L-range of $3 < L < 7.5$ as field perturbations cannot be reliably distinguished from the changing background field near orbital perigee.

Figure 5.6 shows the power spectral density of the magnetic field P_B (green) and electric field P_E (pink) as a function of L^* for the four previously specified 1-hour time periods. Magnetic power spectral density is substantially enhanced at an increasing rate through the geomagnetic storm (Figure 5.6, panels b - d) compared to the pre-storm period (Figure 5.6a). Due to data gaps in electric field measurements (associated with spacecraft charging and eclipse events), the number of electric field power spectral density measurements is variable throughout the storm, making it difficult to make comparisons between the four intervals (e.g., Figure 5.4a&d). However, during the first compressive phase (Figure 5.6b), P_E appears high at low L^*, and decreases with increasing L^*. During the net-loss phase (Figure 5.6c), P_E decreased at all L^* compared to the previous compressive phase. During the second compressive phase (Figure 5.6d), there was only one measurement of P_E at $L^* = 3.7$, which was increased compared to the previous net loss phase (Figure 5.6c). Auroral geomagnetic indices (not shown) indicate enhanced substorm activity during this interval, which will produce fluctuations in electric potential in the magnetosphere, and thus contribute towards the power

spectral density of the electric field. It is therefore highly likely that P_E was enhanced during interval (d) in a similar manner to interval (b). Irrespective of this, the overall rate of diffusion of the electrons is dependent on the combination of diffusion from the magnetic field and electric potential fluctuations and the PSD gradient in *L**. Therefore, we conclude that outwards radial diffusion was enhanced for both intervals (c) and (d) as both periods have enhanced power spectral densities, and sharp PSD gradients in *L**.

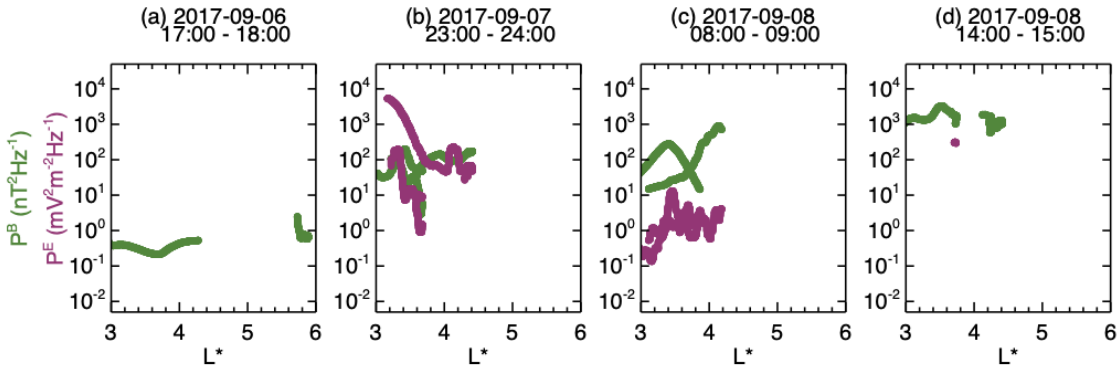

Figure 5.6 Estimated magnetic field (green) and electric field (purple) power spectral densities for (a) 17 - 18 UT 6th Sept, (b) 23 UT 7th - 00 UT 8th, (c) 08 – 09 UT 8th, and (d) 14 - 15 UT 8th. Each panel shows the power spectral density, summed over a frequency range of 1 to 15 mHz, plotted as a function of the *L value. Observations from both Probe A and Probe B are included (Staples et al., in review).**

Without knowing the number of particles accelerated during the local acceleration we cannot measure the number of particles lost via indirect shadowing, and therefore cannot evaluate the respective contributions of direct and indirect shadowing to overall electron loss. In future work, the contributions of each mechanism could instead be estimated by replicating this event with a radiation belt model which includes both source and loss mechanisms.

To highlight how the time and spatial resolution of the multi-mission PSD dataset enhanced observations, and improved our understanding of the complex spatiotemporal dynamics of the outer radiation belt, Figure 5.5 showed observations of the PSD profiles as a function of *L** corresponding to intervals shown in Figure 5.4, but only considered data from the Van Allen Probes. Through the intervals shown, the maximum *L** measured by the Van

Allen Probes was L^* = 4.8, whereas the multi-mission data measured up to L^* = 7.5. Though this difference is less important during the compressive phases, large L^* regions of PSD are not measured by the Van Allen Probes during the pre-storm and recovery phases. Moreover, key observations necessary to accurately characterise the development PSD through the storm were absent when only analysing Van Allen Probes data. Namely, the growing PSD peak at L^* = 3.7 was not observed at μ ~ 400 MeV/G, and the negative PSD gradient at L^* > 3.7 resulting from direct magnetopause shadowing (Figure 5.4c) was not observed in Van Allen Probe observations at μ ~ 900 MeV/G. Olifer et al. (2021) also observed that the PSD measured by the Van Allen Probes could produce misleading results during the September 2017 storm, when 'phantom peaks' where observed. However, the high-resolution multi-mission dataset used in our analysis resolved that the observed peak in PSD is indeed growing on very fast timescales for electrons with μ of 400 and 900 MeV/G, which we attribute to local acceleration. Measurements of PSD on timescales shorter than the Van Allen Probe orbits are crucial to understand radiation belt dynamics.

Finally, we acknowledge possible limitations to this work, specifically the magnetic field model used as it is known to influence calculations of the adiabatic invariants and LCDS (Albert et al., 2018). The T01s external field model was chosen for this work due to its suitability during geomagnetic storm conditions, but different magnetic field models may yield a different L^* location of the LCDS. Furthermore, the LCDS may be calculated by either considering Shabansky drift orbits as closed drift paths, whereas other calculations consider these bifurcating orbits as open (Öztürk & Wolf, 2007; Shabansky, 1971). In this work, we have used the last non-bifurcated drift shell as the LCDS, which could give an underestimation of the outer boundary to trapped electrons if those following bifurcated orbits return to the radiation belts following the compression. Despite this, these limitations are unlikely to change the interpretation of our observations as PSD profiles show clear evidence of magnetopause shadowing, outward radial transport, and local acceleration.

Chapter 6 Multi-Dimensional Analysis of Magnetopause Shadowing Induced Electron Losses

6.1 Introduction

Chapter 5 investigated the evolution of an electron flux dropout during an event in early September 2017 where a sequence of interacting CMEs compressed the magnetopause within geostationary orbit and induced a compound geomagnetic storm. Using PSD measurements, the dominant mechanism of electron loss during the dropout phase was identified to be magnetopause shadowing, induced by strong magnetopause compressions. Magnetopause shadowing characteristics were further identified during the recovery phase of the geomagnetic storm, despite a net-increase in the radiation belts due to local acceleration of electrons. By using a multi-satellite dataset of PSD, large scale changes to the radiation belt structure were resolved to occur on sub-hour timescales during strong magnetospheric compressions. What is more, it was noted that the source of these dynamics could be misinterpreted if a PSD profiles across L^* were measured by single or even dual spacecraft.

As with most studies which analyse dynamics of relativistic electrons, Chapter 5 investigated PSD at a limited range of μ and K, and analysed PSD characteristics across a wide L^* range to interpret the physical mechanisms acting. Whilst observations presented in Chapter 5 showed that the radiation belt dropout during the September 2017 case study was produced by magnetopause shadowing, it is possible that electron loss via precipitation was significant. The steep gradients in PSD across L^* created by magnetopause shadowing precludes the possibility of identifying electron loss by analysing PSD as a function of L^*. What is more, analysing PSD as a function of L^* requires simultaneous measurements of PSD at multiple L^*, which is currently unavailable from a single spacecraft mission. Instead, missions which analyse radiation belt dynamics, such as the Van Allen probes, must traverse the radiation belt to obtain PSD as a function of L^*, which severely limits observations of phenomena which act quicker than the time resolution available, such as flux dropouts or prompt acceleration.

Xiang et al. (2017) discussed how observations of PSD at a wide range of μ and *K,* for a given *L*,* gives credible clues to the dominant mechanism of electron loss. If different acceleration and loss processes may be characterised across a range of μ and *K,* then the dominant processes contributing the PSD dynamics may be deciphered at a single *L** with a time resolution of instrument cadence (i.e., how fast it can measure a full range of energy and pitch angles) and the dwell time of the satellite at that *L*.* This chapter evaluates electron PSD characteristics across a wide range of μ and *K* values during the electron flux dropout during the September 2017 storm. First, the way in which each mechanism contributes to loss at different μ and *K* is first discussed, then compared to multi-satellite observation of PSD for this event.

Observations have shown that EMIC wave scattering of electrons into the loss cone will result in PSD depletions above the μ and *K* values of minimum electrons resonance with EMIC waves (Ma et al., 2020; Xiang et al., 2017). For example, Ma et al. (2020) used Van Allen probe observations of PSD at a range of μ and *K* to identify EMIC wave induced precipitation during a flux dropout on 12 September 2014. Figure 6.1 shows how PSD decreased at different values of μ and *K* between time periods where the Van Allen probes passed through the outer belt, using a quantity called 'PSD drop'. PSD drop is given by the logarithm of the ratio between the previous period PSD to the later period PSD at the same *L** i.e., $PSD_{drop} = \log_{10}(PSD_{i-1}/PSD_i)$, where PSD_i is PSD during the ith orbit. For example, if PSD drop = 2 then the PSD decreased by two orders of magnitude between orbits. Ma et al. (2020) further indicated the values of μ and *K* at which minimum resonance with H^+ band EMIC waves are expected to occur. The authors observed that during the dropout period (Figure 6.1 e-h), PSD drop showed distinct dependencies upon μ and *K* at different *L**. At *L** = 3.9 and 4.6, PSD decreased above minimum resonance with EMIC waves (red line in Figure 6.1), attributed to precipitation into the atmosphere.

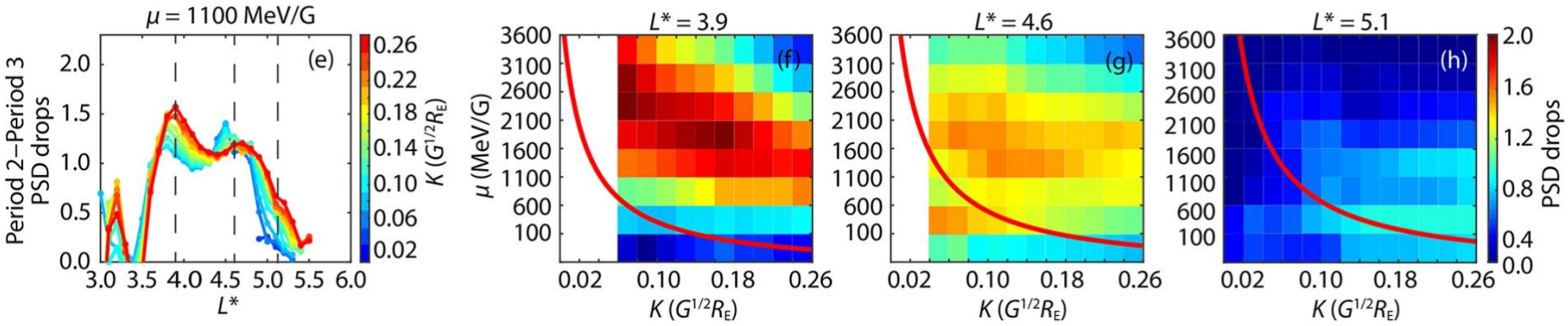

Figure 6.1 Electron PSD drops observed between three orbits of the Van Allen probes during a geomagnetic storm on 12 September 2017. Panels e – h show PSD drop calculated between period 2 and period 3 (20:30 UT on 12 September to 01:00 UT on 13 September, main storm phase). Red lines in panels b-d and f-h indicate the minimum electron energy for cyclotron resonance with H^+ band EMIC waves (Ma et al., 2020).

At L^* = 4.6, losses were also observed below the minimum resonance with EMIC waves. This loss was attributed to magnetopause shadowing based upon previous work by Xiang et al. (2017), which concluded that high rates of loss at low values of μ were due to magnetopause shadowing. The rationale behind this conclusion invoked that there is less ULF wave power available to interact with higher energy electrons, resulting in lower radial diffusion rates. Whilst this is a reasonable explanation for the observations of Xiang et al. (2017), their observations of electrons at different pitch angles were highly limited during critical intervals of the dropout case study, and this interpretation of shadowing at different μ and K values may not be applicable under all magnetospheric conditions. Additionally, these observations have not been found to hold during different geomagnetic storms. During an electron flux dropout event in September 2012, Turner et al. (2014b) found that electron losses were produced by magnetopause shadowing at all μ and K above $L^* \sim$ 3.5, with loss timescales which were independent of μ and K at $\mu >$ 1000 MeV/G and $K < 0.02\ G^{0.5}R_E$.

In this thesis we argue that the effect of magnetopause shadowing at different μ and K values is highly multifaceted. There are several different aspects to magnetopause shadowing which could lead to different rates of electron loss at different μ and K, each related to how likely an electron drift path is to intersect the magnetopause, or how effectively electrons are diffused towards the magnetopause. Electrons which have a low K value (high pitch angle) are more likely to be directly shadowed by the magnetopause because the drift paths of these particles extend to higher radial distances through drift shell splitting (see Section 1.7.4). Of the electrons which follow open drift paths, electrons with high μ (approximately corresponding to high energy electrons) are more likely to encounter the magnetopause because their drift orbits are shorter. Direct magnetopause shadowing creates steep negative PSD gradients with increasing L^* (such as discussed in Chapter 5). If the third adiabatic invariant is violated, by ULF wave activity for example, both the PSD gradient and ULF wave power will determine the rate at which electrons diffuse towards the magnetopause. If electrons at high μ and low K are more likely to be directly shadowed, this could create steeper radial gradients in PSD which

could lead to higher rates of radial diffusion (Tu et al., 2019). However, the rate at which electrons diffuse is not only dependent upon the radial gradients, but also upon particle interactions with ULF waves. As argued by Xiang et al. (2017), electrons with low μ in theory have higher diffusion rates than high μ electrons because there is greater wave power at frequencies which resonate with lower drift frequencies (Liu et al., 2016; Tu et al., 2012). Drift orbit bifurcations have also been shown to result in the super-diffusive transport of electrons towards the magnetopause (Desai et al., 2021a). Therefore electrons with low *K* values, which are more likely to follow bifurcated drift orbits, could also show high rates of loss through indirect magnetopause shadowing.

By these arguments, magnetopause shadowing could potentially result in electron loss at any μ and *K,* depending on different magnetic topologies and ULF wave power. In this chapter, we shall investigate changes to PSD across μ*, K,* and *L*,* in a similar manner to Ma et al. (2020), to characterise magnetopause shadowing loss rates at different μ and *K,* and to identify whether scattering of electrons into the atmosphere was appreciable in the September 2017 case study.

6.2 PSD Data Processing

In this chapter the same multi-satellite PSD dataset as discussed in Chapter 5 is used between the 6 to 10 September 2017. For a full description of the computation of PSD in the adiabatic coordinates for this dataset, and the intercalibration technique, see Section 3.4.

This chapter uses PSD observations averaged over specific ranges of μ, *K*, and *L** at 1-hour intervals. The resolution of the averaged dataset is as follows:

- μ = 100 MeV/G resolution, from 0 - 4000 MeV/G,
- *K* = 0.05 $G^{0.5}R_E$ resolution, from 0 - 2 $G^{0.5}R_E$,
- *L** = 0.1 R_E, from 0 to 10 R_E.

Figure **6.2** demonstrates the averaged dataset of PSD measured by Van Allen Probes, THEMIS, MMS, GOES, and GPS, for (a) 400 < μ < 500 MeV/G

and (b) 900 < μ < 1000 MeV/G at 0.10 < K <0.15 $G^{0.5}R_E$. These μ and K ranges are selected to approximately correspond to ranges used in Figure 5.3 for comparison.

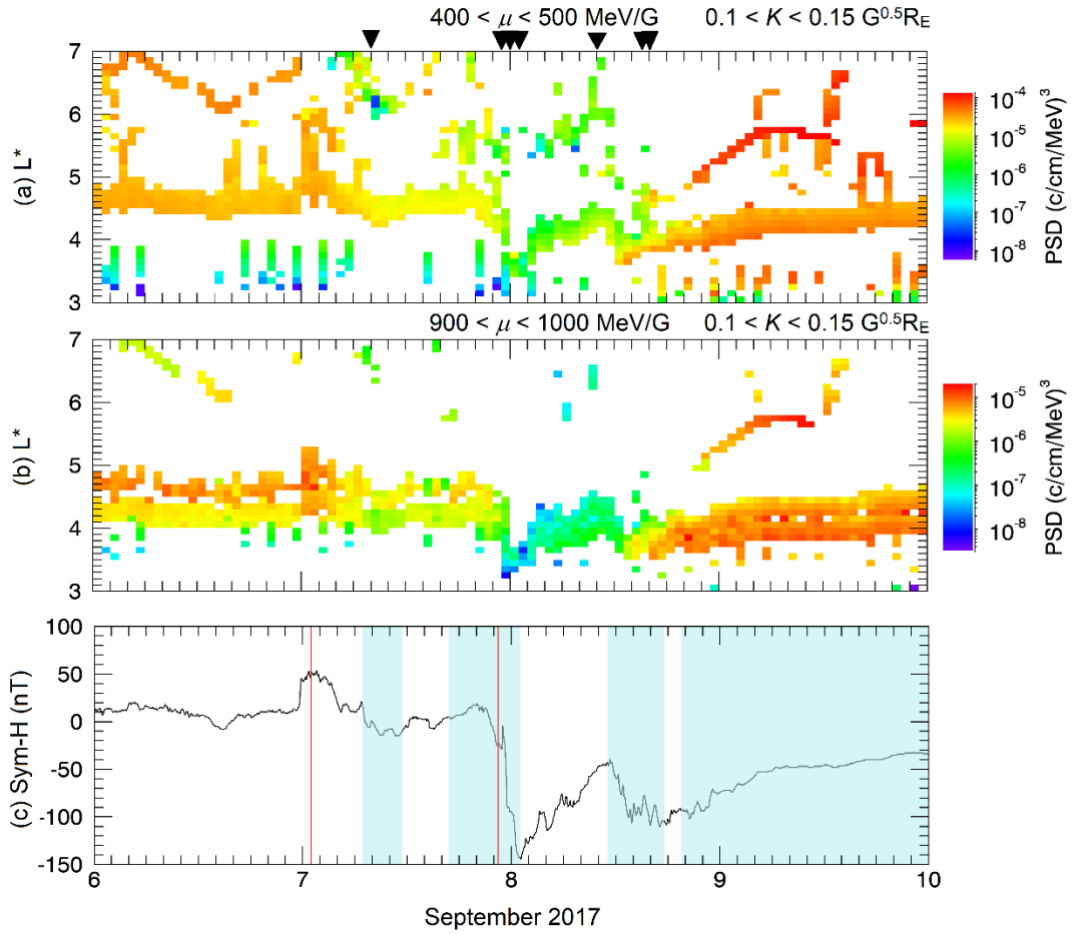

Figure 6.2 **Averaged Phase Space Density by colour as a function of L* for 6 - 10 September 2017 for (a) 400 < μ < 500 MeV/G and (b) 900 < μ < 1000 MeV/G. 0.10 < K <0.15 $G^{0.5}R_E$ for both a and b. (c) show the corresponding Sym-H index with blue shaded areas corresponding intervals where CME ejecta were passing the bow shock, and red lines are when interplanetary shock reach the bow shock. Black triangles mark the beginning of each time interval shown in Figure 6.5 and Figure 6.4.**

In this study we use a quantity '*ΔPSD*' which is similar to 'PSD drop' used by Ma et al. (2020), though defined in a different manner. *ΔPSD* is calculated as the logarithm of the average measured PSD, divided by the pre-storm PSD, for specified μ, K, and L^*:

$$\Delta PSD = \log_{10} \frac{Measured\ PSD}{Pre-storm\ PSD}$$

For example, if *ΔPSD* = -1, then PSD decreased by a factor of 10 compared to the average pre-storm PSD at the same μ, *K*, and *L*.* If *ΔPSD* = 2, then PSD increased by a factor of 100.

The pre-storm PSD is represented by the average PSD on the 6 September 2017. *ΔPSD* is chosen to be normalised to the pre-storm value so that data coverage across μ, *K*, and *L** is maximised. If instead *ΔPSD* was compared to the previous hour, PSD data would be limited by spacecraft locations from the previous hour. The rate of change in PSD was not chosen for investigation for the same reason.

Note that the calculation of *ΔPSD* differs to PSD drop used in Ma et al. (2020). Positive values of PSD drop indicate a decrease in PSD compared to the previous Van Allen orbit. In this chapter *ΔPSD* considers both increases and decreases; so positive and negative *ΔPSD* respectively correspond to an increase or decrease in PSD compared to the pre-storm value.

6.3 Results

In order to interpret the dynamics of PSD at different values of *K*, it is important to first understand the differences in the LCDS location for different *K*. Figure **6**.**3** shows computations of the LCDS (Figure **6**.**3**c) for specified electron pitch angles at the magnetic equator (Figure **6**.**3**a) which correspond to *K* shown in Figure **6**.**3**b. The LCDS was determined by numerically computing the maximum *L** at which particles of a given pitch angle follow a closed drift orbit in the T01s magnetic external field model. Figure **6**.**3**b showed that the computation of *K* varied sporadically for near equatorial bouncing electrons (α ~ 90^o, yellow line) by up to 2 orders of magnitude. During the initial storm main phase, early on 8 September (when Sym-H index decreases suddenly, Figure **6**.**3**d), *K* increased by up to one order of magnitude. Values of *K* computed for electrons with higher pitch angles ≥ 80^o did not significantly vary from their respective average *K,* apart from during the main phases of the geomagnetic storm when *K* decreased by up to 1 order of magnitude for α ~ 80^o electrons, and by lesser magnitudes electrons with increasing pitch angles.

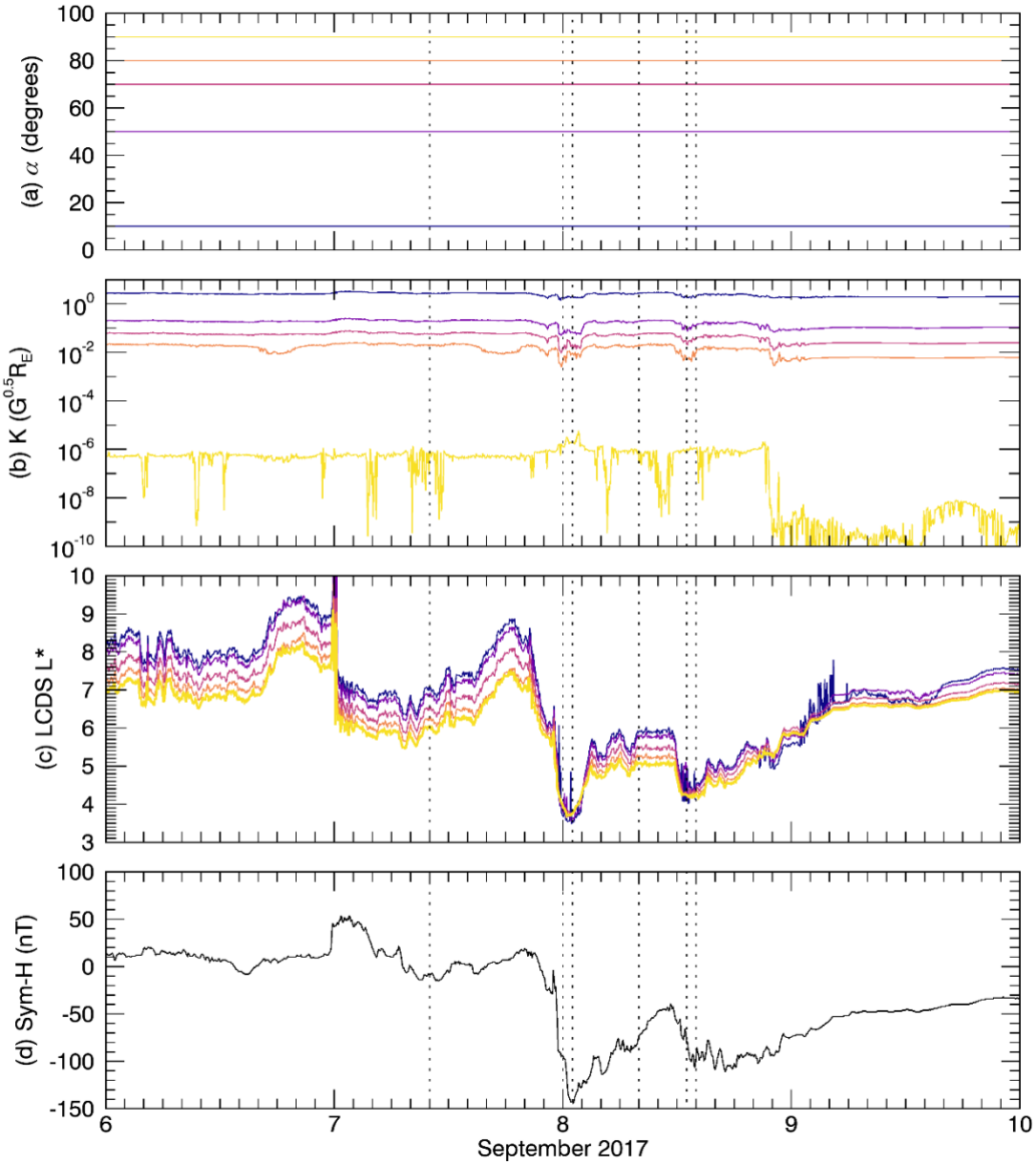

Figure 6.3 **For specified equatorial pitch angles (a), the second adiabatic invariant, K, (b) and the L* of the LCDS (c) are shown for computations using the T01s external magnetic field model. The colours correspond each equatorial pitch angle used to compute K and the LCDS. (d) shows the Sym-H index over the storm. Vertical dotted lines refer to the start times of the intervals shown in Figure 6.5 and Figure 6.4.**

Prior to the geomagnetic storm, Figure **6.3**c shows that there was a wide spread of the LCDS location in *L**, depending upon *K*. The LCDS was located ~ 1.5 *L** closer to Earth for near equatorial electrons (lower *K*) than the highest *K* electrons. During the main phase of the storm, the *L** location of the LCDS decreased for all electrons, with a minimum *L** = 3.5 for electrons at low pitch angles of 10^{o} (which corresponded to *K* ~ 1.5 $G^{0.5}R_E$). At minimum *L**, the

LCDS for near equatorial bouncing electrons (α ~ 90^o, which corresponded to K ~ 1.5 x 10^{-6} $G^{0.5}R_E$) was at L^* = 3.7. Usually, the LCDS of low K electrons is expected to reach lower L^* than for high K electrons due to the drift shell splitting effect; whereby near equatorial electrons drift to higher radial distances to conserve the adiabatic invariants. Observations of the LCDS during the main phase of the storm in Figure **6**.**3**c show the opposite behaviour. This could be due to the presence of drift orbit bifurcations at high K electrons, which are not considered as closed drift shells in our computation of the LCDS. Figure **6**.**3**c may therefore indicate that, during the storm main phase, electrons where K > 0.4 $G^{0.5}R_E$ follow bifurcated drift paths beyond the computed LCDS. This observation repeats during the secondary main phase of the compound geomagnetic storm, at 13 UT 8 September.

Figure 6.4 shows how ΔPSD varies as a function of μ and K through the net-loss phase of the storm. Because most electrons are found near the equator at low K values, Figure 6.4 resolves ΔPSD for very low values of K < 0.125 $G^{0.5}R_E$ (corresponding to $log_2(K)$ < -3, or approximately α > 70^o) by averaging PSD on a logarithmic basis of K. The average pre-storm PSD is shown in the first column, four 1-hour intervals through the net-loss phase are shown (a-d), and two intervals at the beginning of the net-acceleration phase are shown (e-f). The start time of each interval is indicated by black triangles in Figure **6**.**2** and dotted lines in Figure **6**.**3**. Three different L^* are shown, ranging from 3.5 < L^* < 4.1, each with 0.1 L^* resolution, chosen based upon best data coverage.

Figure 6.5 shows how ΔPSD varies as a function of μ and K through the net-loss phase of the storm for all K values on a linear basis. Figure 6.4 and

Figure 6.5 are in the same format but differ in having a logarithmic or linear x-axis. The ranges of K shown in the Figures also differ; Figure 6.4 shows ΔPSD at K < 0.125 $G^{0.5}R_E$, whereas

Figure 6.5 shows ΔPSD between 0 – 2 $G^{0.5}R_E$.

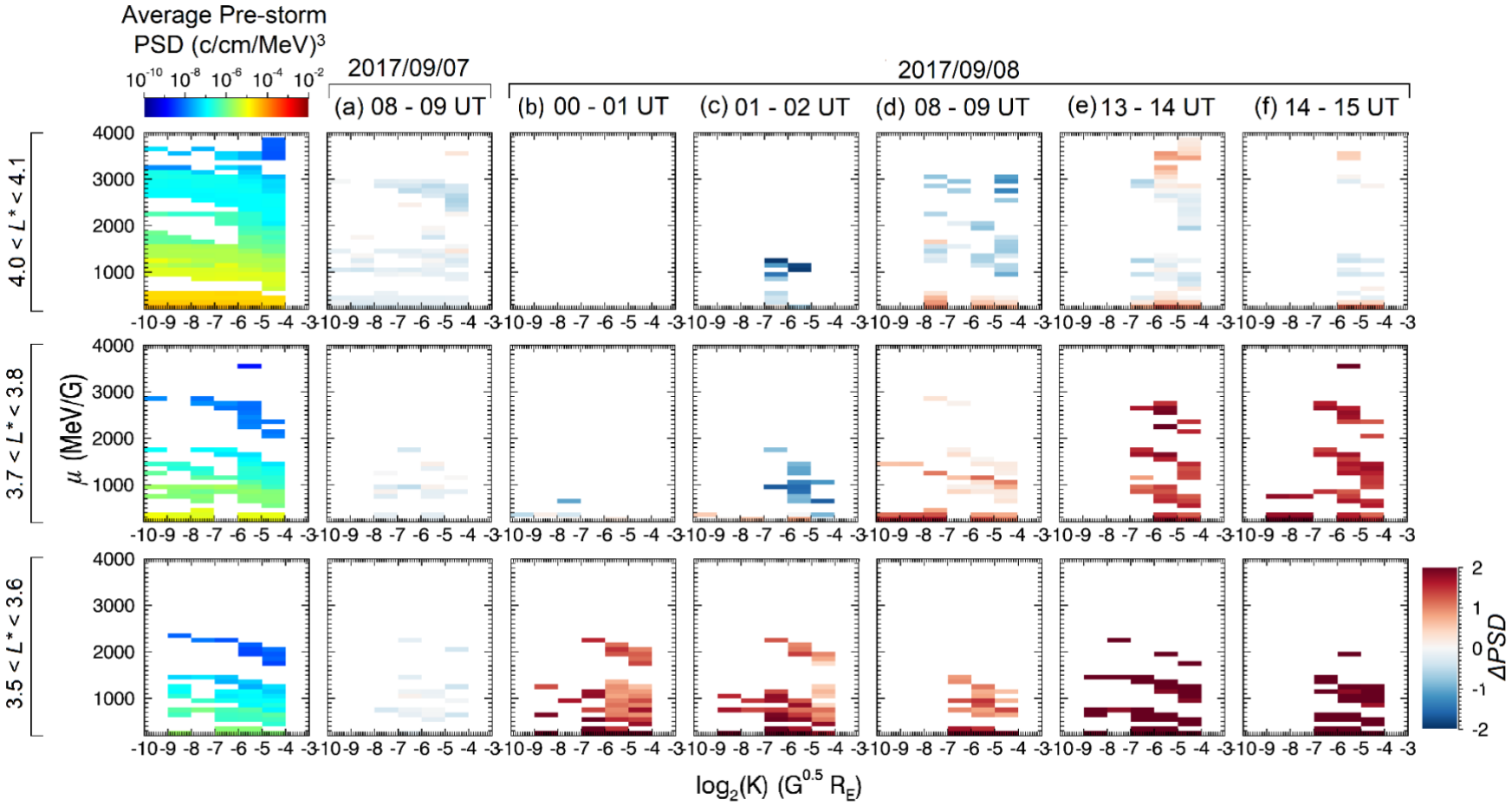

Figure 6.4 Left column shows the average pre-storm PSD by colour as a function of μ and *K* for three different *L between 3.5 < *L** < 4.1, each row with 0.1 *L** resolution. In this figure, PSD is averaged on a logarithmic basis of K. Columns (a-f) show 1-hour intervals during the dropout phase of the September 2017 storm. *ΔPSD* is shown by colour as a function of μ and *K*.**

Observation of PSD at low $K < 0.125\ G^{0.5}R_E$, which corresponds to low latitude bouncing electrons, are shown in Figure 6.4. Observations of *ΔPSD* prior to the storm at 08 – 09 UT 7 September, while the LCDS was moderately compressed, are shown in Figure 6.4a. Figure 6.4a shows that a higher fraction of electrons were lost at high μ for $L^* > 4.0$. For example, at $\log_2(K) = -3$ to $-4\ G^{0.5}R_E$ ($K \sim 0.03 – 0.07\ G^{0.5}R_E$), at $\mu \sim 2500$ MeV/G, *ΔPSD* = -0.6, whilst at $\mu \sim 800$ MeV/G *ΔPSD* = -0.2. At $L^* < 3.8$ there was a small amount of PSD loss, since *ΔPSD* < 0 at all μ and *K*.

Whilst the LCDS was at maximum compression at 00 - 01 UT 8 September (Figure 6.4b), a prompt increase in PSD was observed at $L^* < 3.6$ for all μ and *K*. This is consistent with a diffusive transport of electrons to low L^* which occurs simultaneously to magnetopause shadowing (e.g., Figure 2.4; Figure 5.4). As the LCDS began to increase to higher L^* over the following interval at 01 - 02 UT 8 September (Figure 6.4c), electron losses were observed at $L^* > 3.7$ which were greater for high μ. For example, at $L^* \sim 4.0$ and $\log_2(K) = -6$ to $-7\ G^{0.5}R_E$ ($K \sim 0.007 – 0.016\ G^{0.5}R_E$), at $\mu \sim 1200$ MeV/G, *ΔPSD* = -2 (or less since the colour bar saturates at $\pm$ 2), whilst at $\mu = 400$ MeV/G, *ΔPSD* = -0.3. This suggests that electrons lost through indirect magnetopause shadowing were lost at a greater rate for high μ. PSD at $L^* < 3.6$ continued to be enhanced compared to pre-storm PSD, indicating the electrons continue to radially diffuse through the radiation belt.

Following the electron dropout, while the LCDS was located at $L^* > 5$ at 08 – 09 UT 8 September, Figure 6.4d shows that PSD loss compared to pre-storm values was still a prevalent characteristic at $L^* > 4.0$ for low *K* electrons with high $\mu > 600$ MeV/G. While at $L^* < 3.8$, PSD exceeded pre-storm PSD for low $K < 0.125\ G^{0.5}R_E$.

During the second compressive phase at 13 -15 UT 8 September (Figure 6.4e-f), electron losses at $K < 0.125\ G^{0.5}R_E$ and $L^* > 4.0$ were observed to occur at specific μ values between ~ 400 – 3000 MeV/G, while at $\mu < 400$ MeV/G and $\mu > 3000$ MeV, PSD was increased compared to the pre-storm PSD. At $L^* < 3.8$, PSD increased by two or more orders of magnitude compared to pre-storm

PSD for all μ and K. This was consistent with Chapter 5 observations of a local acceleration mechanism acting at $L^* \sim 3.7$.

Figure 6.5 shows PSD dynamics for high K electrons. Observations of ΔPSD in Figure 6.5a were during the pre-storm interval at 08 – 09 UT 7 September, whilst the LCDS was compressed. At $L^* > 4.0$, there was greater PSD loss at high μ (as observed in Figure 6.4a), but also at high K. For example, at $\mu \sim$ 1100 MeV/G and $K \sim 0.3\ G^{0.5}R_E$, $\Delta PSD = -0.8$, whilst at $\mu \sim 400$ MeV/G and $K \sim 0.2\ G^{0.5}R_E$, $\Delta PSD = -0.02$. This suggests that proximity to the LCDS does not necessarily imply greater rates of indirect magnetopause shadowing loss, as the LCDS was at the lowest L^* for low K electrons during this interval (Figure **6**.**3**c). Instead, the rate of radial transport of electrons towards the outer boundary determines the rate of loss within the LCDS.

During the maximum compression of the LCDS at 00 – 01 UT 8 September, Figure 6.5b shows that there were PSD enhancements for electrons at low $K < 0.4\ G^{0.5}R_E$. Between $3.7 < L^* < 3.8$, PSD loss was simultaneously observed to PSD enhancements, dependent upon μ; between $\mu \sim 600 – 1000$ MeV/G PSD decreased, whereas PSD increased at $\mu < 600$ MeV/G and $\mu > 1000$ MeV/G. This observation was analogous to μ dependent loss observed during the second compression in Figure 6.4e-f. However, at high K the μ at which loss was observed shows a non-linear dependence on K. During the same interval, Figure 6.5b showed that losses were observed for high $K > 0.4\ G^{0.5}R_E$, between $3.5 < L^* < 3.6$, simultaneous to PSD enhancements observed for low K (Figure 6.4b). Whilst this loss showed similar characteristics to the PSD loss observed at $3.7 < L^* < 3.8$, we cannot be certain of a relationship between PSD loss and K, because enhancements occurred at low K compared to pre-storm PSD.

As the LCDS began to expand to higher L^* at 01 – 02 UT 8 September, Figure 6.5c showed that PSD was lost at high μ and K values compared to pre-storm PSD, which was universal for $K > 0.1\ G^{0.5}R_E$ at $L^* > 3.7$. At $3.5 < L^* < 3.6$, loss was observed at $K > 0.3\ G^{0.5}R_E$. The enhancements in PSD at low K were less than this.

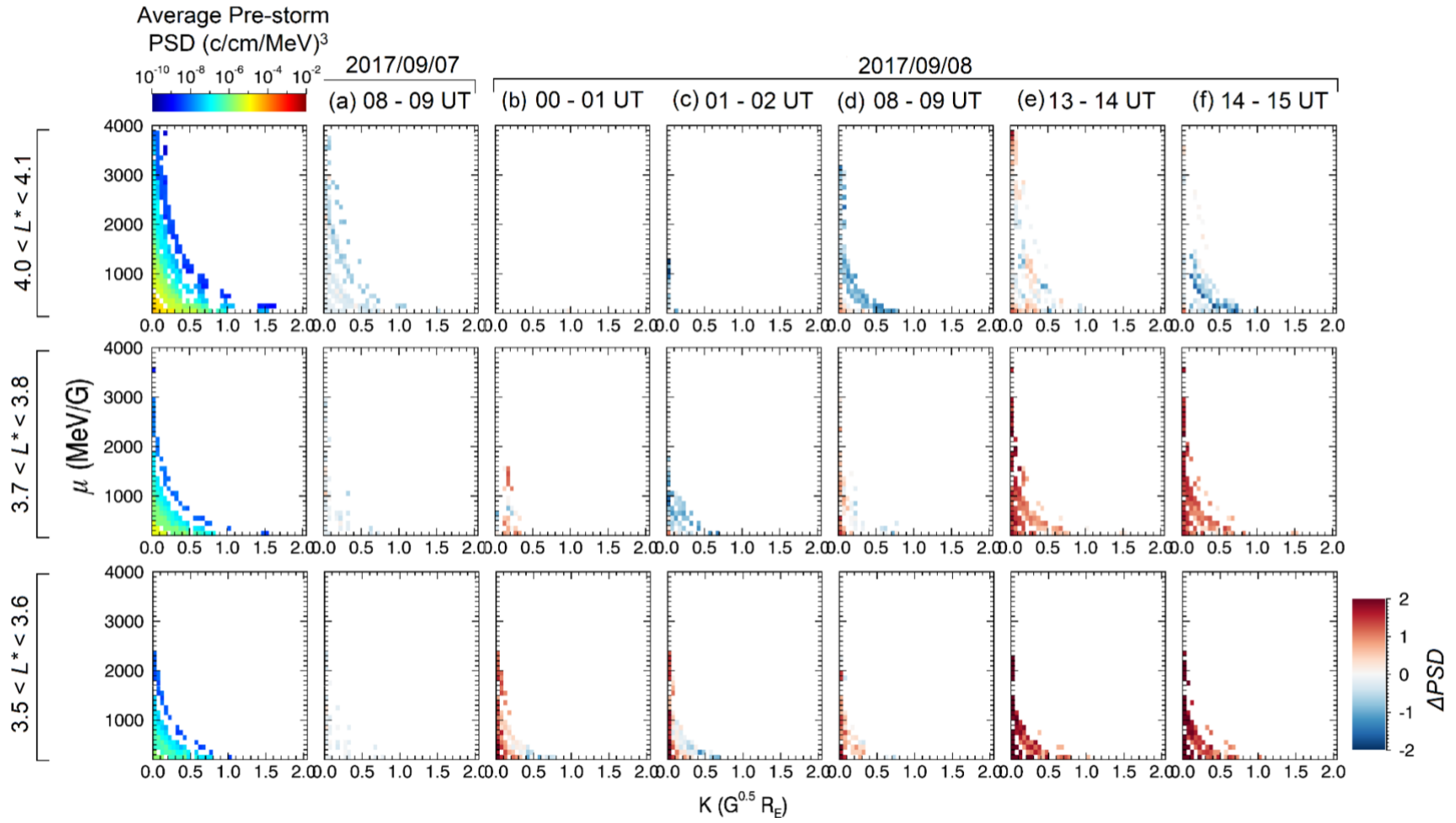

Figure 6.5 Left column shows the average pre-storm PSD by colour as a function of μ and *K* for three different *L between 3.5 < *L** < 4.1, each row with 0.1 *L** resolution. Columns (a-f) show 1-hour intervals during the dropout phase of the September 2017 storm. *ΔPSD* is shown by colour as a function of μ and *K*.**

Following the dropout, at 08 – 09 UT 8 September Figure 6.5d showed that PSD at $L^* < 3.8$ increased at all K values > 0.1 $G^{0.5}R_E$ compared to the previous interval, indicating that electron acceleration dominated the dynamics. At $L^* > 4$, losses due to shadowing at high μ and K remained the dominant feature compared to pre-storm PSD. However, we note that L^* was not defined during the previous interval, therefore in this region electrons followed open drift paths and were directly shadowed by the magnetopause. Therefore, PSD observed at Figure 6.5d will consist of electrons from acceleration regions at low L^*, which have radially diffused down radial gradient created by magnetopause incursions.

Figure 6.5e-f shows intervals during the second compression of the magnetosphere at 13 – 15 UT 8 September, and the LCDS was located at a minimum $L^* = 4$. At $L^* < 3.8$ acceleration remained the dominate PSD characteristics for all μ and K. At $L^* \sim 4.0$ however, electron losses were observed which showed a dependence on both μ and K. At a specific K, PSD loss would occur within a specific range of μ, the values of which varied non-linearly with K. For example, at $4.0 < L^* < 4.1$ on 14-15 UT 8 September (Figure 6.5e), maximum PSD loss was observed at $\mu \sim 900$ MeV/G for $K \sim 0.1$ $G^{0.5}R_E$, but at $K \sim 0.4$ $G^{0.5}R_E$ the maximum PSD loss was observed at $\mu \sim 200$ MeV/G. This loss, which occurred at a characteristic 'banded' structure in μ and K space, showed similar characteristics to precipitation losses induced by electron interactions with EMIC waves presented by Ma et al. (2020) i.e., Figure 6.1f-g.

6.4 Discussion

This chapter presented an analysis of how loss mechanisms affect electron PSD for a wide range of μ and K values. A limited number of studies have considered how different loss processes contribute to PSD dynamics at different μ and K, in particular magnetopause shadowing has not yet been convincingly characterised in this way.

Observations were presented by showing the change in PSD compared to the average pre-storm PSD (Figure 6.4 and Figure 6.5). Whilst this method

maximised the data availability of *ΔPSD,* instantaneous changes to PSD were not easily extracted. Instead, *ΔPSD* represented the culmination of all acceleration, loss, and transport processes which occurred since the 6 September, which was defined as pre-storm. The conclusions which follow make careful consideration of the time history of *ΔPSD* in the wider context of this storm.

Observations of the change in PSD, compared to a pre-storm average for a dropout event in September 2017, showed that there was one key characteristic of indirect magnetopause shadowing in μ and *K* space which was observed through the storm: greater rates of electron loss at high μ. Electrons at high μ have short drift periods due to their high energies. Therefore, high μ electrons are more likely than their low μ counterparts to intercept the magnetopause during a magnetopause incursion into the inner magnetosphere. While Figure **6.3** showed that the LCDS was strongly compressed for ~ 2 hours on 8 September, the magnetopause was not at minimum compression for this entire period (Figure 5.1d). GOES measurements showed two incursions of the magnetopause within geostationary orbit at 00:32 - 00:44 UT and at 01:31 - 01:35 UT on 8 September. Because these incursions had a period of 5 – 10 minutes, it is feasible that a greater fraction of high μ electrons on open drift paths encountered the magnetopause than low μ electrons. This would lead to PSD gradients across *L** which are steeper for high μ electrons. Because radial diffusion depends upon the gradient of PSD in *L**, as well as ULF wave power, this leads to higher rates of radial diffusion towards the magnetopause, and hence higher rates of loss through indirect magnetopause shadowing.

As discussed in Section 6.1, interactions between electrons and ULF waves violate the third adiabatic invariant, allowing the radial diffusion of electrons. High importance is therefore bestowed on the calculation of radial diffusion coefficients, which help quantify rates of electron diffusion by considering the variability of electromagnetic fields in the magnetosphere. Past studies have shown that these diffusion coefficients are significantly greater for electrons at low μ because there is greater wave power available at frequencies which

resonate with low μ drift frequencies (Liu et al., 2016; Tu et al., 2012; Xiang et al., 2017). Xiang et al. (2017) observed that loss due to magnetopause shadowing was indeed greater at low μ than compared to high μ due to higher rates of radial diffusion towards the magnetopause. Observations presented in this chapter show the contrary, that electrons at high μ are lost at greater rates through indirect magnetopause shadowing. This suggests that, for the scenario of magnetopause shadowing, the PSD gradient created by direct magnetopause shadowing has a greater influence on outwards radial diffusion of electrons than ULF wave-particle interactions. We emphasise that, whilst direct and indirect magnetopause shadowing are often discussed separately in this thesis, indirect shadowing is inextricably linked to direct magnetopause shadowing through the creation of negative radial gradients in PSD.

Observations also showed loss which occurred at specific μ values which were non-linearly dependent upon *K.* We highlighted that this produced 'banded' structures of loss in μ and *K* space with similar characteristics to precipitation losses induced by resonant electron interactions with EMIC waves presented by Ma et al. (2020) i.e., Figure 6.1f-g. This is a feasible explanation for observed μ and *K* dependent loss since observations coincide with strong magnetosphere compressions, when EMIC waves are known to be produced by temperature anisotropies in adiabatically heated dayside plasma (e.g., Anderson & Hamilton, 1993; Engebretson et al., 2002). However, during these intervals (Figure 6.5b and f), there is significant acceleration of electrons at low *K* since pre-storm times (Figure 6.4b and f) which may obscure observations of PSD loss. Observations of EMIC waves are therefore necessary to confidently conclude that precipitation loss is significant during these intervals. We emphasise that, if we are to assume the electron precipitation is indeed occurring during Figure 6.4b, then this chapter demonstrates how this method of analysing PSD, which was similarly used by Ma et al. (2020) and Turner et al. (2014b), may be used to identify local electron losses via precipitation without the need to observe a deepening PSD minima, as a function of *L**. This is highly beneficial during short periods electron precipitation, where precipitation loss is quicker than the time resolution of PSD observations across *L*.*

In Section 6.1, it was hypothesised as to whether PSD observations across a wide range of μ and K may be used to determine the dominant loss process for a given L^* on a very short timescale. Using the method of PSD analysis used in this chapter, where PSD is compared to a pre-storm value, we do not believe this is realistic as all acceleration, loss, and transport mechanisms since the pre-storm must be considered. This requires PSD measurements at multiple L^* throughout a storm. However, this does not preclude the possibility that observations of the change in PSD with μ and K could feasibly be used to correctly interpret electron dynamics during a less complex geomagnetic storm; especially since this chapter has shown that there are distinct characteristics between magnetopause shadowing and EMIC induced precipitation loss.

We acknowledge that there are certain limitations to the analysis possible with the available PSD data. Specifically, the lack of pitch angle resolution available from GPS data, which comprises the majority of PSD observations shown in Figure 6.5. The computation of PSD at different K values for GPS satellites relies upon intercalibrations with Van Allen Probe B's pitch-angle resolved electron flux observations, assuming a sinusoidal relationship. For most scenarios, this is a valid assumption since electrons bounce once through the equator, where they are measured by Van Allen probes at low latitudes. This intercalibration technique is not valid for times when the pitch angle distribution deviates significantly from a singularly peaked distribution, or for periods where for electrons follow bifurcated drift orbits, so do not pass through the magnetic equator. In this study, possible intercalibration errors were avoided by only considering electrons which were stably trapped (so do not follow bifurcated drift paths), and we completed a visual inspection of Van Allen Probe data to confirm that there were no butterfly pitch angle distributions during the interval presented in this study.

Chapter 7 Conclusions and Future Work

This thesis presented an analysis of magnetopause incursions into the inner magnetosphere, and how this produces dropouts in relativistic electron flux in the outer Van Allen radiation belt. The principal unresolved question regarding electron flux dropout events surrounds the respective contributions of magnetopause shadowing and electron precipitation into the atmosphere to overall electron loss. The gap in our understanding of these dynamic events stems from the limited availability of in-situ electron measurements on the timescale necessary to observe sudden dropouts in flux. This thesis also hypothesised that statistical parameterisations of the magnetopause location, which have not been validated for use under sudden solar wind compressions of the magnetosphere, could lead to inaccurate interpretations of the magnetopause shadowing contributions to electron losses. A key objective of the analysis presented in this thesis was to combine multi-mission measurements of magnetic topologies and particle flux to explore the rapid dynamics of the outer radiation belt, and to evaluate parameterisation of the magnetopause location.

Observations of the magnetopause over a twenty-year period showed that, during periods of slowly varying solar wind conditions and quiescent geomagnetic activity, the Shue et al. (1998) model is a good estimate of magnetopause location within ±1 R_E. The time-dependent response of the magnetopause to fast changes is determined by solar wind conditions (e.g., interplanetary shocks). This cannot be captured by statistical models, such as the Shue et al. (1998) model. It was further shown that a new parameterisation may be critical when quantifying electron flux dropouts in the radiation belts, particularly at very high energies. As well as new parameterisations of the magnetopause location, future work should focus on the inclusion of magnetopause measurements wherever possible. Magnetopause measurements could include in-situ crossings of spacecraft, or use novel measurements from the upcoming SMILE mission, which will use soft x-ray emissions from the magnetosheath to infer the location of the magnetopause.

This thesis also analysed electron dynamics during the early September 2017 geomagnetic storm by using multi-point electron phase space density measurements from 36 satellites, which provided unprecedented spatiotemporal resolution. By comparing PSD to flux measurements, adiabatic transport of electrons was identified during the event, highlighting the importance of considering adiabatic coordinates to interpret flux changes during geomagnetic storms. Analysis of electron PSD measurements showed capability to identify and isolate intervals of loss, energisation, and mixed intervals of acceleration at low L^* and loss at high L^*. Observations of the flux dropout showed PSD evolution characteristic of direct magnetopause shadowing, as described by Turner et al. (2012b). It was further shown that magnetopause shadowing continued to influenced electron dynamics during the recovery phase of the storm, in conjunction with acceleration processes at low L^*. Observed PSD gradients, and ULF wave power showed signatures, during this period indicated indirect magnetopause shadowing (e.g., Loto'aniu et al. (2010), Shprits et al. (2006), and Turner et al. (2014b)) was significant.

It was further demonstrated that Van Allen Probe data alone was not sufficient to correctly interpret the fast acceleration and loss processes through observations of PSD as a function of L^*, which were identifiable with the extremely high spatial and temporal resolution of multi-spacecraft measurements. This emphasises the need to expand future analysis beyond dual spacecraft observations of PSD, which cannot always capture the rapid timescales of these complex dynamics. Using this new multi-mission dataset of PSD observations, future work could revisit the analysis of Turner et al. (2014b) to characterise the timescale of electron losses through magnetopause shadowing. Though, instead of considering the loss timescale at a given L^*, it would be more beneficial to analyse loss timescales based on distance from the outer boundary, and rate of radial diffusion, which determine event specific behaviours of indirect shadowing losses at a specific L^*.

It was hypothesised whether observations of PSD as a function of μ and K could preclude the need for observations of PSD evolution as a function of L^* by the interpretation of loss characteristics at different μ and K values.

Characteristic differences in PSD loss at different μ and K values were identified; magnetopause shadowing produced greater electron loss at high μ, whilst electron precipitation results in PSD depletions at μ *and* K values where electrons resonate with EMIC waves. However, observational differences of magnetopause shadowing characteristic presented in this thesis and previous observations by Turner et al. (2014b) and Xiang et al. (2017) remain unexplained.

Future work could complete a wider scale study by repeating analysis on more magnetopause shadowing events, especially those where there is little to no electron acceleration. Where data is available, the change in PSD should be considered instead of comparisons with pre-storm PSD, so that only processes which occurred during the observation period need to be considered. More observational evidence is also needed to conclude with certainty that EMIC induced electron precipitation is responsible for characteristic PSD loss at characteristic μ and K values in the September 2017 storm. This could be through in-situ measurements of electromagnetic fluctuations (e.g., Min et al., 2012; Saikin et al., 2015), or remote sensing of precipitation effects in the upper atmosphere (e.g., Clilverd et al., 2009; Rodger et al., 2012; Woodger et al., 2015). Until more evidence on the characteristics of electron loss at different μ and K values is provided, PSD evolution at different μ and K should be used as a complementary analysis to interpretations of PSD evolution in L^*.

Bibliography

Abel, B., & Thorne, R. M. (1998). Electron scattering loss in Earth's inner magnetosphere: 1. Dominant physical processes. *Journal of Geophysical Research: Space Physics*, *103*(A2), 2385-2396. https://doi.org/10.1029/97JA02919

Albert, J. M., Selesnick, R. S., Morley, S. K., Henderson, M. G., & Kellerman, A. C. (2018). Calculation of Last Closed Drift Shells for the 2013 GEM Radiation Belt Challenge Events. *Journal of Geophysical Research: Space Physics*, *123*(11), 9597-9611. https://doi.org/10.1029/2018JA025991

Allan, W., White, S. P., & Poulter, E. M. (1986). Impulse-excited hydromagnetic cavity and field-line resonances in the magnetosphere. *Planetary and Space Science*, *34*(4), 371-385. https://doi.org/10.1016/0032-0633(86)90144-3

Amata, E., Savin, S. P., Ambrosino, D., Bogdanova, Y. V., Marcucci, M. F., Romanov, S., & Skalsky, A. (2011). High kinetic energy density jets in the Earth's magnetosheath: A case study. *Planetary and Space Science*, *59*(7), 482-494. https://doi.org/10.1016/j.pss.2010.07.021

Anderson, B. J., & Hamilton, D. C. (1993). Electromagnetic ion cyclotron waves stimulated by modest magnetospheric compressions. *Journal of Geophysical Research: Space Physics*, *98*(A7), 11369-11382. https://doi.org/10.1029/93JA00605

Angelopoulos, V. (2008). The THEMIS Mission. *Space Science Reviews*, *141*(1), 5. 10.1007/s11214-008-9336-1

Angelopoulos, V. (2014). The ARTEMIS Mission. In C. Russell & V. Angelopoulos (Eds.), *The ARTEMIS Mission* (pp. 3-25). Springer New York. https://doi.org/10.1007/978-1-4614-9554-3_2

Archer, M. O., Hartinger, M. D., & Horbury, T. S. (2013). Magnetospheric "magic" frequencies as magnetopause surface eigenmodes. *Geophysical Research Letters*, *40*(19), 5003-5008. https://doi.org/10.1002/grl.50979

Archer, M. O., Horbury, T. S., & Eastwood, J. P. (2012). Magnetosheath pressure pulses: Generation downstream of the bow shock from solar wind discontinuities. *Journal of Geophysical Research: Space Physics*, *117*(A5). https://doi.org/10.1029/2011JA017468

Archer, M. O., Turner, D. L., Eastwood, J. P., Horbury, T. S., & Schwartz, S. J. (2014). The role of pressure gradients in driving sunward magnetosheath flows and magnetopause motion. *Journal of Geophysical Research: Space Physics*, *119*(10), 8117-8125. https://doi.org/10.1002/2014JA020342

Aseev, N. A., Shprits, Y. Y., Drozdov, A. Y., Kellerman, A. C., Usanova, M. E., Wang, D., & Zhelavskaya, I. S. (2017). Signatures of Ultrarelativistic Electron Loss in the Heart of the Outer Radiation Belt Measured by Van Allen Probes. *Journal of Geophysical Research: Space Physics*, *122*(10), 10,102-110,111. https://doi.org/10.1002/2017JA024485

Auster, H. U., Glassmeier, K. H., Magnes, W., Aydogar, O., Baumjohann, W., Constantinescu, D., . . . Wiedemann, M. (2008). The THEMIS Fluxgate

Magnetometer. *Space Science Reviews*, *141*, 235. 10.1007/s11214-008-9365-9

Bailey, D. K. (1968). Some quantitative aspects of electron precipitation in and near the auroral zone. *Reviews of Geophysics*, *6*(3), 289-346. https://doi.org/10.1029/RG006i003p00289

Baker, D. N., Blake, J. B., Callis, L. B., Cummings, J. R., Hovestadt, D., Kanekal, S., . . . Zwickl, R. D. (1994). Relativistic electron acceleration and decay time scales in the inner and outer radiation belts: SAMPEX. *Geophysical Research Letters*, *21*(6), 409-412. https://doi.org/10.1029/93GL03532

Baker, D. N., Kanekal, S. G., Hoxie, V. C., Batiste, S., Bolton, M., Li, X., . . . Friedel, R. (2014). The Relativistic Electron-Proton Telescope (REPT) Instrument on Board the Radiation Belt Storm Probes (RBSP) Spacecraft: Characterization of Earth's Radiation Belt High-Energy Particle Populations. In N. Fox & J. L. Burch (Eds.), *The Van Allen Probes Mission* (pp. 337-381). Springer US. https://doi.org/10.1007/978-1-4899-7433-4_11

Baker, D. N., Li, X., Blake, J. B., & Kanekal, S. (1998). Strong electron acceleration in the Earth's magnetosphere. *Advances in Space Research*, *21*(4), 609-613. https://doi.org/10.1016/S0273-1177(97)00970-8

Baker, D. N., Li, X., Turner, N., Allen, J. H., Bargatze, L. F., Blake, J. B., . . . Rostoker, G. (1997). Recurrent geomagnetic storms and relativistic electron enhancements in the outer magnetosphere: ISTP coordinated measurements. *Journal of Geophysical Research: Space Physics*, *102*(A7), 14141-14148. https://doi.org/10.1029/97JA00565

Balogh, A., Carr, C. M., Acuña, M. H., Dunlop, M. W., Beek, T. J., Brown, P., . . . Schwingenschuh, K. (2001). The Cluster Magnetic Field Investigation: overview of in-flight performance and initial results. *Ann. Geophys.*, *19*(10/12), 1207-1217. 10.5194/angeo-19-1207-2001

Baumjohann, W., & Treumann, R. (1996). *Basic space plasma physics*. World Scientific.

Berchem, J., & Russell, C. T. (1982). The thickness of the magnetopause current layer: ISEE 1 and 2 observations. *Journal of Geophysical Research: Space Physics*, *87*(A4), 2108-2114. https://doi.org/10.1029/JA087iA04p02108

Bingham, S. T., Mouikis, C. G., Kistler, L. M., Boyd, A. J., Paulson, K., Farrugia, C. J., . . . Kletzing, C. (2018). The Outer Radiation Belt Response to the Storm Time Development of Seed Electrons and Chorus Wave Activity During CME and CIR Driven Storms. *Journal of Geophysical Research: Space Physics*, *123*(12), 10,139-110,157. https://doi.org/10.1029/2018JA025963

Blake, J. B., Carranza, P. A., Claudepierre, S. G., Clemmons, J. H., Crain, W. R., Dotan, Y., . . . Zakrzewski, M. P. (2014). The Magnetic Electron Ion Spectrometer (MagEIS) Instruments Aboard the Radiation Belt Storm Probes (RBSP) Spacecraft. In N. Fox & J. L. Burch (Eds.), *The Van Allen Probes Mission* (pp. 383-421). Springer US. https://doi.org/10.1007/978-1-4899-7433-4_12

Blake, J. B., Mauk, B. H., Baker, D. N., Carranza, P., Clemmons, J. H., Craft, J., . . . Westlake, J. (2016). The Fly's Eye Energetic Particle

Spectrometer (FEEPS) Sensors for the Magnetospheric Multiscale (MMS) Mission. *Space Science Reviews*, *199*, 309. 10.1007/s11214-015-0163-x

Blum, L. W., Remya, B., Denton, M. H., & Schiller, Q. (2020). Persistent EMIC Wave Activity Across the Nightside Inner Magnetosphere. *Geophysical Research Letters*, *47*(6), e2020GL087009. https://doi.org/10.1029/2020GL087009

Blum, L. W., Schiller, Q., Li, X., Millan, R., Halford, A., & Woodger, L. (2013). New conjunctive CubeSat and balloon measurements to quantify rapid energetic electron precipitation. *Geophysical Research Letters*, *40*(22), 5833-5837. https://doi.org/10.1002/2013GL058546

Borovsky, J. E., & Denton, M. H. (2009). Relativistic-electron dropouts and recovery: A superposed epoch study of the magnetosphere and the solar wind. *Journal of Geophysical Research: Space Physics*, *114*(A2). https://doi.org/10.1029/2008JA013128

Bortnik, J., & Thorne, R. M. (2010). Transit time scattering of energetic electrons due to equatorially confined magnetosonic waves. *Journal of Geophysical Research: Space Physics*, *115*(A7). https://doi.org/10.1029/2010JA015283

Bortnik, J., Thorne, R. M., & Meredith, N. P. (2008). The unexpected origin of plasmaspheric hiss from discrete chorus emissions. *Nature*, *452*(7183), 62-66. 10.1038/nature06741

Bortnik, J., Thorne, R. M., O'Brien, T. P., Green, J. C., Strangeway, R. J., Shprits, Y. Y., & Baker, D. N. (2006). Observation of two distinct, rapid loss mechanisms during the 20 November 2003 radiation belt dropout event. *Journal of Geophysical Research: Space Physics*, *111*(A12). https://doi.org/10.1029/2006JA011802

Boscher, D., Bourdarie, S., O'Brien, T. P., & Guild, T. (2013). *The International Radiation Belt Environment Modeling (IRBEM) library.*

Boyd, A. J., Spence, H. E., Claudepierre, S. G., Fennell, J. F., Blake, J. B., Baker, D. N., . . . Turner, D. L. (2014). Quantifying the radiation belt seed population in the 17 March 2013 electron acceleration event. *Geophysical Research Letters*, *41*(7), 2275-2281. https://doi.org/10.1002/2014GL059626

Boynton, R. J., Mourenas, D., & Balikhin, M. A. (2017). Electron Flux Dropouts at L ∼ 4.2 From Global Positioning System Satellites: Occurrences, Magnitudes, and Main Driving Factors. *Journal of Geophysical Research: Space Physics*, *122*(11), 11,428-411,441. https://doi.org/10.1002/2017JA024523

Brizard, A. J., & Chan, A. A. (1999). Nonlinear relativistic gyrokinetic Vlasov-Maxwell equations. *Physics of Plasmas*, *6*(12), 4548-4558. 10.1063/1.873742

Burch, J. L., Moore, T. E., Torbert, R. B., & Giles, B. L. (2016). Magnetospheric Multiscale Overview and Science Objectives. *Space Science Reviews*, *199*(1), 5-21. 10.1007/s11214-015-0164-9

Cahill, J. L. J., & Winckler, J. R. (1992). Periodic magnetopause oscillations observed with the GOES satellites on March 24, 1991. *Journal of Geophysical Research: Space Physics*, *97*(A6), 8239-8243. https://doi.org/10.1029/92JA00433

Cannon, P., Angling, M., Barclay, L., Curry, C., Dyer, C., Edwards, R., . . . Jackson, D. (2013). *Extreme space weather: impacts on engineered systems and infrastructure*. Royal Academy of Engineering.

Capannolo, L., Li, W., Ma, Q., Zhang, X.-J., Redmon, R. J., Rodriguez, J. V., . . . Reeves, G. D. (2018). Understanding the Driver of Energetic Electron Precipitation Using Coordinated Multisatellite Measurements. *Geophysical Research Letters*, *45*(14), 6755-6765. https://doi.org/10.1029/2018GL078604

Carpenter, D. L. (1966). Whistler studies of the plasmapause in the magnetosphere: 1. Temporal variations in the position of the knee and some evidence on plasma motions near the knee. *Journal of Geophysical Research (1896-1977)*, *71*(3), 693-709. https://doi.org/10.1029/JZ071i003p00693

Case, N. A., & Wild, J. A. (2013). The location of the Earth's magnetopause: A comparison of modeled position and in situ Cluster data. *Journal of Geophysical Research: Space Physics*, *118*(10), 6127-6135. https://doi.org/10.1002/jgra.50572

Chappell, C. R. (1972). Recent satellite measurements of the morphology and dynamics of the plasmasphere. *Reviews of Geophysics*, *10*(4), 951-979. https://doi.org/10.1029/RG010i004p00951

Chaston, C. C., Bonnell, J. W., Wygant, J. R., Reeves, G. D., Baker, D. N., Melrose, D. B., & Cairns, I. H. (2017). Radial transport of radiation belt electrons in kinetic field-line resonances. *Geophysical Research Letters*, *44*(16), 8140-8148. https://doi.org/10.1002/2017GL074587

Chen, A., & Wolf, R. (1972). Effects on the plasmasphere of a time-varying convection electric field. *Planetary and Space Science*, *20*(4), 483-509. https://doi.org/10.1007/BF00152248

Chen, L., & Hasegawa, A. (1974). A theory of long-period magnetic pulsations: 2. Impulse excitation of surface eigenmode. *Journal of Geophysical Research (1896-1977)*, *79*(7), 1033-1037. https://doi.org/10.1029/JA079i007p01033

Chen, L., Li, W., Bortnik, J., & Thorne, R. M. (2012). Amplification of whistler-mode hiss inside the plasmasphere. *Geophysical Research Letters*, *39*(8). https://doi.org/10.1029/2012GL051488

Chen, Y., Friedel, R. H. W., & Reeves, G. D. (2006). Phase space density distributions of energetic electrons in the outer radiation belt during two Geospace Environment Modeling Inner Magnetosphere/Storms selected storms. *Journal of Geophysical Research: Space Physics*, *111*(A11). https://doi.org/10.1029/2006JA011703

Claudepierre, S. G., Elkington, S. R., & Wiltberger, M. (2008). Solar wind driving of magnetospheric ULF waves: Pulsations driven by velocity shear at the magnetopause. *Journal of Geophysical Research: Space Physics*, *113*(A5). https://doi.org/10.1029/2007JA012890

Claudepierre, S. G., Hudson, M. K., Lotko, W., Lyon, J. G., & Denton, R. E. (2010). Solar wind driving of magnetospheric ULF waves: Field line resonances driven by dynamic pressure fluctuations. *Journal of Geophysical Research: Space Physics*, *115*(A11). https://doi.org/10.1029/2010JA015399

Claudepierre, S. G., O'Brien, T. P., Fennell, J. F., Blake, J. B., Clemmons, J. H., Looper, M. D., . . . Spence, H. E. (2017). The hidden dynamics of

relativistic electrons (0.7–1.5 MeV) in the inner zone and slot region. *Journal of Geophysical Research: Space Physics*, *122*(3), 3127-3144. https://doi.org/10.1002/2016JA023719

Clilverd, M. A., Rodger, C. J., Thomson, N. R., Brundell, J. B., Ulich, T., Lichtenberger, J., . . . Turunen, E. (2009). Remote sensing space weather events: Antarctic-Arctic Radiation-belt (Dynamic) Deposition-VLF Atmospheric Research Konsortium network. *Space Weather*, *7*(4). https://doi.org/10.1029/2008SW000412

Collinson, G. A., & Kataria, D. O. (2010). On variable geometric factor systems for top-hat electrostatic space plasma analyzers. *Measurement Science and Technology*, *21*(10), 105903. 10.1088/0957-0233/21/10/105903

Cornwall, J. M. (1965). Cyclotron instabilities and electromagnetic emission in the ultra low frequency and very low frequency ranges. *Journal of Geophysical Research (1896-1977)*, *70*(1), 61-69. https://doi.org/10.1029/JZ070i001p00061

Cornwall, J. M., Coroniti, F. V., & Thorne, R. M. (1970). Turbulent loss of ring current protons. *Journal of Geophysical Research (1896-1977)*, *75*(25), 4699-4709. https://doi.org/10.1029/JA075i025p04699

Coroniti, F. V., & Kennel, C. F. (1972). Changes in magnetospheric configuration during the substorm growth phase. *Journal of Geophysical Research (1896-1977)*, *77*(19), 3361-3370. https://doi.org/10.1029/JA077i019p03361

Criswell, D. R. (1969). Pc 1 micropulsation activity and magnetospheric amplification of 0.2- to 5.0-Hz hydromagnetic waves. *Journal of Geophysical Research (1896-1977)*, *74*(1), 205-224. https://doi.org/10.1029/JA074i001p00205

Crooker, N. U., & Siscoe, G. L. (1975). Subsonic magnetosheath observations from Explorer 33. *Journal of Geophysical Research (1896-1977)*, *80*(31), 4368-4371. https://doi.org/10.1029/JA080i031p04368

Daglis, I. A., Thorne, R. M., Baumjohann, W., & Orsini, S. (1999). The terrestrial ring current: Origin, formation, and decay. *Reviews of Geophysics*, *37*(4), 407-438. https://doi.org/10.1029/1999RG900009

Degeling, A. W., Ozeke, L. G., Rankin, R., Mann, I. R., & Kabin, K. (2008). Drift resonant generation of peaked relativistic electron distributions by Pc 5 ULF waves. *Journal of Geophysical Research: Space Physics*, *113*(A2). https://doi.org/10.1029/2007JA012411

Desai, R. T., Eastwood, J. P., Horne, R. B., Allison, H. J., Allanson, O., Watt, C. E. J., . . . Chittenden, J. P. (2021a). Drift Orbit Bifurcations and Cross-field Transport in the Outer Radiation Belt: Global MHD and Integrated Test-Particle Simulations. *Journal of Geophysical Research: Space Physics*, e2021JA029802. https://doi.org/10.1029/2021JA029802

Desai, R. T., Freeman, M. P., Eastwood, J. P., Eggington, J. W. B., Archer, M. O., Shprits, Y. Y., . . . Horne, R. B. (2021b). Interplanetary Shock-Induced Magnetopause Motion: Comparison Between Theory and Global Magnetohydrodynamic Simulations. *Geophysical Research Letters*, *48*(16), e2021GL092554. https://doi.org/10.1029/2021GL092554

Dessler, A. J., Francis, W. E., & Parker, E. N. (1960). Geomagnetic storm sudden-commencement rise times. *Journal of Geophysical Research*

(1896-1977), *65*(9), 2715-2719. https://doi.org/10.1029/JZ065i009p02715

Dessler, A. J., & Karplus, R. (1961). Some effects of diamagnetic ring currents on Van Allen radiation. *Journal of Geophysical Research (1896-1977)*, *66*(8), 2289-2295. https://doi.org/10.1029/JZ066i008p02289

Dmitriev, A. V., Suvorova, A. V., Chao, J.-K., Wang, C. B., Rastaetter, L., Panasyuk, M. I., . . . Myagkova, I. N. (2014). Anomalous dynamics of the extremely compressed magnetosphere during 21 January 2005 magnetic storm. *Journal of Geophysical Research: Space Physics*, *119*(2), 877-896. https://doi.org/10.1002/2013JA019534

Dungey, J. W. (1961). Interplanetary magnetic field and the auroral zones. *Physical Review Letters*, *6*(2), 47. c10.1103/PhysRevLett.6.47

Echer, E., Gonzalez, W. D., & Tsurutani, B. T. (2011). Statistical studies of geomagnetic storms with peak Dst≤−50nT from 1957 to 2008. *Journal of Atmospheric and Solar-Terrestrial Physics*, *73*(11), 1454-1459. https://doi.org/10.1016/j.jastp.2011.04.021

Elkington, S. R., Hudson, M. K., & Chan, A. A. (1999). Acceleration of relativistic electrons via drift-resonant interaction with toroidal-mode Pc-5 ULF oscillations. *Geophysical Research Letters*, *26*(21), 3273-3276. https://doi.org/10.1029/1999GL003659

Elkington, S. R., Hudson, M. K., & Chan, A. A. (2003). Resonant acceleration and diffusion of outer zone electrons in an asymmetric geomagnetic field. *Journal of Geophysical Research: Space Physics*, *108*(A3). https://doi.org/10.1029/2001JA009202

Engebretson, M. J., Peterson, W. K., Posch, J. L., Klatt, M. R., Anderson, B. J., Russell, C. T., . . . Fukunishi, H. (2002). Observations of two types of Pc 1–2 pulsations in the outer dayside magnetosphere. *Journal of Geophysical Research: Space Physics*, *107*(A12), SMP 20-21-SMP 20-20. https://doi.org/10.1029/2001JA000198

Escoubet, C. P., Fehringer, M., & Goldstein, M. (2001). Introduction
The Cluster mission. *Ann. Geophys.*, *19*(10/12), 1197-1200. 10.5194/angeo-19-1197-2001

Fälthammar, C.-G. (1965). Effects of time-dependent electric fields on geomagnetically trapped radiation. *Journal of Geophysical Research (1896-1977)*, *70*(11), 2503-2516. https://doi.org/10.1029/JZ070i011p02503

Farris, M. H., & Russell, C. T. (1994). Determining the standoff distance of the bow shock: Mach number dependence and use of models. *Journal of Geophysical Research: Space Physics*, *99*(A9), 17681-17689. https://doi.org/10.1029/94JA01020

Fennell, J. F., Claudepierre, S. G., Blake, J. B., O'Brien, T. P., Clemmons, J. H., Baker, D. N., . . . Reeves, G. D. (2015). Van Allen Probes show that the inner radiation zone contains no MeV electrons: ECT/MagEIS data. *Geophysical Research Letters*, *42*(5), 1283-1289. https://doi.org/10.1002/2014GL062874

Forsyth, C., Rae, I. J., Murphy, K. R., Freeman, M. P., Huang, C.-L., Spence, H. E., . . . Watt, C. E. J. (2016). What effect do substorms have on the content of the radiation belts? *Journal of Geophysical Research: Space Physics*, *121*(7), 6292-6306. https://doi.org/10.1002/2016JA022620

Freeman, M., Freeman, N., & Farrugia, C. (1995). A linear perturbation analysis of magnetopause motion in the Newton-Busemann limit. Annales Geophysicae,

Friedel, R. H. W., Reeves, G. D., & Obara, T. (2002). Relativistic electron dynamics in the inner magnetosphere — a review. *Journal of Atmospheric and Solar-Terrestrial Physics*, *64*(2), 265-282. https://doi.org/10.1016/S1364-6826(01)00088-8

Gabrielse, C., Angelopoulos, V., Runov, A., & Turner, D. L. (2014). Statistical characteristics of particle injections throughout the equatorial magnetotail. *Journal of Geophysical Research: Space Physics*, *119*(4), 2512-2535. https://doi.org/10.1002/2013JA019638

Gao, X., Li, W., Bortnik, J., Thorne, R. M., Lu, Q., Ma, Q., . . . Wang, S. (2015). The effect of different solar wind parameters upon significant relativistic electron flux dropouts in the magnetosphere. *Journal of Geophysical Research: Space Physics*, *120*(6), 4324-4337. https://doi.org/10.1002/2015JA021182

Glauert, S. A., Horne, R. B., & Meredith, N. P. (2014). Three-dimensional electron radiation belt simulations using the BAS Radiation Belt Model with new diffusion models for chorus, plasmaspheric hiss, and lightning-generated whistlers. *Journal of Geophysical Research: Space Physics*, *119*(1), 268-289. https://doi.org/10.1002/2013JA019281

Gloag, J. M., Lucek, E. A., Alconcel, L.-N., Balogh, A., Brown, P., Carr, C. M., . . . Soucek, J. (2010). FGM Data Products in the CAA. In H. Laakso, M. Taylor, & C. P. Escoubet, *The Cluster Active Archive* Dordrecht.

Gosling, J. T., Asbridge, J. R., Bame, S. J., Feldman, W. C., Paschmann, G., Sckopke, N., & Russell, C. T. (1982). Evidence for quasi-stationary reconnection at the dayside magnetopause. *Journal of Geophysical Research: Space Physics*, *87*(A4), 2147-2158. https://doi.org/10.1029/JA087iA04p02147

Green, J. C., & Kivelson, M. G. (2004). Relativistic electrons in the outer radiation belt: Differentiating between acceleration mechanisms. *Journal of Geophysical Research: Space Physics*, *109*(A3). https://doi.org/10.1029/2003JA010153

Haaland, S., Hasegawa, H., De Keyser, J., & Maes, L. (2017). Dawn-Dusk Asymmetries at the Terrestrial Magnetopause. In *Dawn-Dusk Asymmetries in Planetary Plasma Environments* (pp. 73-84). https://doi.org/https://doi.org/10.1002/9781119216346.ch6

Hasegawa, H., Fujimoto, M., Phan, T. D., Rème, H., Balogh, A., Dunlop, M. W., . . . TanDokoro, R. (2004). Transport of solar wind into Earth's magnetosphere through rolled-up Kelvin–Helmholtz vortices. *Nature*, *430*(7001), 755-758. 10.1038/nature02799

Henderson, M., Morley, S., Niehof, J., & Larsen, B. (2018). *drsteve/LANLGeoMag: v1.5.16 (v1.5.16).* https://doi.org/https://doi.org/10.5281/zenodo.1195041

Hendry, A. T., Rodger, C. J., Clilverd, M. A., Thomson, N. R., Morley, S. K., & Raita, T. (2012). Rapid Radiation Belt Losses Occurring During High-Speed Solar Wind Stream–Driven Storms: Importance of Energetic Electron Precipitation. In *Dynamics of the Earth's Radiation Belts and Inner Magnetosphere* (pp. 213-224). https://doi.org/https://doi.org/10.1029/2012GM001299

Herrera, D., Maget, V. F., & Sicard-Piet, A. (2016). Characterizing magnetopause shadowing effects in the outer electron radiation belt during geomagnetic storms. *Journal of Geophysical Research: Space Physics*, *121*(10), 9517-9530. https://doi.org/10.1002/2016JA022825

Hietala, H., Kilpua, E. K. J., Turner, D. L., & Angelopoulos, V. (2014). Depleting effects of ICME-driven sheath regions on the outer electron radiation belt. *Geophysical Research Letters*, *41*(7), 2258-2265. https://doi.org/10.1002/2014GL059551

Hofmann-Wellenhof, B., Lichtenegger, H., & Collins, J. (2012). *Global positioning system: theory and practice*. Springer Science & Business Media.

Hones, E. W. (1976). Observations in the Earth's magnetotail relating to magnetic merging. *Solar Physics*, *47*(1), 101-113. https://doi.org/10.1007/BF00152248

Horne, R. B., & Thorne, R. M. (1998). Potential waves for relativistic electron scattering and stochastic acceleration during magnetic storms. *Geophysical Research Letters*, *25*(15), 3011-3014. https://doi.org/10.1029/98GL01002

Horne, R. B., Thorne, R. M., Glauert, S. A., Albert, J. M., Meredith, N. P., & Anderson, R. R. (2005). Timescale for radiation belt electron acceleration by whistler mode chorus waves. *Journal of Geophysical Research: Space Physics*, *110*(A3). https://doi.org/10.1029/2004JA010811

Horne, R. B., Thorne, R. M., Glauert, S. A., Meredith, N. P., Pokhotelov, D., & Santolík, O. (2007). Electron acceleration in the Van Allen radiation belts by fast magnetosonic waves. *Geophysical Research Letters*, *34*(17). https://doi.org/10.1029/2007GL030267

Hughes, W. J. (1994). Magnetospheric ULF Waves: A Tutorial with a Historical Perspective. In *Solar Wind Sources of Magnetospheric Ultra-Low-Frequency Waves* (pp. 1-11). https://doi.org/https://doi.org/10.1029/GM081p0001

Hwang, J. A., Lee, D.-Y., Lyons, L. R., Smith, A. J., Zou, S., Min, K. W., . . . Park, Y. D. (2007). Statistical significance of association between whistler-mode chorus enhancements and enhanced convection periods during high-speed streams. *Journal of Geophysical Research: Space Physics*, *112*(A9). https://doi.org/10.1029/2007JA012388

Iyemori, T. (1990). Storm-Time Magnetospheric Currents Inferred from Mid-Latitude Geomagnetic Field Variations. *Journal of geomagnetism and geoelectricity*, *42*(11), 1249-1265. 10.5636/jgg.42.1249

Iyemori, T., Takeda, M., Nose, M., Odagi, Y., & Toh, H. (2010). *Mid-latitude geomagnetic indices "ASY" and "SYM" for 2009 (Provisional)* (Data Analysis Center for Geomagnetism and Space Magnetism, Graduate School of Science, Kyoto University, Japan, Issue.

Jacobs, J. A., Kato, Y., Matsushita, S., & Troitskaya, V. A. (1964). Classification of geomagnetic micropulsations. *Journal of Geophysical Research (1896-1977)*, *69*(1), 180-181. https://doi.org/10.1029/JZ069i001p00180

Jacobsen, K. S., Phan, T. D., Eastwood, J. P., Sibeck, D. G., Moen, J. I., Angelopoulos, V., . . . Fornaçon, K.-H. (2009). THEMIS observations of extreme magnetopause motion caused by a hot flow anomaly. *Journal*

of Geophysical Research: Space Physics, *114*(A8). https://doi.org/10.1029/2008JA013873

Jaynes, A. N., Ali, A. F., Elkington, S. R., Malaspina, D. M., Baker, D. N., Li, X., . . . Wygant, J. R. (2018). Fast Diffusion of Ultrarelativistic Electrons in the Outer Radiation Belt: 17 March 2015 Storm Event. *Geophysical Research Letters*, *45*(20), 10,874-810,882. https://doi.org/10.1029/2018GL079786

Kang, S.-B., Fok, M.-C., Komar, C., Glocer, A., Li, W., & Buzulukova, N. (2018). An Energetic Electron Flux Dropout Due to Magnetopause Shadowing on 1 June 2013. *Journal of Geophysical Research: Space Physics*, *123*(2), 1178-1190. https://doi.org/10.1002/2017JA024879

Kellogg, P. J. (1959). Possible explanation of the radiation observed by Van Allen at high altitudes in satellites. *Il Nuovo Cimento (1955-1965)*, *11*(1), 48-66.

Kennel, C. F., & Petschek, H. E. (1966). Limit on stably trapped particle fluxes. *Journal of Geophysical Research (1896-1977)*, *71*(1), 1-28. https://doi.org/10.1029/JZ071i001p00001

Kepko, L., Spence, H. E., & Singer, H. J. (2002). ULF waves in the solar wind as direct drivers of magnetospheric pulsations. *Geophysical Research Letters*, *29*(8), 39-31-39-34. https://doi.org/10.1029/2001GL014405

Kilpua, E., Balogh, A., von Steiger, R., & Liu, Y. (2017). Geoeffective properties of solar transients and stream interaction regions. *Space Science Reviews*, *212*(3), 1271-1314. https://doi.org/10.1007/s11214-017-0411-3

Kilpua, E. K. J., Hietala, H., Turner, D. L., Koskinen, H. E. J., Pulkkinen, T. I., Rodriguez, J. V., . . . Spence, H. E. (2015). Unraveling the drivers of the storm time radiation belt response. *Geophysical Research Letters*, *42*(9), 3076-3084. https://doi.org/10.1002/2015GL063542

Kilpua, E. K. J., Turner, D. L., Jaynes, A. N., Hietala, H., Koskinen, H. E. J., Osmane, A., . . . Claudepierre, S. G. (2019). Outer Van Allen Radiation Belt Response to Interacting Interplanetary Coronal Mass Ejections. *Journal of Geophysical Research: Space Physics*, *124*(3), 1927-1947. https://doi.org/10.1029/2018JA026238

Kim, K.-C., & Lee, D.-Y. (2014). Magnetopause structure favorable for radiation belt electron loss. *Journal of Geophysical Research: Space Physics*, *119*(7), 5495-5508. https://doi.org/10.1002/2014JA019880

Kletzing, C., Kurth, W., Acuna, M., MacDowall, R., Torbert, R., Averkamp, T., . . . Connerney, J. (2013). The electric and magnetic field instrument suite and integrated science (EMFISIS) on RBSP. *Space Science Reviews*, *179*(1-4), 127-181. 10.1007/s11214-013-9993-6

Kokubun, S., Yamamoto, T., Acu, ntilde, a, M. H., Hayashi, K., . . . Kawano, H. (1994). The GEOTAIL Magnetic Field Experiment. *Journal of geomagnetism and geoelectricity*, *46*(1), 7-21. 10.5636/jgg.46.7

Korth, A., Kremser, G., Daly, P. W., & Amata, E. (1982). Observations of field-aligned energetic electron and ion distributions near the magnetopause at geosynchronous orbit. *Journal of Geophysical Research: Space Physics*, *87*(A12), 10413-10419. https://doi.org/10.1029/JA087iA12p10413

Kudela, K., Sibeck, D. G., Slivka, M., Fischer, S., Lutsenko, V. N., & Venkatesan, D. (1992). Energetic electrons and ions in the

magnetosheath at low and medium latitudes: Prognoz 10 data. *Journal of Geophysical Research: Space Physics*, *97*(A10), 14849-14857. https://doi.org/10.1029/92JA01134

Landau, L. D. (1946). *Oscillations of an electron plasma*. US Atomic Energy Commission.

Lejosne, S., & Kollmann, P. (2020). Radiation Belt Radial Diffusion at Earth and Beyond. *Space Science Reviews*, *216*(1), 19. 10.1007/s11214-020-0642-6

Lenchek, A. M., Singer, S. F., & Wentworth, R. C. (1961). Geomagnetically trapped electrons from cosmic ray albedo neutrons. *Journal of Geophysical Research (1896-1977)*, *66*(12), 4027-4046. https://doi.org/10.1029/JZ066i012p04027

Li, W., Thorne, R. M., Angelopoulos, V., Bonnell, J. W., McFadden, J. P., Carlson, C. W., . . . Auster, H. U. (2009). Evaluation of whistler-mode chorus intensification on the nightside during an injection event observed on the THEMIS spacecraft. *Journal of Geophysical Research: Space Physics*, *114*(A1). https://doi.org/10.1029/2008JA013554

Li, X., Baker, D. N., Temerin, M., Cayton, T. E., Reeves, E. G. D., Christensen, R. A., . . . Kanekal, S. G. (1997a). Multisatellite observations of the outer zone electron variation during the November 3–4, 1993, magnetic storm. *Journal of Geophysical Research: Space Physics*, *102*(A7), 14123-14140. https://doi.org/10.1029/97JA01101

Li, X., Baker, D. N., Temerin, M., Larson, D., Lin, R. P., Reeves, G. D., . . . Mewaldt, R. A. (1997b). Are energetic electrons in the solar wind the source of the outer radiation belt? *Geophysical Research Letters*, *24*(8), 923-926. https://doi.org/10.1029/97GL00543

Lin, R. L., Zhang, X. X., Liu, S. Q., Wang, Y. L., & Gong, J. C. (2010). A three-dimensional asymmetric magnetopause model. *Journal of Geophysical Research: Space Physics*, *115*(A4). https://doi.org/10.1029/2009JA014235

Liu, W., Tu, W., Li, X., Sarris, T., Khotyaintsev, Y., Fu, H., . . . Shi, Q. (2016). On the calculation of electric diffusion coefficient of radiation belt electrons with in situ electric field measurements by THEMIS. *Geophysical Research Letters*, *43*(3), 1023-1030. https://doi.org/10.1002/2015GL067398

Loewe, C. A., & Prölss, G. W. (1997). Classification and mean behavior of magnetic storms. *Journal of Geophysical Research: Space Physics*, *102*(A7), 14209-14213. https://doi.org/10.1029/96JA04020

Lorentzen, K. R., Mazur, J. E., Looper, M. D., Fennell, J. F., & Blake, J. B. (2002). Multisatellite observations of MeV ion injections during storms. *Journal of Geophysical Research: Space Physics*, *107*(A9), SMP 7-1-SMP 7-11. https://doi.org/10.1029/2001JA000276

Loto'aniu, T. M., Singer, H. J., Waters, C. L., Angelopoulos, V., Mann, I. R., Elkington, S. R., & Bonnell, J. W. (2010). Relativistic electron loss due to ultralow frequency waves and enhanced outward radial diffusion. *Journal of Geophysical Research: Space Physics*, *115*(A12). https://doi.org/10.1029/2010JA015755

Lui, A. T. Y. (1991). A synthesis of magnetospheric substorm models. *Journal of Geophysical Research: Space Physics*, *96*(A2), 1849-1856. https://doi.org/10.1029/90JA02430

Lyons, L. R., & Thorne, R. M. (1972). Parasitic pitch angle diffusion of radiation belt particles by ion cyclotron waves. *Journal of Geophysical Research (1896-1977)*, *77*(28), 5608-5616. https://doi.org/10.1029/JA077i028p05608

Lyons, L. R., & Thorne, R. M. (1973). Equilibrium structure of radiation belt electrons. *Journal of Geophysical Research (1896-1977)*, *78*(13), 2142-2149. https://doi.org/10.1029/JA078i013p02142

Ma, Q., Li, W., Bortnik, J., Thorne, R. M., Chu, X., Ozeke, L. G., . . . Claudepierre, S. G. (2018). Quantitative Evaluation of Radial Diffusion and Local Acceleration Processes During GEM Challenge Events. *Journal of Geophysical Research: Space Physics*, *123*(3), 1938-1952. https://doi.org/10.1002/2017JA025114

Ma, X., Xiang, Z., Ni, B., Fu, S., Cao, X., Hua, M., . . . Zhu, Q. (2020). On the loss mechanisms of radiation belt electron dropouts during the 12 September 2014 geomagnetic storm. *Earth and Planetary Physics*, *4*(6), 598-610. https://doi.org/10.26464/epp2020060

Mann, I. R., O'Brien, T. P., & Milling, D. K. (2004). Correlations between ULF wave power, solar wind speed, and relativistic electron flux in the magnetosphere: solar cycle dependence. *Journal of Atmospheric and Solar-Terrestrial Physics*, *66*(2), 187-198. https://doi.org/10.1016/j.jastp.2003.10.002

Mann, I. R., & Ozeke, L. G. (2016). How quickly, how deeply, and how strongly can dynamical outer boundary conditions impact Van Allen radiation belt morphology? *Journal of Geophysical Research: Space Physics*, *121*(6), 5553-5558. https://doi.org/10.1002/2016JA022647

Matsumura, C., Miyoshi, Y., Seki, K., Saito, S., Angelopoulos, V., & Koller, J. (2011). Outer radiation belt boundary location relative to the magnetopause: Implications for magnetopause shadowing. *Journal of Geophysical Research: Space Physics*, *116*(A6). https://doi.org/10.1029/2011JA016575

Mauk, B., Blake, J., Baker, D., Clemmons, J., Reeves, G., Spence, H. E., . . . Cooper, S. (2016). The energetic particle detector (EPD) investigation and the energetic ion spectrometer (EIS) for the magnetospheric multiscale (MMS) mission. *Space Science Reviews*, *199*(1-4), 471-514. https://doi.org/10.1007/s11214-014-0055-5

Mauk, B. H., Fox, N. J., Kanekal, S. G., Kessel, R. L., Sibeck, D. G., & Ukhorskiy, A. (2014). Science Objectives and Rationale for the Radiation Belt Storm Probes Mission. In N. Fox & J. L. Burch (Eds.), *The Van Allen Probes Mission* (pp. 3-27). Springer US. https://doi.org/10.1007/978-1-4899-7433-4_2

McFadden, J. P., Carlson, C. W., Larson, D., Ludlam, M., Abiad, R., Elliott, B., . . . Angelopoulos, V. (2008). The THEMIS ESA Plasma Instrument and In-flight Calibration. *Space Science Reviews*, *141*(1), 277-302. 10.1007/s11214-008-9440-2

McIlwain, C. E. (1961). Coordinates for mapping the distribution of magnetically trapped particles. *Journal of Geophysical Research (1896-1977)*, *66*(11), 3681-3691. https://doi.org/10.1029/JZ066i011p03681

McPherron, R. L., Russell, C. T., & Aubry, M. P. (1973). Satellite studies of magnetospheric substorms on August 15, 1968: 9. Phenomenological

model for substorms. *Journal of Geophysical Research (1896-1977)*, *78*(16), 3131-3149. https://doi.org/10.1029/JA078i016p03131

Meredith, N. P., Horne, R. B., & Anderson, R. R. (2001). Substorm dependence of chorus amplitudes: Implications for the acceleration of electrons to relativistic energies. *Journal of Geophysical Research: Space Physics*, *106*(A7), 13165-13178. https://doi.org/10.1029/2000JA900156

Min, K., Lee, J., Keika, K., & Li, W. (2012). Global distribution of EMIC waves derived from THEMIS observations. *Journal of Geophysical Research: Space Physics*, *117*(A5). https://doi.org/10.1029/2012JA017515

Miyoshi, Y., Morioka, A., Misawa, H., Obara, T., Nagai, T., & Kasahara, Y. (2003). Rebuilding process of the outer radiation belt during the 3 November 1993 magnetic storm: NOAA and Exos-D observations. *Journal of Geophysical Research: Space Physics*, *108*(A1), SMP 3-1-SMP 3-15. https://doi.org/10.1029/2001JA007542

Morley, S. K., Friedel, R. H. W., Cayton, T. E., & Noveroske, E. (2010a). A rapid, global and prolonged electron radiation belt dropout observed with the Global Positioning System constellation. *Geophysical Research Letters*, *37*(6). https://doi.org/10.1029/2010GL042772

Morley, S. K., Friedel, R. H. W., Spanswick, E. L., Reeves, G. D., Steinberg, J. T., Koller, J., . . . Noveroske, E. (2010b). Dropouts of the outer electron radiation belt in response to solar wind stream interfaces: Global positioning system observations. *Proceedings of the Royal Society A: Mathematical, Physical and Engineering Sciences*, *466*(2123), 3329-3350.

Mukai, T., Machida, S., Saito, Y., Hirahara, M., Terasawa, T., Kaya, N., . . . Nishida, A. (1994). The Low Energy Particle (LEP) Experiment onboard the GEOTAIL Satellite. *Journal of geomagnetism and geoelectricity*, *46*(8), 669-692. 10.5636/jgg.46.669

Murphy, K. R., Mann, I. R., & Sibeck, D. G. (2015). On the dependence of storm time ULF wave power on magnetopause location: Impacts for ULF wave radial diffusion. *Geophysical Research Letters*, *42*(22), 9676-9684. https://doi.org/10.1002/2015GL066592

Murphy, K. R., Watt, C. E. J., Mann, I. R., Jonathan Rae, I., Sibeck, D. G., Boyd, A. J., . . . Fennell, J. (2018). The Global Statistical Response of the Outer Radiation Belt During Geomagnetic Storms. *Geophysical Research Letters*, *45*(9), 3783-3792. https://doi.org/10.1002/2017GL076674

Nachar, N. (2008). The Mann-Whitney U: A Test for Assessing Whether Two Independent Samples Come from the Same Distribution. *Tutorials in Quantitative Methods for Psychology*, *4*(1), 13-20. 10.20982/tqmp.04.1.p013 (IN FILE)

Ni, B., Shprits, Y., Hartinger, M., Angelopoulos, V., Gu, X., & Larson, D. (2011). Analysis of radiation belt energetic electron phase space density using THEMIS SST measurements: Cross-satellite calibration and a case study. *Journal of Geophysical Research: Space Physics*, *116*(A3). https://doi.org/10.1029/2010JA016104

Nishida, A. (1994). The Geotail Mission. *Geophysical Research Letters*, *21*(25), 2871-2873. https://doi.org/10.1029/94GL01223

O'Brien, T. P., Looper, M. D., & Blake, J. B. (2004). Quantification of relativistic electron microburst losses during the GEM storms. *Geophysical Research Letters*, *31*(4). https://doi.org/10.1029/2003GL018621

O'Brien, T. P., McPherron, R. L., Sornette, D., Reeves, G. D., Friedel, R., & Singer, H. J. (2001). Which magnetic storms produce relativistic electrons at geosynchronous orbit? *Journal of Geophysical Research: Space Physics*, *106*(A8), 15533-15544. https://doi.org/10.1029/2001JA000052

Olifer, L., Mann, I. R., Morley, S. K., Ozeke, L. G., & Choi, D. (2018). On the Role of Last Closed Drift Shell Dynamics in Driving Fast Losses and Van Allen Radiation Belt Extinction. *Journal of Geophysical Research: Space Physics*, *123*(5), 3692-3703. https://doi.org/10.1029/2018JA025190

Olifer, L., Mann, I. R., Ozeke, L. G., Morley, S. K., & Louis, H. L. (2021). On the Formation of Phantom Electron Phase Space Density Peaks in Single Spacecraft Radiation Belt Data. *Geophysical Research Letters*, *48*(11), e2020GL092351. https://doi.org/10.1029/2020GL092351

Oliveira, D. (2017). Magnetohydrodynamic shocks in the interplanetary space: A theoretical review. *Brazilian Journal of Physics*, *47*(1), 81-95. https://doi.org/10.1007/s13538-016-0472-x

Onsager, T., Grubb, R., Kunches, J., Matheson, L., Speich, D., Zwickl, R., & Sauer, H. (1996). *Operational uses of the GOES energetic particle detectors* (Vol. 2812). SPIE. https://doi.org/10.1117/12.254075

Onsager, T. G., Rostoker, G., Kim, H.-J., Reeves, G. D., Obara, T., Singer, H. J., & Smithtro, C. (2002). Radiation belt electron flux dropouts: Local time, radial, and particle-energy dependence. *Journal of Geophysical Research: Space Physics*, *107*(A11), SMP 21-21-SMP 21-11. https://doi.org/10.1029/2001JA000187

Ozeke, L. G., Mann, I. R., Claudepierre, S. G., Henderson, M., Morley, S. K., Murphy, K. R., . . . Baker, D. N. (2019). The March 2015 Superstorm Revisited: Phase Space Density Profiles and Fast ULF Wave Diffusive Transport. *Journal of Geophysical Research: Space Physics*, *124*(2), 1143-1156. https://doi.org/10.1029/2018JA026326

Ozeke, L. G., Mann, I. R., Olifer, L., Dufresne, K. Y., Morley, S. K., Claudepierre, S. G., . . . Degeling, A. W. (2020). Rapid Outer Radiation Belt Flux Dropouts and Fast Acceleration During the March 2015 and 2013 Storms: The Role of Ultra-Low Frequency Wave Transport From a Dynamic Outer Boundary. *Journal of Geophysical Research: Space Physics*, *125*(2), e2019JA027179. https://doi.org/10.1029/2019JA027179

Öztürk, M. K., & Wolf, R. A. (2007). Bifurcation of drift shells near the dayside magnetopause. *Journal of Geophysical Research: Space Physics*, *112*(A7). https://doi.org/10.1029/2006JA012102

Petrinec, S. M. (2002). The location of the Earth's bow shock. *Planetary and Space Science*, *50*(5), 541-547. https://doi.org/10.1016/S0032-0633(02)00033-8

Plaschke, F., Glassmeier, K.-H., Auster, H. U., Constantinescu, O. D., Magnes, W., Angelopoulos, V., . . . McFadden, J. P. (2009a). Standing Alfvén waves at the magnetopause. *Geophysical Research Letters*, *36*(2). https://doi.org/10.1029/2008GL036411

Plaschke, F., Glassmeier, K. H., Sibeck, D. G., Auster, H. U., Constantinescu, O. D., Angelopoulos, V., & Magnes, W. (2009b). Magnetopause surface oscillation frequencies at different solar wind conditions. *Ann. Geophys.*, *27*(12), 4521-4532. 10.5194/angeo-27-4521-2009

Plaschke, F., Hietala, H., Angelopoulos, V., & Nakamura, R. (2016). Geoeffective jets impacting the magnetopause are very common. *Journal of Geophysical Research: Space Physics*, *121*(4), 3240-3253. https://doi.org/10.1002/2016JA022534

Plaschke, F., Hietala, H., Archer, M., Blanco-Cano, X., Kajdič, P., Karlsson, T., . . . Sibeck, D. (2018). Jets Downstream of Collisionless Shocks. *Space Science Reviews*, *214*(5), 81. 10.1007/s11214-018-0516-3

Pu, Z.-Y., & Kivelson, M. G. (1983). Kelvin:Helmholtz Instability at the magnetopause: Solution for compressible plasmas. *Journal of Geophysical Research: Space Physics*, *88*(A2), 841-852. https://doi.org/10.1029/JA088iA02p00841

Raab, W., Branduardi-Raymont, G., Wang, C., Dai, L., Donovan, E., Enno, G., . . . Zheng, J. (2016). *SMILE: a joint ESA/CAS mission to investigate the interaction between the solar wind and Earth's magnetosphere* (Vol. 9905). SPIE. https://doi.org/10.1117/12.2231984

Rae, I. J., Donovan, E. F., Mann, I. R., Fenrich, F. R., Watt, C. E. J., Milling, D. K., . . . Balogh, A. (2005). Evolution and characteristics of global Pc5 ULF waves during a high solar wind speed interval. *Journal of Geophysical Research: Space Physics*, *110*(A12). https://doi.org/10.1029/2005JA011007

Raymer, K. (2018). *Influences on the location of the Earth's magnetopause* University of Leicester]. http://hdl.handke.net/2381/43064

Redmon, R. J., Seaton, D. B., Steenburgh, R., He, J., & Rodriguez, J. V. (2018). September 2017's Geoeffective Space Weather and Impacts to Caribbean Radio Communications During Hurricane Response. *Space Weather*, *16*(9), 1190-1201. https://doi.org/10.1029/2018SW001897

Reeves, G. D., Chen, Y., Cunningham, G. S., Friedel, R. W. H., Henderson, M. G., Jordanova, V. K., . . . Zaharia, S. (2012). Dynamic Radiation Environment Assimilation Model: DREAM. *Space Weather*, *10*(3). https://doi.org/10.1029/2011SW000729

Reeves, G. D., Friedel, R. H. W., Larsen, B. A., Skoug, R. M., Funsten, H. O., Claudepierre, S. G., . . . Baker, D. N. (2016). Energy-dependent dynamics of keV to MeV electrons in the inner zone, outer zone, and slot regions. *Journal of Geophysical Research: Space Physics*, *121*(1), 397-412. https://doi.org/10.1002/2015JA021569

Reeves, G. D., McAdams, K. L., Friedel, R. H. W., & O'Brien, T. P. (2003). Acceleration and loss of relativistic electrons during geomagnetic storms. *Geophysical Research Letters*, *30*(10). https://doi.org/10.1029/2002GL016513

Reeves, G. D., Spence, H. E., Henderson, M. G., Morley, S. K., Friedel, R. H. W., Funsten, H. O., . . . Niehof, J. T. (2013). Electron Acceleration in the Heart of the Van Allen Radiation Belts. *Science*, *341*(6149), 991-994. 10.1126/science.1237743

Rodger, C. J., Clilverd, M. A., Kavanagh, A. J., Watt, C. E. J., Verronen, P. T., & Raita, T. (2012). Contrasting the responses of three different ground-

based instruments to energetic electron precipitation. *Radio Science*, *47*(2). https://doi.org/10.1029/2011RS004971

Rodger, C. J., Clilverd, M. A., Thomson, N. R., Gamble, R. J., Seppälä, A., Turunen, E., . . . Berthelier, J.-J. (2007). Radiation belt electron precipitation into the atmosphere: Recovery from a geomagnetic storm. *Journal of Geophysical Research: Space Physics*, *112*(A11). https://doi.org/10.1029/2007JA012383

Rodger, C. J., Turner, D. L., Clilverd, M. A., & Hendry, A. T. (2019). Magnetic Local Time-Resolved Examination of Radiation Belt Dynamics during High-Speed Solar Wind Speed-Triggered Substorm Clusters. *Geophysical Research Letters*, *46*(17-18), 10219-10229. https://doi.org/10.1029/2019GL083712

Rodriguez, J. V. (2014a). *GOES 13-15 MAGE/PD pitch angles algorithm theoretical basis document.* https://ngdc.noaa.gov/stp/satellite/goes/documentation.html.

Rodriguez, J. V. (2014b). *GOES EPEAD science-quality electron fluxes algorithm theoretical basis document.* https://ngdc.noaa.gov/stp/satellite/goes/doc/EPEAD_Electron_Science_Reprocessing_ATBD_v1.0.pdf

Rodriguez, J. V., Onsager, T. G., & Mazur, J. E. (2010). The east-west effect in solar proton flux measurements in geostationary orbit: A new GOES capability. *Geophysical Research Letters*, *37*(7). https://doi.org/10.1029/2010GL042531

Roederer, J. G. (1967). On the adiabatic motion of energetic particles in a model magnetosphere. *Journal of Geophysical Research (1896-1977)*, *72*(3), 981-992. https://doi.org/10.1029/JZ072i003p00981

Rosenberg, T. J., Lanzerotti, L. J., Bailey, D. K., & Pierson, J. D. (1972). Energy spectra in relativistic electron precipitation events. *Journal of Atmospheric and Terrestrial Physics*, *34*(12), 1977-1990. https://doi.org/10.1016/0021-9169(72)90179-1

Rostoker, G., Skone, S., & Baker, D. N. (1998). On the origin of relativistic electrons in the magnetosphere associated with some geomagnetic storms. *Geophysical Research Letters*, *25*(19), 3701-3704. https://doi.org/10.1029/98GL02801

Russell, C. T., Ginskey, M., Petrinec, S., & Le, G. (1992). The effect of solar wind dynamic pressure changes on low and mid-latitude magnetic records. *Geophysical Research Letters*, *19*(12), 1227-1230. https://doi.org/10.1029/92GL01161

Saikin, A. A., Zhang, J.-C., Allen, R. C., Smith, C. W., Kistler, L. M., Spence, H. E., . . . Jordanova, V. K. (2015). The occurrence and wave properties of H+-, He+-, and O+-band EMIC waves observed by the Van Allen Probes. *Journal of Geophysical Research: Space Physics*, *120*(9), 7477-7492. https://doi.org/10.1002/2015JA021358

Samsonov, A. A., Gordeev, E., Tsyganenko, N. A., Šafránková, J., Němeček, Z., Šimůnek, J., . . . Raeder, J. (2016). Do we know the actual magnetopause position for typical solar wind conditions? *Journal of Geophysical Research: Space Physics*, *121*(7), 6493-6508. https://doi.org/10.1002/2016JA022471

Samsonov, A. A., Sergeev, V. A., Kuznetsova, M. M., & Sibeck, D. G. (2015). Asymmetric magnetospheric compressions and expansions in response to impact of inclined interplanetary shock. *Geophysical Research Letters*, *42*(12), 4716-4722. https://doi.org/10.1002/2015GL064294

Sandanger, M. I., Søraas, F., Sørbø, M., Aarsnes, K., Oksavik, K., & Evans, D. S. (2009). Relativistic electron losses related to EMIC waves during CIR and CME storms. *Journal of Atmospheric and Solar-Terrestrial Physics*, *71*(10), 1126-1144. https://doi.org/10.1016/j.jastp.2008.07.006

Santolík, O., Němec, F., Gereová, K., Macúšová, E., de Conchy, Y., & Cornilleau-Wehrlin, N. (2004). Systematic analysis of equatorial noise below the lower hybrid frequency. *Ann. Geophys.*, *22*(7), 2587-2595. 10.5194/angeo-22-2587-2004

Schulz, M., & Lanzerotti, L. J. (1974). Particle diffusion in the radiation belts. *Physics and Chemistry in Space*. https://doi.org/10.1016/0031-9201(74)90066-1

Scolini, C., Chané, E., Temmer, M., Kilpua, E. K. J., Dissauer, K., Veronig, A. M., . . . Poedts, S. (2020). CME–CME Interactions as Sources of CME Geoeffectiveness: The Formation of the Complex Ejecta and Intense Geomagnetic Storm in 2017 Early September. *The Astrophysical Journal Supplement Series*, *247*(1), 21. 10.3847/1538-4365/ab6216

Selesnick, R. S. (2015). High-energy radiation belt electrons from CRAND. *Journal of Geophysical Research: Space Physics*, *120*(4), 2912-2917. https://doi.org/10.1002/2014JA020963

Selesnick, R. S., Baker, D. N., Jaynes, A. N., Li, X., Kanekal, S. G., Hudson, M. K., & Kress, B. T. (2014). Observations of the inner radiation belt: CRAND and trapped solar protons. *Journal of Geophysical Research: Space Physics*, *119*(8), 6541-6552. https://doi.org/10.1002/2014JA020188

Selesnick, R. S., Baker, D. N., Kanekal, S. G., Hoxie, V. C., & Li, X. (2018). Modeling the Proton Radiation Belt With Van Allen Probes Relativistic Electron-Proton Telescope Data. *Journal of Geophysical Research: Space Physics*, *123*(1), 685-697. https://doi.org/10.1002/2017JA024661

Selesnick, R. S., & Blake, J. B. (2000). On the source location of radiation belt relativistic electrons. *Journal of Geophysical Research: Space Physics*, *105*(A2), 2607-2624. https://doi.org/10.1029/1999JA900445

Sellers, F., & Hanser, F. (1996). *Design and calibration of the GOES-8 particle sensors: the EPS and HEPAD* (Vol. 2812). SPIE. https://doi.org/10.1117/12.254083

Shabansky, V. P. (1971). Some processes in the magnetosphere. *Space Science Reviews*, *12*(3), 299-418. 10.1007/BF00165511

Shen, C., Xu, M., Wang, Y., Chi, Y., & Luo, B. (2018). Why the Shock-ICME Complex Structure Is Important: Learning from the Early 2017 September CMEs. *The Astrophysical Journal*, *861*(1), 28. 10.3847/1538-4357/aac204

Shprits, Y. Y., Drozdov, A. Y., Spasojevic, M., Kellerman, A. C., Usanova, M. E., Engebretson, M. J., . . . Aseev, N. A. (2016). Wave-induced loss of

ultra-relativistic electrons in the Van Allen radiation belts. *Nature Communications*, *7*(1), 12883. 10.1038/ncomms12883

Shprits, Y. Y., Horne, R. B., Kellerman, A. C., & Drozdov, A. Y. (2018). The dynamics of Van Allen belts revisited. *Nature Physics*, *14*(2), 102-103. 10.1038/nphys4350

Shprits, Y. Y., Kellerman, A., Aseev, N., Drozdov, A. Y., & Michaelis, I. (2017). Multi-MeV electron loss in the heart of the radiation belts. *Geophysical Research Letters*, *44*(3), 1204-1209. https://doi.org/10.1002/2016GL072258

Shprits, Y. Y., Thorne, R. M., Friedel, R., Reeves, G. D., Fennell, J., Baker, D. N., & Kanekal, S. G. (2006). Outward radial diffusion driven by losses at magnetopause. *Journal of Geophysical Research: Space Physics*, *111*(A11). https://doi.org/10.1029/2006JA011657

Shue, J.-H., Chao, J.-K., Song, P., McFadden, J. P., Suvorova, A., Angelopoulos, V., . . . Plaschke, F. (2009). Anomalous magnetosheath flows and distorted subsolar magnetopause for radial interplanetary magnetic fields. *Geophysical Research Letters*, *36*(18). https://doi.org/10.1029/2009GL039842

Shue, J.-H., Chao, J. K., Fu, H. C., Russell, C. T., Song, P., Khurana, K. K., & Singer, H. J. (1997). A new functional form to study the solar wind control of the magnetopause size and shape. *Journal of Geophysical Research: Space Physics*, *102*(A5), 9497-9511. https://doi.org/10.1029/97JA00196

Shue, J.-H., Song, P., Russell, C. T., Steinberg, J. T., Chao, J. K., Zastenker, G., . . . Kawano, H. (1998). Magnetopause location under extreme solar wind conditions. *Journal of Geophysical Research: Space Physics*, *103*(A8), 17691-17700. https://doi.org/10.1029/98JA01103

Sibeck, D. G., Baumjohann, W., Elphic, R. C., Fairfield, D. H., Fennell, J. F., Gail, W. B., . . . Takahashi, K. (1989). The magnetospheric response to 8-minute period strong-amplitude upstream pressure variations. *Journal of Geophysical Research: Space Physics*, *94*(A3), 2505-2519. https://doi.org/10.1029/JA094iA03p02505

Sibeck, D. G., Borodkova, N. L., Schwartz, S. J., Owen, C. J., Kessel, R., Kokubun, S., . . . Zastenker, G. N. (1999). Comprehensive study of the magnetospheric response to a hot flow anomaly. *Journal of Geophysical Research: Space Physics*, *104*(A3), 4577-4593. https://doi.org/10.1029/1998JA900021

Sillanpää, I., Ganushkina, N. Y., Dubyagin, S., & Rodriguez, J. V. (2017). Electron Fluxes at Geostationary Orbit From GOES MAGED Data. *Space Weather*, *15*(12), 1602-1614. https://doi.org/10.1002/2017SW001698

Singer, H., Matheson, L., Grubb, R., Newman, A., & Bouwer, D. (1996). *Monitoring space weather with the GOES magnetometers* (Vol. 2812). SPIE. https://doi.org/10.1117/12.254077

Singer, S. F. (1958). "Radiation Belt" and Trapped Cosmic-Ray Albedo. *Physical Review Letters*, *1*(5), 171-173. 10.1103/PhysRevLett.1.171

Sorathia, K. A., Merkin, V. G., Ukhorskiy, A. Y., Mauk, B. H., & Sibeck, D. G. (2017). Energetic particle loss through the magnetopause: A combined global MHD and test-particle study. *Journal of Geophysical Research:*

Space Physics, *122*(9), 9329-9343. https://doi.org/10.1002/2017JA024268

Southwood, D. J. (1974). Some features of field line resonances in the magnetosphere. *Planetary and Space Science*, *22*(3), 483-491. https://doi.org/10.1016/0032-0633(74)90078-6

Spence, H. E., Reeves, G. D., Baker, D. N., Blake, J. B., Bolton, M., Bourdarie, S., . . . Thorne, R. M. (2014). Science Goals and Overview of the Radiation Belt Storm Probes (RBSP) Energetic Particle, Composition, and Thermal Plasma (ECT) Suite on NASA's Van Allen Probes Mission. In N. Fox & J. L. Burch (Eds.), *The Van Allen Probes Mission* (pp. 311-336). Springer US. https://doi.org/10.1007/978-1-4899-7433-4_10

Staples, F. A., Kellerman, A. C., Murphy, K. R., Rae, I. J., Sandhu, J. K., & Forsyth, C. (in review). Resolving Magnetopause Shadowing Using Multi-Mission Measurements of Phase Space Density. *Journal of Geophysical Research: Space Physics*. https://doi.org/10.1002/essoar.10506455.1

Staples, F. A., Rae, I. J., Forsyth, C., Smith, A. R. A., Murphy, K. R., Raymer, K. M., . . . Imber, S. M. (2020). Do Statistical Models Capture the Dynamics of the Magnetopause During Sudden Magnetospheric Compressions? *Journal of Geophysical Research: Space Physics*, *125*(4), e2019JA027289. https://doi.org/10.1029/2019JA027289

Sugiura, M., & Poros, D. (1971). *Hourly values of equatorial Dst for the years 1957 to 1970*. NASA, Goddard Space Flight Center.

Summers, D., Thorne, R. M., & Xiao, F. (1998). Relativistic theory of wave-particle resonant diffusion with application to electron acceleration in the magnetosphere. *Journal of Geophysical Research: Space Physics*, *103*(A9), 20487-20500. https://doi.org/10.1029/98JA01740

Suvorova, A. V., & Dmitriev, A. V. (2015). Magnetopause inflation under radial IMF: Comparison of models. *Earth and Space Science*, *2*(4), 107-114. https://doi.org/10.1002/2014EA000084

Taylor, H. E. (1969). Sudden commencement associated discontinuities in the interplanetary magnetic field observed by IMP 3. *Solar Physics*, *6*(2), 320-334. 10.1007/BF00150957

Thébault, E., Finlay, C. C., Beggan, C. D., Alken, P., Aubert, J., Barrois, O., . . . Zvereva, T. (2015). International Geomagnetic Reference Field: the 12th generation. *Earth, Planets and Space*, *67*(1), 79. 10.1186/s40623-015-0228-9

Thorne, R. M., & Horne, R. B. (1992). The contribution of ion-cyclotron waves to electron heating and SAR-arc excitation near the storm-time plasmapause. *Geophysical Research Letters*, *19*(4), 417-420. https://doi.org/10.1029/92GL00089

Thorne, R. M., & Kennel, C. F. (1971). Relativistic electron precipitation during magnetic storm main phase. *Journal of Geophysical Research (1896-1977)*, *76*(19), 4446-4453. https://doi.org/10.1029/JA076i019p04446

Thorne, R. M., O'Brien, T. P., Shprits, Y. Y., Summers, D., & Horne, R. B. (2005). Timescale for MeV electron microburst loss during geomagnetic storms. *Journal of Geophysical Research: Space Physics*, *110*(A9). https://doi.org/10.1029/2004JA010882

Tsurutani, B. T., & Lakhina, G. S. (1997). Some basic concepts of wave-particle interactions in collisionless plasmas. *Reviews of Geophysics*, *35*(4), 491-501. https://doi.org/10.1029/97RG02200

Tsurutani, B. T., & Smith, E. J. (1974). Postmidnight chorus: A substorm phenomenon. *Journal of Geophysical Research (1896-1977)*, *79*(1), 118-127. https://doi.org/10.1029/JA079i001p00118

Tsyganenko, N. A., Singer, H. J., & Kasper, J. C. (2003). Storm-time distortion of the inner magnetosphere: How severe can it get? *Journal of Geophysical Research: Space Physics*, *108*(A5). https://doi.org/10.1029/2002JA009808

Tu, W., Elkington, S. R., Li, X., Liu, W., & Bonnell, J. (2012). Quantifying radial diffusion coefficients of radiation belt electrons based on global MHD simulation and spacecraft measurements. *Journal of Geophysical Research: Space Physics*, *117*(A10). https://doi.org/10.1029/2012JA017901

Tu, W., Xiang, Z., & Morley, S. K. (2019). Modeling the Magnetopause Shadowing Loss During the June 2015 Dropout Event. *Geophysical Research Letters*, *46*(16), 9388-9396. https://doi.org/10.1029/2019GL084419

Turner, D. L., Angelopoulos, V., Li, W., Bortnik, J., Ni, B., Ma, Q., . . . Rodriguez, J. V. (2014a). Competing source and loss mechanisms due to wave-particle interactions in Earth's outer radiation belt during the 30 September to 3 October 2012 geomagnetic storm. *Journal of Geophysical Research: Space Physics*, *119*(3), 1960-1979. https://doi.org/10.1002/2014JA019770

Turner, D. L., Angelopoulos, V., Li, W., Hartinger, M. D., Usanova, M., Mann, I. R., . . . Shprits, Y. (2013). On the storm-time evolution of relativistic electron phase space density in Earth's outer radiation belt. *Journal of Geophysical Research: Space Physics*, *118*(5), 2196-2212. https://doi.org/10.1002/jgra.50151

Turner, D. L., Angelopoulos, V., Morley, S. K., Henderson, M. G., Reeves, G. D., Li, W., . . . Rodriguez, J. V. (2014b). On the cause and extent of outer radiation belt losses during the 30 September 2012 dropout event. *Journal of Geophysical Research: Space Physics*, *119*(3), 1530-1540. https://doi.org/10.1002/2013JA019446

Turner, D. L., Kilpua, E. K. J., Hietala, H., Claudepierre, S. G., O'Brien, T. P., Fennell, J. F., . . . Reeves, G. D. (2019). The Response of Earth's Electron Radiation Belts to Geomagnetic Storms: Statistics From the Van Allen Probes Era Including Effects From Different Storm Drivers. *Journal of Geophysical Research: Space Physics*, *124*(2), 1013-1034. https://doi.org/10.1029/2018JA026066

Turner, D. L., Morley, S. K., Miyoshi, Y., Ni, B., & Huang, C.-L. (2012a). Outer Radiation Belt Flux Dropouts: Current Understanding and Unresolved Questions. In *Dynamics of the Earth's Radiation Belts and Inner Magnetosphere* (pp. 195-212). https://doi.org/https://doi.org/10.1029/2012GM001310

Turner, D. L., Shprits, Y., Hartinger, M., & Angelopoulos, V. (2012b). Explaining sudden losses of outer radiation belt electrons during geomagnetic storms. *Nature Physics*, *8*(3), 208-212. 10.1038/nphys2185

Tuszewski, M., Cayton, T. E., Ingraham, J. C., & Kippen, R. M. (2004). Bremsstrahlung effects in energetic particle detectors. *Space Weather*, *2*(10). https://doi.org/10.1029/2003SW000057

Usanova, M. E., Drozdov, A., Orlova, K., Mann, I. R., Shprits, Y., Robertson, M. T., . . . Wygant, J. (2014). Effect of EMIC waves on relativistic and ultrarelativistic electron populations: Ground-based and Van Allen Probes observations. *Geophysical Research Letters*, *41*(5), 1375-1381. https://doi.org/10.1002/2013GL059024

Van Allen, J. A., Ludwig, G. H., Ray, E. C., & McIlwain, C. E. (1958). Observation of High Intensity Radiation by Satellites 1958 Alpha and Gamma. *Journal of Jet Propulsion*, *28*(9), 588-592. https://doi.org/10.2514/8.7396

Vernov, S., Chudakov, A., Vakulov, P., & Logachev, Y. I. (1959). STUDY OF COSMIC RAYS AND TERRESTRIAL CORPUSCULAR RADIATION BY COSMIC ROCKET. Doklady Akad. Nauk SSSR,

Walker, A. D. M. (1981). The Kelvin-Helmholtz instability in the low-latitude boundary layer. *Planetary and Space Science*, *29*(10), 1119-1133. https://doi.org/10.1016/0032-0633(81)90011-8

Walt, M. (1994). *Introduction to geomagnetically trapped radiation*. Cambridge University Press.

Wang, D., Yuan, Z., Deng, X., Zhou, M., Huang, S., Li, M., . . . Pang, Y. (2014). Compression-related EMIC waves drive relativistic electron precipitation. *Science China Technological Sciences*, *57*(12), 2418-2425. 10.1007/s11431-014-5701-3

Wang, Y., Sibeck, D. G., Merka, J., Boardsen, S. A., Karimabadi, H., Sipes, T. B., . . . Lin, R. (2013). A new three-dimensional magnetopause model with a support vector regression machine and a large database of multiple spacecraft observations. *Journal of Geophysical Research: Space Physics*, *118*(5), 2173-2184. https://doi.org/10.1002/jgra.50226

Wanliss, J. A., & Showalter, K. M. (2006). High-resolution global storm index: Dst versus SYM-H. *Journal of Geophysical Research: Space Physics*, *111*(A2). https://doi.org/10.1029/2005JA011034

Webb, D. F., & Allen, J. H. (2004). Spacecraft and Ground Anomalies Related to the October-November 2003 Solar Activity. *Space Weather*, *2*(3). https://doi.org/10.1029/2004SW000075

Werner, A. L. E., Yordanova, E., Dimmock, A. P., & Temmer, M. (2019). Modeling the Multiple CME Interaction Event on 6–9 September 2017 with WSA-ENLIL+Cone. *Space Weather*, *17*(2), 357-369. https://doi.org/10.1029/2018SW001993

Williams, D. J. (1987). Ring current and radiation belts. *Reviews of Geophysics*, *25*(3), 570-578. https://doi.org/10.1029/RG025i003p00570

Woodger, L. A., Halford, A. J., Millan, R. M., McCarthy, M. P., Smith, D. M., Bowers, G. S., . . . Liang, X. (2015). A summary of the BARREL campaigns: Technique for studying electron precipitation. *Journal of Geophysical Research: Space Physics*, *120*(6), 4922-4935. https://doi.org/10.1002/2014JA020874

Wright, A. N., & Rickard, G. J. (1995). ULF pulsations driven by magnetopause motions: Azimuthal phase characteristics. *Journal of Geophysical*

Research: Space Physics, *100*(A12), 23703-23710. https://doi.org/10.1029/95JA01765

Wygant, J. R., Bonnell, J. W., Goetz, K., Ergun, R. E., Mozer, F. S., Bale, S. D., . . . Tao, J. B. (2014). The Electric Field and Waves Instruments on the Radiation Belt Storm Probes Mission. In N. Fox & J. L. Burch (Eds.), *The Van Allen Probes Mission* (pp. 183-220). Springer US. https://doi.org/10.1007/978-1-4899-7433-4_6

Xiang, Z., Tu, W., Li, X., Ni, B., Morley, S. K., & Baker, D. N. (2017). Understanding the Mechanisms of Radiation Belt Dropouts Observed by Van Allen Probes. *Journal of Geophysical Research: Space Physics*, *122*(10), 9858-9879. https://doi.org/10.1002/2017JA024487

Zirker, J. B. (1977). Coronal holes and high-speed wind streams. *Reviews of Geophysics*, *15*(3), 257-269. https://doi.org/10.1029/RG015i003p00257